Advancing airborne remote sensing of CO_2 and CH_4 emissions from point sources

Jakob Borchardt

Universität Bremen, 2022

Advancing airborne remote sensing of CO_2 and CH_4 emissions from point sources

Vom Fachbereich für Physik und Elektrotechnik
der Universität Bremen

zur Erlangung des akademischen Grades

Doktor der Naturwissenschaften (Dr. rer. nat.)

genehmigte Dissertation

von

M. Sc. Jakob Borchardt

wohnhaft in Bremen

1. Gutachter:	Prof. Dr. J. P. Burrows
2. Gutachter:	Prof. Dr. M. Vrekoussis
Eingereicht am:	03.08.2022
Datum des Promotionskolloquium:	07.12.2022

Abstract

The global mean surface temperature (GMST) on Earth in the period $2011 - 2020$ has increased $\sim 1.1\,°C$ above preindustrial temperatures. This temperature change results mainly from the increased radiative forcing due to increased levels of anthropogenic greenhouse gases in the atmosphere, especially CO_2 and CH_4. For an efficient reduction of CO_2 and CH_4 emissions, their locations and emission strengths have to be known. Additionally, emission reductions must be monitored, and new satellite sensors must be validated. Airborne remote sensing instruments allow observing dedicated regions for source detection, emission monitoring, and satellite validation. However, new instruments and methods to infer gas concentrations from the acquired data are needed to advance the airborne remote sensing of greenhouse gases.

In this thesis, three research questions were studied: Is it possible to apply the weighting function modified differential optical absorption spectroscopy (WFM-DOAS) retrieval method to hyperspectral data to infer greenhouse gas emissions? Is the observation and quantification of emissions improved with a new imaging instrument specifically designed for that task? And can the retrieval of greenhouse gases from airborne remote sensing measurements be improved by taking scattering in the atmosphere into account?

The first question was studied by applying the WFM-DOAS retrieval to AVIRIS-NG hyperspectral data (spectral resolution $\sim 5.5\,nm$) acquired during the ABoVE measurement campaign in Canada and a data set containing the observation of a coal mine ventilation shaft plume. In the data set, multiple methane emission plumes could be detected, and the emissions were estimated for five of them. Additionally, the influence of different surface types on the retrieval results was studied. For some surface types, the biases reached $\pm 5 - 10\,\%$, while the retrieval precision was $2 - 5\,\%$ total column increase.

The second question was examined by developing, building, and deploying the MAMAP2D-Light instrument successfully. It is an imaging airborne remote sensing spectrometer with $\sim 1.1\,nm$ spectral resolution covering the absorption bands of CO_2 and CH_4 between 1560 and 1690 nm. It observes 28 ground scenes with a spatial resolution of $22 \times 6\,m^2$, creating an image of the ground while flying over it. The total column precision was $0.28\,\%$ after binning to $100 \times 100\,m^2$ ground scenes, and $0.7\,\%$ unbinned. During the first measurement flight over the coal-fired power plant Jänschwalde in Eastern Germany in June 2021, the CO_2 emission plume was mapped successfully, and emissions of $10.3\,Mt\ CO_2\ yr^{-1}$ were estimated, which were close to the emission estimate based on activity data of $11.6\,Mt\ CO_2\ yr^{-1}$.

For the third question, a forward model adapted to the airborne geometry was implemented in the optimal estimation-based Fast atmOspheric traCe gAs retrievaL (FOCAL AIR). It included a parametrized treatment of scattering. Nevertheless, the Jacobian of the forward

model could be calculated analytically for all atmospheric parameters, reducing the computational resources needed for the retrieval. In synthetic measurements, treating scattering parametrized reduced errors compared to an absorption-only forward model by up to 50 %. Additionally, applying the FOCAL AIR retrieval and the WFM-DOAS on the MAMAP data set acquired over the power plant Jänschwalde in May 2018, different FOCAL AIR retrieval configurations were tested. With the best retrieval configuration, an emission of 18.6 Mt CO_2 yr^{-1} was estimated for the power plant Jänschwalde, close to the emission estimate from WFM-DOAS retrieval results of 19.4 Mt CO_2 yr^{-1}.

Publications

Parts of this thesis have already been published and presented in articles, conference and workshop contributions.

Peer reviewed publications

Borchardt, J., Gerilowski, K., Krautwurst, S., Bovensmann, H., Thorpe, A. K., Thompson, D. R., Frankenberg, C., Miller, C. E., Duren, R. M., and Burrows, J. P. Detection and quantification of CH4 plumes using the WFM-DOAS retrieval on AVIRIS-NG hyperspectral data. *Atmospheric Measurement Techniques*, 14, no. 2:pp. 1267–1291. doi: 10.5194/amt-14-1267-2021, 2021.

Frankenberg, C., Thorpe, A. K., Thompson, D. R., Hulley, G., Kort, E. A., Vance, N., Borchardt, J., Krings, T., Gerilowski, K., Sweeney, C., Conley, S., Bue, B. D., Aubrey, A. D., Hook, S., and Green, R. O. Airborne methane remote measurements reveal heavy-tail flux distribution in Four Corners region. *Proceedings of the National Academy of Sciences*, 113, no. 35:pp. 9734–9739. doi:10.1073/pnas.1605617113. `http://www.pnas.org/content/early/2016/08/10/1605617113.full.pdf`, URL `http://www.pnas.org/content/early/2016/08/10/1605617113.abstract`, 2016.

Krautwurst, S., Gerilowski, K., Borchardt, J., Wildmann, N., Gałkowski, M., Swolkień, J., Marshall, J., Fiehn, A., Roiger, A., Ruhtz, T., Gerbig, C., Necki, J., Burrows, J. P., Fix, A., and Bovensmann, H. Quantification of CH4 coal mining emissions in Upper Silesia by passive airborne remote sensing observations with the Methane Airborne MAPper (MAMAP) instrument during the CO2 and Methane (CoMet) campaign. *Atmospheric Chemistry and Physics*, 21, no. 23:pp. 17345–17371. doi:10.5194/acp-21-17345-2021, 2021.

Krautwurst, S., Gerilowski, K., Jonsson, H. H., Thompson, D. R., Kolyer, R. W., Iraci, L. T., Thorpe, A. K., Horstjann, M., Eastwood, M., Leifer, I., Vigil, S. A., Krings, T., Borchardt, J., Buchwitz, M., Fladeland, M. M., Burrows, J. P., and Bovensmann, H. Methane emissions from a Californian landfill, determined from airborne remote sensing and in situ measurements. *Atmospheric Measurement Techniques*, 10, no. 9:pp. 3429–3452. doi:10.5194/amt-10-3429-2017, 2017.

Noël, S., Reuter, M., Buchwitz, M., Borchardt, J., Hilker, M., Bovensmann, H., Burrows, J. P., Di Noia, A., Suto, H., Yoshida, Y., Buschmann, M., Deutscher, N. M., Feist,

D. G., Griffith, D. W. T., Hase, F., Kivi, R., Morino, I., Notholt, J., Ohyama, H., Petri, C., Podolske, J. R., Pollard, D. F., Sha, M. K., Shiomi, K., Sussmann, R., Té, Y., Velazco, V. A., and Warneke, T. XCO_2 retrieval for GOSAT and GOSAT-2 based on the FOCAL algorithm. *Atmospheric Measurement Techniques*, 14, no. 5:pp. 3837–3869. doi:10.5194/amt-14-3837-2021. URL `https://amt.copernicus.org/articles/14/3837/2021/`, 2021.

Noël, S., Reuter, M., Buchwitz, M., Borchardt, J., Hilker, M., Schneising, O., Bovensmann, H., Burrows, J. P., Noia, A. D., Parker, R. J., Suto, H., Yoshida, Y., Buschmann, M., Deutscher, N. M., Feist, D. G., Griffith, D. W. T., Hase, F., Kivi, R., Liu, C., Morino, I., Notholt, J., Oh, Y.-S., Ohyama, H., Petri, C., Pollard, D. F., Rettinger, M., Roehl, C., Rousogenous, C., Sha, M. K., Shiomi, K., Strong, K., Sussmann, R., Té, Y., Velazco, V. A., Vrekoussis, M., and Warneke, T. Retrieval of greenhouse gases from GOSAT and GOSAT-2 using the FOCAL algorithm. *Atmospheric Measurement Techniques*, 15, no. 11:pp. 3401–3437. doi:10.5194/amt-15-3401-2022, 2022.

Reuter, M., Bovensmann, H., Buchwitz, M., Borchardt, J., Krautwurst, S., Gerilowski, K., Lindauer, M., Kubistin, D., and Burrows, J. P. Development of a small unmanned aircraft system to derive CO2 emissions of anthropogenic point sources. *Atmospheric Measurement Techniques*, 14, no. 1:pp. 153–172. doi:10.5194/amt-14-153-2021, 2021.

Thorpe, A. K., Frankenberg, C., Thompson, D. R., Duren, R. M., Aubrey, A. D., Bue, B. D., Green, R. O., Gerilowski, K., Krings, T., Borchardt, J., Kort, E. A., Sweeney, C., Conley, S., Roberts, D. A., and Dennison, P. E. Airborne DOAS retrievals of methane, carbon dioxide, and water vapor concentrations at high spatial resolution: application to AVIRIS-NG. *Atmospheric Measurement Techniques*, 10, no. 10:pp. 3833–3850. doi:10.5194/amt-10-3833-2017, 2017.

Selected oral presentations

Borchardt, J., Gerilowski, K., Krautwurst, S., Bovensmann, H., Buchwitz, M., and Burrows, J. P. Methane retrieval and interpretation using high spatial resolution airborne measurements. Seminar on Physics and Chemistry of the Atmosphere, University of Bremen, Germany, 10 November 2017.

Borchardt, J., Krautwurst, S., Gerilowski, K., Thomsson, W., Franke, J., Bovensmann, H., and Burrows, J. P. Observation of greenhouse gas point sources using airborne remote sensing measurements. Seminar on Physics and Chemistry of the Atmosphere, University of Bremen, Germany, 5 February 2021.

Borchardt, J., Krautwurst, S., Gerilowski, K., Thomsson, W., Franke, J., Reuter, M., Bovensmann, H., and Burrows, J. P. Advancing airborne remote sensing of CO2and

CH4 emissions from point sources. Seminar on Ocean, Ice and Atmosphere, University of Bremen, Germany, 12 July 2021.

Borchardt, J., Thorpe, A. K., Eastwood, M., Thompson, D. R., Frankenberg, C., Green, R. O., Gerilowski, K., Krautwurst, S., Ruhtz, T., Buchwitz, M., Krings, T., Bovensmann, H., and Burrows, J. P. Methane retrieval and interpretation using high spatialresolution AVIRIS-NG aircraft radiances. DPG Spring Meeting, Erlangen, Germany, 4 - 9 March 2018.

Selected poster presentations

Borchardt, J., Gerilowski, K., Krautwurst, S., Thomssen, W., Franke, J., Kumm, M., Janen, P., Wellhausen, J., Bovensmann, H., and Burrows FRS, J. The New Imaging Spectrometer MAMAP2D-Light Initial Calibration and First Measurement Results. In *AGU Fall Meeting Abstracts*, volume 2021, pp. A25G–1759, 2021.

Borchardt, J., Gerilowski, K., Krautwurst, S., Thomsson, W., Franke, J., Bovensmann, H., Burrows, J. P., Kumm, M., Janßen, P., and Wellhausen, J. MaMaP2D-Light- A new imaging spectrometer for greenhouse gasmeasurements. ATMOS conference, Online, 14. -17. June 2021.

Borchardt, J., Gerilowski, K., Krautwurst, S., Thomsson, W., Franke, J., Kumm, M., Janßen, P., Wellhausen, J., Bovensmann, H., and Burrows, J. P. The New Imaging Spectrometer MAMAP2D-Light –First Measurement Results. IWGGMS conference, Online, 25 November 2021.

Borchardt, J., Reuter, M., Krautwurst, S., Gerilowski, K., Hilker, M., Noel, S., Bovensmann, H., and Burrows FRS, J. P. FOCAL-AIR: Adaption of the Fast atmOspheric traCe gAs retrievaL to airborne high spectral resolution remote sensing measurements. In *AGU Fall Meeting Abstracts*, volume 2020, pp. A210–0011, 2020.

Contents

Publications vi

1. Introduction 1

2. Sources and sinks of the greenhouse gases CH_4 and CO_2 6
2.1. Sources and sinks of CH_4 . . . 6
2.2. Sources and sinks of CO_2 . . . 12

3. Theoretical background 16
3.1. The atmosphere of the Earth . . . 16
3.2. Radiative transfer in the atmosphere . . . 19
3.3. Relevant spectroscopy of the molecules CH_4, CO_2 and O_2 . . . 23
3.3.1. Absorption in atoms and molecules . . . 23
3.3.2. Molecular structure and absorption of CH_4 . . . 32
3.3.3. Molecular structure and absorption of CO_2 . . . 34
3.3.4. Molecular structure and absorption of O_2 . . . 35
3.4. Radiation budget of the Earth and greenhouse effect . . . 36
3.5. Dynamics in the lower troposphere . . . 39

4. Application of spectroscopy to observe CO_2 and CH_4 concentrations in the atmosphere 42
4.1. In Situ measurements of the greenhouse gases CH_4 and CO_2 . . . 42
4.2. Remote sensing measurements of the greenhouse gases CH_4 and CO_2 . . . 44

5. Instruments, data sets and methods 48
5.1. Airborne remote sensing systems and data sets for observation of CO_2 and CH_4 total column anomalies . . . 48
5.1.1. The AVIRIS-NG remote sensing system and data sets . . . 50
5.1.2. The MAMAP remote sensing system and data sets . . . 52
5.1.3. The MAMAP2D-Light remote sensing instrument and data sets . . . 54
5.2. Retrieval of column enhancements . . . 63
5.2.1. The WFM-DOAS algorithm . . . 63
5.2.2. The FOCAL AIR retrieval method . . . 65
5.2.3. Destriping of imaging data . . . 82
5.3. Cross-sectional flux method . . . 84

6. Results 87
6.1. Retrieval of AVIRIS-NG imaging data for plume detection and quantification 87
6.1.1. Fitting windows for AVIRIS-NG data . . . 87

6.1.2. WFM-DOAS sensitivity analysis using AVIRIS-NG synthetic measurements . . . 90
6.1.3. Low radiance scenes . . . 96
6.1.4. Detected plumes . . . 98
6.1.5. Comparison of WFM-DOAS retrieval results with IMAP-DOAS and MF results . . . 104
6.1.6. Emission and uncertainty estimation . . . 107
6.1.7. Assessment of WFM-DOAS retrieval method applied to AVIRIS-NG data . . . 108
6.2. Results acquired with MAMAP2D-Light . . . 109
6.2.1. Characterization of the MAMAP2D-Light instrument . . . 109
6.2.2. Emission estimation of the Jänschwalde power plant on 17.06.2021 . . . 117
6.2.3. Performance summary of the MAMAP2D-Light instrument . . . 120
6.3. Investigation of the FOCAL AIR retrieval algorithm . . . 122
6.3.1. FOCAL AIR retrieval on synthetic measurements . . . 122
6.3.2. Noise and zero-level offset model for FOCAL AIR on MAMAP measurements . . . 126
6.3.3. Comparison of FOCAL AIR xCO_2, $xCO_2(CH_4)$ and WFM-DOAS retrieval results . . . 129
6.3.4. Emission estimation of the Jänschwalde power plant plume from FOCAL AIR retrieval results . . . 142
6.3.5. Conclusion on the improvement of total column retrievals by including scattering in the retrieval . . . 145

7. Discussion **148**
7.1. Comparison of instruments . . . 148
7.2. Comparison of retrieval methods . . . 153
7.3. Emission estimate from plume images . . . 157

8. Summary and outlook **160**

A. Appendix **165**
A.1. Comparison of ERA5 50m height averaged data with surface weather stations 165
A.2. Cross-sections through the plume for flux inversion of MAMAP2D-Light data 167
A.3. Aerosol scenarios for FOCAL AIR simulated measurements . . . 172
A.4. Updated spectral calibration of the MAMAP instrument . . . 175
A.4.1. Calibration setup and data description . . . 175
A.4.2. Calibration caluclation and results . . . 175
A.5. Flux inversion and uncertainty analysis of the WFM-DOAS retrieval results for the Jänschwalde power plant from MAMAP data . . . 180
A.6. FOCAL AIR cross-tracks for cross-sectional flux method . . . 185
A.6.1. Cross-tracks for flux inversion of FOCAL AIR absorption-only 2-window retrieval results . . . 185
A.6.2. Cross-tracks for flux inversion of FOCAL AIR scattering 2-window retrieval results . . . 189

A.6.3. Cross-tracks for flux inversion of FOCAL AIR absorption-only 1-window retrieval results 193
A.6.4. Cross-tracks for flux inversion of FOCAL AIR scattering 1-window retrieval results 197

List of Figures **201**

List of Tables **205**

List of Abbreviations **207**

Acknowledgements **211**

Bibliography **213**

1. Introduction

In 2015, the United Nations noted "that the estimated aggregate greenhouse gas emission levels in 2025 and 2030 resulting from the intended nationally determined contributions do not fall within least-cost 2 °C scenarios ... and also notes that much greater emission reduction efforts will be required ... to hold the increase in the global average temperature to below 2 °C above pre-industrial levels." (Paris Agreement, 2015). To reach this goal, greenhouse gas (GHG) emissions must be reduced drastically and fast, much faster than most countries currently pledged (IPCC 2018, 2018). Although pledges to reduce emissions have been made, the global mean surface temperature for the period $2011 - 2020$ has been 1.1° higher than in preindustrial times (S.K.Gulev et al., 2021), and is therefore already close to the 1.5 °C goal. The main contributor to the temperature increase in the long term is carbon dioxide (CO_2), due to its abundance and longevity (Joos et al., 2013). For shorter timescales, however, the global warming potential over 100 years (GWP_{100}) of methane (CH_4) is approximately 33 (including feedbacks, see Shindell et al., 2009), thus being an excellent target for immediate action to reduce global warming. Additionally, the short atmospheric lifetime of CH_4 of ~ 10 yr means the reduction of emissions reduces atmospheric concentrations in the atmosphere quickly compared to CO_2, and therefore also the warming due to CH_4 can quickly be reduced.

The importance of the atmosphere for the temperature of the Earth was already known in the 19th century, with Fourier (1827) describing the role of the atmosphere in distributing the heat, and Pouillet (1838) calculating the Earth's heat balance and the according temperatures in the presence of the atmosphere. In 1906, Arrhenius estimated the increase in surface temperature due to a doubling of CO_2 to 4 °C. Continuous measurements of atmospheric CO_2 at the surface started in the late 1950s (Revelle and Suess, 1957; Keeling et al., 2017), and continuous CH_4 measurements followed in the 1980s.

While global atmospheric methane levels had stabilized for a decade, starting at the end of the 20th century, methane levels are again rising at least at a constant rate (Dlugokencky, 2018) since 2007. However, although the stabilization period took place over a decade ago, it is still not finally settled what caused the stabilization period at the beginning of the 20th century (see for example Schaefer, 2019, and sources within). Additionally, Nisbet et al. (2019) concluded in a recent study that the renewed increase in atmospheric CH_4 since 2007 offsets the planned and assumed decrease in CO_2 emissions to limit the global warming to 1.5 °C above pre-industrial mean global temperatures, and not cutting down CH_4 emissions would need heroic effort in removing CO_2 from the atmosphere. In contrast to CH_4, CO_2 atmospheric concentrations have been rising continuously (Dlugokencky and Tans, 2020 [last access 28.03.2022]), despite emission reduction pledges. Independent observations of CO_2 and CH_4 sources must be made to monitor compliance with these emission reduction pledges, and origin, magnitude, and consistency must be known.

The main CO_2 sources causing an increase in global CO_2 atmospheric concentrations are anthropogenic, with the main contribution due to the burning of fossil fuels (Friedlingstein et al., 2020). The locations of these main sources are known and relatively well understood, so monitoring the reduction pledges is the main focus. On the other hand, between $\sim 50\,\%$ and $\sim 60\,\%$ of the methane emissions are anthropogenic according to the Global Carbon Project (GCP, Saunois et al., 2020). Of those, roughly 2/3 are caused by agriculture and waste, and nearly 1/3 by fossil fuel extraction and use, with a small contribution ($\sim 10\,\%$) of biomass and biofuel burning. However, those emissions are often either diffuse or diffuse-like (animal herds, landfills, open cast mines) or occur at point sources for which the location usually is not known (e.g., pipeline leaks and broken valves). Even the CH_4 emissions of known potential point sources such as gas compressor stations vary considerably with time (Frankenberg et al., 2016; Varon et al., 2018; Duren et al., 2019). To make large sources or source areas visible, satellite instruments such as SCIAMACHY (Burrows et al., 1995; Bovensmann et al., 1999) and TROPOMI (Veefkind et al., 2012; Hu et al., 2016) have proven to be usefull (Frankenberg et al., 2006; Schneising et al., 2009; Buchwitz et al., 2017; Hu et al., 2018; Schneising et al., 2019; Pandey et al., 2019). While the image resolution of global monitoring satellites is increasing [1], it is still much too coarse to attribute methane emissions to single point sources. Especially in areas like gas or oil fields, there are hundreds of possible emitters within one satellite pixel. Satellite measurements in these areas are well suited to estimate total emissions (e.g., Frankenberg et al., 2006; Schneising et al., 2019), which, however, have to be validated independently. For example, the upper Silesian basin, a coal mining hot spot in Europe with a total emission of $\sim 500\,\mathrm{kt\,yr^{-1}}$ and local sources of up to $60\,\mathrm{kt\,yr^{-1}}$, is only faintly visible in TROPOMI measurements (Schneising et al., 2019). Similar instruments such as TROPOMI are planned but do not exist for CO_2. The Orbiting Carbon Observatory (OCO-2, Frankenberg et al., 2015; Crisp et al., 2017) only covers small stripes around the Earth, and OCO-3 on board the International Space Station (Taylor et al., 2020) is designed to scan areas ($\sim 85 \times 85\,\mathrm{km^2}$) of interest with a footprint size of $\sim 1.6 \times 2.2\,\mathrm{km^2}$. While emission estimates from power plants in combination with NO_2 data from TROPOMI were successful for selected cases (Reuter et al., 2019; Nassar et al., 2021), global monitoring of anthropogenic CO_2 emissions is not possible. In recent years the observation of CH_4 point sources from high spatial resolution instruments has emerged. These comprise, on the one hand, land imaging instruments like the PRecursore IperSpettrale della Missione Applicativa (PRISMA, Cusworth et al., 2021b) or multispectral instruments such as MSI on Sentinel-2 (Varon et al., 2021), with which so-called super-emitters could be detected. On the other hand, the GHGSat instruments (Jervis et al., 2021), which are cube satellites designated for the detection of CH_4 plumes from space with $\sim 50 \times 50\,\mathrm{m^2}$ ground scene resolution for $12 \times 12\,\mathrm{km^2}$ scenes, have also successfully detected anomalously large CH_4 emissions from oil and gas infrastructure (Varon et al., 2019).

Additional knowledge can be gathered by airborne remote sensing campaigns, where a defined area or source is sampled with higher spatial resolution and enhanced sensitivity to local column enhancements. The airborne measurements can enhance the knowledge of local source distributions or enable the validation of satellite measurements over dedi-

[1] TROPOMI maps the Earth with a center resolution of $\sim$ 7km $\times$ 7km (Veefkind et al., 2017), while SCIAMACHY had $\sim$ 30km $\times$ 60km resolution (Bovensmann et al., 1999)

cated areas. With the Methane Airborne MAPper (MAMAP, Gerilowski et al., 2011), a non-imaging nadir pointing instrument, CO_2 emissions from power plants and power plant clusters (Krings et al., 2011, 2018) as well as CH_4 emissions from coal mines (Krings et al., 2013; Krautwurst et al., 2021) and even smaller areal sources such as a landfill (Krautwurst et al., 2017) have been quantified successfully. However, its viewing geometry requires flying orthogonal to the plume, and the non-imaging capabilities hinder the detection of small unknown sources. Imaging instruments solve this problem by simultaneously observing multiple ground scenes across the flight track, creating a 2D image of the ground by flying over a scene. Developments of such airborne instruments dedicated to the measurement of CH_4 and CO_2 have been emerging, e.g. the MethaneAIR instrument (Staebell et al., 2021), which measures CH_4 and CO_2 absorption in similar bands as the MAMAP instrument and uses O_2 absorption around 1270 nm for optical path corrections.

Data from multiple hyperspectral airborne imaging instruments have already been analyzed to map and quantify CH_4 emissions. These include measurements in the thermal infrared spectral region (e.g., the Spatially Enhanced Broadband Array Spectrograph System (SEBASS, Vaughan et al., 2003) or the Hyperspectral Thermal Emission Spectrometer (HyTES, Hook et al., 2013)), which successfully detected CH_4 plumes when flying low. However, detection problems arise at higher flight altitudes, which are required for a larger swath width.

In the shortwave infrared (SWIR), the AVIRIS-NG instrument was used for the detection and quantification of methane sources (Thompson et al., 2015; Frankenberg et al., 2016; Thorpe et al., 2016, 2017; Duren et al., 2019; Cusworth et al., 2019; Thorpe et al., 2020). As the instrument was not designed to detect atmospheric absorbers, the spectral resolution is much coarser than SWIR instruments designed to measure CO_2 and CH_4. However, AVIRIS-NG has a very high signal-to-noise ratio and meter-scale spatial resolution. Successful methane retrievals were mostly done using a cluster tuned match filter approach (Thompson et al., 2015), which uses a hypothesis test between the presence and absence of additional CH_4 to infer CH_4 increases. Additionally, the IMAP-DOAS retrieval (Frankenberg et al., 2005), an iterative optimal estimation-based algorithm, has successfully been adapted to AVIRIS-NG airborne data (Thorpe et al., 2013). The latter, however, was only applied to subsets of the acquired data for previously detected point sources, as processing time is too high to evaluate data sets obtained over longer measurement campaigns (Thorpe et al., 2017).

The retrievals applied to infer both CH_4 and CO_2 enhancements from airborne remote sensing data depend on some knowledge of the atmospheric state, or at least the atmospheric state remaining unchanged in parameters not fitted. Especially for anthropogenic emissions, however, aerosol loads in the atmosphere can change significantly. For example, higher aerosol loads might be present over anthropogenic greenhouse gas emission hotspots, which introduces enhanced multiple scattering. Multiple scattering increases the light path and, therefore, the absorption of light along the light path, which leads to biases in the retrieved total columns or enhancements of greenhouse gases (Houweling et al., 2005; Schneising et al., 2008; Huang et al., 2020). A possible solution is a full-physics retrieval incorporating numerical models for atmospheric scattering in the forward model (Butz et al., 2011; O'Dell et al., 2012). On the downside, these take much time and computational power. To at

least reduce the computational needs but also include scattering effects in the retrieval, Reuter et al. (2017b) designed the Fast atmOspheric traCe gAs retrievaL (FOCAL), which parametrizes the scattering by analytic formulas. Until now, for airborne measurements, scattering was typically neglected (see, e.g., Ayasse et al., 2018) or, in the case of the WFM-DOAS retrieval, a standard aerosol scenario was used in the forward calculation, and biases canceled out by using a well-mixed gas as a proxy. For the proxy method, the concentration of the well-mixed gas used in the light path correction is assumed to be constant. Using CO_2 as the proxy in the CH_4 retrieval (or vice versa) therefore only is valid on small scales and in the absence of sources of the normalization gas. Inclusion of scattering in the retrieval could remove the need to correct the light path by normalization via another gas (proxy method).

Based on the above, the following three research questions were studied in this thesis, each requiring different instruments, data sets, and retrieval methods:

1. Is it possible to retrieve greenhouse gas enhancements and estimate emissions from hyperspectral (i.e., lower spectral resolution) data with the WFM-DOAS retrieval algorithm?
2. Can the quantification and observation of greenhouse gas emissions be improved by imaging instruments specifically designed for this task?
3. Is it possible to improve the retrieval of CH_4 and CO_2 total columns from airborne instruments by including the treatment of scattering in the retrieval?

For the first task, data from the AVIRIS-NG instrument were used as an example of a hyperspectral instrument. AVIRIS-NG was chosen, as CH_4 (and also CO_2) plumes from point sources have been detected already, although using different retrieval techniques. In addition to the retrieval of an actual data set, a sensitivity study was conducted using simulated measurements to estimate the performance of the WFM-DOAS retrieval on hyperspectral data.

The second task was tackled by building the MAMAP2D-Light instrument. A significant part of this work was assisting in finalizing the design, assembling the instrument in the laboratory, programming the instruments' controls, performing initial calibration measurements, and planning and performing the first test and measurement flights. The performance of the MAMAP2D-Light instrument was assessed using data from the calibration measurements and the first measurement flight. This first measurement flight aimed to validate the instrument by mapping the Jänschwalde power plant CO_2 plume and estimating the emission from the acquired data.

The third task involved the inclusion of the treatment of scattering in the retrieval method. By design, the WFM-DOAS method does not retrieve scattering parameters. Therefore, another retrieval method had to be adapted to airborne geometry. The retrieval of choice here was the FOCAL algorithm. This algorithm still incorporates analytic formulations of the radiative transfer problem, including a parametrization of scattering, making it faster than full-physics retrievals using numerical models. Therefore, the FOCAL algorithm was adapted to airborne geometry during this work. The retrieval was tested against simulated

measurements under different scenarios with and without aerosols and with actual measurement data. The application to actual measured airborne remote sensing data required a data set that includes different spectral bands to determine the scattering contribution to the radiative transfer. Therefore, MAMAP data sets comprising measurements of CH_4 and CO_2 absorption bands in the SWIR and the strong O_2A absorption band in the near-infrared (NIR) were used to test the retrieval with an actual data set. Additionally, this data set was retrieved with the WFM-DOAS method, and emission estimates for the different retrievals were compared.

For the estimation of emissions from all data sets, the cross-sectional flux method (White et al., 1976) adapted to airborne remote sensing measurements was used, as it is a conceptually straightforward method, which can be applied equally to non-imaging and imaging data (Krings et al., 2013; Krautwurst et al., 2017; Varon et al., 2018; Krautwurst et al., 2021).

The thesis is structured in the following way. After this introduction, the sources and sinks of the major anthropogenic greenhouse gases CH_4 and CO_2 are described in Chapter 2. In Chapter 3 the description of the atmosphere (Sect. 3.1), the radiative transfer in the atmosphere (Sect. 3.2), and absorption and molecular structures of CH_4, CO_2, and O_2 are described (Sect. 3.3). Next, the current state of measuring atmospheric concentrations of CH_4 and CO_2 with different instruments is detailed in Chapter 4.

With the basics in place, Chapter 5 describes the instruments, data sets, and methods examined in this thesis. In Sect. 5.1, the instruments MAMAP, MAMAP2D-Light, and AVIRIS-NG, and the according data sets investigated in this thesis are described. The retrieval of column enhancements from passive remote sensing spectra with the WFM-DOAS retrieval and the FOCAL AIR retrieval developed during this thesis are introduced in Sect. 5.2 and the de-striping of imaging data is described there. Inversion of observed plumes is done with the cross-sectional flux method described in Sect. 5.3.

The results of the methods applied to the data sets are given in Chapter 6. First, the retrieval of column enhancements from AVIRIS-NG with the WFM-DOAS method is given in Sect. 6.1, where comparisons with other retrievals and inversion of detected plumes with the cross-sectional flux method are also shown. The calibration of the MAMAP2D-Light instrument and the observations and inversion from the first measurement flight over the power plant Jänschwalde are given in Sect. 6.2. Finally, a thorough investigation of the FOCAL AIR retrieval on synthetic measurements and MAMAP data acquired over the power plant Jänschwalde for two different fit window configurations and two different retrieval configurations is done in Sect. 6.3. In the discussion in Chapter 7, the obtained results are analyzed to compare the instruments, retrievals, and flux inversions investigated across the three main research questions. Finally, the thesis is summed up, and an outlook for further investigations is given in Chapter 8.

2. Sources and sinks of the greenhouse gases CH_4 and CO_2

As mentioned in the introduction, CO_2 and CH_4 are the most important anthropogenic greenhouse gases in the atmosphere. While the magnitude of different sources and sinks is still a significant focus of research, the general processes of producing and removing CH_4 and CO_2 from the atmosphere and the general mechanisms leading to the climate on Earth as it is now are pretty well understood. In this chapter, the sources, sinks, and global distribution of CH_4 and CO_2 are described in more detail, with CH_4 in Sect. 2.1 and CO_2 in Sect. 2.2.

2.1. Sources and sinks of CH_4

Atmospheric CH_4 is produced mainly by three process types acting on organic matter, which are called biogenic, thermogenic, and pyrogenic (Saunois et al., 2020). Biogenic CH_4 is produced by bacteria, which decompose organic matter in anaerobic environments. Thermogenic CH_4 is produced in the Earth's crust from compressed hot organic matter and is released into the atmosphere via seeps. Pyrogenic CH_4 is a result of incomplete combustion.

The amount of CH_4 emitted to the atmosphere is estimated in two ways: The so-called "Bottom Up" and "Top Down" approaches. For the "Top Down" approach, atmospheric measurements, e.g., by satellites, tower networks, or others (see also Chapter 4 for detailed descriptions) are used as constraints to atmospheric inversions. These comprise either the total methane flux or the fluxes from a limited set of source categories. In the "Bottom Up" approach, the CH_4 fluxes from a source category are estimated by emission models either modeling CH_4 emitting processes, scaling observation-based emissions, or inventory models. However, as the processes are modeled separately, the total CH_4 flux from "Bottom Up" estimates is not constrained. The effect can be seen in Fig. 2.1 (after data from Saunois et al. (2020)), where the combined "Bottom Up" estimates for CH_4 fluxes for the decade 2008 - 2017 ($735\,\mathrm{Tg\ CH_4\,yr^{-1}}$) are significantly higher than the according "Top Down" estimates ($576\,\mathrm{Tg\ CH_4\,yr^{-1}}$), which are constrained by measurements.

The sources are further divided into natural and anthropogenic sources. The major natural source are wetlands ("Bottom Up" $149\,\mathrm{Tg\ CH_4\,yr^{-1}}$, "Top Down" $181\,\mathrm{Tg\ CH_4\,yr^{-1}}$), defined as ecosystems, in which the anaerobic conditions due to saturated or inundated soils or peats facilitate methane production (see Saunois et al., 2020, for further information) and which are not cultivated or oceanic. Other natural sources ("Bottom Up" $222\,\mathrm{Tg\ CH_4\,yr^{-1}}$, "Top Down" $37\,\mathrm{Tg\ CH_4\,yr^{-1}}$) mostly comprise emissions from freshwaters

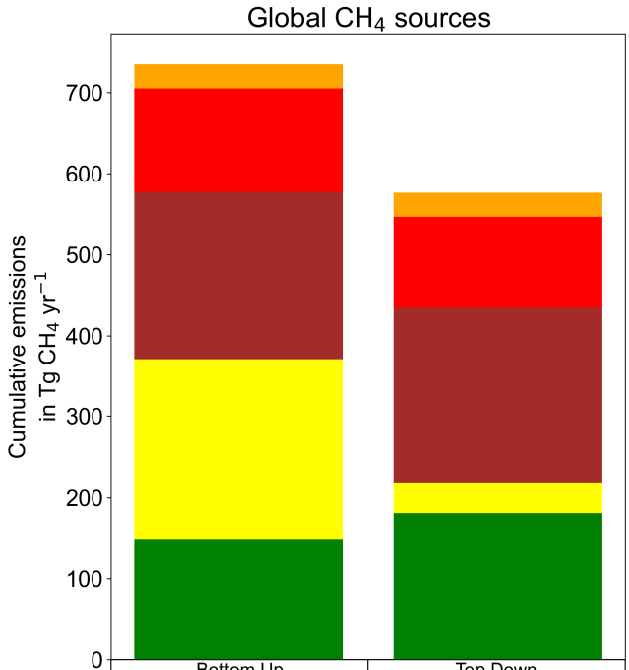

	Bottom Up in Tg CH_4 yr^{-1}	Top Down in Tg CH_4 yr^{-1}
Biomass and biofuel burning	30 [26 - 40]	30 [22 - 36]
Fossil fuels	128 [113 - 154]	111 [81 - 131]
Agriculture and waste	206 [191 - 223]	217 [207 - 240]
Other natural sources	222 [143 - 306]	37 [21 - 50]
Wetlands	149 [102 - 179]	181 [159 - 200]
Total sources	735 [594 - 881]	576 [550 - 594]

Figure 2.1.: Sources of atmospheric CH_4 after Saunois et al. (2020). The values in brackets are the uncertainty range of each category and the total budget. The large discrepancy between "Bottom Up" and "Top Down" is mostly due to the cumulated "Other natural sources". See text for more information.

such as lakes or rivers, onshore and offshore geological sources, termites, wild animals, and oceanic sources. On the other hand, the major anthropogenic sources are agriculture and waste ("Bottom Up" 206 Tg $CH_4\,yr^{-1}$, "Top Down" 217 Tg $CH_4\,yr^{-1}$) comprising emissions from enteric fermentation and manure from livestock, landfills and waste deposits, and rice cultivation, followed by fossil fuel emissions ("Bottom Up" 128 Tg $CH_4\,yr^{-1}$, "Top Down" 111 Tg $CH_4\,yr^{-1}$) from mainly the oil and gas production and usage chain and coal mining, and biomass and biofuel burning (Both 30 Tg $CH_4\,yr^{-1}$). The "Global Methane Budget" (Saunois et al., 2020) estimates total "Bottom Up" sources with (737 Tg $CH_4\,yr^{-1}$). The difference of 2 Tg $CH_4\,yr^{-1}$ originates from the Global Methane Budget estimating total anthropogenic emissions from separate models than the individual contributions from the three subcategories, as done in Fig. 2.1.

The discrepancy of 159 Tg $CH_4\,yr^{-1}$ between total "Bottom Up" and "Top Down" CH_4 fluxes is mainly due to the "Other natural sources" category. Especially for the total anthropogenic fluxes, both approaches agree. Nevertheless, the uncertainties on the fluxes range from $\sim 10\,\%$ for agriculture and waste to 27 % for biomass and biofuel burning and fossil fuels in the "Top Down" approach. Moreover, when breaking down the anthropogenic emissions to regional budgets as done by Stavert et al. (2021), the "Bottom Up" and "Top Down" estimates even disagree significantly for some regions. Also, the emission uncertainties get larger on regional scales, which can be qualitatively seen in Stavert et al. (2021, Fig. 4). Finally, the "Bottom Up" estimations provide no information on the exact emission source locations.

The global CH_4 emissions for the decade 2008 - 2017 were larger than for the two decades before (Saunois et al., 2016, 2020; Canadell et al., 2021), however, regionally, the picture is slightly more diverse. While for 16 of the 18 regions studied by Stavert et al. (2021) the emissions have increased, and in the case of the Chinese region even more than doubled compared to 2000, in the European and combined Korean and Japanese regions the emissions declined. Nevertheless, global atmospheric CH_4 concentrations are higher than likely any time in the last 650.000 years (Spahni et al., 2005), with pre-industrial atmospheric concentrations of ~ 800 ppb.

Our knowledge about CH_4 in the atmosphere greatly comes from atmospheric measurements, which started in 1978 (Blake et al., 1982) with air samples collected over the pacific. The coverage improved with the establishment of in situ and flask measurement networks (e.g., by the National Oceanic and Atmospheric Administration (NOAA) Steele et al., 1987). With the launch of the SCIAMACHY satellite (Burrows et al., 1995; Bovensmann et al., 1999) in 2002, global total column measurements of CH_4 over cloud-free scenes were available, and since then, satellite measurements of the total column of CH_4 have been conducted (see also Sect. 4 for a discussion of different measurement techniques and their advantages and disadvantages).

The globally averaged marine surface monthly mean data set from NOAA (Dlugokencky and Tans, 2020 [last access 28.03.2022]) covers the period starting in 1983 until today (see Fig. 2.2) and is therefore well suited for the discussion of longer-term developments. After a phase of rapid CH_4 accumulation in the atmosphere in the 1980s, the atmospheric growth rate decreased, likely due to a reduction in fossil fuel emissions (Rice et al., 2016). During the late 1990s and early 2000s, the CH_4 concentrations had nearly stabilized, following a drastic

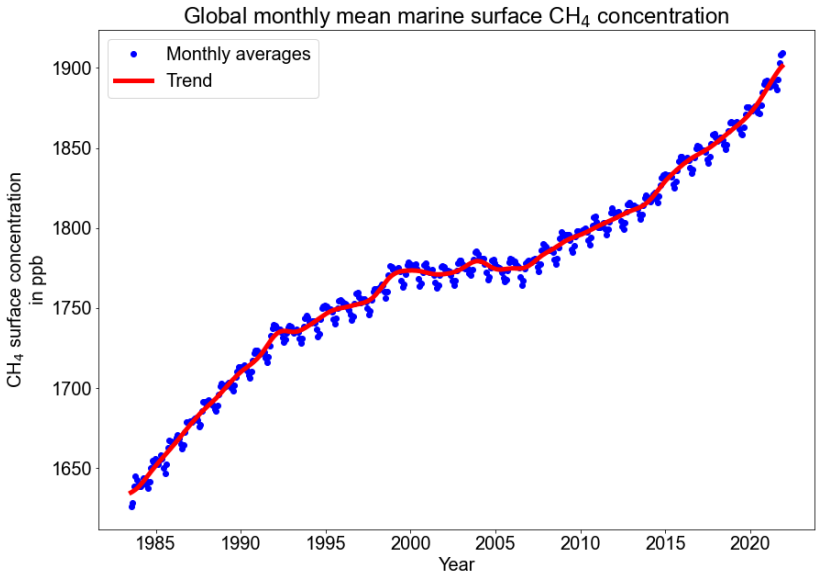

Figure 2.2.: Globally averaged marine surface concentrations of CH_4 based on data from NOAA(Dlugokencky and Tans, 2020 [last access 28.03.2022]).

reduction in oil- and gas-related emissions (Dlugokencky, 2003). Since 2007 the atmospheric concentrations of CH_4 increased again, with growth rates in recent years nearly as high as during the 1980s. The cause for the increase is heavily debated. While, e.g., Nisbet et al. (2016) and Schaefer et al. (2016) concluded that wetland and biogenic methane emissions significantly increased based on isotopic data, e.g., Hausmann et al. (2016) and Rice et al. (2016) stated additional contributions from the fossil fuel sector to the renewed increase. Other discussions include a change in the OH sink of CH_4 (Rigby et al., 2017; Turner et al., 2017). Finally, Turner et al. (2019) provided a different view on the stabilization period as an anomaly and, therefore, the need to find the cause for the stabilization period instead.

As indicated above, not only emission processes but also the removal of CH_4 from the atmosphere is important. The main removal process accounting for $\sim 90\,\%$ of the total sink ("Bottom Up" $553[476-677]\,\mathrm{Tg\ CH_4\,yr^{-1}}$) is the chemical reaction chain of CH_4 with OH (hydroxyl radical) in the troposphere (Saunois et al., 2020), while the other atmospheric losses are by atmospheric photochemistry in the stratosphere ("Bottom Up" $31[12-37]\,\mathrm{Tg\ CH_4\,yr^{-1}}$) and photochemistry in the marine boundary layer with Chlorine (Cl, "Bottom Up" $11[1-35]\,\mathrm{Tg\ CH_4\,yr^{-1}}$), while additional losses occur in oxic soils due to methanotrophic bacteria ("Bottom Up" $30[11-49]\,\mathrm{Tg\ CH_4\,yr^{-1}}$). The total chemical sink accounts for $595[489-749]\,\mathrm{Tg\ CH_4\,yr^{-1}}$ in "Bottom Up" and $518[474-532]\,\mathrm{Tg\ CH_4\,yr^{-1}}$ in "Top Down" approaches (Saunois et al., 2020). The chemical losses are described below in detail. The chemical reaction chains are based on the textbooks of Warneck (2000), John H. Seinfeld (2016) and Roedel and Wagner (2017).

The atmospheric loss due to reaction with the OH radical needs the presence of OH. OH is produced in the troposphere as a byproduct from the reaction chain following O_3 photolysis including an excited singlet oxygen atom $O(^1D)$, which is one of the two photolysis products of O_3:

$$\begin{aligned} O_3 + h\nu &\longrightarrow O_2 + O && (2.1)\\ &\longrightarrow O_2 + O(^1D) && (2.2) \end{aligned}$$

The ground state O atom can quickly recombine with O_2 to form O_3 again. While most of the $O(^1D)$ removes its excitation energy by collision with N_2 or O_2, a non-negligible part of the $O(^1D)$ reacts with H_2O

$$O(^1D) + H_2O \longrightarrow 2\,OH \qquad (2.3)$$

The OH molecule then reacts with CH_4 to form the methyl radical, which, under collision with another molecule, reacts with O_2 to the methyl peroxy radical.

$$\begin{aligned} CH_4 + OH &\longrightarrow CH_3 + H_2O\\ CH_3 + O_2 + M &\longrightarrow CH_3O_2 + M \end{aligned}$$
$$\overline{\qquad\qquad\qquad\qquad}$$
$$CH_4 + OH \xrightarrow{O2} CH_3O_2 + H_2O \qquad (2.4)$$

The methyl peroxy radical then reacts to the largest part either with NO or HO_2 radicals. Other reactions include NO_2 and itself, but those are less important. The reaction with NO forms NO_2 and the methoxy radical, which (under tropospheric conditions) directly reacts with O_2 to form formaldehyde (HCHO):

$$\begin{aligned} CH_3O_2 + NO &\longrightarrow CH_3O + NO_2\\ CH_3O + O_2 &\longrightarrow HCHO + HO_2 \end{aligned}$$
$$\overline{\qquad\qquad\qquad\qquad\qquad\qquad\qquad\qquad}$$
$$CH_3O_2 + NO \xrightarrow{O2} HCHO + HO_2 + NO_2 \qquad (2.5)$$

The reaction of CH_3O_2 with HO_2 forms methyl hydroperoxide (CH_3OOH, reaction 2.6), which is either photolyzed (reaction 2.7) or reacts with OH to either form methyl peroxy radical (reaction 2.8) or again HCHO (2.9)

$$\begin{aligned} CH_3O_2 + HO_2 &\longrightarrow CH_3OOH + O_2 && (2.6)\\ CH_3OOH + h\nu &\longrightarrow CH_3O + OH && (2.7)\\ CH_3OOH + OH &\longrightarrow H_2O + CH_3O_2 && (2.8)\\ &\longrightarrow H_2O + CH_2OOH \\ CH_2OOH &\longrightarrow HCHO + OH && (2.9) \end{aligned}$$

The methoxy radical in reaction 2.7 again reacts with O_2 (reaction 2.5), and some part of the CH_3O_2 formed by reaction 2.8 enters again reaction 2.6, while another part undergoes the reactions 2.5. As a result, virtually every CH_4 molecule is converted to HCHO, which forms the so-called first-generation oxidation product of CH_4. HCHO is either photolyzed to HO_2 or H_2 with CO as byproduct (reactions 2.10 and 2.11), or reacts with OH

$$\begin{aligned} HCHO + h\nu &\longrightarrow H + HCO\\ H + O_2 &\longrightarrow HO_2\\ HCO + O_2 &\longrightarrow HO_2 + CO\\ \hline HCHO + h\nu &\longrightarrow 2\,HO_2 + CO \end{aligned} \qquad (2.10)$$

$$HCHO + h\nu \xrightarrow{O2} H_2 + CO \qquad (2.11)$$

The reaction of HCHO with OH forms HO_2, CO and H_2O

$$\begin{aligned} HCHO + OH &\longrightarrow HCO + H_2O\\ HCO + O_2 &\longrightarrow HO_2 + CO\\ \hline HCHO + OH &\xrightarrow{O2} HO_2 + CO + H_2O \end{aligned} \qquad (2.12)$$

As a result of both the photolysis and reaction of HCHO, CO is formed, which over several months is converted to CO_2 leaving atomic hydrogen H, which directly reacts with O_2:

$$\begin{aligned} CO + OH &\longrightarrow CO_2 + H\\ H + O_2 + M &\longrightarrow HO_2 + M\\ \hline CO + OH &\xrightarrow{O2} CO_2 + HO_2 \end{aligned} \qquad (2.13)$$

The hydroperoxy radical HO_2 reacts differently in different air masses. If NO is abundant, i.e. in polluted air masses, HO_2 reacts with NO to form NO_2 and finally HNO_3

$$\mathrm{HO_2 + NO \longrightarrow NO_2 + OH} \tag{2.14}$$
$$\mathrm{NO_2 + OH + M \longrightarrow HNO_3 + M} \tag{2.15}$$

In clean air masses, little to no NO is present. Then, HO_2 reacts with itself to form hydrogen peroxide (H_2O_2), which either reacts with OH to form HO_2 and H_2O (reaction 2.16) or is photolyzed to OH (reaction 2.17), which is further removed by reaction 2.15.

$$\mathrm{H_2O_2 + OH \longrightarrow HO_2 + H_2O} \tag{2.16}$$
$$\mathrm{H_2O_2 + h\nu \longrightarrow 2\,OH} \tag{2.17}$$

A small fraction of the tropospheric CH_4 is transported to the stratosphere, where it undergoes different reactions, mainly according to altitude (le Texier et al., 1988). The main loss of CH_4 is by reaction with OH (reaction 2.4) similar to the tropospheric reaction. Additionally, CH_4 can react with $O(^1D)$ (reactions 2.18), be photolyzed (reaction 2.19), or react with chlorine or fluorine (Cl/F, reaction 2.20).

$$\begin{aligned}\mathrm{CH_4 + O(^1D)} &\longrightarrow \mathrm{CH_3 + OH} \\ &\longrightarrow \mathrm{HCHO + H_2}\end{aligned} \tag{2.18}$$
$$\mathrm{CH_4 + h\nu \longrightarrow CH_3 + H} \tag{2.19}$$
$$\mathrm{CH_4 + Cl \longrightarrow CH_3 + HCl} \tag{2.20}$$

Finally, also in the troposphere, halogen atoms oxidize CH_4 (Allan et al., 2007), mainly over marine surfaces, where NaCl in evaporation droplets reacts with NO_2 and the resulting Cl is photodissociated by UV radiation.

Averaged over all processes, the lifetime of CH_4 in the atmosphere is approximately 9.7 ± 1.1 yr.

2.2. Sources and sinks of CO_2

Carbon dioxide (CO_2) is the atmosphere's main anthropogenic and long-lived greenhouse gas. To systematically assess the changes in the carbon cycle, the Global Carbon Project (GCP) was initialized in 2001 (Canadell et al., 2003) and has since released regular updates of the carbon budget, with the newest release being the GCP report of 2020 (Friedlingstein et al., 2020). Unlike for CH_4, the CO_2 budget is calculated from "Bottom Up" data from

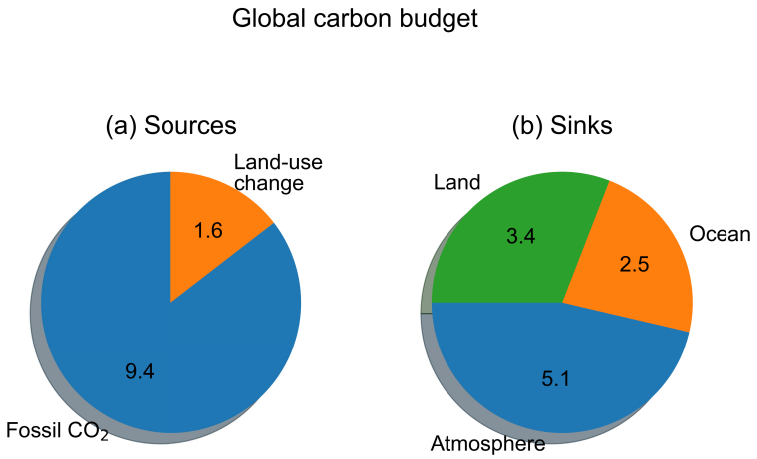

Figure 2.3.: Global carbon budget in $\mathrm{Gt\,C\,yr^{-1}}$ based on GCP data (Friedlingstein et al., 2020). In (a), the sources and in (b), the sinks are depicted, neglecting seasonal cycling, e.g., in the biosphere. See text for further description.

models or based on the reporting of national budgets to the UNFCCC (United Nations Framework Convention on Climate Change), with the atmospheric growth rate estimated from measurements as a constraint. Over large natural cycles of CO_2, anthropogenic CO_2 emissions are overlayed. The yearly net carbon fluxes for the decade 2010 - 2019 estimated by the GCP are given in Fig. 2.3 in $\mathrm{Gt\,C\,yr^{-1}}$. Fossil CO_2 emissions account for a net flux to the atmosphere of $9.4\,\mathrm{Gt\,C\,yr^{-1}}$, and are largely produced by the combustion of fossil fuels and the production of cement (minus carbon uptake during cement carbonation). The second net source for CO_2 in the atmosphere is from land use, land-use change, and forestry, and accounts for $1.6\,\mathrm{Gt\,C\,yr^{-1}}$. All land-related anthropogenic activity is included in this part of the budget. These are especially de- and afforestation, changes in cultivation, and regrowth of forests after land use, e.g., after abandoning agricultural areas. Explicitly excluded are fluxes due to environmental changes on managed land, which are attributed to the land sink. While some components of this budget act as sinks and others act as sources for CO_2, the net flux is positive. Therefore, the category containing land use, land-use change, and forestry is a net source of CO_2.

The reservoirs taking up the emitted CO_2 are the atmosphere, the land, and the ocean. While the land and ocean sink combined removed $5.9\,\mathrm{Gt\,C\,yr^{-1}}$ (or roughly 50 %) between 2010 and 2019, $5.1\,\mathrm{Gt\,C\,yr^{-1}}$ remained in the atmosphere between 2010 and 2019 (Friedlingstein et al., 2020, see Fig. 2.3), leading to atmospheric concentrations of CO_2 of ~ 412 ppm in 2020 (see Fig. 2.4). Unlike for CH_4, no stabilization period is visible in the CO_2 data. While globally, the fossil emissions increased steadily, regionally, there are differences. In 24 of the 27 nations of the EU, and also in the USA, the CO_2 emissions decreased in recent

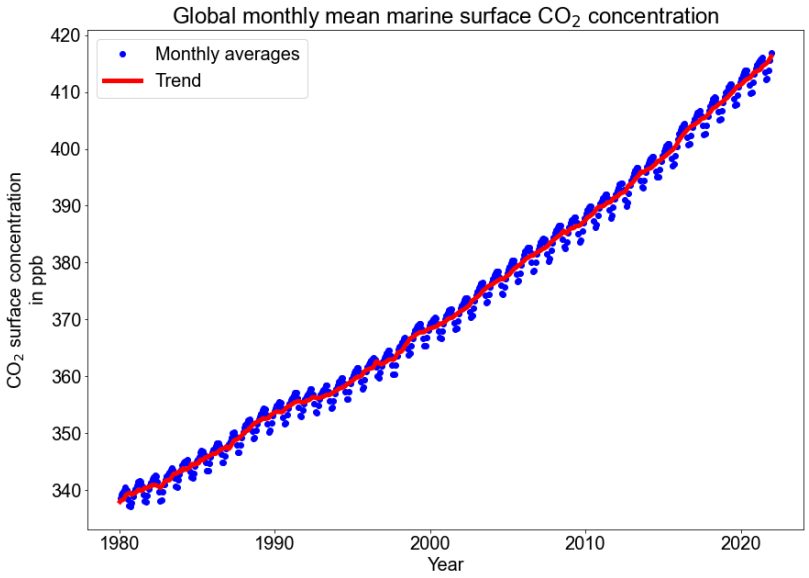

Figure 2.4.: Globally averaged marine surface concentrations of CO_2 based on NOAA data (Dlugokencky and Tans, 2020 [last access 28.03.2022]).

years. Nevertheless, the CO_2 levels observed today are higher than at any time in the last 800.000 years (Lüthi et al., 2008).

These emissions occur on top of the natural cycle of CO_2 over the land (cycling 120 Gt C yr^{-1}) and the ocean (90 Gt C yr^{-1}). Over the land during spring, the onsetting growth of plants removes CO_2 from the atmosphere by photosynthesis, which consumes CO_2 and water vapor to produce oxygen, and is released by respiration and decay, which is the inverse reaction. While the concrete reaction chains are very complicated, both ways can be summarized by the following reaction equation in the presence of sunlight (see, e.g., Wallace and Hobbs, 2006; Archer, 2011)

$$CO_2 + H_2O \longleftrightarrow CH_2O + O_2. \tag{2.21}$$

Only $\sim 0.1\,\%$ of the CO_2 bound by the reaction above over land is buried and contributes to the land sink. The rest cycles between photosynthesis and respiration (Wallace and Hobbs, 2006).

The oceans finally act as an important sink for atmospheric CO_2. Over the water surfaces, an equilibrium between dissolved carbon and atmospheric carbon exists

$$CO_2 + CO_2^{2-} + H_2O \rightleftharpoons 2\,HCO_3^-. \tag{2.22}$$

Some marine organisms then use the carbonic acid in combination with calcium to form shells and skeletons, of which a fraction subsides to the bottom of the ocean, forming limestone over longer time frames:

$$\mathrm{Ca^{2+}} + 2\,\mathrm{HCO_3^-} \longrightarrow \mathrm{CaCO_3} + \mathrm{H_2CO_3} \tag{2.23}$$

$$\mathrm{CaSiO_3} + \mathrm{CO_2} \longrightarrow \mathrm{CaCO_3} + \mathrm{SiO_2}. \tag{2.24}$$

The atmospheric lifetime for CO_2 highly depends on the calculation assumptions. The often-recalled lifetime of CO_2 of $\sim 100\,\mathrm{yr}$ is based on the average time the emitted CO_2 molecules stay in the atmosphere. However, as seen by the cycling processes above, this does not necessarily mean that the CO_2 molecules have been permanently removed from the atmosphere by this time. Therefore, another definition is the time it takes for the atmospheric concentration to return to pre-emission concentrations. The lifetime calculated in this manner is more in the order of several ten thousand years and might even be more than 100 000 years (see e.g. Archer et al., 2009, and sources within).

3. Theoretical background

This study focuses on atmospheric measurements made in the troposphere. However, the objects under study, i.e., point sources of CH_4 and CO_2, are located close to the surface, and their emission plumes are confined in the planetary boundary layer. Therefore, understanding the Earth's current atmosphere, especially its composition and layering, but also its dynamics, is important, and an overview is given in Sect. 3.1. The atmosphere's constituents modulate the sunlight by absorption and scattering and emit radiance due to their temperature. These processes are introduced in Sect. 3.2, while the concrete absorption spectra of CH_4, CO_2, and O_2 used for interpreting the airborne remote sensing data during this thesis are explained in detail in Sect. 3.3. All of the mechanisms above are important for the radiative budget of the Earth, especially through the greenhouse effect, which is described in Sect. 3.4. Finally, the movement of air released at the surface to the atmosphere is introduced in Sect. 3.5.

3.1. The atmosphere of the Earth

Past and current atmospheric composition

The atmosphere of the Earth changed drastically over time, starting from the first atmosphere formed simultaneously with the formation of the Earth from the solar nebula ~ 4.5 billion years ago (Dalrymple, 2001) over different stages up to the current atmosphere. No geological evidence of its composition has been found for the first atmosphere. However, it was likely composed mostly of hydrogen (H_2). After a period of accumulation of the solar nebula, this atmosphere mostly escaped the planet, likely due to heating of the atmosphere from impacts of other planetesimals (precursors of planets) or large asteroids or comets. During the first ~ 600 million years (the so-called *Hadean*), a so-called second atmosphere formed, most likely due to volcanic outgassing and degassing of meteorites (Zahnle et al., 2010, and sources within). This atmosphere likely contained CH_4, CO_2, CO, H_2, H_2O, N_2 and NH_3 (Schaefer and Fegley, 2007, 2010). After the Earth's mantle and crust had cooled down, the first oceans accumulated, and structures formed from microbial mats have been dated back to ~ 3.5 billion years ago (Schopf et al., 2007; Vankranendonk et al., 2008). The oxygen (O_2) produced by cyanobacteria turned the atmosphere from oxidizing to reducing around 2.45 billion years ago. At the same time, the volcanic activity reduced (O'Neill et al., 2013) and likely also the oceans became more acidic (Canfield, 2005), leading to a surplus of oxygen and enabling the development of more complex aerobic life forms. In the nearer past, around ~ 60 million years ago, CO_2 concentrations reached about 2000 ppm

(Anagnostou et al., 2020), nearly 5 times the current atmospheric concentration. Consequently, the global mean surface temperature (GMST) was $\sim 18\,^{\circ}$ above pre-industrial GMST levels (Inglis et al., 2020). In the following, CO_2 levels and GMST decreased, and during the last $\sim 800\,\mathrm{ka}$ the CO_2 levels stayed between $\sim 170 - 300\,\mathrm{ppm}$ (Lüthi et al., 2008) prior to the industrial revolution, oscillating with the glacial-interglacial cycle. During this time frame, CH_4 mixing ratios varied between ~ 350 and $\sim 800\,\mathrm{ppb}$ (Loulergue et al., 2008).

In the current atmosphere (averaged for the year 2020), global mean atmospheric surface concentrations of CO_2 and CH_4 have reached $\sim 412\,\mathrm{ppm}$ and $\sim 1879\,\mathrm{ppb}$, respectively (Dlugokencky and Tans, 2020 [last access 28.03.2022]). The major components of the current atmosphere are, however, nitrogen (N_2, $\sim 78.08\,\%$), oxygen (O_2, $\sim 20.95\,\%$), and argon (Ar, $\sim 0.93\,\%$). Water vapor is a highly variable constituent of the atmosphere, varying from $\sim 10\,\mathrm{ppm}$ in cold and dry regions up to $\sim 5\,\%$ in hot and humid regions (Wallace and Hobbs, 2006). Because of its high variability, a differentiation between the total column of air (molecules from ground to infinity over a fixed area, e.g., molec cm^{-2}) excluding ("dry") and including ("moist") water vapor is made. Other trace gases such as, e.g., ozone (O_3) or nitrous dioxide (N_2O), are even less abundant than CH_4 and a more extensive list of constituents of the atmosphere can be found in, e.g., Wallace and Hobbs (2006) or Salby (2012).

Vertical structure of the atmosphere

Two major factors drive the vertical structure of the current atmosphere: First, the pressure of air dependent on altitude, and second, the temperature structure. The density of the atmospheric gases follows the ideal gas law. Additionally, in the gravity field of the Earth with gravitational constant g, the weight of an air parcel between two pressure levels at pressures p and $p + \mathrm{d}p$ of volume $\mathrm{d}V = \mathrm{d}A\,\mathrm{d}z$ and density ρ is equal to the net pressure force between the two layers

$$p\,\mathrm{d}A - (p + \mathrm{d}p)\,\mathrm{d}A = -\rho g\,\mathrm{d}V \tag{3.25}$$

$$\frac{\mathrm{d}p}{\mathrm{d}z} = -\rho g. \tag{3.26}$$

Integrating this hydrostatic balance from the surface z_s to an altitude z gives the barometric formula for the pressure p at altitude z:

$$p = p_s \cdot \exp\Big(-\int_{z_s}^{z} \frac{M_{\mathrm{dry}\,g}}{RT(z')}\mathrm{d}z'\Big), \tag{3.27}$$

with the molar mass of dry air M_{dry}, the universal gas constant R, and p_s the pressure at the surface. As can be seen from Eq. (3.27), the pressure generally decreases exponentially with height (see also Fig. 3.1).

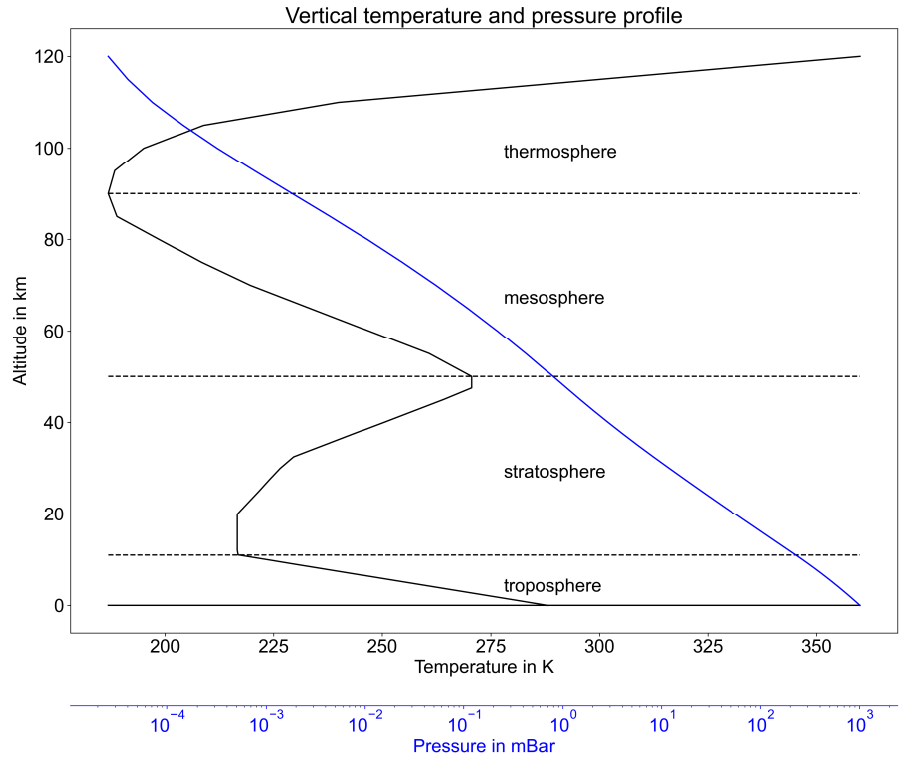

Figure 3.1.: Vertical temperature and pressure profile of the Earth, based on the U.S Standard Atmosphere (United States National Oceanic and Atmospheric Administration and United States Air Force, 1976). While the pressure decreases exponentially with height, the temperature shows a clear structure, which is used to define the vertical structure of the atmosphere.

Unlike the pressure, the temperature does not change monotonically with increasing height. Instead, the temperature profile can be separated into regions governed by different temperature gradients (Wallace and Hobbs, 2006; Salby, 2012, and Fig. 3.1). Starting at the bottom is the troposphere. In the troposphere, the temperature decreases by $\sim 6.5\,\mathrm{K\ km^{-1}}$ on average. The surface is heated through solar radiation, and the heat is transported upwards through convection. Additionally, the bulk of the molecules in the total column is confined to the troposphere. At an altitude of $\sim 8\,\mathrm{km}$ at the poles and up to 16 km in the tropics, a local temperature minimum is reached, defining the tropopause. Above the tropopause, the temperature gradient changes, and the temperature increases again, caused by the heating of O_3 through the absorption of solar UV radiation. Unlike in the troposphere, there is only slow vertical motion. The stratopause marks the local temperature maximum at around 50 km. The mesosphere above the stratopause is characterized by decreasing temperature again up to the mesopause at $\sim 85\,\mathrm{km}$, where another local temperature minimum is reached. In the thermosphere above, temperature increases again due to the photodissociation of N_2 and O_2 and photoionization.

3.2. Radiative transfer in the atmosphere

The atmosphere of the Earth, as described above, is made of multiple different gases and particles, which change the light as it passes through the atmosphere. These processes are described by the radiative transfer equation, which will be introduced in this section. Unless otherwise stated, this section is based on Roedel and Wagner (2017) and Salby (2012).

The radiative transfer equation describes the amount of radiance behind an air parcel of volume $\mathrm{d}V = A \cdot \mathrm{d}s$, where $\mathrm{d}s$ is oriented along the axis of the incoming primary beam, and A is the area perpendicular to this axis. The radiation is diminished by absorption inside the volume and scattering out of the volume ("extinction"), while it is increased by radiation scattered into the primary beam direction from other directions and the thermal emission of the volume itself. These processes are described in more detail in the following, and a schematic is given in Fig. 3.2.

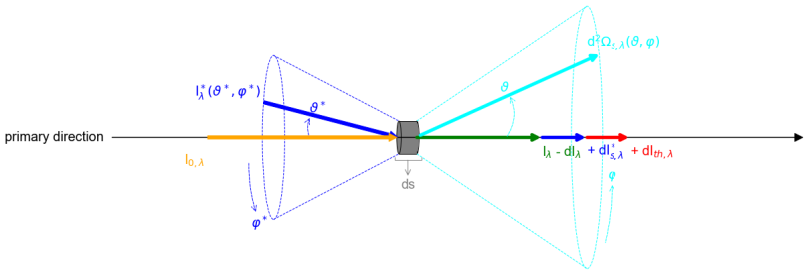

Figure 3.2.: Schematic of the terms contributing to the radiative transfer equation. The incoming light (orange) is absorbed in or scattered out of the volume (resulting green arrow). Scattering in and out of the primary direction is depicted in blue and cyan, respectively, and the red arrow depicts the thermal emission of the volume in the primary beam direction. (Created after Fig. 1.4 in Roedel and Wagner (2017)).

The intensity (or radiance) of a light source at wavelength λ is generally dependent on the light emission direction, therefore $I_\lambda = I_\lambda(\vartheta, \phi)$ with the angle ϑ as the angle between the orthogonal to the emitting surface and the light direction ("zenith angle"), and ϕ the directional angle between a reference direction on the surface (in the Earth system, this is mostly true north) and the projection of the intensity vector onto the surface ("azimuth angle"). When the intensity $I_\lambda(\vartheta, \phi)$ enters a volume $\mathrm{d}V = A \cdot \mathrm{d}s$ with area A perpendicular to the intensity vector and $\mathrm{d}s$ the length element, extinction (i.e., intensity reduction) occurs along the light path. Additionally, radiation is scattered in directions different from the original light path.

The extinction along the light path is caused by absorption and scattering by molecules and particles in the volume. The absorption is thereby described by

$$\mathrm{d}I_\lambda = -\sigma_{a,\lambda}\, N\, I_\lambda\, \mathrm{d}s, \tag{3.28}$$

with N the number density of the absorber in the volume and $\sigma_{a,\lambda}$ the molecular absorption cross-section of one absorber. The amount of intensity lost in the primal beam due to scattering can analogously be written as

$$\mathrm{d}I_\lambda = -\sigma_{s,\lambda}\, N\, I_\lambda\, \mathrm{d}s \tag{3.29}$$

with the scattering cross-section $\sigma_{s,\lambda}$. The power $\mathrm{d}^2\Phi_{s,\lambda}$ of the light scattered out of the volume in the direction $\mathrm{d}\Omega_s$ is dependent on the direction of the incident light given by ϑ and ϕ and the differential scattering cross-section $\frac{\mathrm{d}\sigma_{s,\lambda}}{\mathrm{d}\Omega}(\vartheta,\phi)$:

$$\mathrm{d}^2\Phi_{s,\lambda} = I_\lambda\, \frac{\mathrm{d}\sigma_{s,\lambda}}{\mathrm{d}\Omega}(\vartheta,\phi)\, N\, \mathrm{d}\Omega_s\, \mathrm{d}V. \tag{3.30}$$

The size of the scattering particle categorizes scattering processes in the atmosphere. For Rayleigh scattering, the scattering element is small compared to the wavelength. In contrast, for Mie scattering, the size of the scattering element can no longer be assumed to be small compared to the wavelength. Much larger particles then scatter geometrically. In the following, Rayleigh and Mie scattering are explained further, as they occur mainly in the near- and short-wave infrared.

For Rayleigh scattering at air molecules, the differential scattering cross-section becomes dependent on λ^{-4}

$$\frac{\mathrm{d}\sigma_{s,\lambda}}{\mathrm{d}\Omega}(\vartheta) = \frac{\pi^2\,\chi^2}{2\,\varepsilon_0^2\,\lambda^4}\cdot(1+\cos^2\vartheta), \tag{3.31}$$

which is largest for the forward ($\vartheta = 0\,^\circ$) and backward ($\vartheta = 180\,^\circ$) direction, and gets minimal perpendicular to the incoming radiation. $\varepsilon_0 = 8.85\cdot 10^{-12}\,\mathrm{A\,s\,V^{-1}}$ is the dielectric constant, and χ is the polarizability of the air dependent on the scattering element. For small aerosols and assuming they are dielectric spheres with volume $V = 4\,\pi\,r^3$ and dielectric constant ε, χ and therefore $\frac{\mathrm{d}\sigma_{s,\lambda}}{\mathrm{d}\Omega}(\vartheta)$ becomes

$$\chi = \varepsilon_0 \cdot \frac{4\,\pi\,r^3\,(\varepsilon-1)^2}{(\varepsilon+2)^2} \tag{3.32}$$

$$\frac{\mathrm{d}\sigma_{s,\lambda}}{\mathrm{d}\Omega}(\vartheta) = \frac{8\,\pi^4\,r^6\,(\varepsilon-1)^2}{\lambda^4\,(\varepsilon+2)^2}(1+\cos^2\vartheta). \tag{3.33}$$

With $\alpha = \frac{2\,\pi\,r}{\lambda}$ as the particle size parameter, the scattering cross-section σ_s and the extinction function E as the cross-section normalized to particle size become

$$\sigma_s = \frac{8\,\pi\,r^2\,\alpha^4\,(\varepsilon-1)^2}{3(\varepsilon+2)^2} \tag{3.34}$$

$$E_{\text{Rayleigh}} = \alpha^4 \frac{8\,(\varepsilon-1)^2}{3\,(\varepsilon+2)^2} \tag{3.35}$$

In the Mie scattering case, the scattering cross-sections and, consequently, the extinction function and intensity of scattered radiation can not be expressed analytically. In addition to the particle size, the scattering cross-section also depends on the refraction index of the aerosol. In general, Mie scattering drastically prefers the forward direction, while the intensity as a function of the scattering angle for the other directions oscillates. In the atmosphere, the light virtually always is scattered by a mix of different particles. This particle mix often follows a size distribution $\sim r^{-m}$, with $m \approx 3.5 \pm 1$. Then the extinction cross-section for aerosols under Mie scattering becomes

$$\sigma_{e,\lambda} = (2\,\pi)^{m-2-1}\,\lambda^{2-m+1}\,\frac{1}{N}\int_{r=0}^{\infty} E(\alpha)^{2-m}\,\mathrm{d}\alpha, \tag{3.36}$$

that means the wavelength dependency of the extinction cross-section directly depends on the exponent of the size distribution function, while the integral is solved numerically. The wavelength dependency for Mie scattering is weaker than for Rayleigh scattering and, on average, is $\sim \lambda^{-1.3}$ in the atmosphere (Roedel and Wagner, 2017).

The total extinction along the path $\mathrm{d}s$ is then the combination of the extinction due to absorption and scattering, and with the extinction cross-section $\sigma_{e,\lambda} = \sigma_{a,\lambda} + \sigma_{s,\lambda}$ the change in intensity $\mathrm{d}I_\lambda$ becomes

$$\mathrm{d}I_\lambda = -\sigma_{e,\lambda} N I \lambda\,\mathrm{d}s \tag{3.37}$$

If no other processes, such as thermal emission or scattering of light into the beam, take place, this is solved analytically by the Beer-Lambert-Law:

$$I_\lambda = I_{0,\lambda} \cdot \exp\left(-\int (\sigma_{a,\lambda} + \sigma_{s,\lambda})\,N\,\mathrm{d}s\right) \tag{3.38}$$

As a second source of radiation apart from the primary beam, light can be scattered into the primary beam from outside the volume. The total scattering power related to the intensity originating from a direction given by ϑ^* and ϕ^* relative to the primary beam is given by $I^*_\lambda(\vartheta^*, \phi^*)\,\sigma_{s,\lambda}\,A\,\mathrm{d}s$. The change in intensity in the primary beam $\mathrm{d}I^*_{s,\lambda}$ due to the fraction of the total scattered power in the primary direction $\mathrm{d}\Omega$ is

$$\mathrm{d}I^*_{s,\lambda} = \sigma_{s,\lambda}\, N\, \mathrm{d}s \cdot \int_0^{\pi} \int_0^{2\pi} I^*_\lambda(\vartheta^*, \phi^*)\, \frac{S(\vartheta^*, \phi^*)}{4\,\pi}\, \mathrm{d}\phi^*\, \sin\vartheta^*\, \mathrm{d}\vartheta^* \tag{3.39}$$

The distribution function $S(\vartheta, \phi) = \frac{4\,\pi}{\sigma_{s,\lambda}} \cdot \frac{\mathrm{d}\sigma_{s,\lambda}}{\mathrm{d}\Omega}$ describes the fraction of light scattered in the primary beam direction.

The final source term for intensity is the thermal emission out of the volume due to a non-zero temperature. A body emitting radiation at maximum efficiency independent of the wavelength is called a black body, and the emitted intensity $B_\lambda(T)$ (i.e. the radiant energy per time, per unit area, and per solid angle) is described by Planck's law:

$$B_\lambda(T)\, \mathrm{d}\lambda = \frac{2\,\mathrm{h}\,\mathrm{c}^2}{\lambda^5} \cdot \frac{1}{\exp\left(\frac{\mathrm{h}\,\mathrm{c}}{\lambda\,\mathrm{k}\,T}\right) - 1}\, \mathrm{d}\lambda \tag{3.40}$$

In this formula, $\mathrm{h} = 6.63 \cdot 10^{-34}\,\mathrm{J\,s}$ is the Planck constant, $\mathrm{k} = 1.38\,\mathrm{J\,K^{-1}}$ is the Boltzmann constant, and $c = 2.998 \cdot 10^8\,\mathrm{m\,s^{-1}}$ is the speed of light in vacuum.

In the atmosphere, the gases and particles, however, absorb radiation differently depending on the wavelength. With the body's ability to absorb radiation with the wavelength-dependent absorption cross-section $\sigma_{a,\lambda}$, and due to Kirchhoff's law stating that a body emits radiation with the same efficiency as it absorbs it, i.e. $\sigma_{\epsilon,\lambda} = \sigma_{a,\lambda}$, the thermal emission out of the volume is

$$\mathrm{d}I_{th,\lambda} = \sigma_{\epsilon,\lambda}\, N\, B_\lambda(T)\, \mathrm{d}s \tag{3.41}$$

Combining the equations Eqs. (3.37), (3.39) and (3.41), the equation of radiative transfer for a beam traversing a volume of air along the distance $\mathrm{d}s$ (visualized in Fig. 3.2) becomes

$$\begin{aligned} \frac{\mathrm{d}I_\lambda}{\mathrm{d}s} = &- \sigma_{e,\lambda} N I \lambda && \text{extinction} \\ &+ \sigma_{\epsilon,\lambda}\, N\, B_\lambda(T) && \text{thermal} \\ &+ \sigma_{s,\lambda}\, N\, \mathrm{d}s \cdot \int_0^{\pi} \int_0^{2\pi} I^*_\lambda(\vartheta^*, \phi^*)\, \frac{S(\vartheta^*, \phi^*)}{4\,\pi}\, \mathrm{d}\phi^*\, \sin\vartheta^*\, \mathrm{d}\vartheta^* && \text{scattered in} \end{aligned} \tag{3.42}$$

Eq. 3.42 describes the radiation in the atmosphere. When hitting the surface, only part of the light is reflected, and additionally, as for scattering, the reflection depends on the angle of incident light and the angle of outgoing radiation. This dependency is often described by the bidirectional reflectance-distribution function (Nicodemus et al., 1977) $BRDF_\lambda$, which relates the reflected intensity infinitesimal $I_{r,\lambda}$ in the direction defined by the zenith angle θ_r and the azimuth angle ϕ_r with the incoming flux infinitesimal $dF_{i,\lambda}(\theta_i, \phi_i) = I_{i,\lambda}(\theta_i, \phi_i) \cdot$

$\cos\theta_i d\omega_i$ from the direction defined by the angles θ_i and ϕ_i with opening angle ω_i in the following way:

$$BRDF = \frac{dI_{r,\lambda}(\theta_i, \phi_i, \theta_r, \phi_r, F_{i,\lambda})}{I_{i,\lambda}(\theta_i, \phi_i) \cdot \cos\theta_i \, d\omega_i} \tag{3.43}$$

This function is usually very complex. However, assuming the reflection at the surface is isotropic and the surface acts as a Lambertian reflector, then the $BRDF$ can be approximated by the spectral albedo α_λ, which is the ratio between the incoming flux and outgoing flux and gives a number between 0 and 1:

$$\alpha_\lambda = \frac{F_{r,\lambda}}{F_{i,\lambda}} = \frac{\int_\Omega I_{r,\lambda}(\theta_r) \, \cos\,\theta_r \, d\omega_r}{F_{i,\lambda}} \tag{3.44}$$

3.3. Relevant spectroscopy of the molecules CH_4, CO_2 and O_2

The radiative transfer equation (Sect. 3.2) describes the general modulation of radiation by the atmosphere. However, the interesting quantities studied in this thesis are column abundances of CH_4 and CO_2, which modulate solar radiation in specific ways. In this section, the general absorption of radiation by molecules in the infrared by rotational-vibrational transitions is introduced in Sect. 3.3.1. After that, the molecular structure and absorbing properties of CH_4 (Sect. 3.3.2) and CO_2 (Sect. 3.3.3) are described in detail with a focus on the absorption of both gases around 1650 nm and between 2000 and 2500 nm. Finally, the absorption of O_2 around 760 nm is explained in Sect. 3.3.4.

3.3.1. Absorption in atoms and molecules

As mentioned in previous sections, the molecules in the atmosphere absorb parts of the solar and terrestrial spectrum. The absorption of solar radiation by molecules introduces state changes in these molecules, which are described in this section. The following is based on the textbooks of Haken and Wolf (2006) and Thomas Engel (2013).

The energy carried by a photon at the wavelength λ (or for wavenumber $\overline{\nu}$) is

$$E_{\text{phot}} = \frac{h\,c}{\lambda} = h\,c\,\overline{\nu}, \tag{3.45}$$

with the Planck constant $h = 4.136 \cdot 10^{-15}\,\text{eV}\,\text{s}$, $\hbar = \frac{h}{2\pi}$ and the speed of light c. Exciting an electron bound to a molecule requires the photon's energy to match exactly the energy necessary to transition between two energetic states E_1 and E_2 of the molecule, i.e., $\Delta E = E_2 - E_1$.

From quantum mechanics, it is known that the energy states E of an atom are described by solutions of the (time-independent) Schrödinger equation in 3 dimensions

$$\left[-\frac{\hbar^2}{2m_e}\Delta + V(x,y,z)\right]\Psi(x,y,z) = E\Psi(x,y,z), \tag{3.46}$$

$$\Delta = \nabla^2 = \left(\frac{\partial^2}{\partial x^2} + \frac{\partial^2}{\partial y^2} + \frac{\partial^2}{\partial z^2}\right). \tag{3.47}$$

$V(x,y,z)$ is the potential of the atom acting on the electron, m_e is the electron mass, $\Psi(x,y,z)$ is the electron wave function, and Δ is the Laplace operator. The first term, i.e., the derivative in all directions, describes the electron's kinetic energy.

The solutions to this equation for molecules are usually sets of energies. They are obtained by implementing approximations for the potential describing the interactions between, e.g., the atomic nuclei and the electrons. One significant approximation for the transitions of electrons in molecules is the Born-Oppenheimer-Approximation. It states that the nuclei of a molecule move much slower than the electrons. Then, the interaction between the electrons and the nuclei can be separated in an interaction between the (assumed) static nuclei and the moving electron, and the Coulomb interaction between the moving nuclei.

Additionally, three types of transitions can be separated for molecules, which will be described in the following sections. In electronic transitions, the electronic state changes, which requires the most energy of the transition types. Rotational transitions change the rotation of the molecule and the rotational quantum number J. These require the lowest amount of energy by themselves. Finally, in vibrational transitions, the vibrational state and, therefore, the vibrational quantum number v changes, which requires less energy than electronic but more than rotational transitions. The total energy (apart from the zero level energy, see Thomas Engel (2013)) can be written as the sum of the energy of all three states:

$$E_{\text{molec}} = E_{\text{el}} + E_{\text{ro}} + E_{\text{vi}} \tag{3.48}$$

In the infrared region studied in this thesis, primarily vibrational-rotational transitions occur, i.e., simultaneous transitions in the vibrational and rotational state. However, electronic-vibrational-rotational transitions produce strong absorption bands in the NIR for molecular oxygen, which is essential for the third research question. Therefore, in the following, the single transition types are explained separately, and the vibrational-rotational transition and electronic-vibrational-rotational transition are introduced afterward.

Electronic transitions

In electronic transitions, one of the electrons bound to the molecule change from one orbit to another. The molecular orbits are formed from linear combinations of the separate atomic electron orbits. For a 2-atomic molecule, the Coulomb potential is no longer spherical symmetric due to the influence of the first atom's electrons by the second atom's Coulomb potential. Therefore the orbital angular momentum $\vec{l}$ of the electron precesses around the symmetric axis along the connection line between the two nuclei. The z-component of this orbital angular momentum (along the axis) is quantized in dependence of the magnetic quantum number $m_l = l, l-1, ..., -l$ with

$$l_z = m_l \hbar. \tag{3.49}$$

Additionally, the molecular quantum number

$$\lambda = |m_l| = l, l-1, ..., 0 \tag{3.50}$$

is introduced, as the energy of the quantized states described by l_z are independent of the direction of the precession of the electron in the electric field.

In analogy to the atomic orbitals $s, p, d, ...$, the molecular orbits for $\lambda = 0, 1, 2, ...$ are called $\sigma, \pi, \delta, ...$ Due to Eqs. (3.49) and (3.50), all angular momentum states apart from $\lambda = 0$ are double degenerated, and two electrons with opposing spins can occupy each state. Combining the quantum numbers, the molecular orbits can be described by $nl\lambda$, where n and l are the quantum numbers originating from the atomic states.

For a given orbit, the even (subset g) or odd (subset u) parity denotes if the orbital wave function of the orbit is symmetric or antisymmetric relative to the center of the molecule. The parity results directly from the linear combinations of the atomic orbits. If the linear combination results in a non-binding orbit, i.e., an orbit without a local minimum in the potential, this orbit is additionally marked by a superscript $*$. Therefore $2p\pi*$ denotes a non-binding electronic orbit with an angular momentum quantum number 1, originating from one linear combination of the two $2p$ electronic orbits of the single atoms.

The complete characterization of a molecule's electronic state requires additional consideration of the coupling between the electrons. The angular momentum of completely occupied orbits is 0; only the i outer electrons contribute to the total angular momentum. The coupling between the electrons' angular momentums is usually much smaller than the coupling of each electron to the radial field of the nuclei. Therefore, each angular momentum vector $\vec{l_i}$ precesses around the axis along the connection line between the nuclei with $\pm\lambda_i$ with $\lambda = m_l$. Introducing a new quantum number $\Lambda = |\sum_i \lambda_i|$, the total orbital angular momentum in z-direction becomes

$$\vec{L}_z = \pm \Lambda \hbar. \tag{3.51}$$

Analogously to atomic orbitals $s, p, d...$, the states $\Lambda = 0, 1, 2, ...$ are denoted as Σ, Π, Δ. Furthermore, these states can be of even or uneven parity. The spins of the electrons combine to a total spin $\vec{S}$ with spin quantum number $S = \sum m_{s_i}$, which precesses around

the magnetic field introduced by the movement of the electrons and which is in the axial direction of the molecule. The component in z-direction is then $S_z = \Sigma_{spin}\hbar$ with $\Sigma_{spin} = S, S-1, ..., -S$. The multiplicity of a state is $2S+1$, i.e., for two free electrons, there are triplet ($S = 1$, multiplicity 3) and singlet ($S = 0$, multiplicity 1) states. Due to spin-orbit coupling, these multiplets form different states, only differing in their electronic angular momentum quantum number $\Omega = |\Lambda + \Sigma|$. However, this angular momentum is only the angular momentum due to the movement of the electrons. Additionally, the molecule can rotate, leading to additional angular momentum components. The molecular quantum number defining the electronic state of the molecule is written as ${}^{2S+1}\Lambda_\Omega$, although Ω is often omitted.

For purely electronic dipole transitions, the following selection rules apply: The total spin quantum number S must not change, i.e., $\Delta S = 0$, and the angular momentum quantum number must stay the same or change by one, i.e., $\Delta\Lambda = 0, \pm 1$. Furthermore, the parity must change from "g" to "u" or the other way around. However, in molecules with strong spin-orbit-coupling, the $\Delta S = 0$ selection rule can be less strict, which allows also transitions with a change in multiplicity.

Rotational transitions

For a molecule to be able to change its rotation by interacting with a photon, it needs a permanent dipole moment. This dipole moment can have different origins. Differences in the force of attraction of the nuclei, rotations of the molecule, or asymmetric bending of an otherwise symmetric molecule can all introduce dipole moments.

The so-called dumbbell model is generally used to describe rotational transitions. A bond of fixed length connects two (not necessarily equal) atoms. Solving the time-independent Schrödinger equation for this problem gives the rotational term $F(J) = \frac{E_{\mathrm{rot}}}{h\,c}$ with the rotational quantum number J and the rotational constant B.

$$F(J) = B\,J\,(J+1) \tag{3.52}$$

$$B = \frac{h}{8\,\pi^2\,c\,I} \tag{3.53}$$

$I = m_r\,R^2$ is the moment of inertia of the dumbbell, with the reduced mass of the system $m_r = \frac{m_1\,m_2}{m_1+m_2}$ and distance between the two atoms $R = R_1 + R_2$. Eq. (3.52) states that the energy difference between two adjacent spaces J and $J+1$ increases with increasing J. Additionally, a change in rotation is a change in the moment of inertia. It is equal to the moment of inertia carried by the photon, which has to be conserved during the absorption process.

Using the wavenumber notation, the resulting wavenumber difference between two adjacent rotational states becomes

$$\Delta\overline{\nu} = 2\,B\,(J+1), \tag{3.54}$$

which gives absorption lines equidistant in wavenumber space.

In reality, in addition to the attraction through the bond of the atoms, the rotation induces a centrifugal force, and the bond length changes with increasing rotational speed. A more accurate model substitutes the rigid connection by a spring modeling a harmonic oscillator. This change introduces a correction term to 3.52

$$F(J) = B\,J\,(J+1) - D\,J^2(J+1)^2 \tag{3.55}$$

$$D = \frac{\hbar^3}{4\,\pi\,k\,I^2\,R_e^2\,c}. \tag{3.56}$$

The spring constant k describes the elastic bond, and R_e is the equilibrium distance of the atoms without rotation. The resulting difference in wavenumbers between two adjacent states J and $J+1$ then becomes

$$\Delta\overline{\nu} = 2\,B\,J\,(J+1) - 4\,D\,(J+1)^3. \tag{3.57}$$

For small J, the distance in wavenumbers is still nearly equidistant. However, for larger J, the distance diminishes, which is also seen in real rotational spectra. The energy differences in rotational spectra are minor, and pure rotational spectra are located in the far infrared and microwave region. Thus, they do not affect absorption in the solar spectrum.

Vibrational transitions

In contrast to atoms, molecules can vibrate. Depending on the complexity of the molecule and the number of atoms, the number of energetically different vibrational states varies. All non-linear molecules[1] consisting of n atoms have $3n-6$ vibrational states, while linear molecules have $3n-5$ vibrational states. Symmetry renders vibrational states degenerated, which means that two or more vibrational states store the same amount of energy.

A simple model for the vibration of a diatomic molecule is, as before, the dumbbell connected by a spring. The potential is then harmonic, and the solution of the Schrödinger equation is the solution for the harmonic oscillator. However, the bond between two atoms is better described by an anharmonic potential that considers that moving the atoms closer together increases the repulsion force while bringing them further away from each other reduces the attraction.

[1] These are molecules where the angle between different bonds is not always 180 °

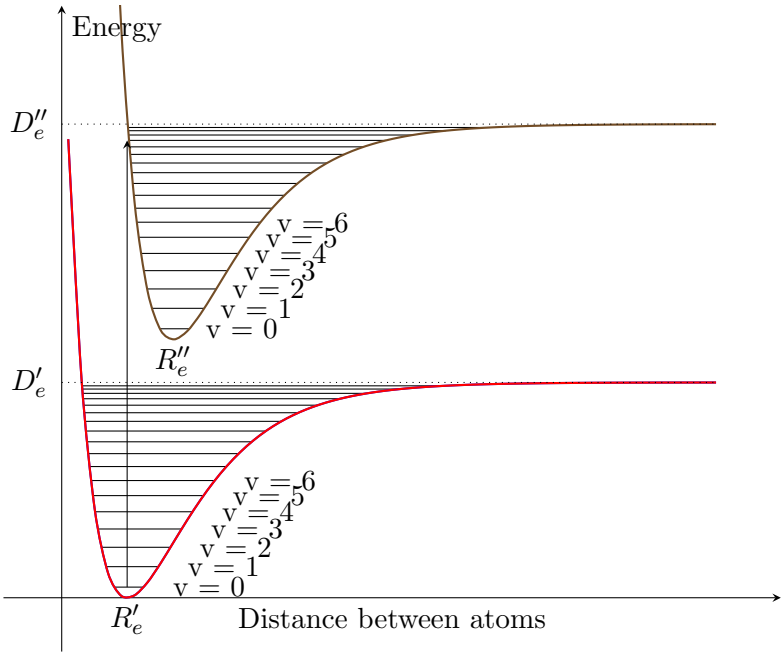

Figure 3.3.: Morse potential for two electronic states with according vibrational states. Electrons exceeding D_e dissociate from the molecule. Therefore, above D_e, no discrete energy levels exist.

A better description of the potential curve than the harmonic oscillator was given by Morse (Morse, 1929, see also Fig. 3.3)

$$V(R) = D_e \left[1 - e^{-a(R-R_e)}\right]^2, \tag{3.58}$$

$$\text{with } a = \sqrt{\frac{m_r}{2\,D_e}}\,\omega_e. \tag{3.59}$$

The angular frequency ω_e is the angular frequency of the harmonic oscillator, and D_e is the dissociation energy. If absorption of a photon leads to an energy level higher than D_e, the electron is dissociated from the molecule.

Solving the Schrödinger equation with the Morse potential gives the following solution for the vibrational energy levels E_υ with anharmonic constant x_e

$$E_\upsilon = \hbar\,\omega_e \left(\upsilon + \frac{1}{2}\right) - x_e\,\hbar\,\omega_e \left(\upsilon + \frac{1}{2}\right)^2, \tag{3.60}$$

$$\text{with } x_e = \frac{\hbar\omega_e}{4\,D_e}. \tag{3.61}$$

$\upsilon = 0, 1, 2, \ldots$ is here the (non-negative) vibrational quantum number. With increasing υ, the difference between adjacent energy levels decreases. Unlike for rotational transitions,

the vibrational state can change freely, with $\Delta\upsilon = \pm 1, \pm 2, \ldots$. In a multi-atom molecule, several vibration modes υ_n exist.

Vibrational-rotational transitions

Pure vibrational spectra do not exist in reality, and a so-called "band" of rotational lines exists at each vibration level. Assuming both energy terms for rotation and vibration independent (as in Eq. (3.48)), the energy of a vibrational-rotational state can be approximated by

$$E_{\upsilon,J,\text{harmonic}} = \hbar \left(\upsilon + \frac{1}{2}\right) + B\, h\, c\, J\,(J+1). \tag{3.62}$$

With a more realistic Morse potential, the mean distance between the atoms in the molecule changes with increasing υ. A larger distance increases the moment of inertia, similarly to higher rotational states. Therefore, an interaction between the vibrational and rotational state exists and has to be taken into account by correcting the rotational constant in equilibrium B_e and the elastic correction term D with molecule-specific numbers α and β, respectively, neglecting higher order correction terms:

$$B_\upsilon = B_e - \alpha \left(\upsilon + \frac{1}{2}\right) \tag{3.63}$$

$$D_\upsilon = D - \beta \left(\upsilon + \frac{1}{2}\right). \tag{3.64}$$

The corrected rotational-vibrational energies then become

$$E_{\upsilon,J} = \hbar\,\omega_e \left(\upsilon + \frac{1}{2}\right) - x_e\,\hbar\,\omega_e \left(\upsilon + \frac{1}{2}\right)^2 + h\,c\,B_\upsilon\,J\,(J+1) - h\,c\,D_\upsilon\,J^2\,(J+1)^2. \tag{3.65}$$

Neglecting the last term in Eq. (3.65) again due to its magnitude, the difference in wavenumbers $\overline{\nu}$ between two states defined by (υ', J') and (υ'', J'') with $\upsilon' > \upsilon''$ becomes

$$\overline{\nu} = \overline{\nu}_e\,(\upsilon' - \upsilon'') - x_e\,\overline{\nu}_e \left[\left(\upsilon' + \frac{1}{2}\right)^2 - \left(\upsilon'' + \frac{1}{2}\right)^2\right] + B_{\upsilon'}\,J'\,(J'+1) - B_{\upsilon''}\,J''\,(J''+1). \tag{3.66}$$

The general selection rule $\Delta J = \pm 1$ produces two so-called branches in the spectrum. Transitions originating from $\Delta J = -1$ form the $P-$branch, while transitions with $\Delta J = +1$ form the $R-$branch (for a schematic see Fig. 3.4). Combining the first two terms

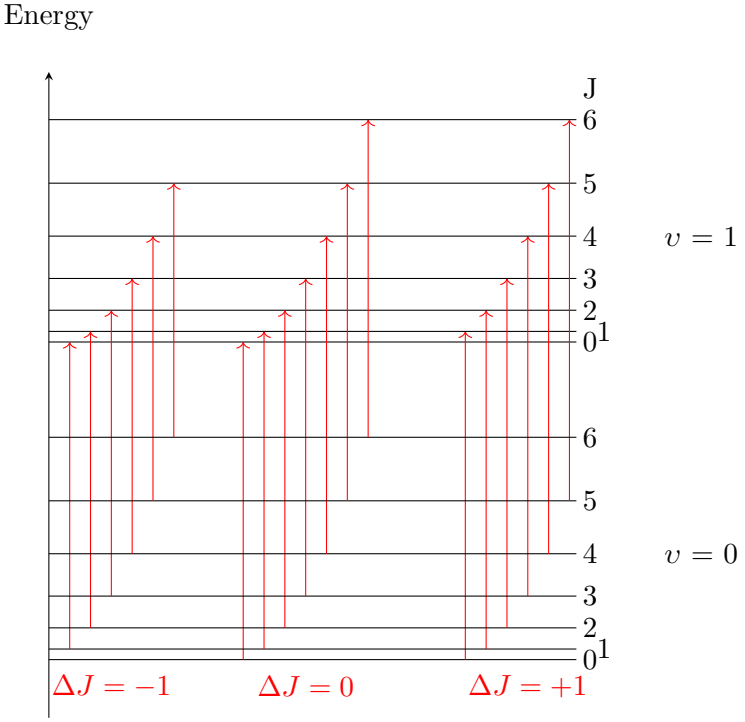

Figure 3.4.: Schematics of the vibrational-rotational transitions between ground level $\upsilon = 0$ and the first vibrational mode $\upsilon = 1$.

in Eq. (3.66) to $\overline{\nu}(\upsilon', \upsilon'')$, the wavenumbers in the $P-$ ($\overline{\nu}_P$) and $R-$branch ($\overline{\nu}_R$) become

$$\overline{\nu}_P = \overline{\nu}(\upsilon', \upsilon'') - 2\,B_{\upsilon''}(J+1) - (B_{\upsilon''} - B_{\upsilon'})\,J\,(J+1) \tag{3.67}$$

$$\overline{\nu}_R = \overline{\nu}(\upsilon', \upsilon'') + 2\,B_{\upsilon''}(J+1) - (B_{\upsilon''} - B_{\upsilon'})\,(J+1)\,(J+2). \tag{3.68}$$

In the $R-$branch, located at shorter wavelengths (greater wavenumbers), the difference in wavenumber decreases with larger J. Contrary, in the $P-$branch, located at longer wavelengths, the difference in wavenumber increases with J. The transitions $\Delta J = 0, \Delta\upsilon = \pm 1, \pm 2, \ldots$ are usually forbidden due to the conservation of the moment of inertia. These become allowed when the rotational axis is along the vibrational mode change. Then, the change in vibration does not alter the moment of inertia of the molecule. This branch is called the $Q-$branch, and an example is the CH_4 absorption band around ~ 1675 nm (see Sect. 3.3.2). When the $Q-$branch is present, then the wavenumber for a transition $\upsilon' \leftarrow \upsilon''$ is

$$\overline{\nu}(\upsilon', \upsilon'') = (\overline{\nu}_e - x_e\,\overline{\nu}_e)\,(\upsilon' - \upsilon'') - x_e\,\overline{\nu}_e\,(\upsilon'^2 - \upsilon''^2). \tag{3.69}$$

The lines in the $Q-$branch (if observable) are located very closely together, as the correction terms are minimal due to the magnitude of x_e.

Electronic-vibrational-rotational transitions

In molecules, not only pure vibrational but also pure electronic transitions do not exist. Usually, the vibrational and rotational state of the molecule also changes as part of the electronic transition. Additionally, the equilibrium distance between the nuclei R_e changes in molecular electronic transitions. For an increase in energy of the molecule, the distance usually increases[2]. However, as before, we assume that the electron's movement is fast compared to the movement of the nuclei. Then, as depicted in Fig. 3.3, the electronic transition occurs most likely to the vibrational state directly above the original state, which has the highest probability at this distance R (Frank-Condon-principle). The energy difference between the two states E' and E'' for an electronic-vibrational transition then ist

$$\begin{aligned}\Delta E_{el,vib} = E' - E'' =& E'_{el} + h\,\nu'_e \left[\left(\upsilon' + \frac{1}{2}\right) - x_e \left(\upsilon' + \frac{1}{2}\right)^2\right] \\ &- \left\{E''_{el} + h\,\nu''_e \left[\left(\upsilon'' + \frac{1}{2}\right) - x_e \left(\upsilon'' + \frac{1}{2}\right)^2\right]\right\},\end{aligned} \tag{3.70}$$

where E'_{el} and E''_{el} are the energy of the original ($''$) and target electronic state ($'$), υ is the vibrational quantum number, and x_e and h are the anharmonic and the Planck constant, respectively.

Each of the vibrational bands is further split into rotational lines. While for the vibrational transitions, no strict selection rules exist, for the rotational part, the following rules apply in the absence of strong spin-orbit coupling:

$$\begin{aligned}\Delta J &= 0, \pm 1 \\ \Delta\Lambda &= \pm 1 \\ \Delta\Sigma &= 0\end{aligned} \tag{3.71}$$

For electronic-vibrational-rotational transitions, the difference between the rotational constants B' and B'' is not neglectable anymore, because the moment of inertia might change significantly when the equilibrium distance between the nuclei changes. Therefore, the quadratic terms of J in Eq. (3.66) are significant contributors to the energy difference between the two states. With Eq. (3.70), the total energy difference for an electronic-vibrational-rotational transition becomes

$$\Delta E_{ges} = \Delta E_{el,vib} + \Delta\left[BhcJ(J+1)\right], \tag{3.72}$$

and the wavenumbers of the spectral lines become

$$\overline{\nu} = \overline{\nu}_{\upsilon',\upsilon''} + B'J'(J'+1) - B''J''(J''+1). \tag{3.73}$$

[2] An exception would be if a non-binding electron is excited to a binding orbit, which would decrease the equilibrium distance between the nuclei.

With the selection rules above, again the three rotational branches P ($\Delta J = -1$), Q ($\Delta J = 0$) and R ($\Delta J = +1$) can be separated. For transitions where both the original and target state are singlet states, the Q-branch is forbidden. Additionally, even when a Q-branch exists, the transition from $J'' = 0$ to $J' = 0$ remains forbidden. The wavenumbers in these three branches become

$$\overline{\nu}_P = \overline{\nu}_{\upsilon',\upsilon''} - (B' + B'')(J' + 1) + (B' - B'')(J' + 1)^2$$
$$\overline{\nu}_R = \overline{\nu}_{\upsilon',\upsilon''} - (B' + B'')(J'' + 1) + (B' - B'')(J'' + 1)^2 \tag{3.74}$$
$$\overline{\nu}_Q = \overline{\nu}_{\upsilon',\upsilon''} - (B' + B'')J'' + (B' - B'')J''^2 \tag{3.75}$$

3.3.2. Molecular structure and absorption of CH_4

Methane is a tetrahedral molecule with one carbon atom in the middle surrounded by four hydrogen atoms (see Fig. 3.5). Due to the symmetry of the molecule, the nine vibrational degrees of freedom (see Sect. 3.3.1) of CH_4 are reduced to four different (partly degenerated) modes of vibration (Tisza, 1933). The four modes are depicted in Fig. 3.5. ν_1 is the symmetric stretching vibration, ν_2 is the doubly degenerated bending vibration, ν_3 is the triple degenerated asymmetric stretching vibration, and ν_4 is the also triple degenerated asymmetric bending vibration. The order of the degeneration is the number of theoretically different but energetically and physically same vibrational modes.

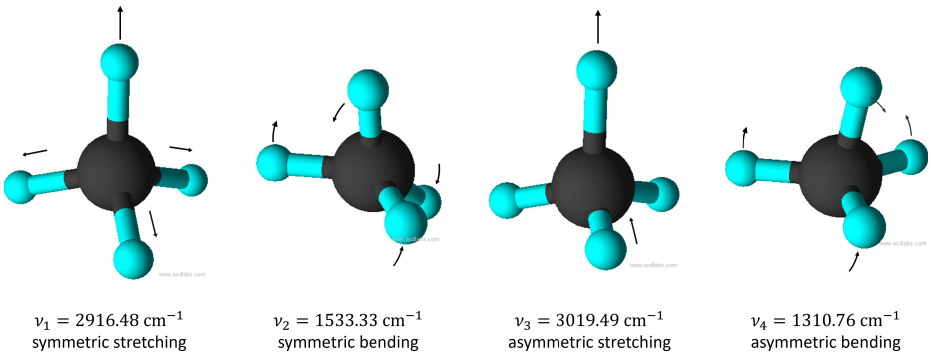

Figure 3.5.: Molecular structure of methane and its four different vibrational modes created with ACD/3D-Viewer. The black center is the carbon atom, while the four cyan spheres are the four hydrogen atoms. The black arrows indicate the direction of the vibration.

The wavenumbers associated with the modes are the wavenumber differences between the ground state and first vibrational state without rotational change ($\Delta\overline{\nu}_k = \overline{\nu}_k(\upsilon_1, \upsilon_0)$, $\Delta J = 0$) including the zero-level energy (Niederer, 2012). CH_4 possesses no pure rotational

spectrum, as it has no permanent dipole. However, the asymmetric vibrational modes exert varying dipoles, so that transitions including ν_3 and/or ν_4 are vibrational-rotational transitions.

Furthermore, the mode frequencies of the four basic modes follow approximately the relationship

$$\nu_1 \approx 2\,\nu_2 \approx \nu_3 \approx 2\,\nu_4. \tag{3.76}$$

This leads to groups of closely related absorption lines in the overtones of the primary modes, the so-called polyads P_n. A vibrational state defined by the four vibrational quantum numbers $(\upsilon_1, \upsilon_2, \upsilon_3, \upsilon_4)$ is assigned to a polyad of order n via the following equation:

$$n = 2\upsilon_1 + \upsilon_2 + 2\upsilon_3 + \upsilon_4. \tag{3.77}$$

In addition to the primary levels of each polyad, there are so-called sublevels of the vibrational levels existing due to the degeneration of three of the four vibrational modes (Boudon et al., 2006).

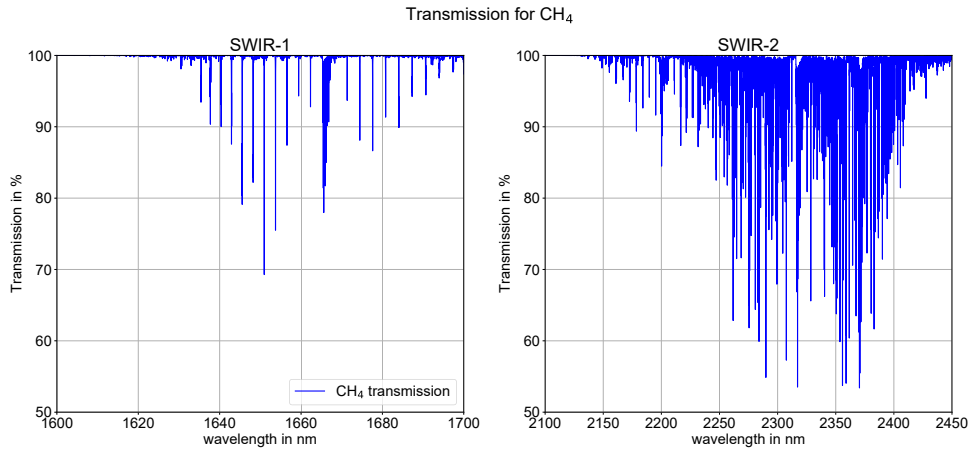

Figure 3.6.: Transmission in the atmosphere due to the presence of a CH_4 enhancement of 10 % around 1665 nm and 2300 nm, based on SCIATRAN simulation data using the HITRAN2016 spectral data base.

In this thesis, absorption bands of CH_4 centered around $\lambda = 1665\,\text{nm}$ ($\nu \sim 6006\,\text{cm}^{-1}$) as well as between $\sim$ 2250 and 2500 nm ($\sim 4440 - 4000\,\text{cm}^{-1}$) are examined. The absorption lines around 1665 nm belong to the tetradecad P_4. The main transition there is from the ground state (0,0,0,0) to the first overtone of the asymmetric stretching vibration (0,0,2,0) (Boudon et al., 2006). Around 2300 nm the absorption bands are part of the octad P_3. There, the dominant transitions are from the ground state to a combination of both asymmetric stretching and bending vibration (0,0,1,1), and from the ground state to a combination of the symmetric stretching and asymmetric bending vibration (1,0,0,1) (Hilico et al., 2001).

In Fig. 3.6, the absorption characteristics of CH_4 in both wavelength ranges is shown. While around 1665 nm the single rotational lines and the $P-, Q-$ and $R-$branch are distinguishable, this is much more difficult around 2300 nm due to the overlapping absorption bands. Additionally, the mode (0,0,1,1) does not possess a $Q-$branch. Instead, there is a small gap in transition lines between the $P-$ and $R-$branch.

3.3.3. Molecular structure and absorption of CO_2

The CO_2 molecule is a linear molecule consisting of three atoms. Therefore, it exhibits four vibrational modes. One mode is double degenerated due to the rotational symmetry of the molecule. The three vibrational modes are the symmetric stretching vibration $\nu_1 \approx 1337\,\mathrm{cm}^{-1}$, the double degenerated bending vibration $\nu_2 \approx 667\,\mathrm{cm}^{-1}$ and the asymmetric stretching vibration $\nu_3 \approx 2349\,\mathrm{cm}^{-1}$, which are depicted in Fig. 3.7. The wavenumbers again describe the transition between the ground state and the first excited state in each vibrational mode.

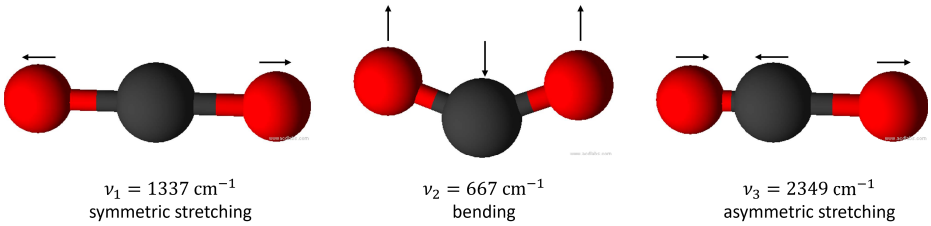

Figure 3.7.: Structure and vibrational modes of the CO_2 molecule, drawn with ACD/3D-Viewer. The black sphere denotes the carbon atom, while the red spheres are the two oxygen atoms. The arrows denote the vibration directions of the molecules.

Again, as for CH_4, the CO_2 vibrational bands are clustered in polyads. However, only ν_1 and ν_2 are coupled by Fermi resonance

$$\nu_1 \approx 2\,\nu_2. \tag{3.78}$$

The standard notation for a vibrational level is $(\upsilon_1\upsilon_2^l\upsilon_3)$, where the υ_i are the vibrational quantum numbers and $l = \upsilon_2, \upsilon_2 - 2, \upsilon_2 - 4, ..., 1, 0$ is the angular momentum of the bending mode. A variant of this notation uses $(\hat{\upsilon_1}\hat{\upsilon_2}^l\hat{\upsilon_3})_r$ (Amat and Pimbert, 1965), where $\hat{\upsilon_i}$ are the base modes of the Fermi polyad and r is the rank, i.e. the number of vibrational modes in the polyad. The Fermi polyad comprises the vibrational modes $\{(\upsilon_1\upsilon_2^l\upsilon_3), ((\upsilon_1 - 1)(\upsilon_2 + 2)^l\upsilon_3), ((\upsilon_1 - 2)(\upsilon_2 + 4)^l\upsilon_3), \ldots, ((0)(\upsilon_2 + 2\upsilon_1)^l\upsilon_3)\}$,

In Fig. 3.8 (a) the absorption structures of CO_2 covering the two energetically lowest bands of the Fermi tetrad ((14^01) and (06^01)) are shown, while in Fig. 3.8 (b) the absorption structures for the Fermi triad are shown. While the absorption bands, including the rotational transitions, are well separated around 1600 nm, around 2000 nm the rotational-vibrational

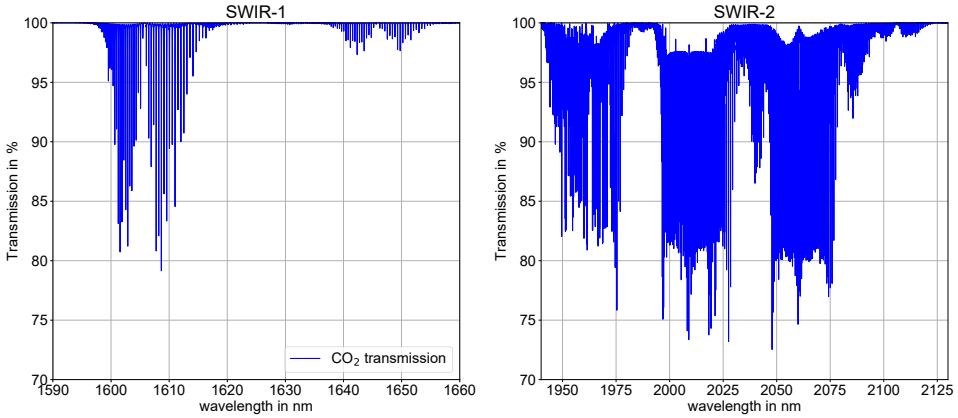

Figure 3.8.: Transmission in the atmosphere due to the presence of a CO_2 enhancement of 5 % around 1675 nm and 2000 nm, based on simulation data using the HITRAN2016 spectral database. In addition to the $(30^01)_{II}$ and $(30^01)_I$ transitions (main bands), smaller bands attributable to isotopes are faintly visible.

bands overlap strongly, so that the $P-$ and $R-$branches can not visually be separated easily. In both cases, no $Q-$branch is present, as the change in vibration is always (partly) perpendicular to the axis of rotation, which forbids the transition without rotational state change.

Around 1600 nm, the Fermi-tetrad P_4 $((30^01)_r)$ is located, which are transitions from the ground state ${}^1\Sigma_g^+$ to the polyad states. Σ denotes that the total angular momentum of the molecule is zero, while the superset $+$ and $-$ denote if the state is symmetric relative to a plane containing the molecular axis $(+)$ or not $(-)$. The g denotes even parity of the wave function, meaning that the wave function is point symmetric to the center of the molecule. The vibrational modes are $\{(30^01), (22^01), (14^01), (06^01)\}$ with the according wavenumbers 6503, 6348, 6196 and 6076 cm^{-1} and center wavelengths 1537.8, 1575.3, 1605.7 and 1645.8 nm, respectively. Around 2000 nm, the Fermi triad P_3 $((20^01)_r)$ is responsible for the main absorption bands, and comprises the vibrational modes $\{(20^01), (12^01), (04^01)\}$ with wavenumbers 4854, 4978 and 5100 cm^{-1} and central wavelengths 2060.2, 2008.8 and 1960.8 nm, respectively (Toth et al., 2008).

3.3.4. Molecular structure and absorption of O_2

Molecular oxygen (O_2) is a diatomic molecule consisting of two oxygen atoms. According to the symmetry and the absence of an electric dipole, no rotational or rotational-vibrational spectrum is allowed. Nevertheless, for O_2 magnetic dipole or quadrupole radiation can be absorbed in the NIR (Babcock and Herzberg, 1948) due to spin-orbit-coupling. Additionally, collision-induced absorption plays an important role in absorption spectra for O_2 in the NIR, as collisions introduce a brief dipole moment. Thus, otherwise forbidden transitions

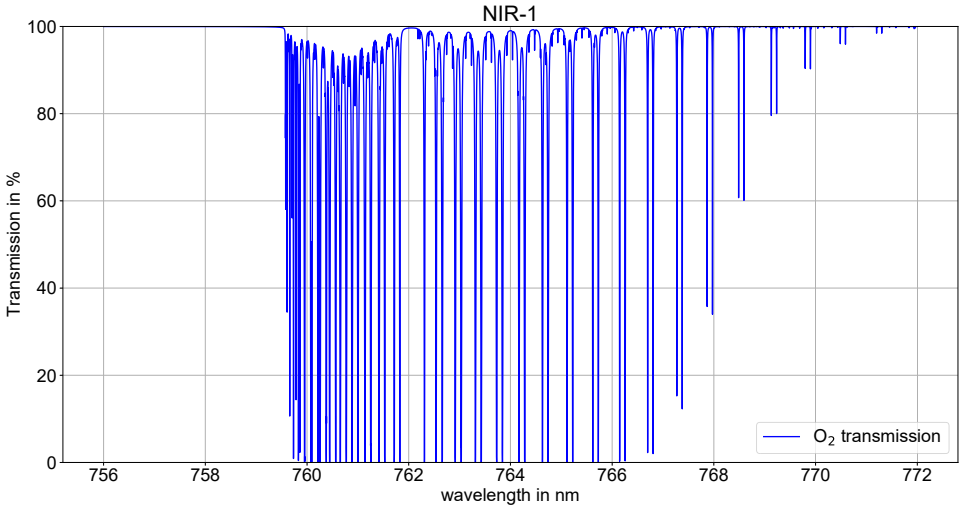

Figure 3.9.: Absorption characteristics of the O_2A band around 760 nm for a 5 % change in O_2 concentration, based on SCIATRAN simulation data using the HITRAN2016 spectral database.

are possible (Karman et al., 2018). The O_2A band absorbing around 760 nm results from electronic-rotational-vibrational transitions between the ground state of O_2 $X^3\Sigma_g^-$ and the excited electronic state $b^1\Sigma_g^+$. The X denotes the triple degenerated ground state, and b is the second excited state, a singleton state.

The electronic-rotational-vibrational transitions between the ground state and the excited b-state are formed by four branches, two P branches (PP and PQ) and two R branches (RQ and RR) (Ritter and Wilkerson, 1987). In Fig. 3.9 the absorption spectrum of the O_2A band is shown. The double lines next to each other are due to the double P- and R-branches. The distance between the pairs increases with increasing wavelength.

3.4. Radiation budget of the Earth and greenhouse effect

The radiative budget and, therefore, the temperature on the surface of the Earth is influenced heavily by the atmosphere. There, the different constituents absorb, emit, and scatter radiation with different efficiencies concerning the wavelength range of the radiation. While the exact processes leading to a change in radiation have been described in more detail in the previous sections, here, the energy budget resulting from these processes in the atmosphere of the Earth is given.

The primary energy source in the Earth system is the solar radiation reaching the Earth. The solar flux through a disc with the radius of the Earth at the mean distance between the sun and the Earth is called the solar constant $SC \approx 1360\,\mathrm{W\ m^{-2}}$ (Kopp et al., 2005).

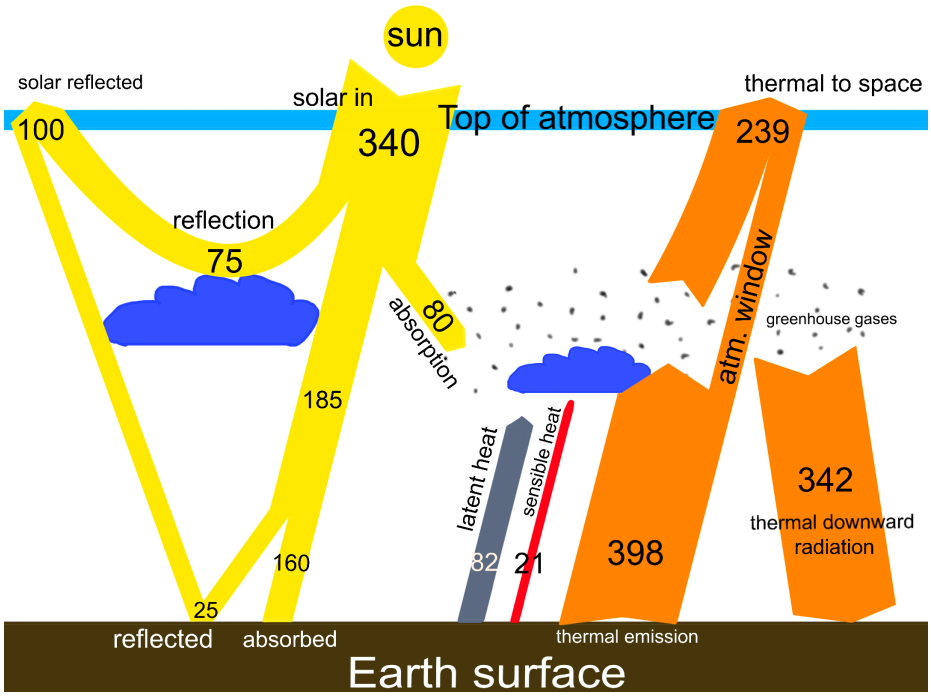

Figure 3.10.: Radiation budget of the atmosphere adapted from (Wild et al., 2014). On the left, the incoming solar radiation is modified by reflection and absorption in the atmosphere and at the surface, while on the right, the thermal radiation from the surface and atmosphere is depicted. All numbers are in $\mathrm{W\,m^{-2}}$.

Assuming the solar spectrum as a black body spectrum and taking into account that the sun covers a solid angle of $\sim 6.8 \cdot 10^{-5}\,\mathrm{sr}$ from Earth, the temperature of this black body can be calculated with the Stefan-Boltzmann law

$$\pi B(T) = \sigma T^4, \tag{3.79}$$

to $\sim 5760\,\mathrm{K}$. $\sigma = 5.7 \cdot 10^{-8}\,\mathrm{W\,m^{-2}\,K^{-4}}$ is hereby the Stefan-Boltzmann constant, not to be confused with the Boltzmann constant k above. This equation is obtained by integrating Eq. (3.40) over all wavelengths and the hemisphere above the emitting surface, assuming that the radiation is emitted in all directions equally (isotropic radiation).

The wavelength of maximum intensity dependent on the temperature of the black body is found by equaling the derivative of Eq. (3.40) equal to zero, which gives Wien's law:

$$\lambda_{\max} = \frac{2898\,\mu\mathrm{m}}{T}. \tag{3.80}$$

For the solar spectrum, the maximum is at $\sim 503\,\mathrm{nm}$, which is at the lower end of the green part of the visible spectrum. As the $1360\,\mathrm{W\,m^{-2}}$ are calculated for a disc with area $\pi\,R^2$, while the Earth is (approximately) a sphere with surface $4\,\pi\,R^2$, the average solar radiation on the Earth is $S_0 = 1360\,\mathrm{W\,m^{-2}} \cdot \frac{\pi\,R^2}{4\,\pi\,R^2} = 340\,\mathrm{W\,m^{-2}}$.

In the wavelength region covered by the solar radiation and for atmospheric temperatures around and below 300 K, the emission of the atmosphere in the radiation budget can be neglected. The solar radiation is then modified only by absorption of the gases in the atmosphere and scattering at particles and molecules (see the left half of Fig. 3.10). Approximately $75\,\mathrm{W\,m^{-2}}$ are scattered back from the atmosphere into space, while $\sim 25\,\mathrm{W\,m^{-2}}$ are reflected at the ground. These reflection and scattering processes have some wavelength dependency, e.g., the λ^{-4} dependency of rayleigh scattering (see Sect. 3.2). Furthermore, the surface does not reflect all wavelengths equally, but those changes with wavelength are relatively continuous.

Contrary to that, the absorption in the atmosphere only occurs at the so-called absorption bands of the corresponding gases. For the solar spectrum, mainly O_3 in the UV below 0.35 µm and H_2O around 0.72 µm, 0.81 µm, 0.93 µm, 1.13 µm, 1.37 µm and 1.85 µm absorb most of the radiation in these wavelength ranges. These absorption bands are optically thick, meaning the incoming solar radiation is completely absorbed in these bands. Several other gases absorb the incoming solar radiation, e.g., CH_4 and CO_2, but also O_2, which are discussed in more detail in Sect. 3.3. However, their contribution to the extinction of solar radiation is small compared to the absorption of H_2O and O_3. The fraction of the incoming solar light neither being reflected nor absorbed by the atmosphere is then absorbed by the surface, which takes up $160\,\mathrm{W\,m^{-2}}$.

The warm surface of the Earth emits $398\,\mathrm{W\,m^{-2}}$ as thermal radiation. Assuming black body radiation again, the average temperature of the Earth's surface becomes (with Eq. (3.79)) 289 K. The wavelength of maximum emission according to Eq. (3.80) is at $\lambda \approx 10.1\,\mu\mathrm{m}$. Additionally, latent and sensible heat transfer 82 and $21\,\mathrm{W\,m^{-2}}$ from the surface to the atmosphere. Latent heat is the energy obtained or released without a temperature change of the substance. The primary mechanism transferring latent heat in the atmosphere is the evaporation and condensation of water and water vapor. Sensible heat is transferred by direct non-radiative heat transfer through contact.

Additionally, the atmosphere also emits thermal radiation, although at slightly lower temperatures. Unlike the surface, the atmosphere emits thermal radiation only in the wavelength ranges where it can absorb thermal radiation. In this manner, the atmosphere radiates $342\,\mathrm{W\,m^{-2}}$ back to the surface. Water vapor has strong absorption bands at $5 - 8\,\mu\mathrm{m}$ and $> 16\,\mu\mathrm{m}$, while CO_2 absorbs strongly between 13 and 17 µm. At around 9.6 µm, an absorption band of O_3 lies in the so-called atmospheric window between the strong and broad absorption bands. At the lower edge of the atmospheric window, between 7 and 8 µm, absorption bands of di-nitrous oxide (N_2O) and CH_4 are located. Therefore, large parts of the thermal spectrum are absorbed in the atmosphere and reemitted in all directions. As the temperature decreases with altitude in the troposphere, where most of the water vapor is located (see Sec. 3.1), this produces a net difference between the thermal radiation emitted at

the surface ($398\,\mathrm{W\,m^{-2}}$) and the thermal radiation that exits the Earth system ($239\,\mathrm{W\,m^{-2}}$) of $G = 159\,\mathrm{W\,m^{-2}}$, which quantifies the so-called greenhouse effect.

The greenhouse effect is, in large parts, natural and even necessary to enable life as we know it on Earth. If the greenhouse effect would not exist, i.e., the Earth would emit thermal radiation unhindered, and assuming an average planetary albedo of ~ 0.3 (combined reflection from the surface and atmosphere) in an otherwise unchanged atmosphere, then the temperature of the Earth would be 30 to 33 K colder. However, on top of this natural part, human activities also influence the greenhouse effect (hence anthropogenic greenhouse effect), mainly due to carbon dioxide and methane emissions into the atmosphere. While comparable small (+1.11 K for the global mean surface temperature in 2020 compared to preindustrial times according to (S.K.Gulev et al., 2021)), the implications for life on Earth are drastic (see e.g. IPCC 2018, 2018).

The causes and magnitude of the anthropogenic influence on the greenhouse effect are assessed by the so-called effective radiative forcing concept (EFR, Myhre et al., 2013; Boucher et al., 2013; Sherwood et al., 2015), which describes the change in the top of atmosphere (TOA) radiation budget due to a perturbation of, e.g., the atmospheric concentration of a greenhouse gas relative to preindustrial times after the system has reached radiative equilibrium again. The forcing is consequently the sum of the instantaneous radiative forcing (IRF) and the forcing due to adjustments. Changes in radiation only caused by surface temperature changes (which are a cause of the perturbation and are called feedbacks) are excluded, as those occur independently of the cause of change in surface temperature (Sherwood et al., 2015). The ERF of greenhouse gases, mainly CO_2, CH_4, and N_2O but also with minor contributions of chlorofluorocarbons (CFCs) and hydrofluorocarbons (HCFCs and HFCs), is assessed to be $3.3\,\mathrm{W\,m^{-2}}$, while ozone contributes additional $\sim 0.5\,\mathrm{W\,m^{-2}}$. Introducing aerosols into the atmosphere, especially due to burning biomass and fossil fuels, contributes an ERF of $-1.1\,\mathrm{W\,m^{-2}}$, thus reducing the outgoing thermal radiation. Other contributions are due to land use change, aviation through contrails and aviation-induced cirrus, and absorbing particles on snow and ice. The total anthropogenic ERF in the industrial period since 1750 is $\sim 2.7\,\mathrm{W\,m^{-2}}$.

3.5. Dynamics in the lower troposphere

The CO_2 and CH_4 molecules in the atmosphere are transported around the globe along the global circulation, including the slow transport through the tropopause in the tropics and further up in the atmosphere. However, this work focuses on point sources of CH_4 and CO_2. As described in Sect. 2, these are located at or near the surface. Therefore, the dynamics of the atmosphere near the surface are of special interest. First, the circulation and wind direction in the boundary layer are described, followed by the layering of the atmosphere dependent on the lapse rate. Finally, turbulent and diffuse mixing is introduced. This section is mainly based on the textbook of Roedel and Wagner (2017) unless otherwise stated.

The horizontal movement of an air parcel is different in the free troposphere and the boundary layer, in which additional effects from the surface play a role. In the free troposphere

and in the presence of a pressure gradient, the air moves from high to low pressure and is deflected by the Coriolis force due to the rotation of the Earth. The Coriolis force is proportional to the air velocity. Therefore, the air parcel gets deflected until the component of the Coriolis force in the direction of the pressure gradient $\vec{\mathrm{F}}_{C,\vec{p}}$ and the pressure gradient force $\vec{\mathrm{F}}_P$ cancel out:

$$\vec{\mathrm{F}}_{C,\vec{p}} + \vec{\mathrm{F}}_P = 2\,\rho\,\left[\vec{v}_g \times \vec{\Omega}\right] - \nabla p = 0. \tag{3.81}$$

Here, ρ is the density of air, $\vec{v}_g$ the velocity vector of the air parcel, $\vec{\Omega} = (0, 0, \Omega \sin\phi)$ is the angular velocity of the Earth perpendicular to the surface of the Earth, and $\nabla p = (\frac{\partial}{\partial x}, \frac{\partial}{\partial y}, \frac{\partial}{\partial z}) \cdot p$ is the gradient of the pressure p. The resulting wind is called "geostrophic wind".

A significant deviation from this geostrophic wind occurs in the presence of friction, e.g., caused by the surface of the Earth. Friction reduces the air parcel's velocity and, consequently, the Coriolis force acting on the air parcel. This causes an imbalance between the Coriolis force and the (unchanged) pressure gradient force. Therefore, the air parcel is moved in the direction of the pressure gradient force, although at a slower speed. The wind speed decreases with altitude until it becomes 0 in the so-called molecular layer at the surface.

Expanding Eq. (3.81) by the frictional force assuming the frictional force applies in x-direction and dividing by ρ gives, with the coefficient of turbulent diffusion in z-direction, K_z,

$$2\,\Omega \sin\phi \cdot (v_y, -v_x) - \frac{\nabla p}{\rho} = \frac{\mathrm{d}}{\mathrm{d}z}\left[K_z \cdot \left(\frac{\partial v_x}{\partial z}, \frac{\partial v_y}{\partial z}\right)\right]. \tag{3.82}$$

Near the surface, the frictional forces dominate, and pressure gradient and Coriolis force can be neglected. This layer, called the Prandtl layer, is usually of the order of $\sim 50\,\mathrm{m}$, and the wind shear is constant in this layer. Above this layer, the pressure gradient and Coriolis force become increasingly important, resulting in the Ekman layer, where the wind direction and wind speed change with altitude.

An air parcel emitted to the atmosphere at the surface will be transported horizontally (as described above) and vertically. For vertical transport, the stability of the atmosphere, described by the so-called lapse rate, is essential. The dry adiabatic lapse rate follows from the assumption of an air parcel at the surface being heated, then rising adiabatically (i.e., without releasing or absorbing energy). As the pressure reduces with altitude (see Sect. 3.1), the air parcel expands, and, following the ideal gas law, the temperature of the air parcel decreases. From the first law of thermodynamics, the dry adiabatic lapse rate Γ_{dry} follows to

$$\Gamma_{\mathrm{dry}} = -\frac{\mathrm{dT}}{\mathrm{dz}} = \frac{\mathrm{M} \cdot g}{\mathrm{C}_p}, \tag{3.83}$$

with the molar mass M, the gravitational constant g, and the specific heat C_p at constant pressure.

Comparing the current adiabatic lapse rate of the air parcel $\gamma_{\text{parcel}} = -\frac{\text{dT}}{\text{dz}}$ with the adiabatic lapse rate of the surrounding air Γ allows for the estimation of stability of the atmosphere. If $\gamma_{\text{parcel}} < \Gamma$, the air parcel cools faster when moved to higher altitudes than the surrounding air. Therefore, it gets denser than the surrounding air and moves back down. Moving down, it heats again until it reaches a stable point, where the air parcel is as warm/cold as the surrounding air. This process results in stable layering.

On the contrary, when $\gamma_{\text{parcel}} > \Gamma$, the air parcel cools slower than the surrounding air when rising. Therefore, it is always warmer than the surroundings and will continue to rise. Additionally, it will heat faster than the surrounding air when moving downwards. Therefore, when moved out of its equilibrium position, an air parcel will continue to move in this direction. This layering is called unstable. If $\gamma_{\text{parcel}} = \Gamma$, called neutral layering, an air parcel will always rest at its position, even after being moved.

On its way through the atmosphere, an air parcel will mix with the surrounding air by diffusion and turbulent mixing. Molecular diffusion only is significant at the boundary between the surface and the atmosphere. In the atmosphere, turbulent transport of momentum and gases mix the atmosphere much more efficiently than molecular diffusion. Unlike molecular diffusion, turbulent diffusion depends on the air's propagation direction, leading to differences in horizontal and vertical turbulent diffusion. Additionally, the diffusion coefficient is not time-independent. For an ensemble of molecules, the mean distance from the origin of the plume $\sigma_x(t)$ under turbulent diffusion in the x-direction at the time t is described by Taylor's theorem:

$$\sigma_x^2(t) = 2\,\overline{v'^2} \int_0^t \int_0^{t'} R_{L,x}(\tau)\,\mathrm{d}\tau\,\mathrm{d}t'. \tag{3.84}$$

$\overline{v'^2}$ is the mean turbulent fluctuation of speed, and $R_{L,x}$ is the Lagrangian autocorrelation function, which describes the correlation of the speed between the current time t and times $\tau = t - t'$ in the past. The mean distance σ is proportional to the diffusion time for short diffusion times, while for long diffusion times, it becomes proportional to $\sqrt{t}$. Simultaneously to the turbulent diffusion, the air is moved by turbulence, resulting in the wave-like shape of plumes observed near their emission source. After averaging over a long time frame of constant emissions, this wave-like shape and the apparent turbulent structure vanish.

For the flux density $j = c\,v$ of an additive with mean concentration $\overline{c}$ and speed $\overline{v}$, and their respective fluctuations c' and v', the average flux density becomes

$$j = \overline{c} \cdot \overline{v} + \overline{c' \cdot v'} = j_{advective} + j_{turbulent}. \tag{3.85}$$

The turbulent flux density is also called the covariance between the fluctuations of concentration and speed c' and v'.

4. Application of spectroscopy to observe CO_2 and CH_4 concentrations in the atmosphere

Continuous measurements of the greenhouse gas CO_2 date back to the late 1950s, when in Antarctica and Hawaii Revell and Keeling established atmospheric carbon dioxide measurement stations (Revelle and Suess, 1957; Keeling, 1960). Continuous CH_4 measurements followed in the 1980s. Since then, the measurement techniques and the coverage of the atmosphere have improved significantly (see e.g. Saunois et al., 2020; Friedlingstein et al., 2020; Chen et al., 2021). Additionally, monitoring not only the average (or background) state of the atmosphere but also regional differences as well as sources and sinks of CH_4 and CO_2 became more critical and detailed. This chapter summarizes an overview of the different measurement techniques to determine atmospheric concentrations of CH_4 and CO_2.

Measurements of greenhouse gases can be separated into two main categories: In situ and remote sensing techniques. In situ describes greenhouse gas concentration measurements directly in an air parcel either on-place or by sampling air for the analysis in a laboratory. Remote sensing applications use a light source and measure the absorption due to the gases in the atmosphere. Typical light sources are the sun for passive and LASER or antennas for active remote sensing. Therefore, the examined air mass is the main difference between these two measurement types. While in situ observations probe an air parcel directly and measure concentrations at a distinct point in the atmosphere, remote sensing measurements probe the total or a partial column of air, dependent on the light source and observation geometry. Both basic measurement categories have advantages and disadvantages, dependent on the target of the observations, the required measurement precision, and the repeatability of the measurement. Also, both measurement types can be performed from different platforms, although only remote sensing measurements are possible from space. The following presents the different types of in situ and remote sensing measurements, and their advantages and disadvantages are discussed.

4.1. In Situ measurements of the greenhouse gases CH_4 and CO_2

For quite some time, measurements of atmospheric CH_4 and CO_2 were only performed by in situ measurements. As described above, atmospheric gas samples are either directly analyzed on-site or sampled in flasks for later analysis in laboratories. The air

samples are either acquired stationary (mostly from tall towers) or mobile from cars or aircraft.

Measurement stations for continuous in situ measurements of CH_4 and CO_2 have been and are often established in networks, often targeting atmospheric background concentrations such as the European Integrated Carbon Observation System (ICOS, ICOS ERIC, 2022; Franz et al., 2018) and the North American tall tower system of the National Oceanic and Atmospheric Administration Earth System Lab, Global Monitoring Division (NOAA ESRL/GMD, Andrews et al., 2014). Recently, also in situ networks monitoring polluted air, e.g., from urban areas, such as the Northeast Corridor greenhouse gas network (Karion et al., 2020) or the Permian Basin tower network (Monteiro et al., 2022, accepted for publication) were established. In combination with atmospheric transport models, these measurements are used to determine the contribution of various sources and sinks to the atmospheric growth rate, especially for CH_4 (e.g. Schwietzke et al., 2016; Rigby et al., 2017), and to assess changes in the state and processes in the atmosphere (e.g. Keeling et al., 2017). Additionally, networks are proposed to reduce uncertainties in global atmospheric models. These proposed network additions target undersampled regions, e.g. Africa (Nickless et al., 2020) and Asia (Park and Kim, 2020). Additionally, stationary networks have been combined, e.g., in the framework of the FLUXNET network (Knox et al., 2019).

Furthermore, in situ measurements have been made on mobile platforms. In situ analyzers and flask samplers have been installed on cars, e.g., to observe local emissions by biogas power plants (Reinelt and Liebetrau, 2019; Bakkaloglu et al., 2021), localize leakages in natural gas distribution networks (von Fischer et al., 2017; Caulton et al., 2018), or analyze typical isotopic signatures of specific areas (e.g., coal mining in southern Poland, Menoud et al., 2021). On drones, systems have been tested for direct measurements of anthropogenic CO_2 point source emission plumes (Reuter et al., 2021), CH_4 emissions from a landfill (Tuzson et al., 2020), or have been mounted on smaller drones to measure CH_4 (Martinez et al., 2020). Also, AirCore systems, which sample air in a thin, long tube that is analyzed later in the laboratory, have been flown successfully with UAV (e.g. Vinković et al., 2022; Andersen et al., 2018). Furthermore, in situ analyzers and flask samplers have been installed on board of aircraft to measure emissions from coal mining (e.g., Fiehn et al., 2020; Kostinek et al., 2021; Neininger et al., 2021), offshore and onshore oil and gas production (e.g., Caulton et al., 2014; Riddick et al., 2019), but also regional gradients (e.g., Gałkowski et al., 2021).

A significant advantage of in situ measurements is the high precision and accuracy, especially in flask measurements. The price for this is, for stationary measurements, the need to rely on atmospheric transport models to calculate the origin of the air parcel measured. Measurements from cars rely on assumptions about the mixing in the atmosphere and the height of the boundary layer, while aircraft measurements cannot sample down to the ground. Combining both car and airborne measurements partly resolves this problem (e.g., Leifer et al., 2018). Nevertheless, the atmospheric concentrations must be interpolated between the measurements at different heights.

4.2. Remote sensing measurements of the greenhouse gases CH_4 and CO_2

Remote sensing measurements sample the whole atmospheric column, eliminating the need for interpolation. However, remote sensing instruments provide these total column estimates with lower precision than in situ measurements.

Remote sensing measurements, as in situ measurements, exist in different settings, depending on the scale in time and space where measurements are taken. The Total Carbon Column Observing Network (TCCON, Wunch et al., 2011) is the association of sparsely but globally distributed measurement stations equipped with EM27 Fourier-Transform infrared spectrometers (FTIR), which measure the direct solar radiation with very high spectral resolution in occultation, i.e. looking directly into the sun. Another global network of stationary remote sensing instruments is the Network for the Detection of Atmospheric Composition Change (NDACC, Mazière et al., 2018), where, additionally to FTIR instruments to measure greenhouse gases, also other (mostly remote sensing) measurements are taken. Due to the high spectral resolution of the FTIR, not only total columns but also vertical profiles are obtained. Additional remote sensing networks have been set up temporarily to measure, e.g., urban methane emissions (Jones et al., 2021) or coal mining emissions (Luther et al., 2019, 2022).

Global networks such as TCCON and NDACC have been used as validation standards for multiple satellite remote sensing systems. The biggest advantage of satellite remote sensing measurements of greenhouse gases is the possibility for global coverage and observation of remote or politically unstable regions otherwise difficult to monitor. The SCIAMACHY instrument (Burrows et al., 1995; Bovensmann et al., 1999) launched onboard the European satellite ENVISAT in 2002 enabled monitoring of CO_2 and CH_4 on a global scale (e.g. Buchwitz et al., 2005; Frankenberg et al., 2006; Schneising et al., 2008) with a spatial resolution between 60 $\times$ 30 to 240 $\times$ 30 km^2 (across x along-track) depending on the solar zenith angle with a swath width of $\sim$ 960 km. The SCIAMACHY instrument comprised 8 spectral channels covering the wavelength range from 240 to 2385 nm nearly continuously with a spectral resolution of 0.4 nm in the O_2A band, 1.4 nm in the SWIR between 970 and 1772 nm and 0.2 nm between 2360 and 2385 nm. Although emission estimates for large high emitting areas were possible (Schneising et al., 2014; Kort et al., 2014), only very high emitting areas could be detected, and attribution of emissions to direct sources (e.g., single power plants or methane leaks) is not possible. SCIAMACHY measurements stopped in 2012.

Since then, quite a few satellites have been deployed to measure total column CH_4 and (to a lesser extent) CO_2. The Greenhouse Gas Observing Satellite (GOSAT, launched 2009, Kuze et al., 2016) and its successor, GOSAT-2 (launched in 2018, Suto et al., 2021) both comprise Fourier transform spectrometers tuned to cover the wavelength ranges of weak and strong CO_2 and CH_4 absorption bands in the SWIR (around 1600 and 2000/2300 nm respectively), the O_2A absorption band at 760 nm and two wavelength bands in the thermal infrared. Both GOSAT instruments have no imaging capabilities, i.e., they measure only one point below the satellite with a diameter of $\sim$ 10 km with significant gaps between single

measurements due to pointing at one footprint during the acquisition of a single FTIR spectrum. Nevertheless, apart from global CH_4 and CO_2 concentration studies (e.g. Butz et al., 2011; Turner et al., 2015; Maasakkers et al., 2019; Noël et al., 2021), also, observations of a gas well blowout at Aliso Canyon (Kuze et al., 2020) have been performed with some success. In 2014, the Orbiting Carbon Observatory-2 was launched (OCO-2, Frankenberg et al., 2015; Crisp et al., 2017). OCO-2 comprises an imaging spectrometer measuring eight adjacent ground scenes across a 10 km wide swath in the wavelength ranges of the O_2A band ($\sim$ 760 nm, FWHM $\approx$ 0.042 nm) and the weak and strong absorption of CO_2 in the SWIR ($\sim$ 1610 nm, FWHM $\approx$ 0.076 nm and $\sim$ 2060 nm, FWHM $\approx$ 0.097 nm respectively). As a trade-off for the high spectral and spatial resolution, no CH_4 absorption features are observed. Furthermore, OCO-2 measurements do not cover the whole Earth, only small "stripes". Nevertheless, OCO-2 measurements have been used to estimate anthropogenic emissions from polluting regions (Hakkarainen et al., 2016) or power plants (Nassar et al., 2021). In 2019, the OCO-3 instrument (Taylor et al., 2020) incorporating a scanning mode to scan regions of interest, e.g., power plants or cities, was added to the International Space Station (ISS).

A major addition to the monitoring capabilities of CH_4 from space was the launch of the TROPOMI instrument (Veefkind et al., 2012) onboard the Sentinel-5 precursor (S5P) satellite. Similar to SCIAMACHY, it is a nadir-looking grating spectrometer. However, the swath width was enhanced to 2600 km, and the nadir ground scene size is approximately $7 \times 7\,\mathrm{km}^2$ for SWIR measurements. CH_4 absorption features are recorded in the strong absorption band in the SWIR at $2305 - 2385$ nm with a spectral resolution of ~ 0.5 nm. This development allowed for the detection of emitting regions from single overpasses (e.g. Schneising et al., 2019), and quantification of emissions from cities (e.g. Plant et al., 2022), coal mining areas (e.g. Sadavarte et al., 2021) and even single sources such as, e.g., a gas well blowout (Pandey et al., 2019).

The GHG-Sat instruments (Jervis et al., 2021) are small CubeSat instruments ($12 \times 12 \times 25\,\mathrm{cm}^3$), which are planned to be flown in a constellation. The instruments comprises a wide-angle fixed-cavity Fabry-Perot interferometer and target absorption features of CH_4 between 1630 and 1675 nm with a spectral resolution of ~ 0.1 nm. Although the swath width is relatively small (the methane retrieval domain size is $12 \times 12\,\mathrm{km}^2$), the single ground scene size, i.e. the spatial resolution, is $50 \times 50\,\mathrm{m}^2$. Intelligent targeting, e.g., by prior knowledge of potential sources (e.g. Varon et al., 2019) or to potential areas of interest such as generally oil and gas infrastructure, facilitates the detection of methane emissions. However, only strong point source emissions could be detected up to now. A fine spatial resolution's advantages are the possibility of pinpointing the exact emission source. Therefore, in the last years, also data from hyperspectral instruments such as the "PRecursore IperSpettrale della Missione Applicativa" (PRISMA, Cusworth et al., 2021b) or multispectral instruments such as MSI on Sentinel-2 (Varon et al., 2021) have been used successfully to observe methane super-emitters.

In addition to satellites measuring absorption in the SWIR, also thermal emission in the thermal infrared region (TIR, between roughly 5 and 25 µm) can be used for observations of CH_4 and CO_2. The most important ones are the TIR bands on the GOSAT and GOSAT-2 instruments (Kuze et al., 2016; de Lange and Landgraf, 2018), the Atmospheric Infrared

Sounder (AIRS, Aumann, 1994), the Infrared Atmospheric Sounding Instrument (IASI, Blumstein et al., 2004) and the Tropospheric Emission Spectrometer (TES, Beer et al., 2001).

Between the high precision stationary measurements and the global or regional satellite measurements being able to detect very large point sources, airborne remote sensing systems are necessary for validation of satellite observations and additional monitoring of lower emitting point sources or areal sources. While TIR remote sensing instruments such as the Spatially Enhanced Broadband Array Spectrograph System (SEBASS, Vaughan et al., 2003) or the Hyperspectral Thermal Emission Spectrometer (HyTES, Hook et al., 2013) were able to detect very low emissions of CH_4 while flying low (Hulley et al., 2016; Scafutto et al., 2018), they have significant difficulties detecting sources at the surface when flying higher (see, e.g., Jongaramrungruang et al., 2019) due to the absorption and reemission of thermal radiation higher up in the atmosphere, basically "shielding" the thermal emissions from ground.

On aircraft, active remote sensing of CH_4 and CO_2 has been implemented by using LASER pulses on- and off-band of CH_4 and CO_2 absorption lines in the "CO_2 and CH_4 Remote Monitoring - Flugzeug" (CHARM-F, Amediek et al., 2017) instrument. Using its self-generated light on board the aircraft allows for measurements during the night or in cloudy conditions, where passive remote sensing measurements fail. However, the LASER has to be very stable, and CHARM-F has no imaging capability, measuring the column below the aircraft at a single point across the flight track.

Passive remote sensing of greenhouse gases from aircraft has been advanced by, on the one hand, the Methane Airborne MAPper (MAMAP, Gerilowski et al., 2011), which was designed especially for that case covering the weak CO_2 and CH_4 absorption bands in the SWIR between 1590 and 1690 nm with ~ 0.9 nm spectral resolution, but only measures one spatial point below the aircraft simultaneously. The MAMAP instrument has been used to estimate the emissions of coal-fired power plants (Gerilowski et al., 2011; Krings et al., 2011, 2018), coal mines (Krings et al., 2013; Krautwurst et al., 2021), and a landfill (Krautwurst et al., 2017). Furthermore, it was even possible to establish an upper bound for the emission of an underwater gas blowout in the North Sea (Gerilowski et al., 2015). While it can detect relative enhancements of CH_4 and CO_2 of $\sim 0.5\,\%$ above the background on a local scale, being a non-imaging instrument requires flying orthogonal to the source, rendering the detection of small or unknown point sources difficult to impossible.

On the other hand, measurements acquired with the Airborne Visible InfraRed Imaging Spectrometer - Next Generation (AVIRIS-NG, Green et al., 1998; Chapman et al., 2019), which is an imaging instrument measuring 600 ground scenes with spatial resolutions of a few square meters covering the spectral range between 380 and 2500 nm with a spectral resolution of $5 - 6$ nm, were successfully used to detect and estimate CH_4 emissions from the fossil fuel industry (e.g. Thompson et al., 2015; Frankenberg et al., 2016; Thorpe et al., 2017, 2020) and landfills (Cusworth et al., 2020). While under favorable conditions, due to the high spatial resolution, even quite low emitting CH_4 sources could be detected (Thorpe et al., 2016), the methane retrieval results show partly strong dependencies of the surface type (Ayasse et al., 2018).

Three categories of retrievals exist to retrieve CH_4 column enhancements from passive remote sensing measurements, especially imaging instruments. Statistical methods such as a matched filter method (Thompson et al., 2015; Foote et al., 2020) make use of hypothesis tests for the presence or absence of absorption in the spectra, training on a large amount of data available, and, in the case of Foote et al. (2020), also utilizing the fact that only very few of the measurements show significant CH_4 enhancements above background. For this method, many measurements without enhancement are needed, which is valid for the high spatial lower spectral resolution measurements such as in AVIRIS-NG, but not for MAMAP measurements. The results are enhancements of the gas above the background.

Linearized methods such as the WFM-DOAS method (Buchwitz et al., 2000; Krings et al., 2011) are based on a radiative transfer model representing the average state of the atmosphere for the measurement, assuming approximately constant conditions in atmospheric parameters not retrieved, and only slight deviations from the assumed gas concentrations over the measurement range. Implementing lookup tables for the most critical parameters not retrieved, e.g., the surface elevation and solar zenith angle (Krautwurst et al., 2017; Schneising et al., 2019), enables to mitigate this problem partly, but only for known parameters. Finally, iterative optimal estimation methods incorporating a forward model, which is calculated for each measurement point, are used mostly for satellite measurements (e.g. Frankenberg et al., 2006; Reuter et al., 2017b; Wu et al., 2018), but have also been applied to airborne remote sensing measurements (e.g. Thorpe et al., 2014). However, as the forward model has to be convolved with the instrument slit function in each forward model calculation, and, for each data point, multiple iterations are needed, optimal estimation-based methods are much slower than the non-iterative methods mentioned before.

5. Instruments, data sets and methods

The research questions introduced at the end of Chapter 1 are studied using different instruments, data sets, and methods. In contrast, a common inversion scheme to estimate emissions and their uncertainties was used for all data sets. This Chapter describes the instruments AVIRIS-NG, MAMAP, and MAMAP2D-Light with their respective data sets in Sect. 5.1. Column enhancements of CH_4 and CO_2 are evaluated from these data sets using the WFM-DOAS and the newly developed FOCAL AIR retrieval method, which are introduced in Sect. 5.2. Finally, the cross-sectional flux method to estimate the emission from observed column enhancements is described in Sect. 5.3.

5.1. Airborne remote sensing systems and data sets for observation of CO_2 and CH_4 total column anomalies

The data analyzed in this thesis to answer the three main research questions originate from the MAMAP2D-Light (Sect. 5.1.3), MAMAP (Sect. 5.1.2) and AVIRIS-NG (Sect. 5.1.1) instruments. While the MAMAP2D-Light system was built with the MAMAP team as part of this thesis at IUP Bremen, the MAMAP and AVIRIS-NG instruments (as mentioned in the introduction, Sect. 1) already existed and were already used successfully to observe and quantify CH_4 and CO_2 emissions plumes.

All three instruments are airborne nadir-looking remote sensing spectrometers. The measured quantity for all instruments is the solar radiation reflected from the ground to the instrument. With subsequent analysis of the absorption features of CO_2 and CH_4 present in the spectra, it is possible to extract deviations of these gases from their local background concentration and estimate emissions from point sources. The three instruments and the data sets used to answer the research questions are described below, with AVIRIS-NG in Sect. 5.1.1, MAMAP in Sect. 5.1.2, and MAMAP2D-Light in Sect. 5.1.3. As an overview, their main characteristics are given in Table 5.1.

Table 5.1.: Main characteristics of the three instruments MAMAP2D-Light, MAMAP, and AVIRIS-NG. This table contains characteristics combined from publications (mostly for AVIRIS-NG and MAMAP non-spectral data) as well as derived during the work for this thesis (MAMAP spectral characteristics and MAMAP2D-Light characteristics). The typical spatial resolution is given for a flight altitude of $\sim 1500\,\mathrm{m}$ and for MAMAP describes the binned burst of 10 consecutive measurements in the along-track direction.

Parameter	**MAMAP2D-Light**	**MAMAP**	**AVIRIS-NG**
Spectral range	$1559.54 - 1690.05\,\mathrm{nm}$	$1587.56 - 1686.90\,\mathrm{nm}^a$ $755.588 - 772.160\,\mathrm{nm}^a$	$380 - 2450\,\mathrm{nm}$
Spectral sampling	$0.34\,\mathrm{nm}$	$0.097\,\mathrm{nm}$ $0.065\,\mathrm{nm}$	$5\,\mathrm{nm}$
Spectral resolution (FWHM)	$1.08\,\mathrm{nm}$	$0.64\,\mathrm{nm}^a$ $0.42\,\mathrm{nm}^a$	$5 - 6\,\mathrm{nm}$
# of spectral points	384 pixels	1024 pixels (SWIR) 256 pixels (NIR)	425 pixels
# of FOV	28	1	600
Across-track spatial resolution	$22\,\mathrm{m}$	$45\,\mathrm{m}$	$1.5\,\mathrm{m}$
Along-track spatial resolution	$6\,\mathrm{m}$	$90\,\mathrm{m}^b$	$1.5\,\mathrm{m}$
Data resolution	16-bit (65536 BU)	16-bit (65536 BU)	14-bit (16384 BU)
SNR	~ 760 (at 33000 BU)	~ 1300 (at 33000 BU)	up to 800 (2200 nm) (conditions unclear)
Total weight and design	$43.8\,\mathrm{kg}$ one structure	$\sim 250\,\mathrm{kg}$ two Falcon racks	$\sim 465\,\mathrm{kg}$ Instrument, racks, and electronic boxes

[a] according to recalibration fit described in Sect. A.4

[b] for a complete burst of 10 measurements

5.1.1. The AVIRIS-NG remote sensing system and data sets

The AVIRIS-NG instrument is an airborne hyperspectral push-broom imaging Offner spectrometer. It comprises a spectrometer unit mounted onto a stabilizing platform, an electronics support rack, and an operator station (Hamlin et al., 2011) with a total weight of $\sim 450\,\mathrm{kg}$ including all components. The instrument was mainly developed for mineralogy and terrestrial ecology (see e.g., Bue et al., 2015; Govil et al., 2018) as its predecessor AVIRIS (Vane et al., 1993), but due to its high SNR and spatial resolution, it also proved capable of detecting and quantifying CH_4 and CO_2 point source emissions using absorption features of both gases between 2.0 and 2.4 µm (see e.g., Thorpe et al., 2013; Dennison et al., 2013; Thorpe et al., 2017; Foote et al., 2020; Thorpe et al., 2020).

5.1.1.1. AVIRIS-NG instrument description

The front optic system is directly mounted in front of the spectrometer and covers an instantaneous FOV of $36^\circ \times 0.1\,\mathrm{mrad}$ (across x along-track), which results in a spatial resolution of $\sim 5\,\mathrm{m}$ and a swath width of 3 km for a flight altitude of 5 km above ground. The spectrometer unit itself comprises a single spectral channel covering the wavelength range from 380 to 2450 nm with a wavelength dependent spectral resolution of $5 - 6\,\mathrm{nm}$ and a spectral sampling of $\sim 5\,\mathrm{nm}$ (Hamlin et al., 2011; Chapman et al., 2019), resulting in slightly undersampled spectra. It uses mirrors for the collimator and camera optics, and a curved grating. The detector is a 640×480 pixel MCT FPA, from which 600×425 pixels (across-track x spectral pixels) capture the reflected solar radiation from ground, while the outer pixels are shielded for dark current monitoring. At 2200 nm, the SNR of AVIRIS-NG is up to 800 (Thorpe et al., 2016). The spectrometer is housed in a cooled vacuum vessel to minimize thermal dark current as well as changes in the optical alignment due to temperature and pressure changes.

5.1.1.2. AVIRIS-NG ABoVE and Four Corners data set

The AVIRIS-NG level-1 data distributed by the operations team contain absolute radiances orthorectified and gridded to a regular grid and observation data. These contain the current flight altitude, solar and instrument zenith and azimuth angles, surface elevation, latitude, and longitude for each sounding.

The AVIRIS-NG data analyzed in this thesis originate from two different measurement campaigns. The targets for both data sets were methane emissions from point sources in the fossil fuel industry. The first data set comprises the observation of a methane plume originating from the ventilation shaft of an underground coal mine near Fruitland in the Four Corners region in the USA. The data was acquired on 22.04.2016 at 16:45 UTC. The coal mine plume was first reported in Frankenberg et al. (2016), where the methane enhancements were retrieved using the Iterative Maximum A Posteriori DOAS retrieval (IMAP-DOAS, Frankenberg et al., 2005; Thorpe et al., 2014, 2017). Additionally, for comparison with WFM-DOAS results, the enhancements were retrieved with a matched filter algorithm

(Thompson et al., 2015). Due to its length and the relatively homogeneous surface, it provides a good target for comparing the WFM-DOAS method applied to AVIRIS-NG data with IMAP-DOAS and MF retrieval results.

The second data set comprises a subset of flight lines acquired as part of the ABoVE measurement campaign, which took place in August 2017. The subset was selected to cover a wide range of surface types (e.g., forest, mountainous regions, sand, grass, and artificial structures), at-sensor radiance levels, and flight altitudes. Additionally, the tracks contained emission sources of varying strength detected using the MF algorithm to test the WFM-DOAS algorithm against known plume locations over different terrain. In this manner, 13 flight lines on five different days were selected. In total, these contain nearly 89 million data points (i.e., single spectra), with the number of data points per flight line ranging from ~ 1.2 million to > 13 million.

For the WFM-DOAS method (Sect. 5.2.1), the mean atmospheric state is needed to calculate the modeled at sensor intensity. In the following, the origin of the state parameters for the AVIRIS-NG data set is given. As described above, several parameters are part of the distributed level-1 data for each ground scene. Relevant parameters for the mean atmospheric and observational state are the surface elevation, the coordinates of the ground scene, the flight altitude, the time of data acquisition, the solar zenith and azimuth angle, and the instrument zenith and azimuth angles. For each flight line, the average value of each parameter was calculated and used as input to the SCIATRAN calculation. For the temperature, pressure, and H_2O profiles, ECMWF ERA5 data (Copernicus Climate Change Service (C3S) (2017), 2017) interpolated to the average time and location of the flight line were calculated. The background total column of CO_2 was estimated with the Simple Empirical CO_2 Model (SECM, Reuter et al., 2012) in the version SECM2018 (Reuter et al., 2020). The background total column of CH_4 was estimated with the approach used by Schneising et al. (2019), where a climatology averaged over the years $2003 - 2005$ is enhanced by the total increase in methane based on globally averaged marine NOAA surface data (Dlugokencky, 2018). To obtain background profiles for CO_2 and CH_4, a US Standard Atmosphere (United States National Oceanic and Atmospheric Administration and United States Air Force, 1976) was scaled so that the total columns of both gases match the estimated background columns.

Table 5.2.: Wind speed for the plumes P1 - P5 as reported by nearby weather stations.

Plume	**Wind speed**
P1	$3.7\,\mathrm{m\,s^{-1}}$
P2	$7.6\,\mathrm{m\,s^{-1}}$
P3	$3.9\,\mathrm{m\,s^{-1}}$
P4	$4.2\,\mathrm{m\,s^{-1}}$
P5	$4.1\,\mathrm{m\,s^{-1}}$

For the inversion of CH_4 plumes detected by AVIRIS-NG, hourly mean wind speed estimates of weather stations as close by as possible were acquired, as ERA5 surface wind speed estimates significantly underestimated the local surface winds (see Sect. A.1). For the five

plumes (P1 to P5) inverted in Sect. 6.1.6, the hourly mean wind speeds as measured by the weather stations are given in Table 5.2.

5.1.2. The MAMAP remote sensing system and data sets

The MAMAP instrument is a nadir-looking non-imaging grating spectrometer measuring reflected and scattered solar radiation in two channels. The instrument is mounted into two Falcon racks, each weighing $\sim$ 120 kg. One rack houses the two spectrometer units and shutter electronics, while the other houses the control and acquisition PCs and an uninterrupted power supply system, including an aircraft battery. Additionally, the front optics unit is mounted directly over the opening in the aircraft looking in the nadir direction. The short wave infrared channel (SWIR) measures between 1590 and 1690 nm and the near-infrared channel (NIR) between 755.6 and 772.1 nm with a spectral resolution of $\sim$ 0.9 nm and 0.48 nm, respectively. In the SWIR channel, absorption bands of CO_2 and CH_4, as well as water vapor, are located (see also Sect. 3.3), while the NIR channel covers the deep absorption lines of the O_2A band, which can be used for light path corrections in the retrieval. The instrument is described in detail in Gerilowski et al. (2011) and Krings (2013), so only the main features are discussed.

5.1.2.1. MAMAP instrument description

The MAMAP instrument comprises the front optics unit connected to the two entrance slits of the spectrometers with a y-fiber, the two spectrometer units, and additional power and control electronics.

The front optics unit comprises a telescope optic with a focal length of 150 mm, mapping one ground scene onto the common end of the y-fiber bundle, which routes the light to the two modified Acton grating spectrometers. Therefore, both spectrometers observe the same ground scene at the same time. The two spectrometer units are Acton grating spectrometers collimating and focusing the light with mirrors. In the SWIR spectrometer, a 600 lines mm^{-1} grating disperses the incoming radiation onto a linear 1024 pixel extended InGaAs focal plane array (FPA). It is cooled with liquid nitrogen to $-120\,C^\circ$ to reduce the thermal dark current of the chip. The spectral sampling of the SWIR channel is $\sim$ 0.1 nm and the spectral resolution is $\sim$ 0.9 nm.

In the NIR channel, the incoming radiation is dispersed by a 1200 lines mm^{-1} grating. The resulting spectral sampling is $\sim$ 0.07 nm and the spectral resolution is $\sim$ 0.45 nm. The detector of the NIR channel is a 512×512 pixel frame transfer CCD, where on the chip already 6×2 pixels are binned. The resulting data has therefore 85×256 pixels. The recorded data are in binary units, requiring dark and white light spectra for conversion to relative intensities. In Fig. 5.1 an example spectrum of the MAMAP instrument in both channels is shown. The signal-to-noise ratio of the MAMAP instrument for a detector filling of $\sim$ 33000 BU is roughly 1300.

The spectral calibration of the MAMAP instrument was updated for this thesis. The procedure and results are described in A.4. In the measurements analyzed in this thesis, the front

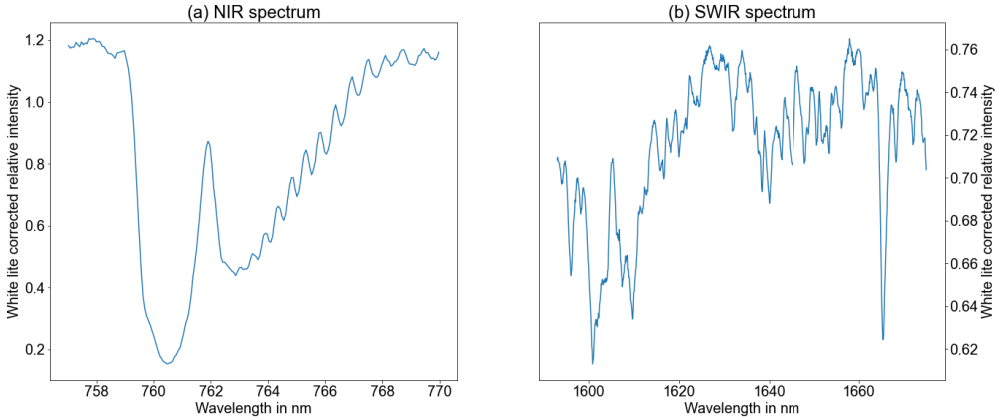

Figure 5.1.: Example spectrum of the MAMAP instrument cropped to the FOCAL AIR fit windows for the 1-window retrieval.

optic was mounted directly over the viewport of the Cessna 207 of the "Freie Universität Berlin" (FUB). For a flight altitude above ground of 1.5 km, a flight speed of $\sim 56\,\mathrm{m\,s^{-1}}$ and a coadded integration time of 1 s (one burst of 10 images), the ground scene size is $\sim 45 \times 90\,\mathrm{m}^2$.

5.1.2.2. MAMAP observational data of the Jänschwalde power plant plume

To compare the WFM-DOAS and the FOCAL-AIR retrieval to assess the advantages and limitations of the latter for future measurements, a data set containing measurements of the target gas(es) and the deep absorption lines of the O_2A band in the NIR spectral region is needed with sufficient spectral resolution. Therefore, neither AVIRIS-NG data (due to the low spectral resolution, see Sect. 5.1.1) nor MAMAP2D-Light data (due to the missing NIR channel, see Sect. 5.1.3) could be used for this analysis. However, the MAMAP instrument measures the relevant spectral channels with relatively high spectral resolution (see Sect. 5.1.2), and the Jänschwalde power plant CO_2 emissions have been previously estimated successfully using MAMAP data retrieved with the WFM-DOAS method (Gerilowski et al., 2011; Krings et al., 2011).

For the comparison, MAMAP measurements recorded over the power plant Jänschwalde during the COMET campaign on 23.05.2018 were analyzed. The instrument was flown on board the Cessna aircraft of the FUB. These data were already analyzed with the WFM-DOAS method previously by Sven Krautwurst, including emission estimations (publication in preparation). Therefore, a direct comparison of the single column retrieval results and the estimated emissions is possible. The surface around the power plant in the direction the plume expanded is a mixture of grassland, farming areas, forests, and some lakes, especially near the power plant. The data set contains $\sim$ 53000 single measurements, i.e. $\sim$ 5300 bursts of 10 measurements. These comprise the flight to the target, the remote sensing

part, an in situ flight pattern, and the flight back to the airport. The remote sensing part of the flight, consisting of 14250 single measurements, was analyzed with the FOCAL AIR method.

As the forward model is calculated for each measurement in the FOCAL AIR algorithm (see Sect. 5.2.2), the forward model parameters and a priori values were estimated for each ground scene separately. The current flight altitude, the location, and the instrument zenith angle were obtained from the MAMAP measurement data. The solar zenith angle was calculated from the date and time of each measurement. The surface elevation was obtained from the Shuttle Radar Topospheric Mission (SRTM V2.1, Farr et al., 2007). The a priori atmospheric profiles for CH_4 and CO_2 were estimated with the Simple cLImatological Model (SLIM, Noël et al., 2022) and sampled to the five combined layers of FOCAL AIR. The atmospheric profile of H_2O, temperature, and pressure, as well as the total amount of dry air molecules, was obtained from ERA5 data (Copernicus Climate Change Service (C3S) (2017), 2017) interpolated to the location of the measurements and cut or extended to the surface elevation obtained from SRTM data. The solar spectrum I_0 for the forward model is a combination of a polynomial fitted to the Thullier-Kurucz solar spectrum for the solar background radiation and the Toon high-resolution solar spectrum (Toon, 2015) in the 2016 version, calculated by Max Reuter.

For the wind speed, the average ECMWF ERA5 hourly horizontal wind data over the whole measurement area between 14.1 and 14.6 ° East and 51.72 and 51.94 ° North averaged over the whole time of the overflight was calculated to $6.2 \pm 1.0\,\mathrm{m\,s^{-1}}$, where the wind speed uncertainty is the $1\,\sigma$ standard deviation of all wind vectors over the boundary layer from which the mean was calculated. The mean wind direction was derived from the apparent plume direction relative to the cross-tracks over the plume.

5.1.3. The MAMAP2D-Light remote sensing instrument and data sets

The MAMAP2D-Light instrument is a lightweight imaging passive remote sensing instrument specifically designed for the detection and quantification of CH_4 and CO_2 points source emissions via solar absorption spectroscopy. It comprises a spectrometer optical bench with one spectral channel covering the wavelength range from 1559 nm to 1690 nm with a spectral resolution of $\sim$ 1.1 nm in a light-tight housing, a front optics unit, data recording and instrument control interfaces. The instrument schematics are displayed in Fig. 5.2 and the spectrometer optical bench without the light-tight housing is shown in Fig. 5.3.

The MAMAP2D-Light instrument was developed and built at the Institute of Environmental Physics in Bremen mainly during the work on this thesis, with significant contributions of the author. His main contributions to the development and building process were the development of the control software and the implementation of the control and acquisition software, as well as assisting in the assembly and adjustment of the spectrometer and assembly of the complete instrument, including the final adjustments needed to fit the instrument into the underwing pod. Finally, the author operated the instrument during the test and measurement flights. The mechanical design of the instrument was developed by the IUP

in cooperation with Jan Franke of the Institute for Integrated Product Development (BIK) at the University of Bremen.

The MAMAP2D-Light instrument design builds on the experience gained with the MAMAP sensor described in Sect. 5.1.2. The goal of the MAMAP2D-Light system was the development of a compact, lightweight, and flexible deployable imaging push-broom spectrometer, which fits inside one underwing pod of a Diamond HK-36 Eco Dimona. One such aircraft was recently acquired by the Jade Hochschule Wilhelmshaven and is operated from there. The limits of the pod constrained the design heavily in weight and dimensions, which resulted in a very compact design (see image 5.4). The spectrometer unit, the IMU sensor, front optics, and control and supply electronics are mounted on the same 3 cm thick aluminum plate. The whole MAMAP2D-Light instrument weighs a total of ~ 43 kg. It additionally serves as a prototype for the SWIR channel of the MAMAP2D system. It was funded partly through the BMBF project AIRSPACE (grant 01LK1701B) and the State and the University of Bremen.

5.1.3.1. MAMAP2D-Light instrument description

The instrument parts are described below in the order in which the light passes through the instrument. Then, the data acquisition hardware and software, the system control hardware and software, and the interface to the aircraft are described. A schematic overview of the MAMAP2D-Light instrument is given in Fig. 5.2.

Front optics unit

The solar radiation backscattered at the ground enters the light through the front optics unit. It comprises a telescope with focal length $F = 25$ mm, which is mounted orthogonally at the end of the base plate. The telescope images the ground onto a custom-designed glass fiber bundle. The fiber bundle comprises 36 rectangular fibers arranged in a slit design. Each fiber has a fiber core of $\sim 300 \times 100\,\mu m^2$. The cladding around the fibers prohibits light from contaminating adjacent fibers. The outer dimensions of the single fibers with cladding are $\sim 315 \times 175\,\mu m^2$. The instantaneous field of view (IFOV) of the front optic assembly is 22.80° across and 0.23° along the flight track.

While the instrument can be flown in various altitudes and is designed to sustain operation altitudes up to 3 km, the typical measurement altitude is rather ~ 1500 km. This results in a typical swath width of ~ 605 m and an instantaneous ground scene size of $\sim 22 \times 6$ m (across x along the flight track). Finally, a MicroStrain 3DM-GX3-35 inertial measurement unit (IMU) is mounted onto the base plate with a fixed geometric relationship to the front optics for later orthorectification of the data.

Spectrometer optical bench

The spectrometer optical bench, a push broom dispersive planar grating imaging spectrometer observing the wavelength range from 1559 nm to 1690 nm with a spectral resolution of

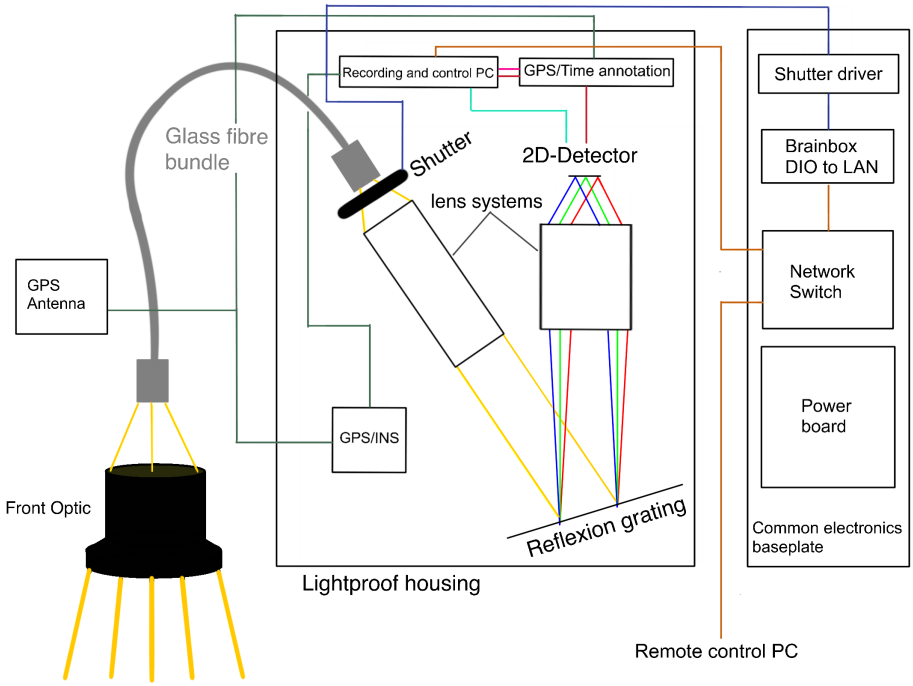

Figure 5.2.: Schematics of the MAMAP2D-Light instrument. The light enters the instrument through the front optics and is routed to the spectrometer with a glass fiber bundle. There, it is dispersed at the grating and finally focused onto the 2D focal plane array of the detector. Additionally, the data paths are depicted as colored lines: dark green lines are the GPS and INS, and dark red lines are camera link data signals. Blue lines denote the shutter control connections, turquoise lines are the detector controls, pink the Ionetrics Annotator controls and orange lines show ethernet connections. The power board provides power to all devices and secures each power line. For the sake of clarity, the power connections are not displayed.

~ 1.1 nm, comprises a custom entrance slit design, two commercial off-the-shelf (CotS) long focal length infrared optics as collimator and camera optic, a planar reflective grating, and an AIM SWIR384 384×288 pixel infrared detector. All optical elements are attached to the base plate via adjustable 6(5)-axis mounts (see schematics in Fig. 5.2 and Fig. 5.3). A light-tight housing covers the optical bench. The different parts are described in more detail below, following the spectrometer's light path. The wavelength range is similar to the wavelength range of the MAMAP instrument covering absorption bands of CO_2 and CH_4, albeit extended at the lower wavelengths to cover also the second set of CO_2 absorption bands located between ~ 1570 and ~ 1580 nm. For smaller scale point source emissions, the experience with the MAMAP instrument shows that quantification is possible using only the SWIR channel (see, e.g. Krings et al., 2011; Gerilowski et al., 2011; Krautwurst et al., 2017; Krings et al., 2018; Krautwurst et al., 2021).

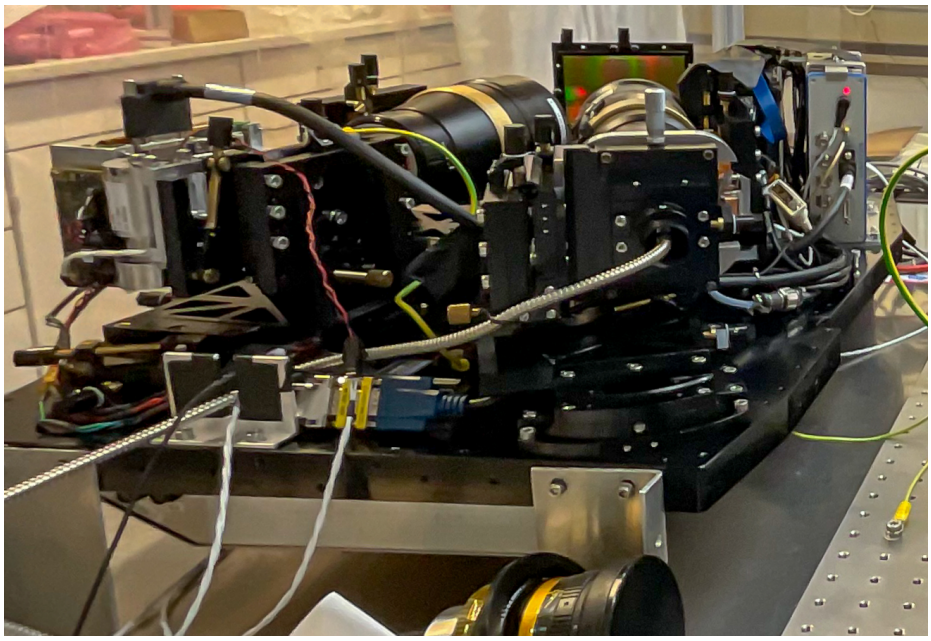

Figure 5.3.: View onto the upper part of the MAMAP2D-Light instrument with the protective light tight cover removed. The spectrometer optical bench comprising the detector, the grating, two optics, the entrance slit design, the control and recording computer unit, an Ionetrics GPS annotator, and the GPS/INS measurement unit are mounted on this side of the common base plate.

Entrance slit unit The entrance slit of the spectrometer hosts the other end of the fiber bundle originating from the front optics unit, an entrance slit, an order-sorting filter and a shutter unit.

The entrance slit can be used to narrow the slit along the spectral axis, which in theory could enhance the spectral resolution. However, this would lead to a mismatch in the spectral and spatial focal plane of the entrance slit unit, which (when focussing on the spectral focal point) would lead to a defocus in the spatial axis. Additionally, this would lead to less light entering the instrument, therefore needing higher integration times for the same signal-to-noise ratio, reducing the along-track spatial resolution. Additionally, the single fibers were not aligned perfectly linear in the fiber bundle, so narrowing the entrance slit would affect different fibers differently. Therefore, the slit was left entirely open for the first measurement campaigns.

The order sorting filter is a high-pass filter with a cut-on wavelength of 1500 nm filtering out shorter wavelengths. It suppresses spectral stray light from higher diffraction orders.

The shutter unit is a Uniblitz shutter with an according shutter driver. The shutter is used to acquire reference dark spectra in-flight. The in-flight dark spectra have to be monitored as the thermal dark current changes with temperature in the non-stabilized MAMAP2D-

Light instrument. In the unpowered state, the shutter remains open. Thus, power loss at the shutter does not abort measurements.

Spectrometer optics and grating The light entering the spectrometer via the entrance slit design is collimated with a CotS optic with a focal length $F = 300\,\text{mm}$ and $F/N = 3.5$. The collimated light is dispersed by a CotS plane ruled grating with $300\,\text{lines}\,\text{mm}^{-1}$ and a nominal blaze angle of $17.5\,^\circ$, operated in the -1^{st} order. The parallel dispersed light originating from the grating is focused onto the detector by a $F = 200\,\text{mm}$ CotS optic with $F/N = 2.4$. The angle between both optics is $32°$.

Detector unit The detector unit is an AIM SWIR384 mercury cadmium telluride (MCT) detector unit with a focal plane array (FPA) composed of 384×288 pixels with a pixel pitch of $24 \times 24\,\mu\text{m}^2$. The spectral cutoff of the detector (the point where the quantum efficiency (QE) has dropped to 50 % of the maximum QE) has been moved from $\sim 2600\,\text{nm}$ (standard) to $< 1800\,\text{nm}$ to reduce the thermal dark current originating from the non-cooled non-thermostabilized instrument to a minimum. Additionally, to reduce the internal thermal dark current, the FPA is cooled to $\sim 150\,\text{K}$ by a single piston linear cooler. The full well of the detector in high gain mode (standard operation) is $\sim 340\,\text{ke}^-$. Additionally, the detector can be run in low gain mode, where the full-well is expanded to $> 1\,\text{Me}^-$. However, to achieve short integration times and, therefore, smaller ground scene sizes while still utilizing the full range of the Analog-to-Digital Converter (ADC), the main operation mode is the high gain mode. The readout noise in high gain mode is $\sim 14\,\text{BU}^-$ and the mean raw detector signal to noise ratio (SNR) is $\text{SNR}_{det} \approx 460.0$. Finally, the ADC converts the electronic charge of each pixel to a 16-bit number.

Currently, the spectra are dispersed along the long axis, while the spatial information is recorded along the short axis. Due to this orientation, 28 of the 36 fibers are projected onto the detector (see discussion in Sect. 7.1 about possible modifications), leading to 28 separate ground scenes being observed by the instrument across the flight track.

Light tight housing and stray light suppression The spectrometer optical bench is covered in matt black optical foil to reduce internal stray light and to block ambient light from entering the spectrometer. One stray light cover is placed between the entrance slit and the detector units. A second one separates the control and recording computer and Ionetrics GPS annotator from the spectrometer.

Data aquisition

The MAMAP2D-Light data acquisition and system controls are realized on one industrial fan-less PC system (PUMA) inside the light-tight housing. The detector camera data (dark red lines in Fig. 5.2) is transferred via CameraLink to the Ionetrics GPS annotator. The annotator replaces 32 consecutive image pixels with the current frame number, GPS time, and GPS location and forwards the data stream to the PUMA. There, a mini PCIe CameraLink frame grabber receives the data. The frames received by the frame grabber are captured by

Figure 5.4.: Mounting of the MAMAP2D-Light instrument inside the wing pod of the Dimona motor glider. The spectrometer is covered inside a matt black, light tight aluminum foil housing, the electronics are mainly mounted below the base plate.

the XCAP-std software, which also controls the frame grabber. In XCAP, the data stream is monitored in a live view window displaying the captured frames. In addition, the frames are recorded to single .tiff files and annotated with the current date and timestamp of the recording PC in the TIFF tags.

The IMU and GPS data are transferred to the PUMA via RS232 and recorded by the MIP Monitor software (dark green lines in Fig. 5.2). Additionally, roll, pitch, and yaw can be displayed in a line plot for monitoring during the flight.

System control and interface

The detector is controlled over an RS232 connection from the control PC mounted inside the light-tight housing to the detector (Fig. 5.2, turquoise line). The shutter driver switching the shutter is controlled via a Brainbox digital IO (DIO) to Ethernet converter mounted on the common electronics base plate (control lines are blue in Fig. (5.2)). The detector and shutter control software is currently written in LabView. For the detector controls, default detector settings and integration times can be activated via buttons, while also manual commands can be sent to the detector. The shutter controls comprise activation or deactivation of the shutter and closing of the shutter for a defined amount of time. The

Ionetrics GPS annotator is configured via a USB connection (pink line in Fig. 5.2) with the Annncle Software.

As the instrument is mainly mounted inside the underwing pod of a motor glider, direct access to the instrument in flight is impossible. Therefore, the system is designed to be operated from an operator PC (e.g., Laptop) over LAN. The system is powered via a single 28 VDC power input from the aircraft. The power supply board mounted on the bottom of the base plate converts the input power to the voltages needed by all electronic components.

5.1.3.2. Calibration data for MAMAP2D-Light

The main spectral calibration of an instrument can be separated into two parts. First, the dispersion of the spectrum onto the detector, i.e., the wavelength grid of the pixels, is necessary to match modeled and measured intensities in the retrievals. For this calibration, a LASER line is shifted over the whole wavelength range, and spectra are recorded for multiple wavelengths. Second, the instrument spectral response function (ISRF) defines the instrument's resolution. The signal at the detector is a convolution of the high spectral resolution input continuum radiance with the ISRF, and the ISRF is the at-detector signal when the instrument is illuminated with monochromatic light (see, e.g., Schowengerdt, 2006). For the calibration of the ISRF, the LASER is tuned in small steps covering a small wavelength range with high precision.

For the calibration of MAMAP2D-Light, the calibration setup shown in Fig. 5.5 was used. A tunable external cavity diode LASER covering the wavelength range $1590-1780$ nm (Sacher TEC-500-1650-020) was coupled into an integrating sphere via a single mode splitter fiber, while 25 % of the LASER light was redirected to a wavemeter. The wavemeter showed the wavelength in nanometers with three digits. However, due to the last digit changing over the measurements, only the first two digits were protocolled. The LASER produced a narrow LASER line with a line width of typically < 10 fm, well below the resolution of MAMAP2D-Light. The MAMAP2D-Light entrance optic was mounted in front of the exit port of the integrating sphere for homogeneous illumination of the entrance fibers. The LASER wavelength was controlled via a control laptop. After each change of wavelength, the LASER had to stabilize again for about $1-2$ min before taking the measurements. Additionally, the LASER could be turned off and a white light source coupled to a second entrance port of the sphere could be activated for the flat field (or gain) correction of the measurements.

Ideally, for the wavelength calibration, measurements covering the whole spectral range of the detector are recorded on a grid as fine as possible. Unfortunately, the lowest possible wavelength reachable by the LASER was ~ 1592 nm, while the lowest wavelength of the MAMAP2D-Light instrument in the current orientation of the grating is ~ 1560 nm. Therefore, extrapolation of the measurements is needed, which is discussed in Sect. 6.2.1. Additionally, the setup is not automated yet, which requires changing the LASER wavelength manually, waiting for the LASER to stabilize, recording the spectra, and manually protocoling the wavelength displayed at the wavemeter.

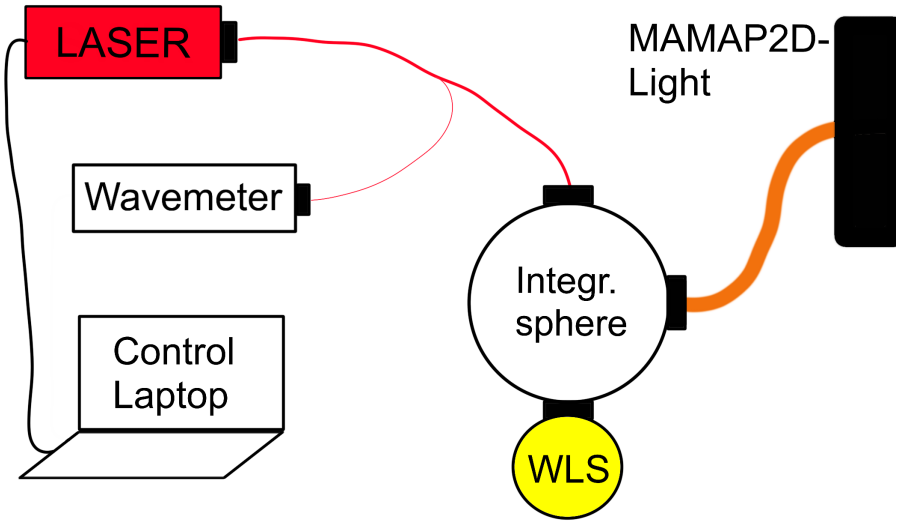

Figure 5.5.: Calibration setup comprising a LASER coupled into the integrating sphere and a wavemeter via a y-fiber, and the entrance fiber of the MAMAP2D-Light instrument mounted at the exit port of the sphere. For white light measurements, a white light source was mounted in front of a second entrance port of the sphere.

As a compromise between coverage and measurement time, measurements were taken at 20 different wavelengths in ~ 5 nm intervals from 1592.70 to 1687.16 nm. At each wavelength, 100 consecutive measurements were recorded. Additionally, 100 spectra with white light illumination for gain correction and 100 dark spectra to remove the dark current from the measurements were acquired as part of the data set. For the initial ISRF calibration, the response of one central spectral data point was averaged over the middle fiber, i.e., six detector pixels in the spatial axis. The ISRF was then sampled at 25 different wavelengths covering the wavelength range from 1626.64 to 1628.24 nm in ~ 0.1 nm steps. The calibration results are explained in Sect. 6.2.1.

5.1.3.3. MAMAP2D-Light observational data of the power plant Jänschwalde

The MAMAP2D-Light observational data comprises measurements obtained during a measurement flight targeting the coal-fired power plant Jänschwalde on 17.06.2021. The data set comprises ~ 3.5 million single spectra, while the data obtained over the power plant plume comprises ~ 1.1 million single spectra in the SWIR spectral range (see Sect. 5.1.3), distributed over 28 viewing directions, and additional GPS and orientation data. The flight took place before noon, with the mean overflight time over the plume between 8:00 and 9:00 UTC (10:00 - 11:00 local).

For the WFM-DOAS method, a background spectrum was calculated with the radiative transfer model SCIATRAN (Rozanov et al., 2017). The SCIATRAN input parameters were acquired as follows. The background dry air mixing ratios of CO_2 and CH_4 were estimated with the Simple cLImatological Model (SLIM, Noël et al., 2022) to 415.5 ppm and 1.870 ppm, respectively, for the day of the overflight. The mean surface elevation was estimated from SRTM data V2.1 (Farr et al., 2007) to $\sim$ 70 m. The mean aircraft altitude was 2.29 km estimated from GPS data logged during the flight. The solar zenith angle at 8:30 UTC for the location of the Jänschwalde power plant was 40.6 °, and the viewing geometry was assumed to be nadir. The latter introduces a viewing-angle-dependent offset, which the proxy should capture. Also, an urban optical property of aerosols and clouds (OPAC, Hess et al., 1998) aerosol scenario accounted for at least some aerosols because the plume went over inhabited areas and originated from a power plant.

The background total column of H_2O, the temperature and pressure profile above ground, the wind speed components, and the planetary boundary layer height were obtained from ERA5 reanalysis data (Copernicus Climate Change Service (C3S) (2017), 2017) by averaging all ERA5 data between 14.1 and 14.6 ° East and 51.72 and 51.94 ° North over the whole overflight period. The mean wind speed was $4.8 \pm 0.8\,\mathrm{m\ s^{-1}}$, and the wind uncertainty was estimated as the $1\,\sigma$ standard deviation of all wind data in the boundary layer. The wind direction was derived from the apparent plume direction relative to the cross tracks.

5.2. Retrieval of column enhancements

This section describes the methods used in this thesis for analyzing the acquired spectra and deriving emission fluxes from the retrieved concentrations. First, the WFM-DOAS method is explained in Sect. 5.2.1, where the column enhancements are retrieved as deviations from an average state of the atmosphere with a linear fit. The WFM-DOAS method was used to examine the first two research questions. Next, the FOCAL AIR retrieval adapted to airborne geometry in this thesis is introduced in Sect. 5.2.2. It is an optimal estimation-based inversion scheme, including fitting a scattering approximation to enable emission estimations over larger areas. Finally, the approach taken to remove striping artifacts in the retrieved column enhancements of imaging data is described in Sect. 5.2.3.

5.2.1. The WFM-DOAS algorithm

To retrieve the CO_2 and CH_4 column anomalies from the acquired spectra I_{mea}, the weighting function modified differential optical absorption spectroscopy (WFM-DOAS) method modified for airborne measurements (Buchwitz et al., 2000; Krings et al., 2011) was applied to AVIRIS-NG and MAMAP2D-Light data in the first part of this thesis. The WFM-DOAS method had been applied successfully to airborne MAMAP measurements before (see e.g. Gerilowski et al., 2011; Krings et al., 2013; Gerilowski et al., 2015; Krautwurst et al., 2017, 2021). For the application to AVIRIS-NG data, optimizations in memory usage had to be made as AVIRIS-NG radiance cubes can easily reach data sizes $> 10\,\mathrm{GB}$. These data cubes slowed down typical desktop systems used for the calculations significantly.

The WFM-DOAS equation is a Taylor expansion of the logarithm of the radiative transfer around a mean state of the atmosphere $\overline{k}$. Deviations from this state causing changes in the radiance I_{mod} are calculated by scaling weighting functions

$$W_i(\lambda, \overline{k_i}) = \frac{\mathrm{d} \ln I_{mod}}{\mathrm{d}k_i}|_{\overline{k_i}} \tag{5.86}$$

for the fit parameters k_i. Those comprise the different absorbers as well as the temperature. The weighting functions are calculated numerically for a small change. Additionally, scattering and continuum effects assumed only slowly to vary depending on wavelength are separated from the higher frequency changes by, e.g., absorption due to gases and approximated by a typically low order polynomial $P_n(\lambda) = \left(\frac{\lambda}{\lambda_{max}-\lambda_{min}} - 0.5\right)^n \cdot k_{poly,n}$. Then, the at-instrument radiance $\ln I_{mea}(\lambda)$ is modeled as

$$\ln I_{mea}(\lambda) \approx \ln I_{mod}(\lambda, \overline{k}) + \sum_i W_i(\lambda, \overline{k}) \frac{k_i - \overline{k_i}}{\overline{k_i}} + P_n(\lambda) + \varepsilon(\lambda). \tag{5.87}$$

Here, $\ln I_{mod}(\lambda, \overline{k})$ is the modeled at-instrument radiance for the mean state of the atmosphere during the overflight and the columns of the matrix $W(\lambda, \overline{k})$ are the weighting functions $W_i(\lambda, \overline{k_i})$. Finally, the $\varepsilon(\lambda)$ are the wavelength-dependent residuals of the fit.

This formulation assumes that the modeled intensity $\ln I_{mod}(\lambda, \overline{k})$ is close enough to the measured intensity $\ln I_{mea}(\lambda)$ for the difference between both being nearly linearly dependent on the fit parameters $\overline{k_i}$. Therefore, $\ln I_{mod}(\lambda, \overline{k})$ contains our best knowledge of the atmosphere at the time of measurement and is modeled via the radiative transfer model (RTM) SCIATRAN (Rozanov et al., 2017) using the HITRAN2016 spectroscopic database (Gordon et al., 2017). Due to the long runtime of the SCIATRAN RTM, only one modeled spectrum based on the average state of the atmosphere during the measurements is calculated for each observation scene. For AVIRIS-NG, a scene is equal to one flight line (due to different dates of the overflights), while for MAMAP2D-Light, the scene is the complete overflight of the power plant plume of Jänschwalde.

Combining the weighting function matrix $W(\lambda, \overline{k})$ and the basis of the polynomial to the matrix $\mathbf{A}$, Eq. (5.87) becomes a linear equation of form

$$\vec{y} - \mathbf{A} \cdot \vec{k} = \varepsilon, \tag{5.88}$$

for which the least squares solution for the scaling factor vector $\vec{k}$ is given as

$$\hat{\vec{k}} = (\mathbf{A}^T \mathbf{A})^{-1} \mathbf{A}^T \vec{y}. \tag{5.89}$$

Eq. 5.89 is a product of known precalculated matrices with the logarithm of the measured intensities. The fit results are profile scaling factors (PSF) of the atmospheric profiles of the different gases, polynomial factors, and a constant shift of the temperature profile. For both AVIRIS-NG and MAMAP2D-Light measurements, the profile scaling factors of CO_2 and CH_4 are retrieved separately by selecting one ideal fit window for each of the gases (see also Sect. 6.1 and Sect. 6.2).

Atmospheric parameters such as the measurement geometry, solar zenith angle, and surface altitude were not adapted to each measured spectrum and, additionally, the aerosol profile was represented only averaged and not well adapted to the scene. Therefore, residual light path differences between the light path assumed in the SCIATRAN RTM and the light path present in the measurements may exist, influencing the retrieved PSF of each gas. To correct for this effect, one can normalize the retrieved PSF by the PSF of another well-mixed gas, which ideally has absorption features close by (see also Frankenberg et al., 2005; Schneising et al., 2009; Krings et al., 2011). In the so-called proxy method applied here, it is either assumed that CH_4 or CO_2 is constant when observing a CO_2 or CH_4 point source, respectively:

$$\mathrm{CH}_{4,proxy,i} = \frac{\mathrm{PSF}_{\mathrm{CH}_4}}{\mathrm{PSF}_{\mathrm{CO}_2}} \tag{5.90}$$

$$\mathrm{CO}_{2,proxy,i} = \frac{\mathrm{PSF}_{\mathrm{CO}_2}}{\mathrm{PSF}_{\mathrm{CH}_4}} \tag{5.91}$$

On small scales, i.e., observing near-surface emission plumes, a reasonable assumption is that the retrieved enhancement above the background is confined to the planetary boundary layer located below the aircraft. As the light passes airmasses twice below the aircraft but only

once above, the measurements are more sensitive to changes below the aircraft than above, leading to an overestimation of the total column increase when scaling the total column. The ratio of retrieved enhancement to true enhancement is described by the height-dependent averaging kernels $A_{AK}(z)$. Assuming the plume is confined to the boundary layer, the retrieved column enhancements above the background must be scaled by the inverse of the averaging kernel below the aircraft $k_{AK,below}$. The enhancements above background are obtained by normalizing the retrieved proxy corrected $\mathrm{CH}_{4,proxy,i}$ or $\mathrm{CO}_{2,proxy,i}$ values by the local background $\mathrm{CH}_{4,proxy,bg}$ or $\mathrm{CO}_{2,proxy,bg}$ respectively and multiplying by the background total column of the gases ($\mathrm{CH}_{4,\mathrm{back}}$ or $\mathrm{CO}_{2,\mathrm{back}}$). This gives the column enhancements $\mathrm{CH}_{4,enh,i}$ and $\mathrm{CO}_{2,enh,i}$ for the i-th measurement:

$$\mathrm{CH}_{4,enh,i} = \left(\frac{\mathrm{CH}_{4,proxy,i}}{\mathrm{CH}_{4,proxy,bg}} - 1 \right) \cdot \mathrm{CH}_{4,\mathrm{back}} \cdot k_{AKCH_4,below} \tag{5.92}$$

$$\mathrm{CO}_{2,enh,i} = \left(\frac{\mathrm{CO}_{2,proxy,i}}{\mathrm{CO}_{2,proxy,bg}} - 1 \right) \cdot \mathrm{CO}_{2,\mathrm{back}} \cdot k_{AKCO_2,below} \tag{5.93}$$

The fit quality was evaluated using the root mean square error (RMS) between the fitted radiance I_{res} (the right hand side of Eq. (5.87)) and the measured radiance I_{mea}:

$$\Delta I(\lambda) = \frac{I_{mea}(\lambda) - I_{res}(\lambda)}{I_{res}(\lambda)} \tag{5.94}$$

$$RMS = \sqrt{\overline{\Delta I^2(\lambda)}}, \tag{5.95}$$

with $\overline{\Delta I^2(\lambda)}$ the mean of the squared normalized difference between measurement and fit result in each pixel.

The WFM-DOAS retrieval method, as described above, needs only precalculated radiative transfer calculations adapted to the mean state of the atmosphere and geometric properties during the flight. The retrieval of deviations from this state is calculated by a simple linear least squares fit, which is computationally not very expensive. However, only small deviations from this linearisation point are captured entirely by the retrieval, and larger deviations impose biases. The proxy method correcting for light path changes mitigates some of these problems. However, it requires the gas used for normalization to be constant. The implications to the data sets studied are discussed in Sect. 6 and 7.2.

5.2.2. The FOCAL AIR retrieval method

The Fast atmOspheric traCe gAs retrievaL - AIRborne (FOCAL AIR) method has been developed in the frame of this thesis. It is an extension of the FOCAL retrieval algorithm (Reuter et al., 2017b,a; Noël et al., 2021; Noël et al., 2022), which has been adapted to account for an airborne remote sensing sensor located within (instead of above) the atmospheric column. The FOCAL AIR retrieval aims to mitigate the problem of needing another

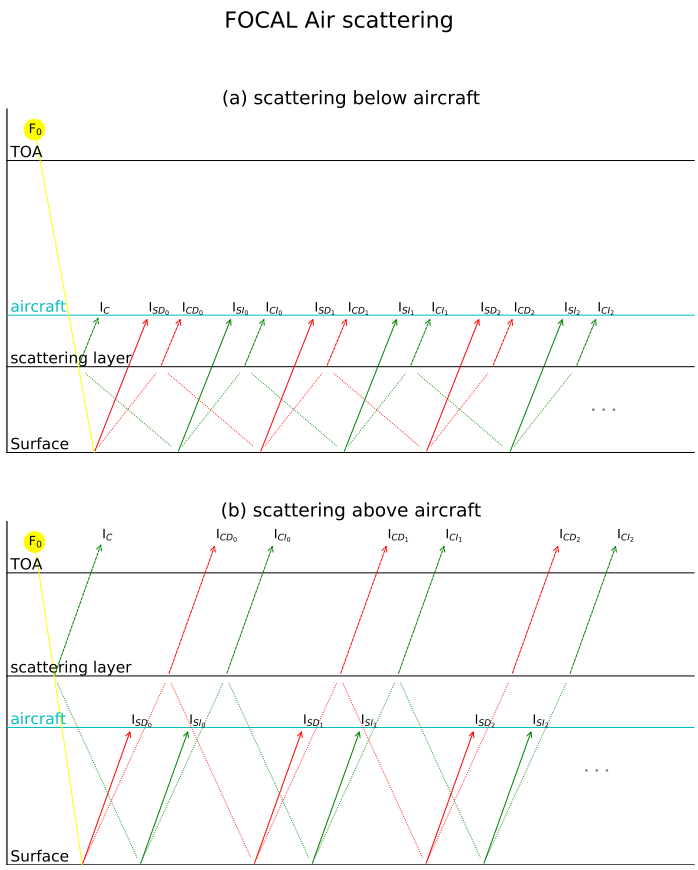

Figure 5.6.: FOCAL-AIR scattering light path (a) if the scattering layer is below the aircraft and (b) if the scattering layer is above the aircraft. Solid lines denote radiances, while dotted lines denote radiant fluxes originating from diffuse scattering or reflection at Lambertian surfaces.

retrieved gas as a proxy to correct for light path changes. It, therefore, implements an optimal estimation-based inversion scheme using a forward model adapted to the geometry of each measurement point individually and includes a parametrized description of scattering in the atmosphere, which still can be solved analytically but should reduce errors due to aerosol optical depths in the retrieval.

The forward model adaption was developed during the work on this thesis. In the following, the idea behind FOCAL AIR, the used forward model, and the inversion process are described in detail. The FOCAL AIR algorithm comprises a simplified forward model of the radiative transfer through the atmosphere, combined with a Levenberg-Marquardt-Fletcher inversion scheme (Fletcher, 1971) to match the calculated and the measured intensities.

The simplified forward model is shown in Fig. 5.6. It is based on the following assumptions:

1. There are no scattering processes in the atmosphere apart from an optically thin scattering layer of variable altitude above ground.
2. The scattering layer acts as a Lambertian surface and is characterized by its altitude above ground, the optical thickness at the reference wavelength of 760 nm, and the Ångström-coefficient describing the wavelength dependency of the optical thickness.
3. The scattering layer can be located above or below the aircraft changing the forward model accordingly.
4. The Earth's surface is a Lambertian surface.
5. The atmosphere is plane-parallel.[1]

In the sections 5.2.2.1 to 5.2.2.3, the terms used are introduced, the approximations made are described, and the multiple scattering between the scattering layer and the surface is parametrized. The analytical forward model is described in the sections 5.2.2.4 to 5.2.2.7 by defining the different contributions to at-sensor radiance dependent on the geometry and introducing the pseudo-spherical approximation. The FOCAL AIR retrieval chain is described in section 5.2.2.8. It comprises a preprocessing step, the retrieval step containing the Levenberg-Marquardt-Fletcher inversion scheme with a description of the state vector and Jacobians, and the post-processing. The two spectral fit window definitions examined in the thesis are additionally introduced in this section.

5.2.2.1. Definition of terms

This section introduces the terminology and the basic parts of the radiative transfer at each step through the atmosphere in the FOCAL AIR forward model.

For simplified notification, the following symbols as in Reuter et al. (2017b) are used: F and I denote a diffuse flux (in the following simply "flux") and a direct radiance (in the following "radiance"), respectively. T is transmittance, and τ is a vertical optical thickness. A super- or subscript g denotes gaseous absorption, and a superscript s denotes a process at the scattering layer. Subscripts e, a, and s denote extinction, absorption, and scattering at the scattering layer, respectively. Finally, a subscript bl or ab denotes radiance terms defined for a scattering layer below or above the aircraft.

In this notation, the transmission of radiance $T_I^g(\tau_g, \mu)$ along a slant light path with solar zenith angle θ, and, therefore, a light path extension of $\mu = \frac{1}{\cos\theta}$, in a parallel plane atmosphere with gaseous absorption by one gas is calculated according to Beer-Lambert's law (see Sect. 3.2):

[1] The generalization to a pseudo spherical atmosphere is explained in Sect. 5.2.2.7 but does not change the general formulation.

$$T_I^g(\tau_g, \mu) = \exp\left(-\mu \int c_g(z) \cdot d(z) \cdot \sigma_g(z) \mathrm{d}z\right) \tag{5.96}$$

$$= \exp\left(-\mu \tau_g\right). \tag{5.97}$$

Here, z is the height above the surface, $c_g(z)$ is the height-dependent mixing ratio of the absorbing gas, $d(z)$ is the height-dependent density of dry air, and $\sigma_g(z)$ is the height-dependent absorption coefficient for the gas. The integral describes the optical thickness due to gaseous absorption τ_g.

The transmittance $T_I^s(\tau_e, \mu)$ of the scattering layer due to absorption and scattering at the scattering layer is

$$T_I^s(\tau_e, \mu) = \exp\left(-\mu \tau_e\right). \tag{5.98}$$

$\tau_e = \tau_a + \tau_s$ is the extinction optical thickness, which is the combination of the absorption (τ_a) and scattering (τ_s) optical thickness of the scattering layer. As light is either transmitted, absorbed, or scattered, one can also write

$$1 = T_I^s(\tau_e, \mu) + S_I(\tau_s, \tau_e, \mu) + A_I(\tau_a, \tau_e, \mu), \tag{5.99}$$

with

$$S_I(\tau_s, \tau_e, \mu) = \frac{\tau_s}{\tau_e}\left[1 - T_I^s(\tau_e, \mu)\right] \tag{5.100}$$

$$A_I(\tau_a, \tau_e, \mu) = \frac{\tau_a}{\tau_e}\left[1 - T_I^s(\tau_e, \mu)\right] \tag{5.101}$$

where $S_I(\tau_s, \tau_e, \mu)$ and $A_I(\tau_a, \tau_e, \mu)$ are the fraction of scattered and absorbed light, respectively. For the scattered light, also the direction of scattering is essential. Therefore, b is the fraction of light scattered backward, i.e., into the hemisphere from which the light originates, and a is the fraction of light scattered forwards, with $a + b = 1$.

Additionally, the hemispheric radiant fluxes contribute to the total at-sensor radiance between the scattering layer and the surface. The transmission through the atmosphere of the flux originating from a Lambertian surface in the whole hemisphere is the integral over the whole hemisphere of the radiance transmission modified by the angle of the incident light θ (see e.g. Roedel and Wagner, 2017; W. Paltridge and R. Platt, 1976):

$$T_F^g(\tau_g) = \frac{1}{\pi} \int_0^{2\pi} \int_0^{\frac{\pi}{2}} T_I^g(\tau_g, \mu) \cdot \cos\theta \cdot \sin\theta \, \mathrm{d}\theta \, \mathrm{d}\phi \tag{5.102}$$

$$= 2 \int_0^{\frac{\pi}{2}} T_I^g(\tau_g, \mu) \cdot \cos\theta \cdot \sin\theta \, \mathrm{d}\theta \tag{5.103}$$

With the substitution $\mu = \frac{1}{\cos\theta}$ and $\mathrm{d}\mu = \frac{\sin\theta}{\cos^2\theta}$, and using the exponential integral notation $\mathrm{E}_n = \int_1^\infty \mathrm{e}^{-x} \cdot x^{-n}\mathrm{d}x$ the integral becomes

$$T_F^g(\tau_g) = 2\int_1^\infty \frac{\exp\left(-\mu\tau_g\right)}{\mu^3}\mathrm{d}\mu \tag{5.104}$$

$$= 2\mathrm{E}_3(\tau_g) \tag{5.105}$$

The transmission of flux below the scattering layer, including extinction at the scattering layer, in the presence of gaseous absorption $\tau_{g\downarrow}$ below the scattering layer is

$$T_F^{gs}(\tau_{g\downarrow} + \tau_e) = 2\int_1^\infty \frac{\exp\left(-\mu(\tau_{g\downarrow} + \tau_e)\right)}{\mu^3}\mathrm{d}\mu \tag{5.106}$$

$$= 2\mathrm{E}_3(\tau_{g\downarrow} + \tau_e). \tag{5.107}$$

With the relative transmission of flux at the scattering layer $\frac{T_F^{gs}(\tau_{g\downarrow}+\tau_e)}{T_F^g(\tau_{g\downarrow})}$, the relative additional extinction at the scattering layer E_F can be written as

$$E_F(\tau_e, \tau_{g\downarrow}) = 1 - \frac{T_F^{gs}(\tau_{g\downarrow} + \tau_e)}{T_F^g(\tau_{g\downarrow})} \tag{5.108}$$

$$= 1 - \frac{\mathrm{E}_3(\tau_{g\downarrow} + \tau_e)}{\mathrm{E}_3(\tau_{g\downarrow})} \tag{5.109}$$

which can be split into a scattering and absorbing part analogously to Eq. (5.100) and (5.101):

$$S_F(\tau_s, \tau_e, \tau_{g\downarrow}) = \frac{\tau_s}{\tau_e}\mathrm{E}_F(\tau_e, \tau_{g\downarrow}) \tag{5.110}$$

$$A_F(\tau_a, \tau_e, \tau_{g\downarrow}) = \frac{\tau_a}{\tau_e}\mathrm{E}_F(\tau_e, \tau_{g\downarrow}) \tag{5.111}$$

5.2.2.2. Approximations

Similar to Reuter et al. (2017b), further approximations are made to reduce the computational cost of the forward model and the computation of the analytical partial derivatives. Distinguishing between the signal originating from scattering and absorption at the scattering layer in the OCO-2 retrieval was already difficult. For significantly lower spectral resolution MAMAP data distinguishing these two signals would be even more challenging. Additionally, the retrieval is not designed to retrieve scattering properties accurately but to enhance greenhouse gas retrieval results by approximating the signal produced by these

processes. Therefore, the absorption within the scattering layer is neglected ($\tau_a = 0$) and, therefore, $\tau_e = \tau_s$.

Furthermore, the scattering layer is assumed to be optically thin, as the MAMAP instrument flies only under clear sky conditions. Therefore, a Taylor approximation around $\tau_e = \tau_s = 0$ can be applied. With this, the Eqs. 5.100, 5.99 and 5.110 become

$$S_I(\tau_s, \tau_e, \mu) \approx \mu \cdot \tau_s = S_I(\tau_s, \mu) \tag{5.112}$$

$$T_I^s(\tau_e, \mu) \approx 1 - S_I(\tau_s, \mu) = \exp(-\mu\tau_s) = T_I^s(\tau_s, \mu) \tag{5.113}$$

$$S_F(\tau_s, \tau_e, \tau_{g\downarrow}) \approx 1 - \frac{E_3(\tau_{g\downarrow} + \tau_s)}{E_3(\tau_{g\downarrow})} \overset{\text{Taylor}}{\approx} = \frac{E_2(\tau_{g\downarrow})}{E_3(\tau_{g\downarrow})} \cdot \tau_s = S_F(\tau_s, \tau_{g\downarrow}) \tag{5.114}$$

5.2.2.3. Multiple scattering between surface and scattering layer

In Fig. 5.6, the dashed lines oscillating between the surface and the scattering layer denote the multiple scattering of the flux between these two layers. In this section, an analytical solution for this path is described.

Assuming a Lambertian surface with albedo α, the transmission of the upward flux originating from the surface can be computed in the following way: The flux passes the atmosphere below the scattering layer with transmittance $T_F^g(\tau_{g\downarrow})$. It then reaches the scattering layer, where the flux is transmitted, absorbed, or scattered forwards or backward. Regarding the backward scattered flux, its fraction is $S_F(\tau_s, \tau_e, \tau_{g\downarrow}) \cdot b$, and the flux downward transmits the atmosphere again, illuminating the surface with albedo α again, which closes the cycle. Mathematically, this can be written as

$$T_{F,multi} = \sum_{i=0}^{\infty} \left(T_F^g(\tau_{g\downarrow}) \cdot S_F(\tau_s, \tau_e, \tau_{g\downarrow}) \cdot b \cdot \alpha \cdot T_F^g(\tau_{g\downarrow}) \right)^i . \tag{5.115}$$

Eq. (5.115) has the form of a geometric series ($\sum_{i=0}^{\infty} k^i = \frac{1}{1-k}$), as the product of all terms is between 0 and 1. Applying the geometric series formula and the approximations introduced in Sect. 5.2.2.2, including a first-order Taylor expansion around $\tau_s = 0$, gives

$$\begin{aligned} T_{F,multi} &= \frac{1}{1 - \alpha \cdot b \cdot S_F(\tau_s, \tau_e, \tau_{g\downarrow}) \cdot [T_F^g(\tau_{g\downarrow})]^2} \\ &\approx 1 + 4 \cdot \alpha \cdot b \cdot E_2(\tau_{g\downarrow}) \cdot E_3(\tau_{g\downarrow}) \cdot \tau_s \end{aligned} \tag{5.116}$$

5.2.2.4. The radiative transfer model for a scattering layer below the aircraft

The at-sensor radiance I for a scattering layer below the aircraft (Fig. 5.6 (a)) can be written as the sum of different radiances, each describing different paths of the solar light through the atmosphere:

$$I_{\text{below}} = I_{\text{C,bl}} + I_{\text{SD,bl}} + I_{\text{CD,bl}} + I_{\text{SI,bl}} + I_{\text{CI,bl}}. \tag{5.117}$$

The first letter in the subscript to I denotes the origin of the radiance reaching the instrument. C stands for the scattering layer and S for the surface. The second letter (when present) describes if the incoming solar radiation transmitted the scattering layer (denoted by D) or was diffusely scattered there (I). Consequently, the term I_C is the radiance directly scattered back to the instrument at the scattering layer before reaching the ground.

The term $I_{0,bl}$ describes all absorption processes taking place above the scattering layer and includes the incoming solar radiation.

$$I_{0,bl} = \frac{F_0}{\pi} \cdot \frac{1}{\mu_0} \cdot T_I^g(\tau_{g,\uparrow}, \mu_0) \cdot T_I^g(\tau_{g,\uparrow,a}, \mu) \tag{5.118}$$

Here, $\tau_{g,\uparrow}$ and $\tau_{g,\uparrow,a}$ are the optical thickness between the scattering layer and the top of the atmosphere and between the scattering layer and the aircraft, respectively, while $\mu_0 = \frac{1}{\cos\theta_0}$ and $\mu = \frac{1}{\cos\theta}$ are the light path extensions due to the solar zenith angle θ_0 and instrument zenith angle θ, respectively.

The term $I_{C,bl}$ is the part of incoming solar light directly scattered backward at the scattering layer before reaching the surface. With Eq. (5.118) and (5.100), $I_{C,bl}$ becomes

$$I_{C,bl} = I_{0,bl} \cdot S_I(\tau_s, \tau_e, \mu_0) \cdot b, \tag{5.119}$$

and applying the approximation in Eq. (5.112):

$$I_{C,bl} \approx I_{0,bl} \cdot \mu_0 \cdot b \cdot \tau_s \tag{5.120}$$

The next two terms in Eq. (5.117), $I_{SD,bl}$ and $I_{CD,bl}$, consider the light paths that originate from the solar radiation transmitting the scattering layer (with transmittance $T_I^s(\tau_e, \mu_0)$) and the atmosphere below the scattering layer (with transmittance $T_I^g(\tau_{g\downarrow}, \mu_0)$ to illuminate the surface with albedo α. The resulting upward flux reaches the scattering layer, where the light is transmitted, absorbed, or scattered forward or backward. For the backward scattered part, Eq. (5.116) models the light path.

For $I_{SD,bl}$ only the radiance parts are regarded, which are directly transmitted from the surface through the atmosphere $T_I^g(\tau_{g\downarrow}, \mu)$ and the scattering layer ($T_I^s(\tau_e, \mu)$) after each hitting the ground. This contribution can then be written as

$$I_{SD,bl} = I_{0,bl} \cdot \alpha \cdot T_I^s(\tau_e, \mu_0) \cdot T_I^g(\tau_{g\downarrow}, \mu_0) \cdot T_I^g(\tau_{g\downarrow}, \mu) \cdot T_I^s(\tau_e, \mu) \cdot T_{F,multi}. \tag{5.121}$$

Applying the approximations in Sect. 5.2.2.2, $I_{SD,bl}$ becomes

$$I_{SD,bl} \approx I_{0,bl} \cdot \alpha \cdot T_I^g(\tau_{g\downarrow}, \mu_0) \cdot T_I^g(\tau_{g\downarrow}, \mu) \cdot (1 - (\mu_0 + \mu) \cdot \tau_s + 4\,\alpha\, b\, E_2(\tau_{g\downarrow}) E_3(\tau_{g\downarrow}) \tau_s) \tag{5.122}$$

For $I_{CD,bl}$, only the radiance parts are regarded, which result from forwards scattering at the scattering layer into the upper part of the atmosphere $S_F(\tau_s, \tau_e, \tau_{g\downarrow}) \cdot a$ at each reaching the scattering layer. Additionally, the first transmission of flux through the atmosphere $T_F^g(\tau_{g\downarrow})$ before reaching the scattering layer on the first way up must be considered. Including the approximations as before $I_{CD,bl}$ becomes:

$$\begin{aligned} I_{CD,bl} &= I_{0,bl}\, \alpha\, T_I^s(\tau_e, \mu_0) T_I^g(\tau_{g\downarrow}, \mu_0) T_F^g(\tau_{g\downarrow}) S_F(\tau_s, \tau_e, \tau_{g\downarrow})\, a \cdot T_{F,multi} \\ &\approx I_{0,bl} \cdot \alpha \cdot 4a \cdot T_I^g(\tau_{g\downarrow}, \mu_0) \cdot E_2(\tau_{g\downarrow}) \cdot \tau_s. \end{aligned} \tag{5.123}$$

The last two terms in Eq. (5.117), $I_{SI,bl}$ and $I_{CI,bl}$, now consider the fraction of the incoming solar radiation that is diffusely scattered forward at the scattering layer ($S_I(\tau_s, \tau_e, \mu_0) \cdot a$), creating a downward flux which is transmitted through the atmosphere below the scattering layer ($T_F^g(\tau_{g\downarrow})$) and illuminates the surface with albedo α. This produces a diffuse flux upwards through the atmosphere to the scattering layer, for which the backscattered part illuminates the surface again, and so on. This process is described by the flux in Eq. (5.116).

For I_{SI}, similar to I_{SD}, the radiance directly transmitted from the surface through the atmosphere ($T_I^g(\tau_{g\downarrow}, \mu)$) and the scattering layer ($T_I^s(\tau_e, \mu)$) to the aircraft after each reflection at the ground contributes. Applying the approximations in Sect. 5.2.2.2, $I_{SI,bl}$ becomes

$$\begin{aligned} I_{SI,bl} &= I_{0,bl} \cdot S_I(\tau_s, \tau_e, \mu_0) \cdot a \cdot T_F^g(\tau_{g\downarrow}) \cdot \alpha \cdot T_I^g(\tau_{g\downarrow}, \mu) \cdot T_F^s(\tau_{g\downarrow}) \cdot T_{F,multi} \\ &\approx I_{0,bl} \cdot \alpha \cdot T_I^g(\tau_{g\downarrow}) \cdot 2a \cdot E_3(\tau_{g\downarrow}) \cdot \mu_0 \cdot \tau_s. \end{aligned} \tag{5.124}$$

The last term $I_{CI,bl}$, similarly to $I_{CD,bl}$, includes the radiance contributions which result from forward scattering at the scattering layer into the upper part of the atmosphere ($S_F(\tau_s, \tau_e, \tau_{g\downarrow}) \cdot a$) every time the scattering layer is reached. Before the first reaching of the scattering layer, the transmission of the flux below the scattering layer $T_F^g(\tau_{g\downarrow})$ has to be taken into account. With the approximations in Sect. 5.2.2.2 this leads to

$$\begin{aligned} I_{CI,bl} &= I_{0,bl} \cdot S_I(\tau_s, \tau_e, \mu_0) \cdot a^2 \cdot T_F^g(\tau_{g\downarrow}) \cdot \alpha \cdot T_F^g(\tau_{g\downarrow}) \cdot S_F(\tau_s, \tau_e, \tau_{g\downarrow}) \cdot T_{F,multi} \\ &= 0. \end{aligned} \tag{5.125}$$

Combining Eqs. (5.120), (5.122), (5.123), (5.124) and (5.125) and replacing $b = 1 - a$ gives the radiative transfer of the forward model for a scattering layer below the aircraft I_{below}:

$$
\begin{aligned}
I_{\text{below}} = & \frac{F_0}{\pi \mu_0} T_I^g(\tau_{g\uparrow}, \mu_0)\, T_I^g(\tau_{g\uparrow,a}, \mu) \cdot \Big[\mu_0\, \tau_s\, (1-a) \\
& + \alpha\, T_I^g(\tau_{g\downarrow}, \mu_0)\, T_I^g(\tau_{g\downarrow}, \mu) \left(1 - (\mu_0 + \mu)\, \tau_s + 4\, \alpha\, (1-a)\, E_2(\tau_{g\downarrow})\, E_3(\tau_{g\downarrow})\, \tau_s\right) \\
& + 2\, \alpha\, T_I^g(\tau_{g\downarrow}, \mu_0)\, E_2(\tau_{g\downarrow})\, \tau_s\, a \\
& + 2\, \alpha\, T_I^g(\tau_{g\downarrow}, \mu)\, E_3(\tau_{g\downarrow})\, \tau_s\, a \Big]
\end{aligned} \tag{5.126}
$$

Comparing Eq. (5.126) with Eq. 25 in Reuter et al. (2017b), there are three differences. First, the fraction between forward and backward scattering at the scattering layer is still a free parameter, while it was set to 0.5 in Reuter et al. (2017b). Second, the transmission above the scattering layer is only calculated up to the aircraft in Eq. (5.126). Third, for MAMAP, no solar-induced fluorescence is retrieved because the SIF weighting function is nearly linear in the SIF retrieval window for the MAMAP spectral resolution.

5.2.2.5. The radiative transfer model for a scattering layer above the aircraft

Unlike for satellites, i.e., an observation system located above the top of the atmosphere, the radiance parts contributing to the at-sensor radiance I change depending on the altitude of the thin scattering layer for an airborne sensor. In case the sensor is below the scattering layer (Fig. 5.6 (b)), the terms I_{SI} and I_{CI} do not contribute to the at-sensor radiance.

When the scattering layer is above the aircraft, the contributions of I_C, I_{CD} and I_{CI} become zero even in the not approximated form, as light leaving the scattering layer into the upper atmosphere has no way back down. Therefore, I_{above} becomes

$$
I_{\text{above}} = I_{SD,ab} + I_{SI,ab}. \tag{5.127}
$$

Furthermore, the terms above the scattering layer simplify, and $I_{0,ab}$ becomes

$$
I_{0,ab} = \frac{F_0}{\pi \mu_0}\, T_I^g(\tau_{g\uparrow}, \mu_0). \tag{5.128}
$$

Finally, as the radiance reaching the aircraft does not pass the full atmosphere below the aircraft (denoted by $T_I^g(\tau_{g\downarrow,a})$) and does not transmit the scattering layer, the remaining terms $I_{SD,ab}$ and $I_{SI,ab}$ get simplified, too:

$$
I_{SD,ab} = I_{0,ab}\, \alpha\, T_I^g(\tau_{g\downarrow}, \mu_0)\, T_I^g(\tau_{g\downarrow,a}, \mu) \cdot \left(1 - \mu_0\, \tau_s + 4\, b\, \alpha\, E_2(\tau_{g\downarrow})\, E_3(\tau_{g\downarrow})\, \tau_s\right) \tag{5.129}
$$

$$
I_{SI,ab} = I_{0,ab}\, \alpha\, T_I^g(\tau_{g\downarrow,a}, \mu)\, 2\, a\, \mu_0\, E_3(\tau_{g\downarrow})\, \tau_s. \tag{5.130}
$$

Therefore, the radiative transfer for a scattering layer above the aircraft becomes

$$I_{\text{above}} = \frac{F_0}{\pi\mu_0}\,\alpha\,T_I^g(\tau_{g\uparrow},\mu_0)\,T_I^g(\tau_{g\downarrow,a},\mu) \cdot \left[T_I^g(\tau_{g\downarrow},\mu_0)\cdot\left(1-\mu_0\,\tau_s+4\,\alpha\,(1-a)\,E_2(\tau_{g\downarrow})\,E_3(\tau_{g\downarrow})\,\tau_s\right)+2\,a\,\mu_0\,E_3(\tau_{g\downarrow})\,\tau_s\right] \tag{5.131}$$

5.2.2.6. Approximation of an absorption-only atmosphere

Additionally to the full FOCAL AIR forward model described above, a radiative transfer model excluding scattering for aircraft geometry was implemented, i.e., for $\tau_s = 0$. With the absorption-only forward model, it was possible to separate retrieval result improvements by using the FOCAL AIR iterative retrieval from possible improvements due to the additional fitting of scattering parameters. As a side effect, this also allowed for a direct comparison of the WFM-DOAS retrieval and the FOCAL AIR retrieval only using the SWIR measurements of MAMAP. With $\tau_s = 0$, the differentiation between above and below the scattering layer vanishes, and the at-sensor radiance is simply

$$I_{abs} = \frac{F_0}{\pi\mu_0}\,\alpha\,T_I^g(\tau_g,\mu_0)\,T_I^g(\tau_{g,a},\mu). \tag{5.132}$$

$T_I^g(\tau_{ga},\mu)$ is here the transmittance of the atmosphere from the surface up to the aircraft under the light path enhancement μ of the backscattered radiance, and $T_I^g(\tau_g,\mu_0)$ the transmittance of the whole atmosphere under the light path enhancement μ_0 of the incoming radiance.

5.2.2.7. Pseudo-spherical geometry

In the previous sections, the solar and aircraft zenith angles have been assumed to be constant. However, both of these quantities are height-dependent in the Earth's atmosphere. With the zenith angle θ_0 at the surface and the radius of the Earth r_e, the angle $\theta(z)$ at height z can be calculated as

$$\theta(z) = \arcsin\left(\frac{r_e}{r_e+z}\cdot\sin(\theta_0)\right). \tag{5.133}$$

As $\mu = \frac{1}{\cos\theta}$, μ_0 and μ have to be replaced with their height-dependent replacements $\mu_0(z)$ and $\mu(z)$ in Eqs. (5.131) and (5.126), respectively. For the transmission of radiance (Eq. (5.96)), this leads to

$$T_I^g(\tau_g,\mu) = \exp\left(-\int_0^{\text{TOA}} c_g(z)\cdot\sigma_g(z)\cdot\mu(z)\mathrm{d}z\right). \tag{5.134}$$

For the transmission of diffuse fluxes, no height dependence of the zenith angle is considered to allow for the simple application of the third exponential integral when simplifying Eq. (5.103). Additionally, the height axis was discretized in layers with constant solar and instrument angles for the computation. The approach is therefore called pseudo-spherical instead of a full-spherical approach.

5.2.2.8. The FOCAL AIR retrieval chain

The FOCAL AIR retrieval chain is constructed in the same way as the FOCAL retrieval chain (Reuter et al., 2017b,a) with the modifications described by Noël et al. (2021) adapted to MAMAP measurements. The retrieval method comprises a preprocessing step, a retrieval step, and a postprocessing step. In the preprocessing step, the data is prepared for the FOCAL AIR retrieval step, and bad retrieval results are filtered out in the post-processing step. The steps are described below.

Preprocessing All required input data for the FOCAL AIR retrieval are gathered in the preprocessing step. First, the MAMAP raw digital numbers are converted to relative radiance by subtracting the dark current and normalizing it to a white light spectrum. Dark spectra are recorded periodically over the flight, so the nearest dark signal measurements are subtracted for each spectrum. The white light measurements have been recorded prior to or after the flight. Spectra with binary units (BU) of below 300 BU or above 60000 BU after subtraction of the dark current are filtered out, as the chip does not behave linearly in the extremes.

Additionally, the measurement noise is estimated as

$$\sigma_\epsilon = \sqrt{\sigma_{\text{shot}}^2 + \sigma_{\text{read}}^2}, \tag{5.135}$$

where σ_{read} is the detector read noise, and $\sigma_{\text{shot}} = \sqrt{BU - DC}$ is an estimate for the radiance dependent noise. However, these estimates do not include the radiative transfer forward model error and are also likely too low for the MAMAP instrument. Therefore, as in Reuter et al. (2017a) and Noël et al. (2021), the noise model is updated with an empirical formula described in the retrieval step with Eq. (5.142). A constant wavelength grid and a wavelength-dependent instrument line shape function are added to the input data.

For each burst of 10 consecutive measurements, latitude, longitude, and recording time are part of the measurement data. With this data, the a priori for CO_2 and CH_4 are estimated using the SLIM empirical model (Noël et al., 2022). Then, the pressure and water vapor profiles are extracted from ERA5 reanalysis data (see Sect. 5.1) interpolated to the time and location of the measurement. Furthermore, The surface elevation is estimated from the Shuttle Radar Tropospheric Mission (SRTM) data set, which is used to extend or cut the profiles according to the actual surface pressure. The solar zenith angle is calculated from the surface pressure and recording time. The instrument zenith angle is part of the MAMAP data.

Retrieval The retrieval finds the most likely state, also known as the maximum a posteriori solution (see, e.g., Rodgers, 2000), in the presence of MAMAP spectral measurements and a priori information about the state of the system, comprising the atmosphere, surface, and measurement system. The algorithm used to find the most probable state is based on the Levenberg-Marquardt-Fletcher algorithm (Fletcher, 1971; Rodgers, 2000), which iteratively optimizes the state $\vec{x}$ with the following solution for the $i+1$th step

$$\vec{x}_{i+1} = \vec{x}_i + \left[(1+\gamma)\,\mathbf{S}_a^{-1} + \mathbf{K}_i^T\,\mathbf{S}_\epsilon^{-1}\,\mathbf{K}_i\right]^{-1}\,\left\{\mathbf{K}_i^T\,\mathbf{S}_\epsilon^{-1}\,\left[\vec{y} - \vec{F}(\vec{x}_i,\vec{b})\right] - \mathbf{S}_a^{-1}\,\left[\vec{x}_i - \vec{x}_a\right]\right\}, \tag{5.136}$$

minimizing the cost function

$$\chi^2 = \frac{1}{m+n}\left[(\vec{y} - \vec{F}(\vec{x}_i,\vec{b}))^T\,\mathbf{S}_\epsilon^{-1}\,(\vec{y} - \vec{F}(\vec{x}_i,\vec{b})) + (\vec{x} - \vec{x}_a)^T\mathbf{S}_a^{-1}(\vec{x} - \vec{x}_a)\right]. \tag{5.137}$$

In the formulas above, $\vec{x}$ and $\vec{b}$ are the state and parameter vectors, $\mathbf{S}_a$ and $\mathbf{S}_\epsilon$ are the a-priori and measurement error covariance matrices, $\vec{y}$ is the measurement vector, $\vec{F}(\vec{x},\vec{b})$ is the forward model evaluated for the state $\vec{x}$ and parameters $\vec{b}$, $\mathbf{K}$ is the Jacobian matrix, and γ is a damping factor changing the direction and length of the iteration step. The cost function χ^2 is the sum of the difference between measurement and forward model on one side and current and a priori state vector on the other. The implementation of each term in the FOCAL AIR retrieval is explained below.

The term γ is the damping factor, which is the core difference between the Levenberg-Marquardt-Fletcher algorithm to the Gauss-Newton algorithm. Levenberg introduced it to solve the problem of a step in the Gauss-Newton retrieval worsening the residual because the underlying problem is too non-linear. The damping factor is scaled by the inverse of the a priori covariance matrix $\mathbf{S}_a$ to ensure that the dampening affects each parameter, i.e., each row of the matrix equation, similarly. In the Levenberg-Marquardt algorithm (see e.g. Rodgers, 2000) after the calculation of x_{i+1} the cost function reduction is compared to the cost function reduction using a linear approximation of the forward model. In case the cost function increases, the difference becomes negative, the solution is not accepted, γ is increased by a factor $f_{inc} = 2$, and a new x_{i+1} is calculated. Otherwise, the iteration is accepted, f_{inc} is set to 2, and γ is decreased based on the cost function reduction $\chi^2_{i+1} - \chi^2_i$. The complete dampening strategy is described in Nielsen (1999).

$\vec{y}$ is the measurement vector containing m spectral points. For the absorption-only retrieval (Eq. (5.132)), only the SWIR measurements of MAMAP form the measurement vector. Two main retrieval configurations were used depending on the number of separate fit windows in the SWIR spectral range. The 1-window retrieval configuration used one large fitting window fw1, covering the wavelength range 1593.0 − 1675.0 nm. In the 2-window retrieval configuration, the SWIR spectral range was divided into two fit windows (fw1: 1591.1 − 1616.5 nm and fw2: 1629.6 − 1673.9 nm) to form the measurement vector. For the FOCAL AIR retrieval including scattering, additionally the O_2A spectral data in the wavelength range of 756.0 − 772.0 nm (fw0) were part of the measurement vector.

The state vector $\vec{x}$ is composed of the free fit parameters (see Table 5.3 for the 1-window and Table 5.4 for the 2-window retrieval), while all other parameters, which are not fitted

but are needed to calculate the radiative transfer, form the parameter vector $\vec{b}$. These are the solar and instrument zenith angles, the aircraft altitude (in hPa), the incoming solar radiation, and the meteorology at the measurement location. The latter comprises the pressure, temperature, and geometric height grid as well as the total dry column of air and the CO_2 and CH_4 profiles above the fitted lowest layers.

Table 5.3.: State vector $\vec{x}$ elements fitted in the FOCAL AIR 1-window retrieval. The fit window number corresponds to the wavelength ranges from low to high, i.e., 0 stands for the O_2A. The column "absorption-only" indicates, if the state vector element is also present in the absorption-only retrieval.

Element	Fit windows	$x_0 = x_a$	σ_a	Abs. only	Comment
co2_lay_00	fw1	SLIM	50 ppm	yes	lowest merged CO_2 layer
ch4_lay_00	fw1	SLIM	0.24 ppm	yes	lowest merged CH_4 layer
h2o_lay_00	fw1	ERA5	898 ppm	yes	lowest merged H_2O layer
p_0	fw0, fw1	0.5	1.0	no	pressure level of scattering layer
$\tau_{s,0}$	fw0, fw1	0.15	2.0	no	scattering optical thickness at 760 nm
$\mathring{A}_0$	fw0, fw1	4.0	2.0	no	Ångström coefficient
α_0^{NIR}	fw0	est.	$0.05 \cdot x_a$	no	0. order polynomial
α_1^{NIR}	fw0	0.0	0.025	no	1. order polynomial
α_2^{NIR}	fw0	0.0	0.01	no	2. order polynomial
α_0^{SWIR}	fw1	est.	$0.05 \cdot x_a$	yes	0. order polynomial
α_1^{SWIR}	fw1	0.0	0.025	yes	1. order polynomial
α_2^{SWIR}	fw1	0.0	0.01	yes	2. order polynomial
α_3^{SWIR}	fw1	0.0	0.005	yes	3. order polynomial
$\lambda_{sh}^{\mathrm{NIR}}$	fw0	0.35	0.05	yes	wavelength shift
$\lambda_{sq1}^{\mathrm{NIR}}$	fw0	0.0	0.05	yes	1st order wavelength squeeze
$\lambda_{sh}^{\mathrm{SWIR}}$	fw1	0.30	0.1	yes	wavelength shift
$\lambda_{sq1}^{\mathrm{SWIR}}$	fw1	-0.03	0.05	yes	1st order wavelength squeeze
k_{ILS}^{NIR}	fw0	1.004	0.03	no	ils squeeze
k_{ILS}^{SWIR}	fw1	0.98	0.05	yes	ils squeeze
$I_{\mathrm{zlo}}^{\mathrm{NIR}}$	fw0	0.0	1.0	no	additive offset
$I_{\mathrm{zlo}}^{\mathrm{SWIR}}$	fw1	0.0	1.0	yes	additive offset
$I_{\mathrm{odd}}^{\mathrm{SWIR}}$	fw1	0.0	0.05	yes	odd/even effect

The a priori vector $\vec{x}_a$ is composed of the a priori values of each state vector element x. These values additionally serve as the first guess values x_0. The a priori uncertainty for each state vector element is denoted as σ_a. For CO_2 and CH_4, the a priori uncertainty of the lowest layer (representing 1/5 th of the atmospheric concentration) is estimated as 50 ppm and 240 ppb, respectively, which translates to a total column uncertainty of roughly 2.5 %. While usually in MAMAP data, the total column enhancement is below 1.5 % even for strong emitters, the uncertainty also considers possible differences between the a priori estimated from SLIM and the true total background column present during the measurements. For H_2O, the a priori total column uncertainty is the same as in Reuter et al. (2017b), as the same data set is used. The zero-order polynomial a priori value is estimated from the continuum radiance at the lower edge of the O_2A fit window (around 758 nm) and in the

middle of the SWIR spectral window (around 1628 nm, see Fig. 5.1). After this first guess retrieval, the 0th order polynomial a priori uncertainty is estimated to be 5 % of the a priori value. All a priori uncertainties are assumed uncorrelated, so the a priori covariance matrix S_a becomes a diagonal matrix with the diagonal element $\sigma^2_{a,i}$ for the ith state vector element.

Table 5.4.: State vector $\vec{x}$ elements fitted in the FOCAL AIR 2-window retrieval. The fit window number corresponds to the wavelength ranges from low to high, i.e., 0 stands for the O_2A. The column "absorption-only" indicates, if the state vector element is also present in the absorption-only retrieval.

Element	Fit windows	$x_0 = x_a$	σ_a	Abs. only	Comment
co2_lay_00	fw1, fw2	SLIM	50 ppm	yes	lowest merged CO_2 layer
ch4_lay_00	fw2	SLIM	0.24 ppm	yes	lowest merged CH_4 layer
h2o_lay_00	fw1, fw2	ERA5	898 ppm	yes	lowest merged H_2O layer
p_0	fw0, fw1, fw2	0.5	1.0	no	pressure level of scattering layer
$\tau_{s,0}$	fw0, fw1, fw2	0.15	2.0	no	scattering optical thickness at 760 nm
$\mathring{A}_0$	fw0, fw1, fw2	4.0	2.0	no	Ångström coefficient
α_0^{NIR}	fw0	est.	$0.05 \cdot x_a$	no	0. order polynomial
α_1^{NIR}	fw0	0.0	0.025	no	1. order polynomial
α_2^{NIR}	fw0	0.0	0.01	no	2. order polynomial
$\alpha_0^{\mathrm{SWIR\ CO_2}}$	fw1	est.	$0.05 \cdot x_a$	yes	0. order polynomial
$\alpha_1^{\mathrm{SWIR\ CO_2}}$	fw1	0.0	0.025	yes	1. order polynomial
$\alpha_2^{\mathrm{SWIR\ CO_2}}$	fw1	0.0	0.01	yes	2. order polynomial
$\alpha_3^{\mathrm{SWIR\ CO_2}}$	fw1	0.0	0.005	yes	3. order polynomial
$\alpha_0^{\mathrm{SWIR\ CH_4}}$	fw2	est.	$0.05 \cdot x_a$	yes	0. order polynomial
$\alpha_1^{\mathrm{SWIR\ CH_4}}$	fw2	0.0	0.025	yes	1. order polynomial
$\alpha_2^{\mathrm{SWIR\ CH_4}}$	fw2	0.0	0.01	yes	2. order polynomial
$\alpha_3^{\mathrm{SWIR\ CH_4}}$	fw2	0.0	0.005	yes	3. order polynomial
$\lambda_{sh}^{\mathrm{NIR}}$	fw0	0.35	0.05	yes	wavelength shift
$\lambda_{sq1}^{\mathrm{NIR}}$	fw0	0.0	0.05	yes	1st order wavelength squeeze
$\lambda_{sh}^{\mathrm{SWIR\ CO_2}}$	fw1	0.30	0.1	yes	wavelength shift
$\lambda_{sq1}^{\mathrm{SWIR\ CO_2}}$	fw1	-0.03	0.05	yes	1st order wavelength squeeze
$\lambda_{sh}^{\mathrm{SWIR\ CH_4}}$	fw2	0.25	0.1	yes	wavelength shift
$\lambda_{sq1}^{\mathrm{SWIR\ CH_4}}$	fw2	0.01	0.05	yes	1st order wavelength squeeze
k_{ILS}^{NIR}	fw0	1.004	0.03	no	ils squeeze
$k_{ILS}^{\mathrm{SWIR\ CO_2}}$	fw1	0.98	0.05	yes	ils squeeze
$k_{ILS}^{\mathrm{SWIR\ CH_4}}$	fw2	0.98	0.05	yes	ils squeeze
$I_{\mathrm{zlo}}^{\mathrm{NIR}}$	fw0	0.0	1.0	no	additive offset
$I_{\mathrm{zlo}}^{\mathrm{SWIR\ CO_2}}$	fw1	0.0	1.0	yes	additive offset
$I_{\mathrm{zlo}}^{\mathrm{SWIR\ CH_4}}$	fw2	0.0	1.0	yes	additive offset
$I_{\mathrm{odd}}^{\mathrm{SWIR\ CO_2}}$	fw1	0.0	0.05	yes	odd/even effect
$I_{\mathrm{odd}}^{\mathrm{SWIR\ CH_4}}$	fw2	0.0	0.05	yes	odd/even effect

$\vec{F}(\vec{x}_i, \vec{b})$ is the high spectral resolution calculation of the FOCAL AIR forward model I_{rtm}

(Eq. (5.132) in the absorption-only case, and Eqs. (5.126) and (5.131) for the scattering retrieval) using precomputed tabulated absorption cross-sections dependent on pressure, temperature, and water vapor concentration. The forward model is then convolved with the instrument line shape function and sampled to the instrument wavelength grid. In addition to the state vector elements, the retrieval includes an additive offset I_{zlo} to account for straylight or other additive offset effects, and an odd/even fit parameter, which has the form [-1, 1, -1, 1, ...] and is also part of the WFM-DOAS retrieval for MAMAP accounting for radiance-dependent differences between neighboring detector pixels.

$$\vec{F}(\vec{x_i}, \vec{b}) = I_{\mathrm{rtm}} \cdot (1 + I_{\mathrm{odd}}) + I_{\mathrm{zlo}} \tag{5.138}$$

The numerical calculation requires a discretization of the forward model equation along the height axis. Therefore, the atmosphere is split into 20 layers containing the same number of dry-air molecules. The profiles of CO_2, CH_4, and H_2O comprise five layers, which are expanded to the 20-layer atmosphere. Therefore, the gas concentrations are constant in 4 consecutive layers of the forward model atmosphere.

Additionally, as the wavelength grid of MAMAP is not precisely characterized yet, a linear shift and a first-order squeeze of the wavelength axis are fitted for each fit window. The final wavelength grid λ' is

$$\lambda' = \lambda + \lambda_{sh} + \lambda_n \cdot \lambda_{sq1}. \tag{5.139}$$

Finally, also the line shape function (ILS) can be squeezed by scaling the wavelength grid λ_{ILS} of the ILS by the factor k_{ILS}:

$$\lambda'_{ILS} = \lambda_{ILS} \cdot k_{ILS}. \tag{5.140}$$

The measurement covariance matrix S_ϵ is a diagonal matrix composed of the square of the noise for each spectral data point. The initial noise N only comprises the measurement noise described above. It is updated to account for the noise introduced by the radiative transfer forward model and better characterize the MAMAP measurement noise. The noise estimation is similar to the approach taken by Reuter et al. (2017a) and Noël et al. (2021). In order to find the parameters of the noise model, S_ϵ is enlarged by quadratically adding 2 % of the continuum radiance to the noise estimate. As a consequence, nearly all data points reach convergence. From the fit residuals, the residual to continuum signal ratio (RSR) and the noise to continuum signal ratio (NSR) are calculated. If the retrieval did not introduce noise and the instrument would be characterized perfectly, these two values would be the same. Therefore, the initial noise N, the updated noise N', the continuum radiance I_{cont}, RSR, and NSR can be correlated by the two parameters n_a and n_b in the following way:

$$RSR = \sqrt{n_a \cdot NSR^2 + n_b^2} \tag{5.141}$$

$$N' = \sqrt{n_a \cdot N^2 + n_b^2 \cdot I_{cont}^2}. \tag{5.142}$$

The results of the updated noise N' are given in Sect. 6.3.2.

The rows of the Jacobian matrix $\mathbf{K}$ are composed of the derivative of the at-sensor radiance I_{below} or I_{above}, respectively, to the state vector elements. For the k-th state vector element K_k is

$$K_k = \frac{\partial I}{\partial x_k}. \tag{5.143}$$

The K_k representing changes in gas concentrations, scattering parameters, and the polynomial can be calculated analytically for faster calculation in the retrieval. The K_k for shifting and squeezing the wavelength grid and squeezing the ILS are calculated numerically by calculating the change in radiance for a minimal change in the respective parameter. In figures 5.7 and 5.8, the elements of $\mathbf{K}$ are shown for a synthetic scene in Eastern Germany on 23.05.2018 at approximately noon, and an aircraft altitude of $\sim 2000\,\mathrm{m}$ above ground. The apparent non-continuity in the odd-even weighting functions (especially observable in the SWIR CO_2 fit window) is due to the MAMAP pixel mask, which was also applied to the synthetic data.

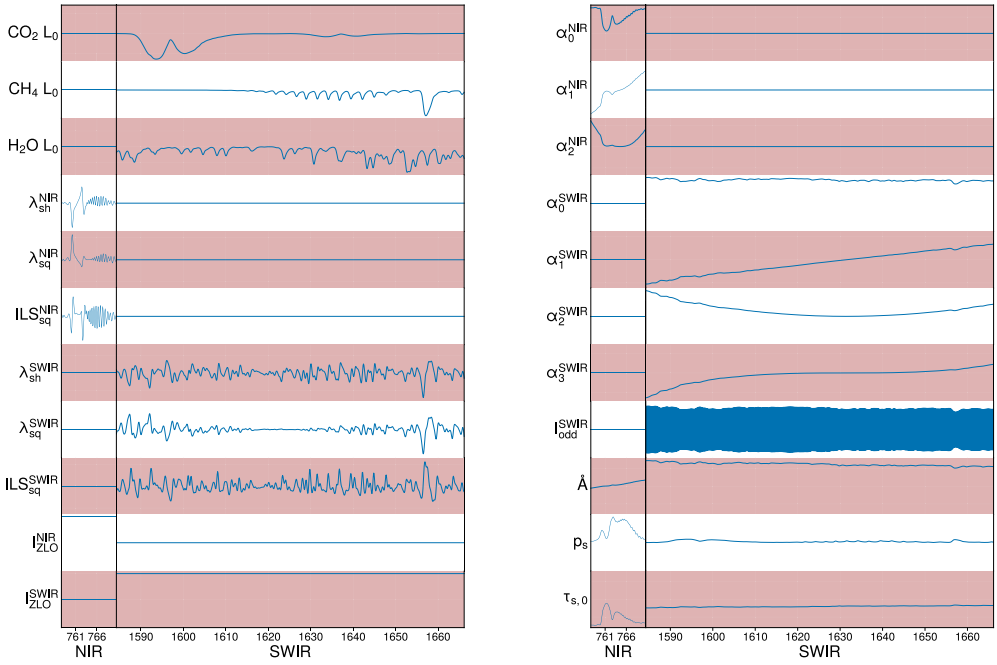

Figure 5.7.: Jacobians of the state vector elements for the FOCAL-AIR scattering 1-window retrieval in both fit windows with the pixel mask applied.

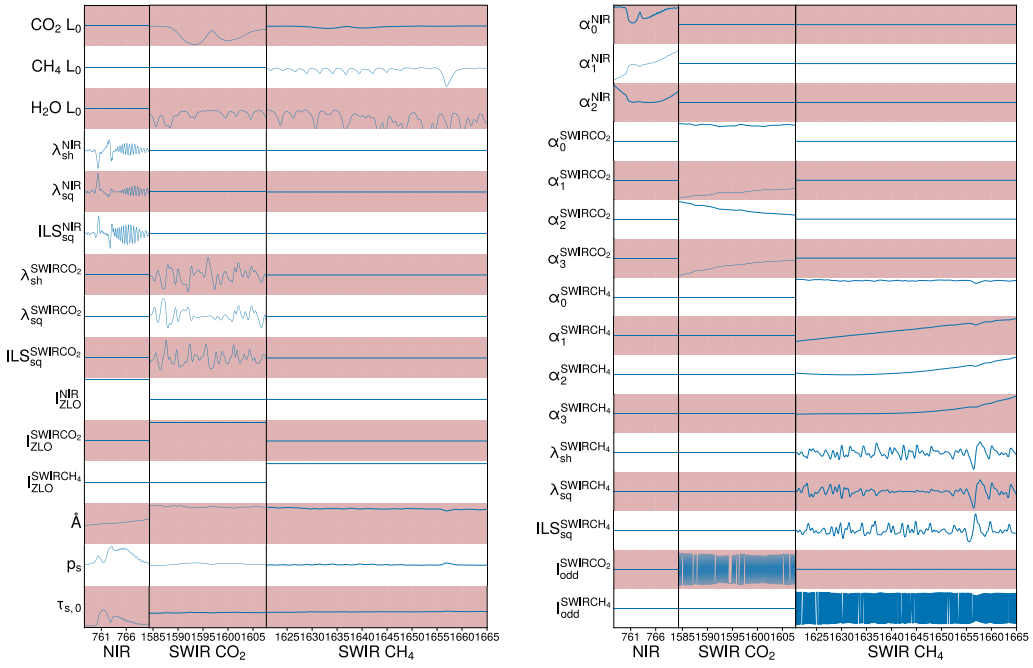

Figure 5.8.: Jacobians of the state vector elements for the FOCAL-AIR scattering 2-window retrieval in both fit windows with the pixel mask applied.

The iterative calculation of $\vec{x}$ is stopped when the step size from the i-th to the $i+1$-th iteration step relative to the a posteriori uncertainty gets small enough, i.e., when

$$(\vec{x}_i - \vec{x}_{i+1})^T \, \hat{\mathbf{S}}^{-1} \, (\vec{x}_i - \vec{x}_{i+1}) \cdot \frac{1}{n} < 0.2. \tag{5.144}$$

Additionally, the retrieval is stopped if no convergence was reached in 100 iterations to prevent infinite iterations.

The final a posteriori covariance matrix

$$\hat{\mathbf{S}} = (\mathbf{K}^T \, \mathbf{S}_\epsilon^{-1} \, \mathbf{K} + \mathbf{S}_a^{-1})^{-1} \tag{5.145}$$

comprises the n parameter uncertainties and their correlations.

Postprocessing In the postprocessing step, the retrieval results are quality filtered, and the retrieved valid mixing ratios are converted to total column enhancements.

Right now, the quality filtering only comprises two filters: All measurements that did not converge were rejected. Additionally, the residuals RMS_{WFM} were calculated as in Eq. (5.95), and retrieval results with $RMS_{\mathrm{WFM}} > 0.7$ were rejected, too.

For the gases, FOCAL AIR retrieves dry air mole fractions for the lowest layer of each gas and returns the average dry air mole fraction for the total column (XCO_2). The number of dry air molecules in the column in molec m^{-2} (n_{dry}) is part of the FOCAL AIR atmospheric input parameters. Therefore, the total column of the gases in molec m^{-2} is calculated as follows:

$$\text{gas}_{col} = \text{Xgas} \cdot n_{dry} \tag{5.146}$$

As in WFM-DOAS (Sect. 5.2.1, in FOCAL AIR absorption-only, light path changes due to a change in the pressure or temperature profile, as well as aerosol and rayleigh scattering, might lead to light path changes which are not captured by the retrieval. It is assumed that, in total, the light path uncertainties are smaller than for the WFM-DOAS retrieval due to the observation geometry being calculated for each measurement point, including aircraft and surface altitude. Nevertheless, some residuals might be present. Therefore, also for FOCAL AIR absorption-only, the proxy method was applied. The proxy corrected total column $CO_{2,col}(CH_4)$ becomes

$$CO_{2,col}(CH_4) = CO_{2,col} \cdot \frac{\overline{CH_{4,col}}}{CH_{4,col}}. \tag{5.147}$$

$\overline{CH_{4,col}}$ is hereby the median of $CH_{4,col}$, assuming a constant methane background. The local enhancement is then calculated as

$$CO_{2,col,enh}(CH_4) = \left(\frac{CO_{2,col}(CH_4)}{CO_{2,col,bg}(CH_4)} - 1 \right) \cdot CO_{2,col,bg}(CH_4) \tag{5.148}$$

5.2.3. Destriping of imaging data

A critical component of a push broom imaging spectrometer is the 2D detector array recording the spectra on one axis and different ground scenes on the other. In an ideal world, all detector pixels would behave equal, meaning their quantum efficiency is the same, the noise of each pixel is the same, and the amplifiers would convert the same voltage to the same digital numbers. However, in reality, this is not the case. Additionally, dead or bad pixels mask different spectral points for different ground scenes. Furthermore, stray light might influence different ground scenes differently. All of the above can lead to offsets in the spectra, which are mostly corrected by the level-0 to 1b processor for AVIRIS-NG, i.e., when converting raw digital numbers to radiances (Chapman et al., 2019). However, some residual structures between different ground scenes remain, which appear only in the retrieval result. Such a processor does not exist for MAMAP2D-Light due to the missing radiative calibration. Therefore, this effect is expected to be stronger.

This scene-to-scene bias imposes an additional total column change on top of the retrieved column enhancements. The AVIRIS-NG retrieval results were corrected for this offset by normalizing the resulting columns by the median column enhancement of one straight flight line. The median was chosen as it is more robust against single outliers, which would impact the correction strongly otherwise. An important assumption for this correction is that the

number of ground scenes enhanced due to emissions is small compared to the number of ground scenes in the flight track column. In the case of the MAMAP2D-Light observations of the Jänschwalde power plant plume, this was not true anymore. There, instead of a global average of one flight line, a moving average of 1500 ground scenes was used for normalization.

5.3. Cross-sectional flux method

The cross-sectional flux method (White et al., 1976) is a conceptually easy method to estimate emissions from enhancements measured across an emission plume. It is based on Gauss's theorem, also known as the divergence theorem, which states that the flux out of a volume is equal to the sum of all sources within it.

Assuming constant wind from one direction, a rectangular volume can be defined in which two sides of the rectangular are parallel to the wind direction. Then, the flux difference between the downwind and upwind walls of the box gives the emission of all sources within the box. If no other sources are located upwind of the examined source, one can define the box wide enough that the flux per area through the downwind wall of the box besides the plume is equal to the flux per area through the upwind track. In this case, only enhanced concentrations in the downwind wall of the box contribute to the net flux.

Remote sensing measurements already integrate the enhancements along the vertical axis, which only leaves the integral across the wall to be calculated. Then, the cross-sectional flux F_c of a constituent *gas* through one cross-section is:

$$F_c = f \cdot \overline{u} \cdot \sin \alpha_c \sum_i gas_{\mathrm{enh},i,c} \cdot \mathrm{d}x_{i,c}. \tag{5.149}$$

In this equation, $\overline{u}$ is the mean wind speed, α is the angle between the cross-section and the mean wind direction, $gas_{\mathrm{enh},i}$ is the retrieved enhancement above local background in the ground scene i, d_i is the length of the i-th ground scene, and f is a conversion factor to the desired units, e.g., kilograms per hour ($\mathrm{kg\,h^{-1}}$) or megatonnes per year ($\mathrm{Mt\ yr^{-1}}$).

For the final emission estimate F, as many independent cross-sections as possible are averaged to reduce the influence of atmospheric variability. It is observable as gaps and accumulations in the 2D-images of AVIRIS-NG and MAMAP2D-Light and as the strongly varying fluxes from track to track for MAMAP:

$$F = \frac{\sum_{c=1}^{N} F_c}{N} = \frac{1}{N} f \cdot \overline{u} \cdot \sum_{c=1}^{N} \sin \alpha_c \sum_i gas_{\mathrm{enh},i,c} \cdot \mathrm{d}x_{i,c} \tag{5.150}$$

To estimate the uncertainty of the cross-sectional flux in Eq. 5.150, the uncertainty of the contributing elements have to be taken into account. Applying uncertainty propagation (JCGM, 2008), the uncertainty of the flux ΔF is calculated as follows:

$$\Delta F = \sqrt{(\Delta F_c)^2 + (\Delta F_{\overline{u}})^2 + (\Delta F_{atm})^2 + (\Delta F_{bgcol})^2}, \tag{5.151}$$

$$\tag{5.152}$$

with the uncertainty of the single flux ΔF_c

$$\Delta F_c = \sqrt{\frac{1}{\sqrt{N-1}}\left((\Delta F_{c,\alpha})^2 + (\Delta F_{c,bgfit})^2 + (\Delta F_{c,prec})^2 + (\Delta F_{c,proxy})^2\right)} \tag{5.153}$$

The uncertainty in the flux due to the uncertainty of the variable x is denoted as ΔF_x, while a c denotes uncertainties present in each cross-section separately. The terms and their origin are described below in more detail. The differences in calculating the uncertainty for WFM-DOAS and FOCAL AIR retrieval results and between the different instruments are also pointed out.

The source of the mean wind speed information is a significant source of uncertainty, more so as in all cases studied in this thesis, no concurrent height-resolved wind measurements were conducted, and the wind speed information originates from model data or wind measurement stations further away from the plume. The wind speed uncertainty $\Delta\overline{u}$ is assumed as a constant for each wind observation type. As the wind speed is not cross-section dependent, this uncertainty is not reduced by the number of cross-sections.

The mean wind direction α relative to the cross-section orientation is another source of uncertainty. For AVIRIS-NG data, the cross-sections were chosen orthogonal to the apparent wind direction, rendering uncertainties in $\sin\alpha$ negligible. For MAMAP and MAMAP2D-Light data, the cross-sections were selected along the flight line. For MAMAP, there are no data to facilitate another choice of cross-sections. For MAMAP2D-Light, in theory, also orthogonal cross-sections could be selected. However, as no dense 2D map of the whole plume was acquired, this would lead to fewer cross-sections in total. Therefore, the cross-sections were also chosen along the flight line for MAMAP2D-Light data. Deviations $\Delta\alpha$ of the true wind direction from the assumed wind direction angle lead to the uncertainty $\Delta F_{c,\alpha}$. It is assumed that the deviation changes from cross-section to cross-section and is dominated by the flight line direction estimate. Therefore, deviations in different cross-sections can cancel out. Therefore, this uncertainty contribution is reduced by the number of cross-sections.

The gas enhancements along a cross-section were normalized by a first-order polynomial fit to the local background. Therefore, the statistical background fit uncertainty for each ground scene in the plume region was estimated to account for the uncertainty due to the linear background fit. The uncertainty in the flux due to the background fit ΔF_{bgfit} is then calculated as the sum of these fit uncertainties in the plume region and normalized by the square root of the number of cross-sections assuming that background fit errors occur randomly.

The enhancements above the background are also influenced by the precision of the retrieved column enhancements. The precision is calculated as the $1\,\sigma$ standard deviation of the background region of the plume. The more measurements are part of the flux estimation, the lower this uncertainty contribution gets, so the uncertainty of the flux due to the precision of the retrieved column $\Delta F_{c,prec}$ is also reduced by the square root of the number of cross-sections.

Applying the proxy method to correct the target gas enhancements by another gas can also introduce errors. Primarily, this could be induced by co-emission of the second gas, which would alter the enhancements across the whole cross-section. Nevertheless, the enhancements must be very low for the gas to not show up as a plume in the non-proxy column results for the second gas, which can be checked for such signals. The relatively low enhancement also implies that the influence diminishes for longer plumes. Consequently, the uncertainty of the flux due to potentially co-emitted gases $\Delta F_{c,proxy}$ is reduced by the square root of the number of cross-sections.

The flux estimates vary vastly from cross-section to cross-section. The primary causes are accumulation and dilution of the plume due to turbulent mixing, also described as atmospheric variability. The uncertainty due to this atmospheric variability ΔF_{atm} is estimated as the standard deviation of the mean of the flux estimates from all cross-sections.

The background column for the WFM-DOAS method gas_{back} was obtained from scaled climatologies. Although these have been validated (Noël et al., 2022; Reuter et al., 2012), there might still be some offsets on small scales. Therefore, $\pm 5\,\%$ deviation of the total column was assumed as upper limit uncertainty for the background column (ΔF_{bgcol}). Calculating the flux for additional cross-sections cannot reduce this uncertainty. For the FOCAL AIR retrieval, absolute total columns and absolute column enhancements are retrieved with their according uncertainties. This uncertainty was assumed to represent the background column uncertainty.

6. Results

Each research question targets a specific part of the problem to estimate emissions from airborne remote sensing systems. This chapter gives the results for the three research questions separately. First, the application of the WFM-DOAS method on AVIRIS-NG data for synthetic and actual measurements is presented in Sect. 6.1. Next, the newly acquired data from the recently built MAMAP2D-Light imaging instrument are analyzed. First, the calibration procedure results for the MAMAP2D-Light instrument are presented. Next, the first measurement flight over the power plant is retrieved, and the power plant emissions for the overflight are estimated in Sect. 6.2. Finally, the potential of the FOCAL AIR retrieval to retrieve column enhancements independent of the proxy and by including scattering for future more complex scenes is explored in Sect. 6.3.

6.1. Retrieval of AVIRIS-NG imaging data for plume detection and quantification

The retrieval of AVIRIS-NG data with the WFM-DOAS algorithm and assessing the retrieval results were done procedurally. First, the best fit window was selected (Sect. 6.1.1), for which then a sensitivity study was performed to assess the limitations of the WFM-DOAS retrieval applied to AVIRIS-NG data (Sect. 6.1.2). Performance over different ground scenes, especially for low radiances, and an according filtering method are presented in Sect. 6.1.3. The detected plumes are discussed in Sect. 6.1.4. A subset of five of these plumes was compared to other established retrievals for AVIRIS-NG data in Sect. 6.1.5, and the emissions for these plumes were estimated in Sect. 6.1.6. The main parts of this chapter have been published in Borchardt et al. (2021).

6.1.1. Fitting windows for AVIRIS-NG data

The fitting window strongly impacts the retrieval results. If selected too narrow, there are too few spectral points, thus not enough independent data to successfully conduct a linear fit to the state parameters. This is especially true for the lower spectral resolution of AVIRIS-NG. Depending on the configuration, there are 5 (2 gases, temperature, 2^{nd} order polynomial) to 7 (3 gases, temperature, 3^{rd} order polynomial) independent parameters that have to be fitted. If all spectral points were completely independent, the minimum fitting window size would be 5 or 7 spectral points. For AVIRIS-NG, this converts to a fit window size of $\sim$ 27.5 nm or $\sim$ 38.5 nm, respectively. However, as the spectral points are not completely independent, wider spectral windows provide more independent information.

On the other hand, if the spectral window gets too wide, additional gases must be fitted, or higher order polynomials are needed to fit scattering and surface reflectance effects better. Especially higher order polynomials might reduce precision in lower spectral resolution data, as was studied by Jongaramrungruang et al. (2021).

Additionally, both CO_2 and CH_4 absorb around 1600 nm as well as around $2000 - 2400$ nm. Therefore, possible fit windows can be chosen to cover either absorption band. Both gases must be retrieved as well as possible for the proxy method. Therefore, the optimal fitting window was determined for each.

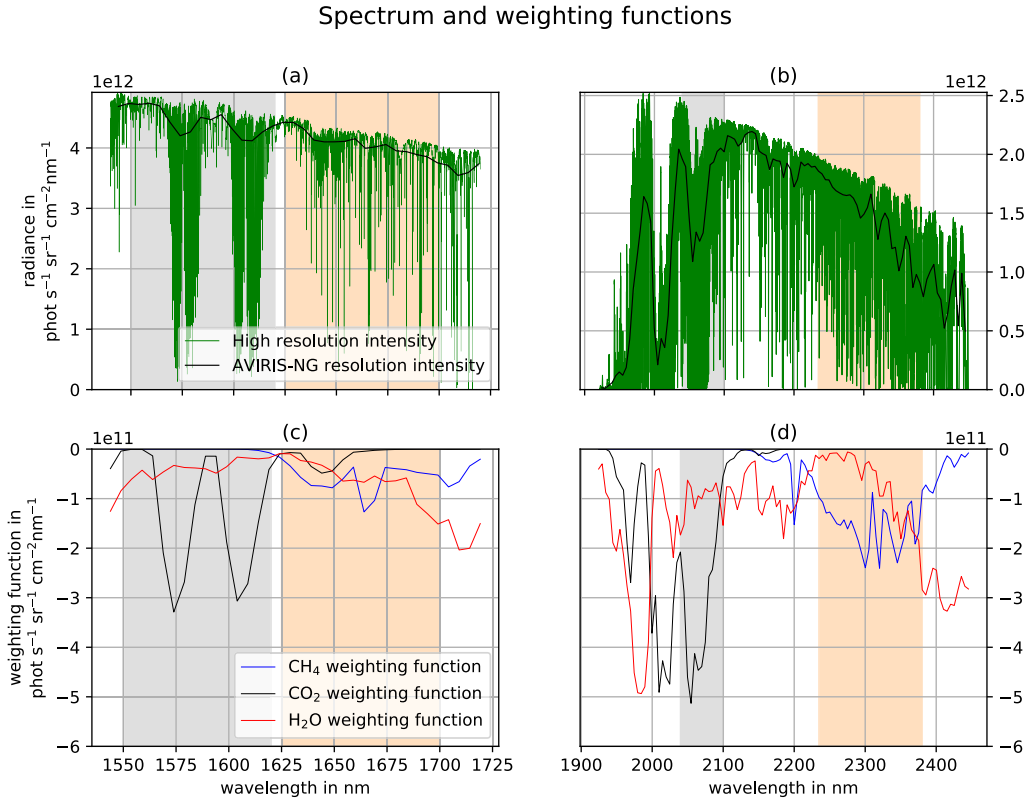

Figure 6.1.: High resolution spectra of the fitting windows around 1600 nm and 2300 nm (green line) are convolved and resampled to AVIRIS-NG spectral characteristics (black line in (a) and (b)). In figures (c) and (d), the weighting functions for CH_4 (blue), CO_2 (black), and H_2O (red) are shown for both fitting windows accordingly. The gray and light orange shades denote the final fitting windows for CO_2 and CH_4, respectively.

In the first step, a high-resolution spectrum and the according weighting functions for CH_4, CO_2, and H_2O were calculated for the same observation conditions, especially the same albedo value. The weighting functions were height averaged and, as well as the high-resolution spectra, then were convolved with the slit function of AVIRIS-NG. As the slit

function does not change much in the fit windows considered here, a single FWHM value for each fit window was used for the convolution. For the wavelength ranges $1540 - 1720$ nm and $1920 - 2450$ nm this is visualized in Fig. 6.1.

While the peak of the weighting function is deeper around 2300 nm by a factor of ~ 2 than around 1650 nm, also the continuum radiance around 2130 nm is approximately a factor of 2 lower than at around 1625 nm. For CO_2, the weighting functions differ only by a factor of ~ 1.6. H_2O absorptions depicted by the H_2O weighting function seem to interfere stronger between $1900 - 2450$ nm than between $1540 - 1720$ nm.

As this did not provide a clear answer to which fit window would be best, a two-step approach was taken. First, a measurement subset over a homogeneous bright surface area was selected, and the retrieval was run, varying the edges of the fit windows one edge at a time iteratively. Then, the residual structures of the fit, a normalized RMS (i.e., summed square of the residual components divided by the width of the fit window), and the retrieval scatter were analyzed to define the best fit window. In the end, the following fit windows provided good RMS and retrieval scatter while showing only moderate structures in the residuum. For CH_4, the chosen fitting windows were $1625 - 1700$ nm and $2235 - 2380$ nm, and for CO_2 $1550 - 1620$ nm and $2040 - 2100$ nm. Following the depth of the absorption lines, in the rest of Sect. 6.1 the fit windows between 1550 and 1700 nm will be called "weak windows", while the fitting windows between 2040 and 2380 nm will be called "strong windows".

For comparison of the measurement precision, the retrieval was applied to the whole flight line containing the subset used to select the fit windows. Then, the proxy was applied, and the PSF_{CH_4}, PSF_{CO_2}, and $PSF_{CH_4,proxy}$ were destriped. Finally, the standard deviation of the retrieval results for PSF_{CH_4}, PSF_{CO_2} and $PSF_{CH_4,proxy}$ in the subregion for the weak and strong fit windows were calculated. The results are shown in Table 6.1. In the weak window, the retrieved PSF_{CH_4} and $PSF_{CH_4,proxy}$ were noisier by a factor of 3.3 and 2.9, respectively, while the retrieved PSF_{CO_2} was still noisier by a factor of 1.5. Consequently, the retrieval was only applied to the strong window of AVIRIS-NG data in further studies in this thesis.

Table 6.1.: Comparison of the standard deviation of PSF_{CH_4}, PSF_{CO_4} and $PSF_{CH_4,proxy}$ in the two fitting windows around 1645 nm and 2300 nm for the AVIRIS-NG data (resolution ~ 6 nm).

	Standard deviation PSF 1645 nm fitting window	Standard deviation PSF 2300 nm fitting window
PSF_{CH_4}	$\pm 6.4\,\%$	$\pm 1.9\,\%$
PSF_{CO_2}	$\pm 1.9\,\%$	$\pm 1.3\,\%$
$PSF_{CH_4,proxy}$	$\pm 6.6\,\%$	$\pm 2.3\,\%$

6.1.2. WFM-DOAS sensitivity analysis using AVIRIS-NG synthetic measurements

The WFM-DOAS method described in Sect. 5.2.1 is based on a single linear fit between a background spectrum and the measurement. The differences between the spectra are minimized by scaling weighting functions for atmospheric gases and temperature and a polynomial. However, the background atmospheric state and the viewing geometry are not constant over a flight track, and weighting functions do not cover all changes. For example, changes in surface elevation or surface pressure are not retrieved. However, they influence the light path and, consequentially, the retrieval. The proxy method aims at eliminating a lot of these changes (see, e.g., Krings et al., 2011), but it is not clear how well this works for instruments with lower spectral resolution such as AVIRIS-NG. Additionally, the polynomial should catch spectral dependencies of the surface reflectance, which is assumed to be constant in the SCIATRAN background case.

Table 6.2.: Parameters studied in the sensitivity analysis and the range in which deviations were analyzed. The second column shows the background scenario used as "truth" in the sensitivity study. The third column notes the range of the perturbation of the parameters. Parameters not mentioned here were constant and estimated as described in Sect. 5.2.1.

Parameter	Standard value	Studied range
Aircraft altitude	5.33 km	4.93 km to 5.93 km
Surface elevation	0.39 km	0.0 km to 0.6 km
Instrument viewing angle	0.00 °	± 18 °
Surface albedo	0.1	0.01 to 0.5
xCH_4	1.833 ppm	(0.8 to 2) · 1.833 ppm
xCO_2	399.2 ppm	(0.97 to 1.03) · 399.2 ppm
H_2O	$5.94 \cdot 10^{22}$ molec cm^{-2}	(0.5 to 2) · $5.94 \cdot 10^{22}$ molec cm^{-2}
Pressure profile	US standard scaled to 1015 hPa at sea level	(0.95 to 1.05) · 1015 hPa
Temperature profile	US standard shifted to 299 K at surface	± 10 K
Aerosol scenario	OPAC urban	OPAC background, OPAC desert
Surface reflectance	Constant albedo 0.1	Rangeland vegetation Barbed goatgrass Soil (Entisol) Grey sandstone Weathered aluminium Weathered steel Paving asphalt Paving concrete

To assess the magnitude of these effects and, therefore, their influence on the retrieved CH_4 enhancements, the at-instrument radiance for a defined atmospheric background state (col-

umn "Standard value" in Table 6.2) was calculated. Then, parameters possibly influencing the retrieved column enhancement were perturbed one at a time to simulate measurements for these different atmospheric states. Finally, the retrieved profile scaling factor for CH_4 and CO_2 as well as the $CH_4(CO_2)$ proxy were calculated and compared to the true profile scaling factors, which were the input to the simulated measurement.

The following set of parameters was perturbed in this sensitivity analysis (the values are given in Table 6.2): aircraft altitude, surface elevation, instrument viewing angle, and surface albedo, as well as the total columns of CH_4, CO_2 and H_2O, the pressure and temperature profiles, and aerosol scenarios. Last, the influence of different surface spectral reflectance spectra compared to a spectrally uniform albedo was analyzed. The solar angle dependency was not analyzed, as the acquisition time for a flight track is in the order of 10 minutes, during which time the angles were effectively constant. Also, the instrument azimuth angle was approximately constant for a single flight line, as these were nearly straight.

The viewing angles represent the maximum viewing angles of AVIRIS-NG for the outermost ground scenes. The surface elevation and aircraft altitude changes were derived from variations observed in one flight line. The surface albedo changes for constant albedo covered the range expected between $2100 - 2300\,\text{nm}$ (Chen et al., 2006).

The surface pressure changes were chosen to represent a possible range of deviations but were selected to be somewhat on the high side. The same is true for the temperature profile, as the temperature profile was acquired from ERA-5 reanalysis data and might deviate strongly from the actual temperature profile at the time of overflight.

The scaling of the CO_2 and H_2O columns covered substantial variations from the assumed background columns for the two gases to examine the upper bound of the error. The chosen range for the CH_4 column covers the range which might be observed exactly over or directly near a strong source.

The OPAC (Hess et al., 1998) urban scenario was used as the background scenario, as for oil and gas production fields, especially near the surface, some contamination with artificial aerosols is expected. Nevertheless, the impact of the choice of aerosol scenario on the retrieval was assessed with simulations using an OPAC background and desert aerosol scenario.

Finally, the influence of actual surface reflectance spectra instead of a constant albedo was analyzed. The examined surface types include surface types present in the survey region (e.g., barbed goatgrass and grey sandstone) or are associated with oil and gas infrastructure (e.g., weathered aluminum and steel). The spectral reflectances were acquired from or based on the ECOSTRESS Spectral Library (Meerdink et al., 2019; Baldridge et al., 2009) and the US Geological Survey Spectral Library, Version 7 (Kokaly et al., 2017). The reflectance spectra are shown in Fig. 6.2.

The deviation from the known true CH_4 and CO_2 total columns was calculated for each parameter variation and plotted as a function of the parameter deviation in Fig. 6.3. For most parameters, the observed deviations of the single parameters are more pronounced than after applying the proxy method. Apart from deviations in the gas concentration, the

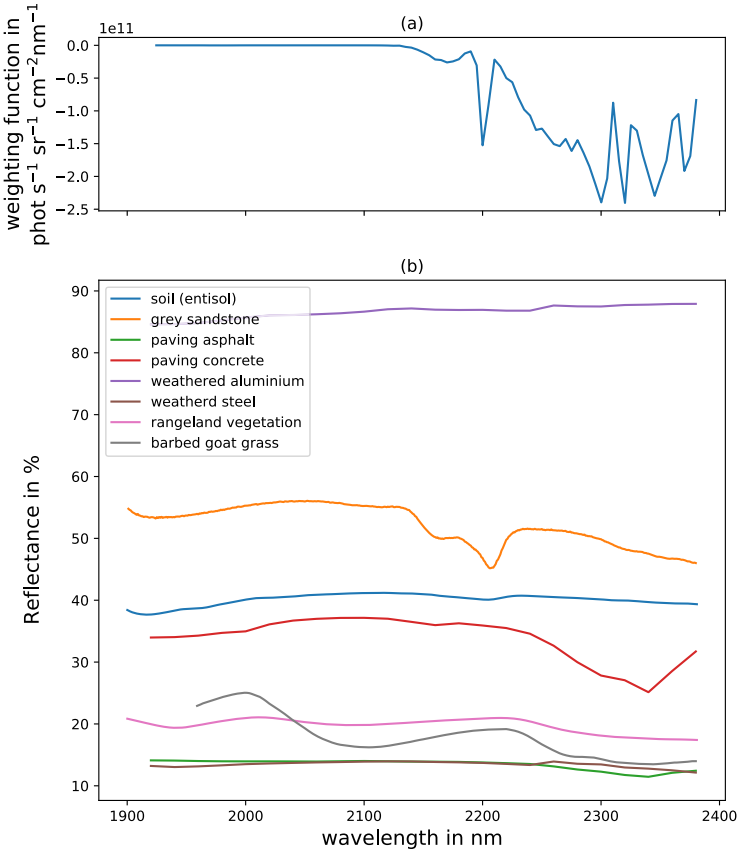

Figure 6.2.: Surface reflectance spectra for different surface types between 1900 and 2400 nm (panel (b)). In panel (a), additionally the weighting function of CH_4 at AVIRIS-NG resolution is shown for comparison.

largest deviation in the CH_4 and CO_2 profile scaling factors were present when changing the surface elevation, followed by a temperature shift, a change in aircraft altitude, and deviations from the nadir viewing angle.

However, after applying the proxy method, nearly all uncertainties were reduced to below 0.5 % for the maximum deviation (see also Table 6.3). Therefore, deviations in aircraft altitude, temperature shifts, surface pressure scaling, viewing angle, and total water vapor column generally do not introduce large errors. The same is true for most albedo changes, apart from very dark scenes. However, dark scenes also introduced other problems and were examined in more detail in 6.1.3. Finally, changing the aerosol scenario from urban to background or desert did not significantly influence the retrieved profile scaling factors.

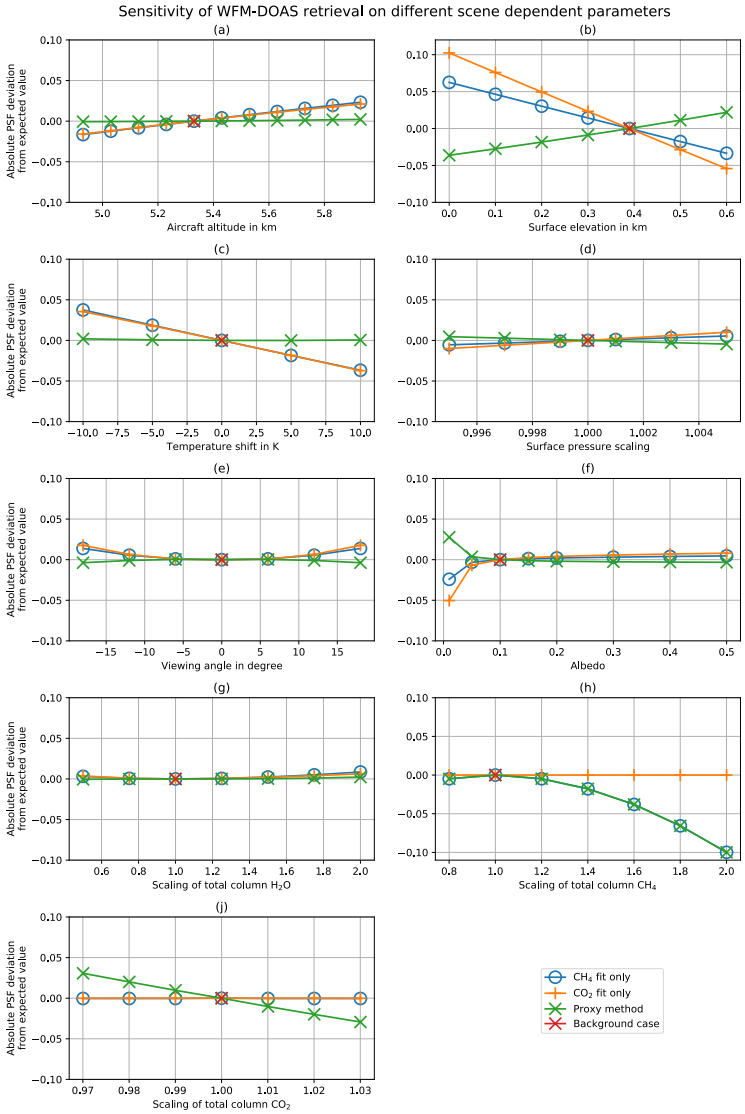

Figure 6.3.: The differences between truth and retrieved profile scaling factor are plotted for CH_4 (blue), CO_2 (orange) and the proxy (green) for the parameter considered in the sensitivity study. The red cross denotes the common background case.

For a change in surface elevation from the background case of 400 m, the deviation from the true proxy profile scaling factor got as large as $\pm 3.6\%$. However, changes of a hundred meters or more in surface elevation only occur on the flanks of very steep mountains. Over relatively flat areas, normalizing over the background of a plume would cancel out a possible bias due to a mismatch between the assumed and actual surface elevation. Furthermore, changes in surface elevation usually do not resemble the shape of emission plumes, so misattributing this bias to an emission source is very unlikely.

Deviating the column concentration from the assumed total column concentration introduced increasing errors the larger the deviation got. In WFM-DOAS, it is assumed that the spectrum changes linearly with changing the gas concentration, which does not hold for strong absorbers. Furthermore, the proxy did not reduce the error for deviations due to changing gas concentrations. In contrast, the proxy method even increased the error in CH_4 in the case of CO_2 deviations.

For CH_4, huge increases ($> 20\%$) were generally underestimated. However, such increases are either present if there is accumulation directly over the source and emission estimation is not possible by the cross-sectional flux method. Alternatively, a very strong plume must be present. In both cases, the source can be detected. In the second case, the flux has to be calculated further downwind of the source. There, the enhancements are lower due to mixing within the atmosphere, and the underestimation is small.

When perturbating the total column of CO_2, the profile scaling factor of CH_4 was retrieved correctly. However, as CO_2 is underestimated more for greater deviations from the background concentration, the proxy introduced errors. For large-scale deviations, this can be considered similar to surface elevation offsets described before. However, if a CO_2 emission source is present near a CH_4 source, theoretically, a CO_2 plume could mask a CH_4 plume and vice versa. Nevertheless, plume-shaped enhancements of CO_2 can be detected in the profile scaling factor maps prior to the application of the proxy. In such cases, only detection is possible with the methods described here, but no quantification.

Table 6.3.: Uncertainty estimate resulting from the assumed constant atmospheric and geometric background parameters (see Fig. 6.3). For each parameter, the maximum deviations for PSF_{CH_4} and PSF_{CO_2}, as well as for $PSF_{CH_{4,proxy}}$, are listed. For albedo, the largest value was excluded from this table (see main text). The two different cases for CH_4 separate strong enhancements only present in the direct vicinity of a strong source (CH_4 (extreme)) and those present further downwind of a strong source or present in plumes from weaker emitters (CH_4 ($\pm 20\,\%$)).

Parameter	Uncertainty on PSF_{CH_4}	Uncertainty on PSF_{CO_2}	Uncertainty on $PSF_{CH_{4,proxy}}$
Aircraft altitude	$\pm 2.3\,\%$	$\pm 2.1\,\%$	$\pm 0.2\,\%$
Surface elevation	$\pm 6.3\,\%$	$\pm 10.2\,\%$	$\pm 3.6\,\%$
Temperature shift	$\pm 3.8\,\%$	$\pm 3.7\,\%$	$\pm 0.2\,\%$
Surface pressure	$\pm 0.5\,\%$	$\pm 1.0\,\%$	$\pm 0.5\,\%$
Viewing angle	$+ 1.4\,\%$	$+ 1.8\,\%$	$- 0.4\,\%$
Albedo	$\pm 0.5\,\%$	$\pm 0.8\,\%$	$\pm 0.4\,\%$
Water vapor	$+0.9\,\%$	$+0.6\,\%$	$+0.2\,\%$
CH_4 ($\pm 20\,\%$)	$-1.0\,\%$	$\pm 0.0\,\%$	$- 1.0\,\%$
CH_4 (extreme)	$- 10.0\,\%$	$\pm 0.0\,\%$	$- 10.0\,\%$
CO_2	$\pm 0.0\,\%$	$\pm 0.0\,\%$	$\pm 3.1\,\%$
Aerosol scenario	$\pm 0.1\,\%$	$\pm 0.3\,\%$	$\pm 0.2\,\%$
Systematic uncertainty	$\pm 8.0\,\%$	$\pm 11.3\,\%$	$\pm 5.4\,\%$

Table 6.4.: Uncertainty estimate of PSF_{CH_4}, PSF_{CO_2} and $PSF_{CH_{4,proxy}}$ due to the assumption of a constant albedo over different surfaces.

Surface type	Uncertainty on PSF_{CH_4}	Uncertainty on PSF_{CH_2}	Uncertainty on $PSF_{CH_{4,proxy}}$
Rangeland vegetation	0.38 %	0.34 %	0.04 %
Barbed goat grass	−7.16 %	−0.06 %	−7.11 %
Soil (Entisol)	0.26 %	0.79 %	−0.53 %
Grey sandstone	0.25 %	0.62 %	−0.37 %
Weathered aluminium	1.30 %	1.05 %	0.25 %
Weathered steel	−0.94 %	0.18 %	−1.11 %
Paving asphalt	2.23 %	0.33 %	1.90 %
Paving concrete	11.89 %	0.77 %	11.04 %

With the results obtained from the simulation study, the maximum systematic uncertainty resulting from deviations from the background state assumed in the forward calculation was calculated. Therefore, all uncertainties in Table 6.3 were combined in quadrature, apart from the extreme case of CH_4. The resulting uncertainties were ± 8.0 % for PSF_{CH_4}, ± 11.3 % for PSF_{CO_2} and ± 5.4 % for $PSF_{CH_{4,proxy}}$. This uncertainty described large-scale biases possibly observable over one flight track. The large-scale bias should not be confused with the single pixel precision, which was less than half that value for a bright surface, see Sect. 6.1.1. Neither does this per se limit detection, as, e.g., smoothly changing elevation leads to a gradient in retrieved enhancement, which locally is superimposed by a plume.

However, studying the influence of the different surface types revealed vastly varying biases at AVIRIS-NG spectral resolution. While for rangeland vegetation, entisol, and grey sandstone, only small biases were induced in the individual PSF as well as in $PSF_{CH_{4,proxy}}$, for weathered aluminium, the bias of the individual PSF exceeded 1 %. Nevertheless, the proxy method reduced the bias again below 1 %. For weathered steel, the contrary was true: While the individual PSF were biased by less than 1 %, the proxy increased the bias to slightly over 1 %. For paving asphalt, the bias was already in the order of the retrieval scatter for PSF_{CH_4} and $PSF_{CH_{4,proxy}}$. For barbed goat grass and paving concrete (i.e., limestone), the bias increased to −7 % and 11 %, respectively. It is expected that some biases will be visible in the retrieved column enhancements for at least the last two surface types, but likely for those with biases larger than 1 %, too.

Considering the reflection spectrum of paving concrete (Fig. 6.2), one can observe a wavelength dependency, which is similar to the weighting function of CH_4. A similar pattern is present for barbed goat grass, although it is less noticeable due to the lower mean reflectance. Therefore, surface types with a reflection feature similar to the broadband curvature of the weighting function likely induce the most significant biases. Especially paving concrete can lead to false positive plume detections if one does not consider the color image of the scene. In these color images, the apparent enhancements should be relatable to artificial structures; therefore, false positives can be excluded. Nevertheless, this could mask parts of a plume or

make inverting the plume more difficult. Barbed goat grass, on the other hand, induces a large negative bias. However, this plant grows typically over large areas, and thus it mostly leads to a local negative offset. Nevertheless, surface types not exhibiting a negative bias in such grass fields might appear locally enhanced. In this case, the correlation with a color image must be considered, too.

6.1.3. Low radiance scenes

As shown in the sensitivity study in the previous section, the retrieval accuracy decreased rapidly in low radiance scenes. Examining the retrieved column enhancements from the complete data set under examination, it was obvious that especially over surfaces with low spectral reflectance, which translates to low signal at the detector, the retrieval mostly produced noise. An example for such surfaces are forests and lakes (see Fig. 6.4).

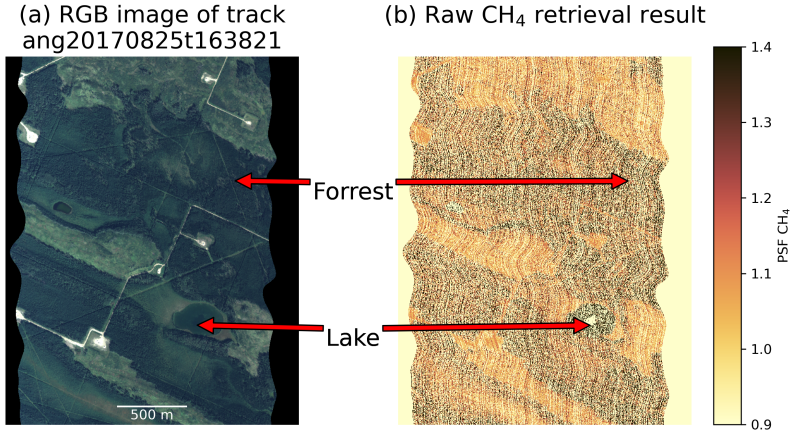

Figure 6.4.: Example for a dark scene in the data set. In panel (b), the raw unfiltered and not destriped PSF_{CH_4} are shown.

These poor fits had to be filtered out, especially those failing due to low radiance. Therefore, the RMS value of each ground scene was plotted against the radiance at 2410 nm in box plots with 0.05 µW cm^{-2} nm^{-1} sr^{-1} wide bins (Fig. 6.5). At radiances below 1.0 µW cm^{-2} nm^{-1} sr^{-1} the fit quality suffered drastically in both the PSF_{CH_4} and the PSF_{CO_2}, which aligned nicely with the findings of Ayasse et al. (2018). They found for synthetic observations that at sensor radiances below 1.0 µW cm^{-2} nm^{-1} sr^{-1} lead to increasingly worse IMAP-DOAS results.

Additionally, retrieval results with an RMS value above 2 % were filtered out to remove the worst outliers. The mean RMS of the fit for non-filtered data was 1.3 %. Interestingly, for radiances around 0.85 µW cm^{-2} nm^{-1} sr^{-1} the RMS spread of the CH_4 fit showed a "bump". The spread might be correlated to surfaces that are relatively bright but whose reflection spectra are correlated with the absorption features of CH_4.

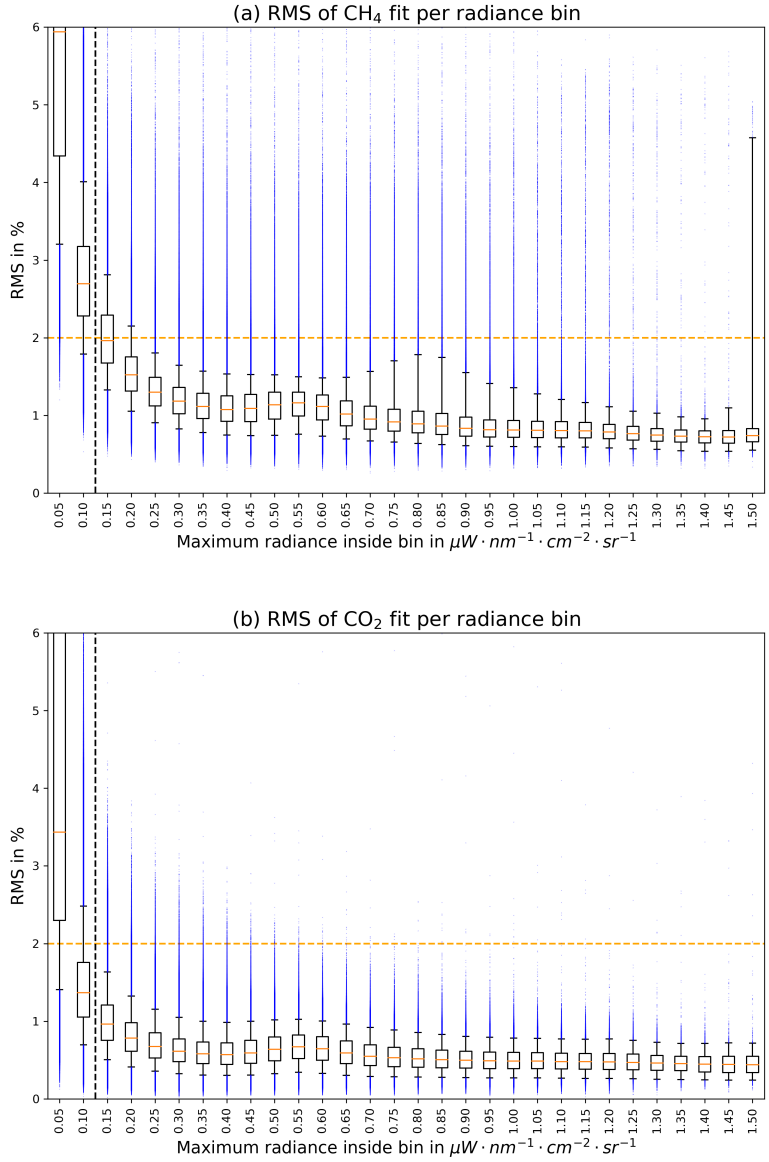

Figure 6.5.: RMS over radiance at 2140 nm, sampled in 0.05 µW cm^{-2} nm^{-1} sr^{-1} wide bins. The boxes cover the first to the third quartile, the whiskers denote the 5th to 95th percentile, and the blue dots mark the outliers outside of the whiskers. The dotted black line marks the 1.0 µW cm^{-2} nm^{-1} sr^{-1} line, the dotted orange line an RMS value of 2 %, which were used as filter values.

6.1.4. Detected plumes

After filtering (Sect. 6.1.3) and destriping (Sect. 5.2.3) of the retrieval results for each flight line, the proxy was applied to the data to reduce the systematic effects, as shown in Sect. 6.1.2. The final $\mathrm{PSF}_{\mathrm{CH_4,proxy}}$ were then plotted as images side by side with RGB images obtained from the radiance data cube and manually inspected for CH_4 plumes. In 10 out of the 13 tracks used for this study, one or multiple plumes were detected. Four plumes were sufficiently well shaped to calculate emissions using the cross-sectional flux method. The other plumes were either too short or faint for the cross-sectional flux method, located near infrastructure interfering with the retrieval results, or simply not consistent during two overflights.

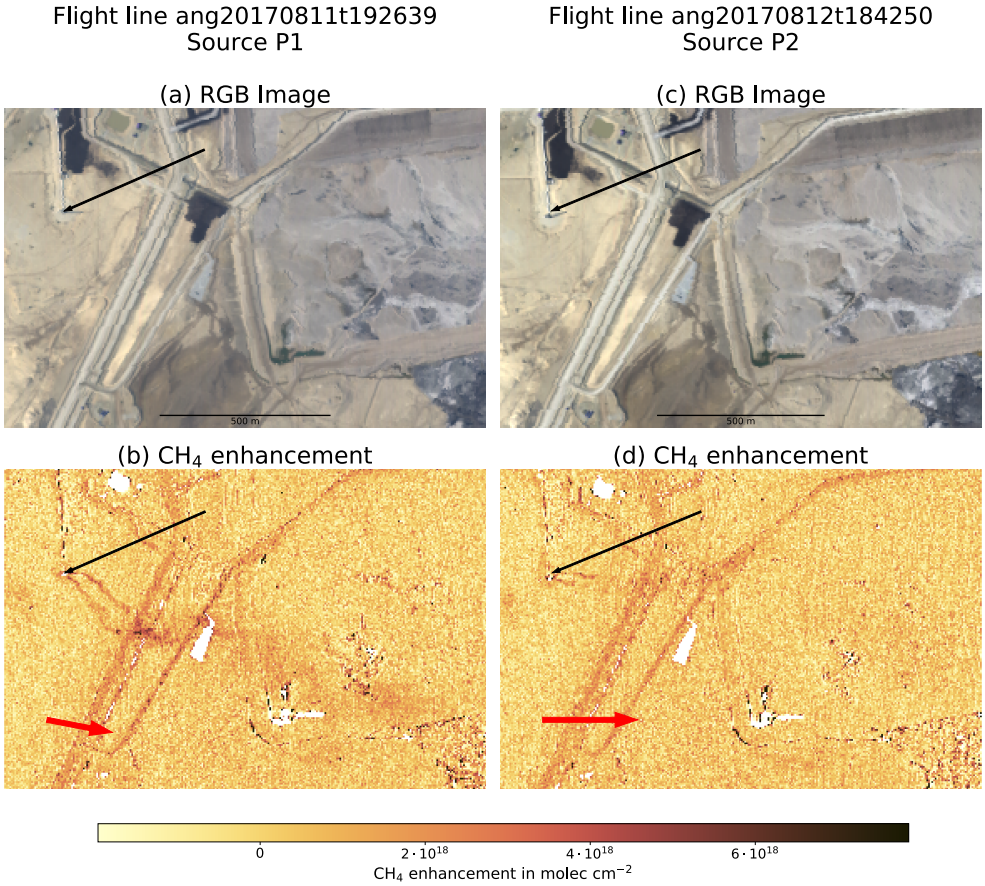

Figure 6.6.: Methane plume originating from a flare at the Fort McMurray oil sand extraction site on two different days (panels (b), (d)) and the according RGB images (panels (a), (c)). The black arrows point to the source, and the red arrows indicate the wind derived from ERA-5 data for comparison with the plume direction. The double plume structure visible in the retrieval results most likely originated from two different light paths transecting the plume only on the way to the surface or after reflection on the ground.

In Fig. 6.6, a well-shaped plume originating from a flare or vent is shown (named in the following P1 and P2). Comparing the RGB image and the retrieval result, systematic biases are observable where roads are present. The plume, however, is not correlated to any structure visible in the RGB images. Additionally, a double plume structure is apparent. While there may be two similarly emitting leaks, this double plume structure is more likely an artifact due to the light paths hitting the detector from different ground scenes and passing the plume only on the way down to the surface or upward to the instrument. The effect is explained in more detail below.

Focussing on the first overflight (panels (a) and (b)), the shadow of the flare goes directly to the right. Therefore, the sunlight comes from the left. With a solar zenith angle of $\sim 42\,^{\circ}$, a ground scene size of $4.9 \times 4.9\,\mathrm{m}^2$, and the shadow of the flare covering ~ 10 ground scenes, this results in a flare height of $\sim 54\,\mathrm{m}$. A plume originating from the top of the flare is narrow at the beginning. Thus, the solar radiation either hits the plume on the way down to the surface and then bypasses the plume after reflection at the surface or only hits the plume after reflection at the surface. Therefore, two plume structures $\sim 50\,\mathrm{m}$ apart from each other are visible near the source. Further down the plume, atmospheric mixing in the atmosphere widens the plume. Then, the solar radiation passes through the plume on both the upward and downward light path, and the double plume structure vanishes.

In Fig. 6.7, well-shaped plumes originating from oil and gas infrastructure are shown (in the following P3 and P4). Although also here the plume crossed a road (panel (b)), or the plume was relatively faint (panel (d)), they were still visible well enough to be considered for the cross-sectional flux method. Especially their very straight extent facilitated the application of the cross-sectional flux method.

In Fig. 6.8 two plumes are shown where the surroundings inhibit the application of the cross-sectional flux method. The first plume originated from a well pad located in a forest. Most of the surrounding data is filtered out due to low radiance. Additionally, the enclosure of the pad due to the forest might have led to the accumulation of methane. Accumulation would simplify the leak detection but result in excessively high emissions in the cross-sectional flux method. The second plume meandered through a facility with oil or gas pipes and several other structures. The plume was channeled through the facility, altering wind speed and direction. Therefore, estimating a representative wind speed and direction for the cross-sectional flux method would be challenging. Additionally, the background was very noisy, and much data was filtered out from the local background. Therefore, estimating the local background needed to determine the enhancements due to emission would be complex.

In Fig. 6.9 two faint plumes observed during consecutive overpasses over two vents or flares at a bitumen extraction site are shown. In Fig. 6.11, methane enhancements at an open cast bituminous coal mine are shown. At the brim (panels (a) - (d)), there seem to be varying emissions, perhaps depending on activity. The enhancements in the middle of the open cast mine are very diffuse and might also be an artifact, although they are not correlated with surface features.

Finally, a plume originating from a coal mine ventilation shaft detected during the Four Corners measurement campaign in 2015 is shown in Fig. 6.10 (in the following P5). This

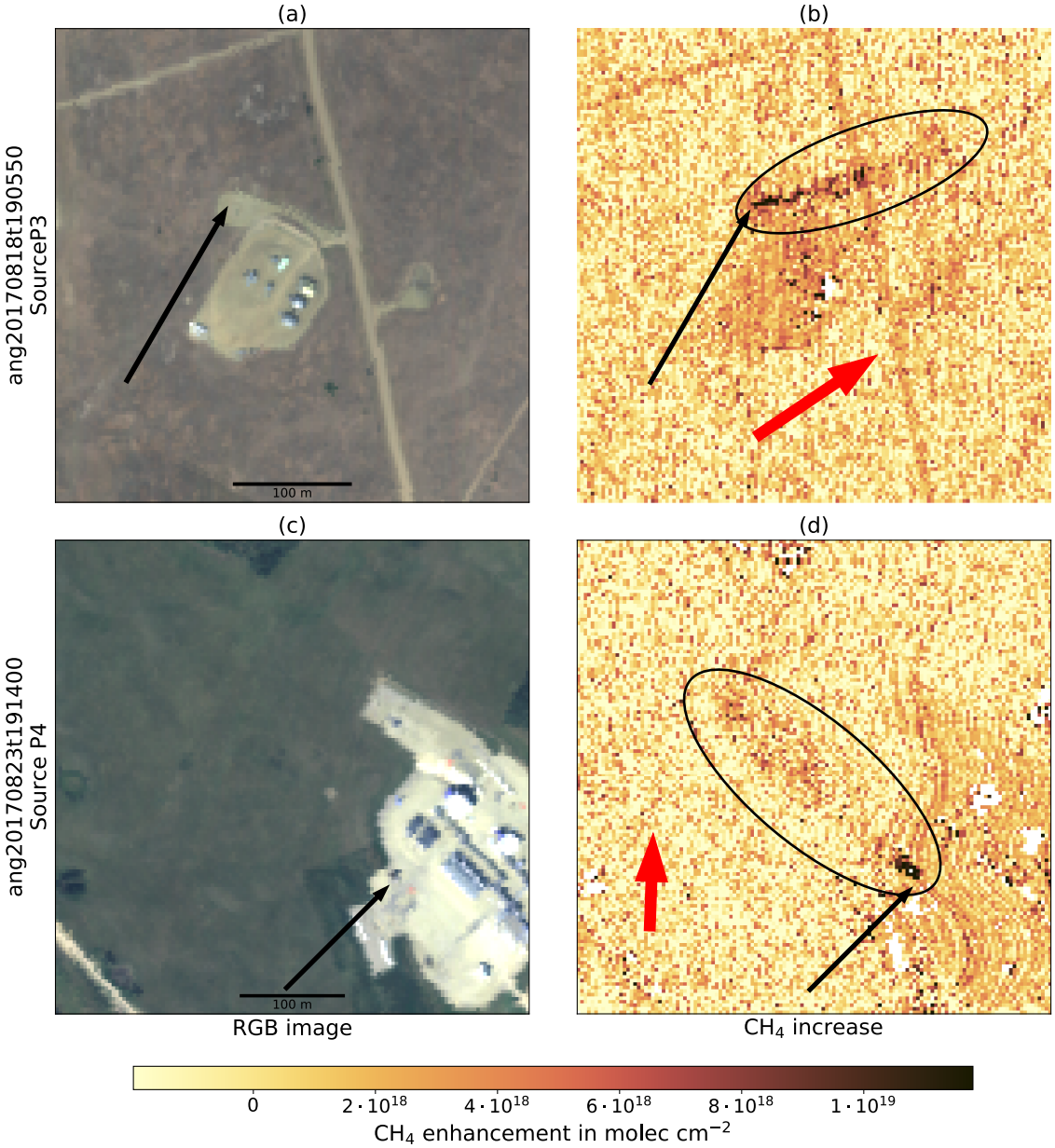

Figure 6.7.: Methane plumes originating from two well pads located west of the Rocky Mountains in Alberta (panels (b), (d)) and the according RGB images (panels (a), (c)). The black arrows point to the source, while the red arrows indicate the wind derived from ERA-5 for comparison with the plume direction. The ellipse additionally highlights the plumes.

plume extends over more than 1 km and shows a relatively straight profile, although it seems as if the plume meanders slightly. Also, the wind direction calculated from ERA-5 reanalysis data does not match the plume direction further downwind of the strongest enhancements.

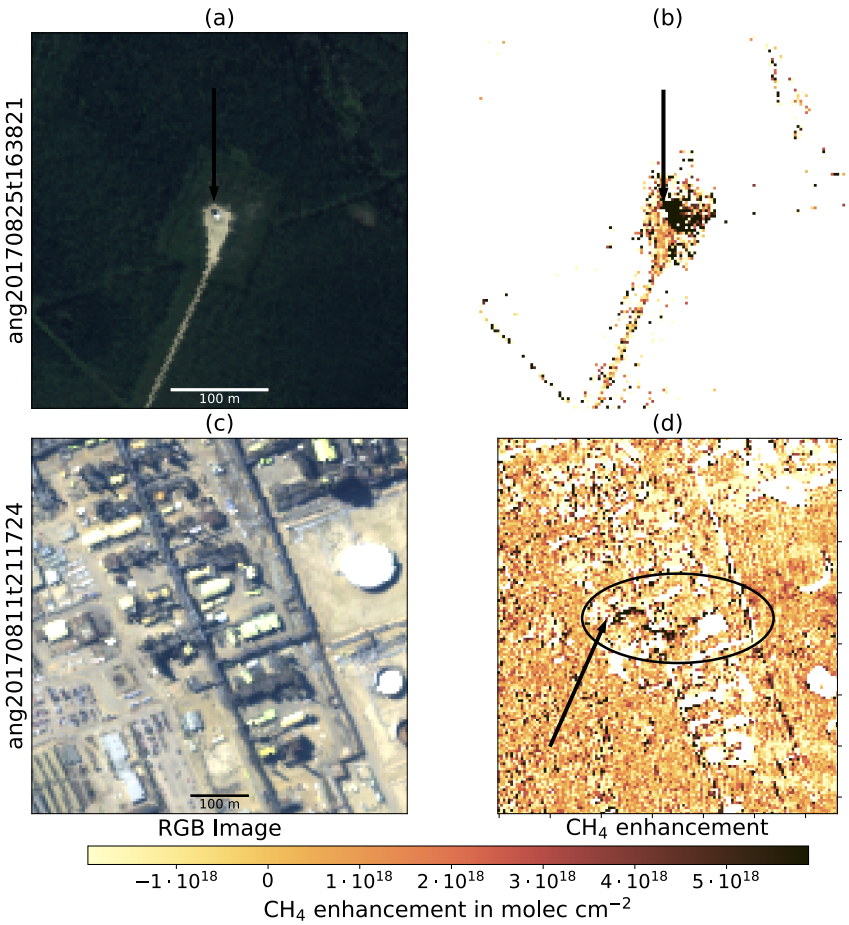

Figure 6.8.: Similar to Fig. 6.7, but for methane enhancements from oil/gas infrastructure. Most results were filtered out due to the low radiance over the forest in panels (a) and (b). In panels (c) and (d), a facility located at a bitumen extraction site is shown.

Finally, nearly no retrieval scatter and only minor biases due to, e.g., roads are visible in this plume.

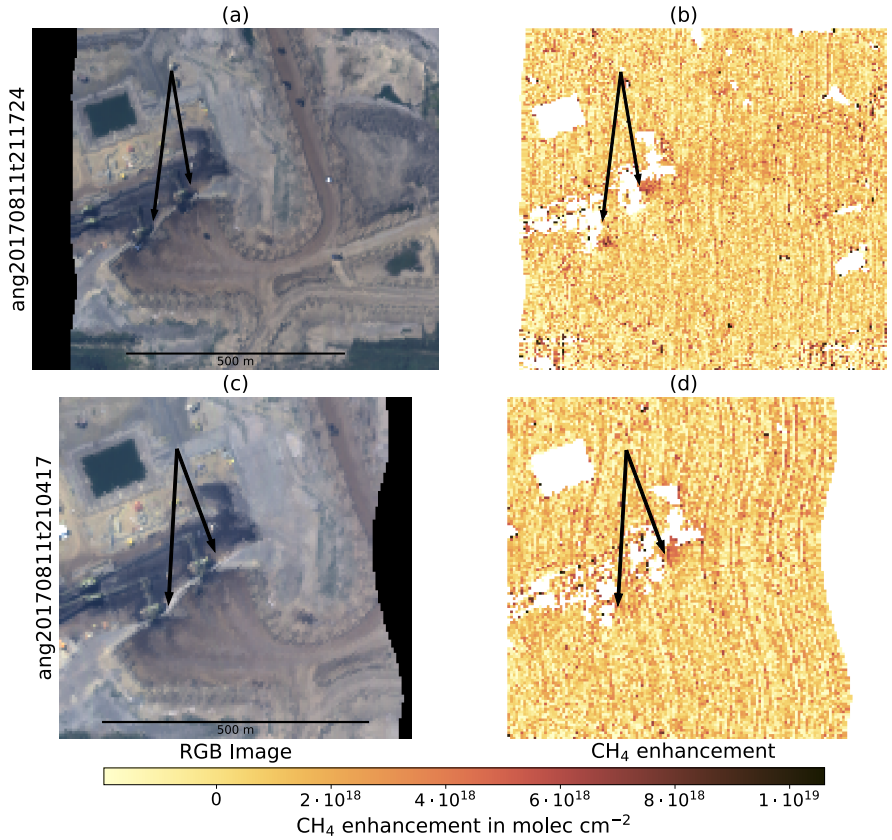

Figure 6.9.: Similar to Fig. 6.7, but for two overflights over vents or flares at a bitumen extraction site nearly 15 minutes apart. The plumes are very faint.

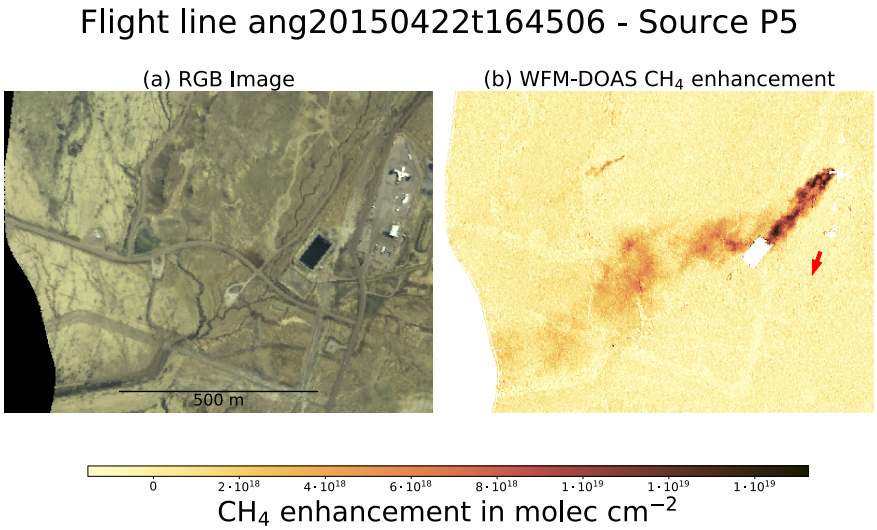

Figure 6.10.: Similar to Fig. 6.7, but for the exhaust plume of a coal mine ventilation shaft observed during a measurement campaign in the Four Corners region.

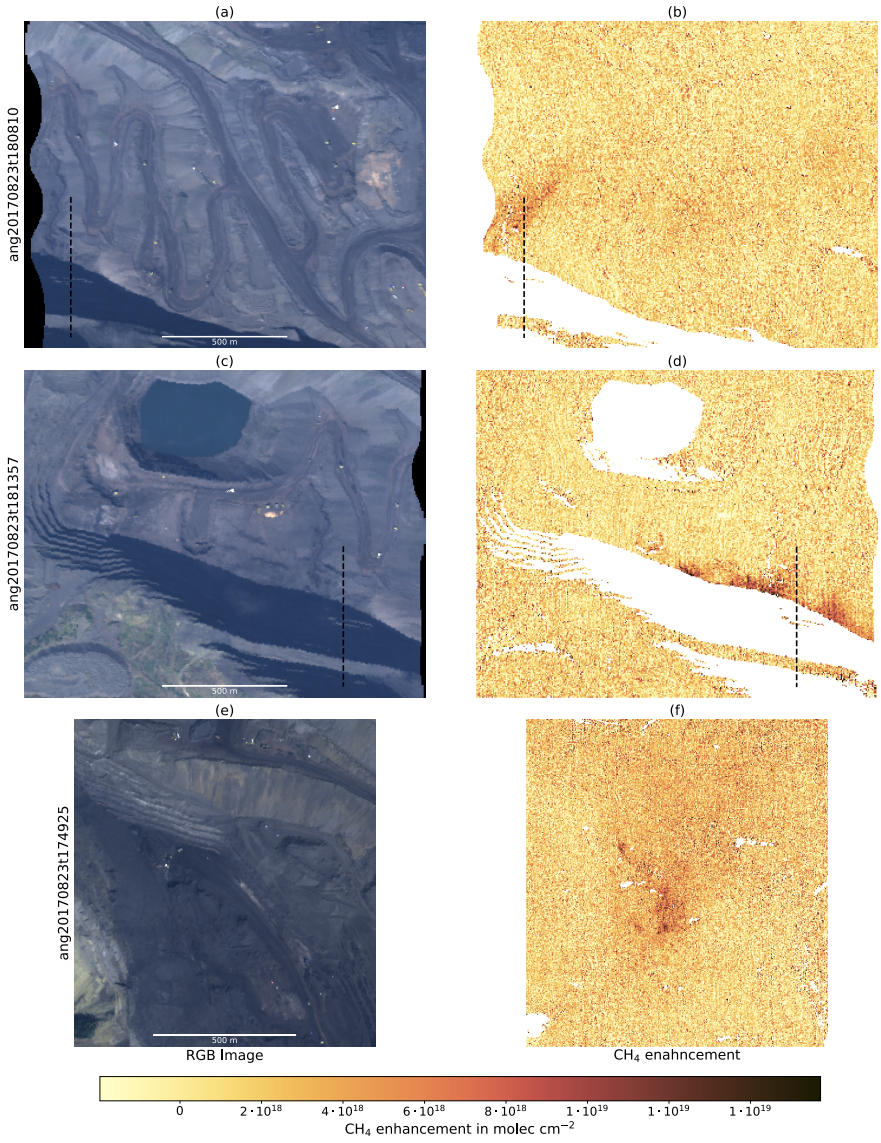

Figure 6.11.: Similar to Fig. 6.7, but for methane enhancements occurring at a bituminous coal extraction site. The upper two rows show subsets of two overpasses ∼ 10 minutes apart. The dashed line is plotted at the same location in all images for comparison. The last row shows enhancements in the middle of the open cast coal mine.

6.1.5. Comparison of WFM-DOAS retrieval results with IMAP-DOAS and MF results

For the five plumes in Fig. 6.6, Fig. 6.7 and Fig. 6.10 the retrieval results were compared to results from a matched filter retrieval (MF, Thompson et al., 2015), which David R. Thompson provided for this purpose. Additionally, the retrieval results of the Four Corners ventilation shaft plume were compared to IMAP-DOAS retrieval results provided by Andrew K. Thorpe.

As the MF and IMAP-DOAS retrieved CH_4 enhancements below the aircraft flying at altitude h_{airc} were provided in ppm · m, they were converted to molec · cm^{-2}:

$$\mathrm{CH}_{4,\mathrm{enh,MF/IMAP}} = \frac{\mathrm{CH}_{4,\mathrm{enh,ppm\ m}}}{h_{\mathrm{airc}}} \cdot \mathrm{subcol}_{\mathrm{tot}} \cdot 10^{-6} \tag{6.154}$$

The total subcolumn below the aircraft $\mathrm{subcol}_{\mathrm{tot}}$ was calculated based on the gas, temperature, and pressure profiles used in the respective WFM-DOAS background simulations. The retrievals were compared in the retrieved enhancements and the retrieval scatter. The latter was estimated as one standard uncertainty ($1\,\sigma$ standard deviation) of the retrieved enhancements over relatively homogeneous areas near the plumes. As can be seen in Table 6.5, for all plumes observed during the ABoVE campaign, the retrieval scatter was lower for WFM-DOAS than for the MF results. The background noise for the Four Corners ventilation shaft plume is similar for all three retrievals, with slightly less noise in the MF results.

Table 6.5.: Comparison of the background noise of the retrievals based on the standard deviation of retrieval results near the plumes. IMAP-DOAS results were present only for the Four Corners ventilation shaft plume. Therefore, the other fields in this row are left empty.

	P1 (molec cm^{-2})	P2 (molec cm^{-2})	P3 (molec cm^{-2})	P4 (molec cm^{-2})	P5 (molec cm^{-2})
WFM-DOAS	$\pm 1.3 \cdot 10^{17}$	$\pm 8.3 \cdot 10^{17}$	$\pm 7.8 \cdot 10^{17}$	$\pm 1.8 \cdot 10^{18}$	$\pm 5.2 \cdot 10^{17}$
MF	$\pm 2.0 \cdot 10^{18}$	$\pm 2.1 \cdot 10^{18}$	$\pm 1.7 \cdot 10^{18}$	$\pm 2.4 \cdot 10^{18}$	$\pm 4.1 \cdot 10^{17}$
IMAP-DOAS					$\pm 5.5 \cdot 10^{17}$

Additionally, the retrieved CH_4 enhancements were compared directly by creating density plots comparing the retrieval results of the central plume area. For the coal mine ventilation shaft plume, the WFM-DOAS retrieval retrieves slightly lower enhancements compared to the IMAP-DOAS retrieval, and slightly higher enhancements than the MF, although all three retrievals show in principle good agreement (see Fig. 6.12).

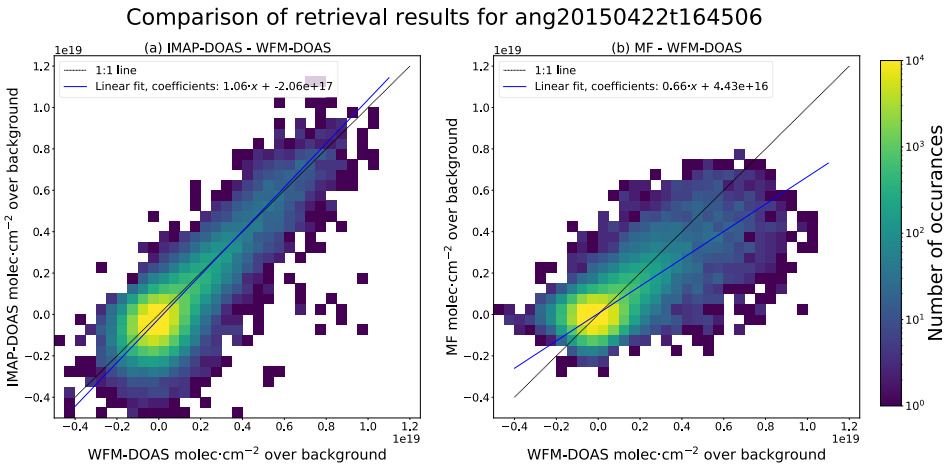

Figure 6.12.: Heat maps of the retrieval results for IMAP-DOAS and WFM-DOAS (panel (a)) and MF and WFM-DOAS (panel (b)) for the coal mine ventilation shaft plume.

For the four additional plumes, MF retrieval results and WFM-DOAS results were compared similarly (see Fig. 6.13). While for one well pad plume (P3) the retrievals seemed to agree at least for higher enhancements, there was a much larger discrepancy between the MF and WFM-DOAS results for the other plumes. Although the retrieval scatter is larger for the MF near those plumes, this alone can not explain this deviation. The root cause is not yet found. However, it might be that using a single target spectrum for the MF retrieval plays a role. Nevertheless, although the absolute values diverge, in principle, both retrievals "see" the enhancement in similar pixels most of the time.

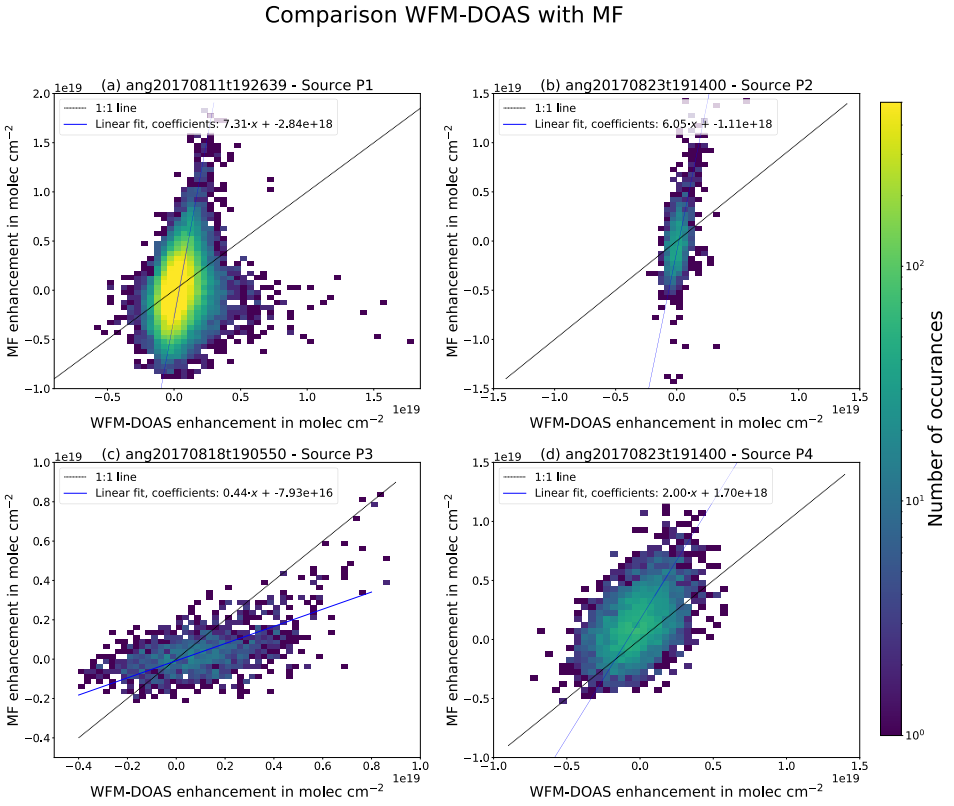

Figure 6.13.: Similar to Fig. 6.12 for four additional plumes, but only for MF and WFM-DOAS.

6.1.6. Emission and uncertainty estimation

The emission and uncertainty estimation was done following the cross-sectional flux method described in Sect. 5.3 with the wind speed data described in Sect. 5.1.1. The cross-sections were selected to be orthogonal to the apparent wind direction. Below, the emission calculation is done exemplarily for P1. All other emissions and uncertainties have been calculated in the same way.

The emission was calculated according to Eq. 5.150. For P1, this resulted in a mean CH_4 emission of $196\,\mathrm{kg\,h^{-1}}$.

Normalizing the enhancements to the local background introduced an uncertainty inside the plume. It was calculated from the error curves of the linear fit to determine the background concentration inside the plume. The uncertainty of the emission derived from this fit uncertainty was $\pm 32\,\mathrm{kg\,h^{-1}}$. The single ground scene precision $\Delta\mathrm{PSF}_{\mathrm{CH_4,proxy}}$ was calculated as the $1\,\sigma$ standard deviation of the local background around the plume. Additional errors due to small variations in CO_2, which might have been co-emitted, but were below the noise in the pure $\mathrm{PSF}_{\mathrm{CO_2}}$ maps were also included. For P1, the ground scene precision was $\sim 3\,\%$ of the background CH_4 column. Combined with the variations in CO_2, this translated to an uncertainty in the final emission of $\pm 15\,\mathrm{kg\,h^{-1}}$. The background column of CH_4 was based on a scaled climatology. To account for uncertainties in the total column of CH_4 at the plume location compared to this climatology, a $\pm 5\,\%$ uncertainty was assumed. For the emission, this translated to an uncertainty of $\pm 10\,\mathrm{kg\,h^{-1}}$.

Weather station data as close as possible to the plume locations was used for the wind estimation. However, these stations only reported hourly wind data and were $5 - 20\,\mathrm{km}$ away from the source. Therefore, an uncertainty of $\pm 1.5\,\mathrm{m\,s^{-1}}$ was assumed. This uncertainty is systematic and could not be reduced by simply averaging over more cross-sections. Therefore, this uncertainty directly translated to an uncertainty of the emission of $\pm 79\,\mathrm{kg\,h^{-1}}$.

The uncertainty due to atmospheric stability was calculated as the $1\,\sigma$ standard deviation of all emissions calculated through the n different cross-sections, divided by $\sqrt{n-1}$. For P1, $n = 61$ and the resulting uncertainty due to atmospheric variability was $\pm 33\,\mathrm{kg\,h^{-1}}$.

The total uncertainty was calculated by combining the single uncertainty terms in quadrature (see Eq. (5.151)). The total uncertainty of the emission for P1 was $\pm 94\,\mathrm{kg\,h^{-1}}$. The contributions of the different uncertainties and the emissions for all examined plumes are listed in Table 6.6.

For nearly all plumes apart from P2, the wind speed uncertainty was one of the most significant contributors to the uncertainty. Additionally, especially for P3 and P4, the ground scene precision contributed nearly as much to the uncertainty. The plumes P1 and P2 originated from the same source, although on different days. The emission estimates for both days overlapped within their uncertainty margins, indicating possibly a relatively constant source, at least for those days. For P2, the atmospheric variability was high due to the plume being quite diluted, which correlates with the higher wind speed on this day.

Table 6.6.: Emission and uncertainty estimation calculated with the cross sectional flux method for the plumes P1 - P5.

	P1	P2	P3
Background normalization	$\pm 32\,\mathrm{kg\,h^{-1}}$ (16 %)	$\pm 27\,\mathrm{kg\,h^{-1}}$ (20 %)	$\pm 65\,\mathrm{kg\,h^{-1}}$ (41 %)
Background total column	$\pm 10\,\mathrm{kg\,h^{-1}}$ (5 %)	$\pm 7\,\mathrm{kg\,h^{-1}}$ (5 %)	$\pm 8\,\mathrm{kg\,h^{-1}}$ (5 %)
Ground scene precision	$\pm 15\,\mathrm{kg\,h^{-1}}$ (8 %)	$\pm 21\,\mathrm{kg\,h^{-1}}$ (16 %)	$\pm 18\,\mathrm{kg\,h^{-1}}$ (11 %)
Wind speed	$\pm 79\,\mathrm{kg\,h^{-1}}$ (40 %)	$\pm 26\,\mathrm{kg\,h^{-1}}$ (20 %)	$\pm 60\,\mathrm{kg\,h^{-1}}$ (38 %)
Atmospheric variability	$\pm 33\,\mathrm{kg\,h^{-1}}$ (17 %)	$\pm 42\,\mathrm{kg\,h^{-1}}$ (32 %)	$\pm 36\,\mathrm{kg\,h^{-1}}$ (23 %)
Total emission	$196\,\mathrm{kg\,h^{-1}}$	$132\,\mathrm{kg\,h^{-1}}$	$157\,\mathrm{kg\,h^{-1}}$
Total uncertainty	$\pm 94\,\mathrm{kg\,h^{-1}}$ (48 %)	$\pm 61\,\mathrm{kg\,h^{-1}}$ (46 %)	$\pm 98\,\mathrm{kg\,h^{-1}}$ (62 %)

	P4	P5
Background normalization	$\pm 71\,\mathrm{kg\,h^{-1}}$ (35 %)	$\pm 21\,\mathrm{kg\,h^{-1}}$ (2 %)
Background total column	$\pm 10\,\mathrm{kg\,h^{-1}}$ (5 %)	$\pm 61\,\mathrm{kg\,h^{-1}}$ (5 %)
Ground scene precision	$\pm 12\,\mathrm{kg\,h^{-1}}$ (6 %)	$\pm 18\,\mathrm{kg\,h^{-1}}$ (1 %)
Wind speed	$\pm 73\,\mathrm{kg\,h^{-1}}$ (36 %)	$\pm 447\,\mathrm{kg\,h^{-1}}$ (37 %)
Atmospheric variability	$\pm 34\,\mathrm{kg\,h^{-1}}$ (17 %)	$\pm 43\,\mathrm{kg\,h^{-1}}$ (4 %)
Total emission	$204\,\mathrm{kg\,h^{-1}}$	$1220\,\mathrm{kg\,h^{-1}}$
Total uncertainty	$\pm 108\,\mathrm{kg\,h^{-1}}$ (53 %)	$\pm 450\,\mathrm{kg\,h^{-1}}$ (37 %)

6.1.7. Assessment of WFM-DOAS retrieval method applied to AVIRIS-NG data

The WFM-DOAS retrieval method provided an efficient and accurate way to handle AVIRIS-NG data quantitatively; applying the WFM-DOAS method to lower spectral resolution data was successful. The WFM-DOAS retrieval applied to the strong fit window produced in nearly all scenes investigated less background noise than the fast, statistical matched filter approach (Sect. 6.1.5). However, over dark surfaces, e.g., forests or lakes, the WFM-DOAS retrieval could not retrieve meaningful results. The according scenes were consequentially filtered out in the retrieval results (Sect. 6.1.3). For surfaces with spectral albedo similar to the absorption of CH_4 at the spectral resolution of $\sim 6\,\mathrm{nm}$, biases were introduced to the retrieved column enhancements, which resulted in residual structures such as paved roads or other anthropogenic structures being observable in the retrieval results. These persisted even after applying the $CH_4(CO_2)$ proxy method (Sect. 6.1.2 and 6.1.4).

Several plumes could be detected in the scenes investigated. Five of these plumes were suitable to be inverted using the cross-sectional flux method (Sect. 6.1.6). Although the wind speed was a significant contributor to the flux uncertainty, depending on the surface type surrounding the plumes also the normalization to the local background and the atmospheric variability contributed strongly to the uncertainty.

6.2. Results acquired with MAMAP2D-Light

For the MAMAP2D-Light instrument, due to its spectral similarities with the SWIR channel of the MAMAP instrument and the narrower wavelength range compared to AVIRIS-NG, the retrieval of choice was the WFM-DOAS retrieval. However, to apply the WFM-DOAS retrieval to the acquired data, the MAMAP2D-Light instrument needed to be calibrated. The basic calibration of the instrument is described in Sect. 6.2.1. In Sect. 6.2.2, the first measurement flight over the power plant Jänschwalde is analyzed, and the power plant emission is estimated.

6.2.1. Characterization of the MAMAP2D-Light instrument

The MAMAP2D-Light instrument was initially characterized using the laboratory setup shown in Fig. 5.5. The main spectral characteristics of the MAMAP2D-Light instrument are given in Table 6.7, which is a subset of Table 5.1.

Table 6.7.: Main characteristics of the MAMAP2D-Light instrument. The typical spatial resolution is given for a flight altitude of $\sim 1500\,\mathrm{m}$. It is an excerpt of Table 5.1.

Parameter	**MAMAP2D-Light**
Spectral range	$1559.54 - 1690.05\,\mathrm{nm}$
Spectral sampling	$0.34\,\mathrm{nm}$
Spectral resolution	$1.08\,\mathrm{nm}$
# of spectral points	384 pixels
# of FOV	28
Spatial resolution (across x along-track)	$22 \times 6\,\mathrm{m}^2$
SNR	~ 760 (at 33000 BU)

This characterization comprised the creation of a pixel mask to flag defective detector pixels, the wavelength characterization of the middle fiber, and the initial characterization of the ISRF of the instrument. Additionally, the first measurement flight was analyzed to estimate the thermal dark current changes during the flight, the wavelength grid for each fiber, and the signal-to-noise ratio of MAMAP2D-Light.

Creation of pixel mask A set of white light measurements were conducted to determine defective pixels. The measurement setup is described in Sect. 5.1.3.2. The white light measurements comprised the following measurement configurations: illuminated white light source and open shutter ("white light measurement"), closed shutter ("shutter measurement"), and open shutter measurements with the white light source switched off ("lid measurement"). The LASER was turned off during these measurements. For each configuration, 1000 spectra were recorded. The integration time was 75 ms, leading to a detector filling of approximately 40000 BU or roughly 66 % of the full well capacity.

During the measurements, an offset between the lid and shutter measurements (both dark current measurements) was discovered. More precisely, the dark current derived from the shutter measurements was significantly (several hundred BU) higher than in the lid measurements. One possible explanation was additional thermal emission due to the black shutter blades compared to the blank aluminum of the shutter mounting structure. As the shutter is open during the measurements, the dark currents obtained with a closed shutter could only be used for stability monitoring, but not directly as in-flight dark current, which is subtracted from the measurements. The effect was further analyzed in Sect. 6.2.2 with data from the Jänschwalde power plant observations. Therefore, only the lid and white light source measurements were used for the pixel mask definition.

Five criteria were used for the definition of dead or bad pixels. First, all pixels in the first two detector rows were filtered out. This is because in the lab and after mounting the instrument in the wing pod, these rows belonged to a fiber only partly projected onto the detector. Also, in the second row, 32 detector pixels are replaced by annotated data. Additionally, all pixels fulfilling at least one of the following criteria were filtered out:

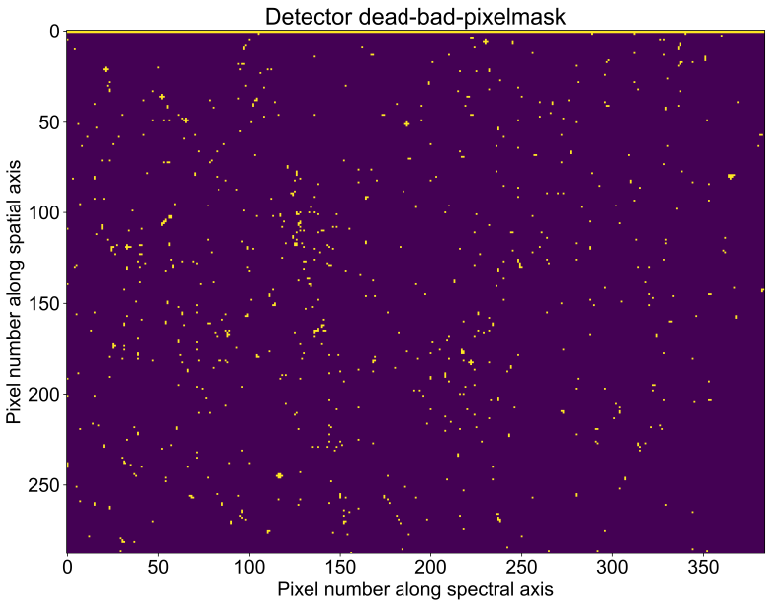

Figure 6.14.: Defective pixel mask of the MAMAP2D-Light detector. In total 1615 pixels ($\sim 1.46\,\%$ of the pixels) were flagged as bad.

1. A deviation of the standard deviation greater than $\pm 30\,\%$ from the median standard deviation in the "lid measurement"
2. A dark current lower than 3500 BU in the "lid measurement"
3. A signal higher than 51000 BU or less than 7500 BU in the "white light measurement"

4. A deviation of more than 1500 BU from a 3rd order polynomial fit along a detector row in the "lid measurement"

The first criterion filtered out pixels with significantly larger noise than most of the pixels. These pixels would lower the SNR in the measurements if not removed. The second and third criteria filtered out (nearly) dead pixels and most of the pixels with a much higher response to illumination than most pixels ("hot pixels"). The first three criteria were applied to all detector pixels.

For evaluating the fourth criterion, only pixels not filtered out by the three criteria before were considered. This criterion filtered out pixels behaving slightly more unusual than the others. The threshold and the order of the polynomial were tuned that the filter did not filter out broader structures across the detector but also no unusual structures like strong dips or peaks were visible when plotting the detector rows as line plots. The resulting pixel mask is shown in Fig. 6.14. In total, 1.46 % of the pixels were flagged as defective pixels.

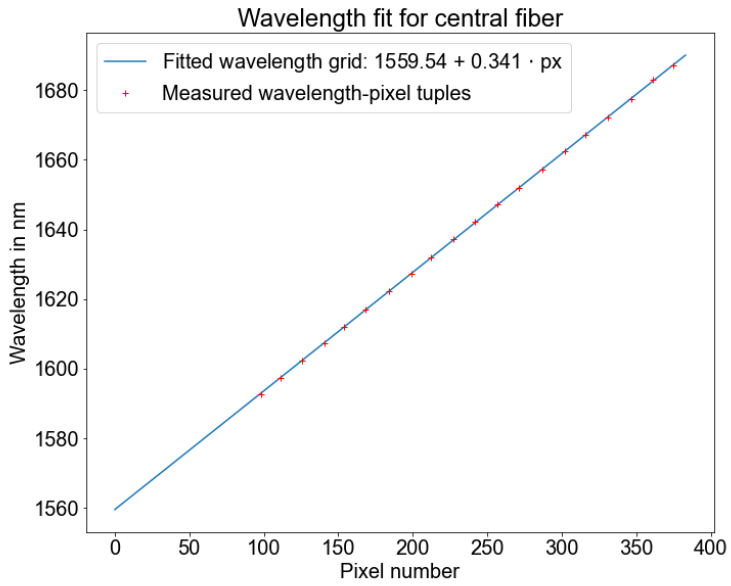

Figure 6.15.: Wavelength calibration results for the MAMAP2D-Light instrument. The middle spatial fiber was characterized. The crosses are the measured points, while the dotted line shows the wavelength grid over the detector. No measurements are present below 1590 nm, as the LASER was not tunable below that value.

Wavelength calibration For the wavelength calibration, the white light source was turned off, and the instrument response was recorded for 20 different wavelengths of the detector, ranging from 1592.70 nm to 1678.16 nm. For each wavelength, 100 spectra were recorded to increase the signal-to-noise ratio. The integration time was 20 ms, not to exceed a maximum

detector count of 40000 BU. These spectra were binned for each wavelength, and the central fiber was extracted and binned along the spatial axis. After filtering out defective pixels, the LASER wavelength was assigned to the pixel with the maximum detector signal. Finally, a linear function was fitted to the wavelength over pixel data to obtain wavelength values for each pixel. The measurements and the fitted curve are shown in Fig. 6.15. A linear fit was chosen as it captured the wavelength dependence well enough. Higher order fits would lead to large differences on the lower end of the wavelength range, where the grid had to be extrapolated beyond the lowest LASER wavelength by $\sim 40\,\text{nm}$, without improving the fit significantly where measurements were taken. The final wavelength grid ranged from 1559.54 nm to 1690.05 nm with a spectral sampling of 0.341 nm.

As simplification and due to the current status of the retrieval software not allowing for separate wavelength grids for different fibers, the wavelength grid for the middle fiber was used for all fibers. Differences between the fibers were accounted for by fiber-specific shift and squeeze parameters, which modify the wavelength grid during the retrieval and were adjusted for each flight.

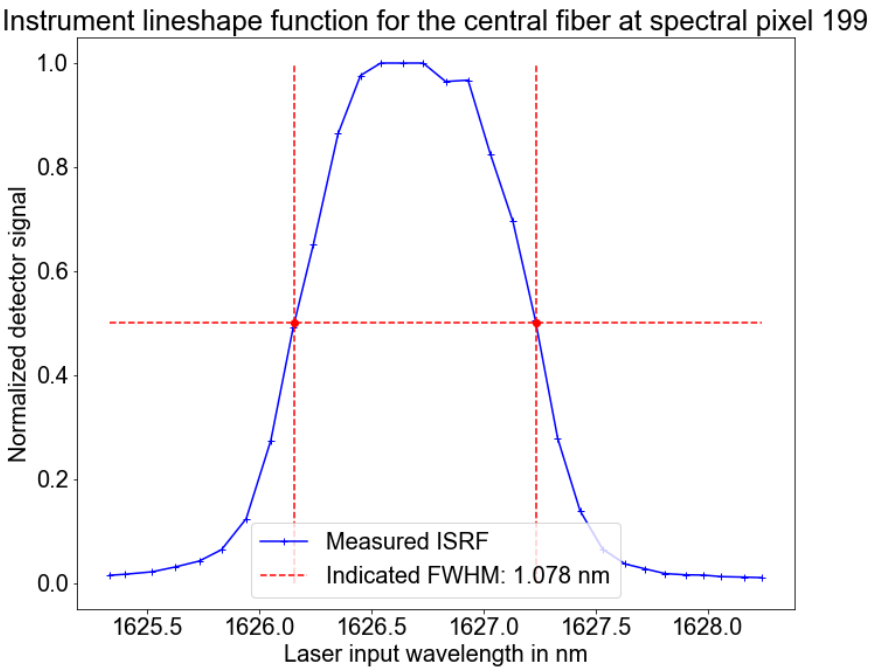

Figure 6.16.: Instrument spectral response function of the MAMAP2D-Light instrument in the central fiber at the spectral pixel 199 (of 384). The measured ISRF is blue, while the red dotted lines show the full width at half maximum.

Determination of ISRF Currently, the WFM-DOAS retrieval does not support measured ISRF shapes. Therefore, the ISRF of MAMAP2D-Light was measured for a central spectral

pixel in the central fiber and later slightly adjusted in the retrieval. 30 LASER measurements covering the wavelength range of $1625.33 - 1628.24\,\mathrm{nm}$ in $\sim 0.1\,\mathrm{nm}$ steps were acquired and dark current and gain corrected. Then, each measurement at each wavelength was normalized to its maximum, and the response of the 199th spectral pixel (at $\sim 1626.6\,\mathrm{nm}$) was examined. At this pixel, an FWHM of 1.08 nm was measured (see Fig. 6.16). The slit function shows a flat top with relatively sharp flanks. However, as the slit function changed slightly across the detector and the PyWFM-DOAS retrieval only supported gaussian or double gaussian slit functions, a gaussian slit function with $FWHM = 1.08\,\mathrm{nm}$ was assumed as the initial guess for the retrieval. The spectral calibration was also adapted with in-flight data, which is described in the next section in more detail.

In-flight dark current correction The raw digital numbers acquired during the measurement flight over the power plant Jänschwalde (Sect. 5.1.3.3) had to be corrected for the dark current and linearity. Therefore, the dark current was subtracted from the measurements. The dark current corrected measurements were then divided by a white light spectrum recorded prior to the flight. However, as already noticed while characterizing the instrument in the lab, the dark current obtained with a closed shutter was $\sim 380\,\mathrm{BU}$ higher than the dark current obtained with an open shutter and a lid on the front lens. Dark current spectra were recorded regularly during the flight by closing the shutter. However, those measurements would give a too high dark current, which would introduce an additive offset to the measurements. Therefore, the possibility of using the dark current recorded on the ground with an open shutter and a closed lid was investigated. The influence of higher temperature during the flight shifting the dark current could be mimicked by adding an offset to the "lid measurements". The magnitude of the offset could be estimated by comparing the dark current "shutter measurements" during the flight with the "shutter measurements" acquired on the ground during the calibration measurements.

This correction assumes that the temperature and, therefore, the dark current in the instrument must not change much during the flight. Therefore all dark current measurements during the flight were taken, the average signal over the detector was calculated, and these values were displayed over flight time. This is shown in Fig. 6.17.

Briefly after the start, the instrument was still relatively hot (visible from the relatively high dark current). However, it quickly cooled down during the transfer flight and was not heated so much during the rest of the flight that it heavily influenced the dark current. During the measurements over the power plant plume, the instrument heated up a bit, most likely due to the sun rising higher. However, the dark current was only shifted by about eight binary units. This is smaller than the 1-sigma standard deviation of the dark spectra of ~ 17 binary units and nearly constant over the flight.

Additionally, the mean signal of the shutter measurements during calibration and the flight only differed by ten binary units. Therefore, the lid measurements acquired on the ground were taken for the dark current correction. In addition, an offset of 10 binary units was added to the lid measurements to represent the slight change observable in the shutter measurements (6.17).

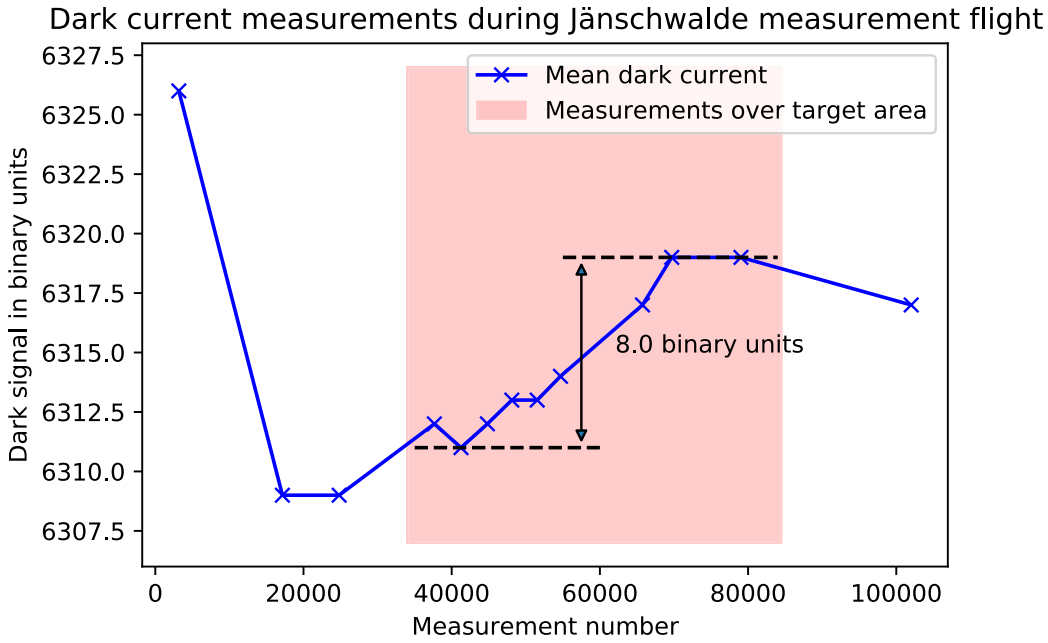

Figure 6.17.: Dark currents recorded during the measurement flight over the power plant Jänschwalde. The red-shaded area denotes the measurements over the power plant. Before and after are dark current measurements acquired during the flights from the airport to the measurement area and back. The arrow marks the maximum difference in dark current during the remote sensing measurements.

Wavelength and ISRF calibration correction From the calibration in Sect. 6.2.1, a fixed FWHM and wavelength grid for the whole detector was used as a first guess in the retrieval. The calibration for each fiber and fit window was adjusted with actual measurements acquired during the flight. Therefore, a subset of 20 measurements over a homogeneous surface across the whole flight line was selected. Then, the initial FWHM was set to 1.08 nm, and the initial shift and squeeze parameters for the wavelength grid were set to zero. Next, a series of retrievals was run on this subset for each fit window, iteratively improving the wavelength shift and squeeze parameters and the FWHM for each fiber in the following order: First, the wavelength shift was fitted. With the adapted shift, the FWHM was refined, then the linear wavelength squeeze, and, afterward, a quadratic squeeze was fitted for the CH_4 fit window. Finally, a combined fit of all parameters other than the FWHM was run for fine-tuning. In the final retrieval over the whole flight, only the wavelength shift remained a free fit parameter for the wavelength calibration. A sample spectrum including the fit and the resulting residuum is shown in Fig. 6.18. The residuals show mostly noise, especially inside the absorption lines. The large negative residual in (c) is likely caused by a defective pixel not filtered out.

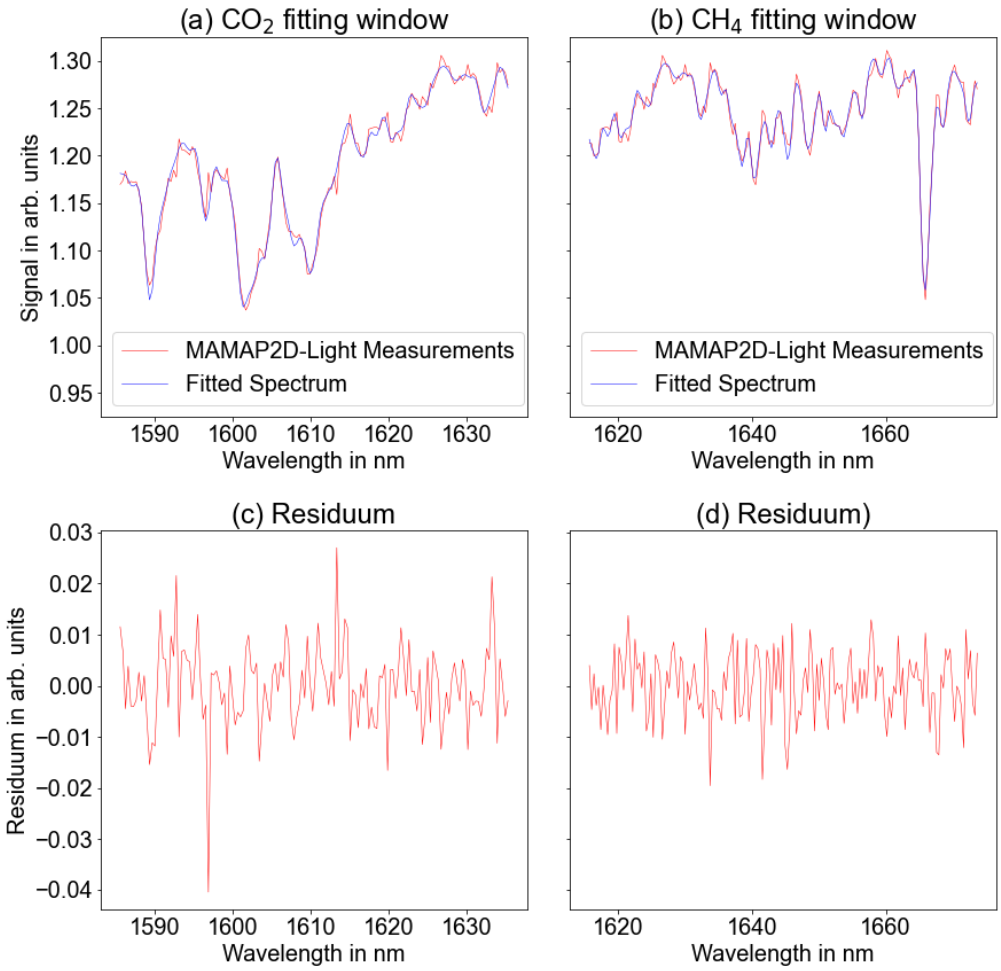

Figure 6.18.: Example spectrum of MAMAP2D-Light with the respective fitted spectra for CO_2 (a) and CH_4 (b). The residuals, i.e., fitted minus measured spectra, are shown in (c) and (d).

Estimation of in-flight signal-to-noise ratio An important measure of the performance of an instrument is the signal-to-noise ratio (SNR). To estimate the SNR for MAMAP2D-Light, a similar approach as for MAMAP in Gerilowski et al. (2011) was taken. Therefore, the retrieval was run on a small subset of the whole measurement flight, which covered a homogeneous surface [1] with a detector filling around $\sim 50\,\%$. In addition to the total RMS, the spectral residuum $\Delta I(\lambda)$ 5.94 was recorded. The instrument SNR estimated from the

[1] in this case some agricultural area

measurements was then calculated from the $\Delta I(\lambda)$ as follows:

$$\mathrm{SNR}_{ret,i} = SD\Big(\Delta I_i(\lambda) - \overline{\Delta I_{i=1,\dots,N}(\lambda)}\Big) \tag{6.155}$$

$$\mathrm{SNR}_{ret} = \overline{\frac{1}{\mathrm{SNR}_{ret,i}}}. \tag{6.156}$$

An index i denotes a value for one single measurement, an overline denotes the mean of the value, and the $1\,\sigma$ standard deviation of a variable x is noted as $SD(x)$.

Only residuals over surfaces with a dark signal corrected detector filling between 32500 and 33500 BU were considered to evaluate the measured SNR. This was a compromise between a mean SNR_{ret} better comparable to theoretical calculations based on detector filling and enough data points for robust estimation. The SNR estimated over 2680 measurements in this way was 751 ± 64 when estimated from the CH_4 fit retrieval results, and 739 ± 68 when estimated from the CO_2 retrieval results.

The theoretical SNR can be estimated from the signal in electrons I_{el} and the detector readout noise $\mathrm{noise}_{\mathrm{readout}}$, taking into account that for each spectrum, due to the optical fiber, five detector rows were binned before the retrieval:

$$\mathrm{SNR}_{theo} = \frac{I_{el}}{\sqrt{I_{el} + \mathrm{noise}^2_{\mathrm{readout}}}} \cdot \sqrt{5} \tag{6.157}$$

For a detector filling of 33000 BU, this results in a theoretical SNR of ~ 910. Although close, it is slightly higher than the SNR estimated from the measurements. Differences could occur from additional pseudo-noise in the retrieval, e.g., due to stray light, which was not characterized as part of this thesis. It will be characterized in a follow-up calibration campaign.

6.2.2. Emission estimation of the Jänschwalde power plant on 17.06.2021

CO_2 column enhancements were retrieved with the WFM-DOAS method (Sect. 5.2.1) from the data set acquired over the coal-fired power plant Jänschwalde with the MAMAP2D-Light instrument in June 2021. The raw retrieval results were filtered for bad fits via an RMS filter rejecting retrieval results with $RMS > 1.0$ (Eq. 5.95). This mostly filtered out scenes with low at-sensor signal, especially lakes, and the water vapor clouds directly at the cooling towers. In a second step, the retrieved and RMS-filtered profile scaling factors were plotted over the mean dark signal corrected binary units in the continuum between 1620 nm and 1623 nm as a measure of detector filling. For low and very high detector signals, the retrieval seemed to perform worse. Therefore, those dark ($BU < 6500$) and very bright ($BU > 49000$) ground scenes were filtered out, too (see Fig. 6.19). The flight over the power plant without the turns contained nearly 700000 ground scenes. The RMS filter filtered out 56175 (or 8.1 %) of all pixels, while the signal filter filtered out additional 10644 ground scenes (or an additional 1.5 %). These additionally filtered ground scenes are mostly located at the border of lakes. After filtering, the mean RMS across all valid measurements was $RMS = 0.54\,\%$.

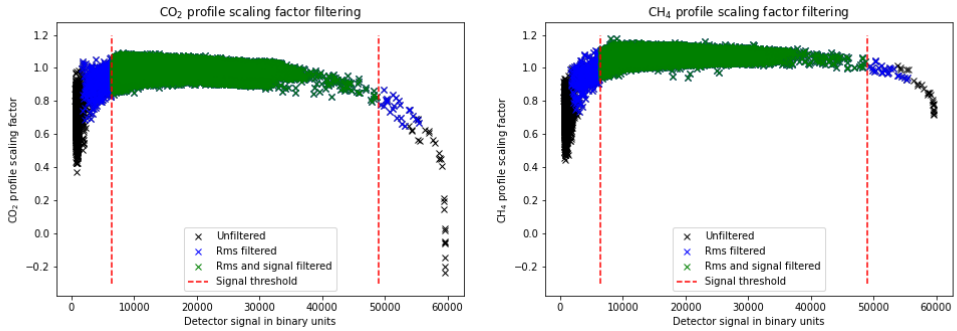

Figure 6.19.: Filtering of the upwind track due to RMS and signal strength. This filtered out non-linear parts of the detector filling and bad fit results. The same filtering was done for the whole data set.

The final data set still showed a slight dependency of the profile scaling factor from the detector filling. To get rid of this remaining dependency, a second order polynomial was fitted to the data (similar to the procedure done by Krautwurst et al., 2017), and the profile scaling factors were then divided by this polynomial, which resulted in the data shown in Fig. 6.20 for the whole data set.

After this correction, the 2d images of the cross-tracks still showed a remaining striping effect. Normalizing each viewing direction to its median for destriping did not consistently remove the striping. Therefore, each pixel was normalized to the median of the surrounding 1500 pixels for each viewing direction.

In Fig. 6.21 the resulting map of CO_2 after application of the proxy and subsequent filtering and corrections is shown. The orthorectification of the data was implemented and performed

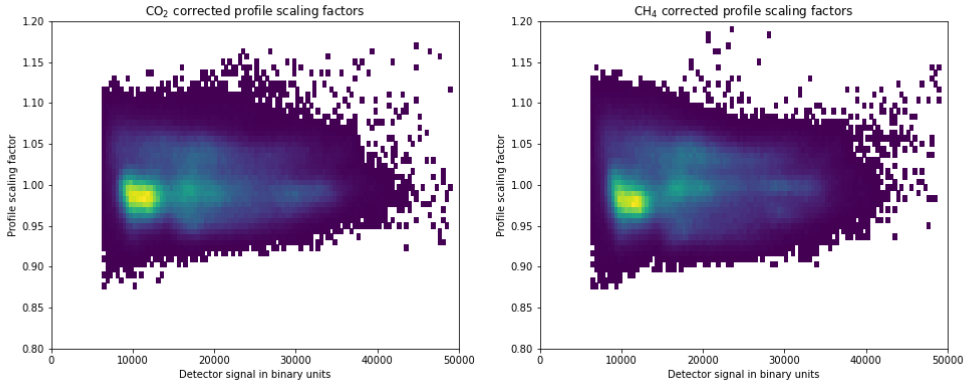

Figure 6.20.: Data set after correction for signal dependency of the retrieval results.

by Sven Krautwurst. The power plant is on the right, and the emission plume is visible up to the second last track. Even in the last track, one can imagine a small signal. The color scale covers total column enhancements of $\pm 2.7\,\%$.

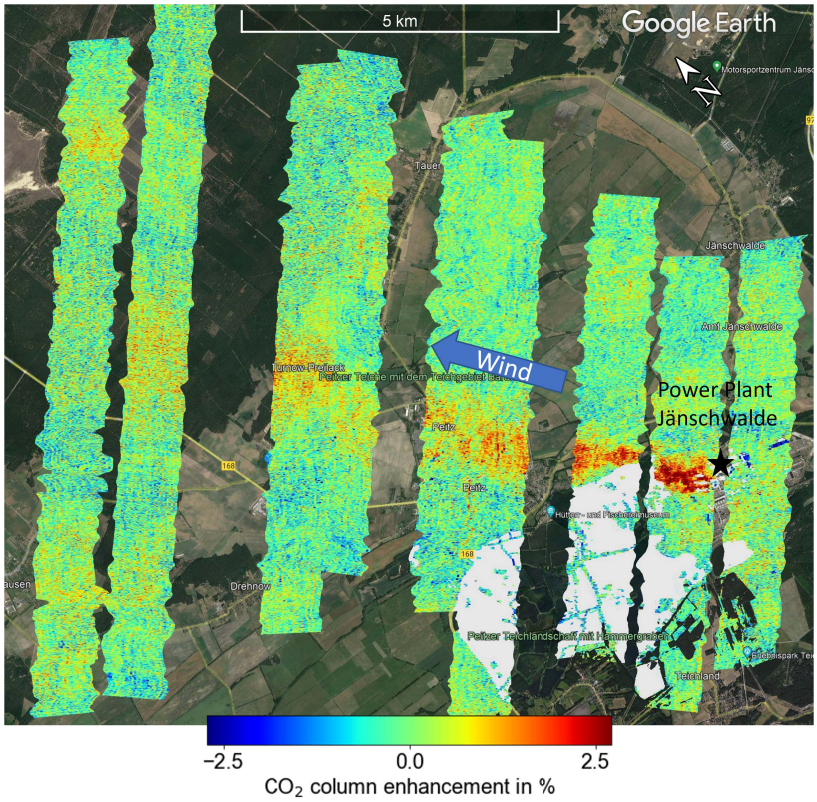

Figure 6.21.: Image of the power plant plume of Jänschwalde. The CO_2 enhancements are visible in a nice plume shape until the second last flight track.

For the emission estimation, the non-orthorectified retrieval results were binned to 100 × 100 m ground scenes for each flight line. This reduced the noise still present in the data, which was about ± 0.70 % over the whole background. Furthermore, it averaged over the small movements of the aircraft. The resulting noise of the binned data was ± 0.28 %.

The cross-sectional flux method (see Sect. 5.3) was applied to each binned column of the retrieved flight tracks across the plume. The cross-sections for all binned viewing directions for each cross-track are shown in the appendix in Sect. A.2. The wind speed was estimated from ERA5 reanalysis data, which were averaged over the measurement area and the boundary layer during the overflight. The average wind direction was estimated from the apparent plume direction. The background CO_2 column was estimated using the SLIM model (see Sect. 5.1.3.3 for all input data).

The emission of the power plant Jänschwalde estimated from MAMAP2D-Light data was 10.3 ± 1.8 Mt CO_2 yr^{-1}. The uncertainty was the combined uncertainty of the emission estimation components, see Eq. 5.151. In the following, the single contributions to the combined uncertainty are given. These are grouped into three blocks, similar to the uncertainty estimation from AVIRIS-NG data (Sect. 6.1.6): First, the uncertainties due to the calculation of the enhancement above background; second, the wind-related uncertainties; third, the uncertainty due to atmospheric variability.

In the first block, the uncertainty due to the normalization of the enhancements to the background was calculated from the error curves of the linear fit for each ground scene integrated over the plume. This introduced a flux uncertainty of ± 0.22 Mt CO_2 yr^{-1} (2 %). The next uncertainty source was the assumed background column of CO_2. As the background was estimated from the SLIM model, which is quite coarsely sampled, this might have deviated from the true local column during the overflight. To estimate an upper bound, an uncertainty of ± 5 % was assumed for the background column, leading to a flux uncertainty ± 0.48 Mt CO_2 yr^{-1} (5 %) due to the assumed background column. Finally, the uncertainty of MAMAP2D-Light column enhancement retrieval results was estimated as the 1 σ standard deviation of the retrieval results outside of the plume. The flux uncertainty due to the measurement and retrieval noise estimated in this way of the binned retrieval results was ± 0.14 Mt CO_2 yr^{-1} (1 %).

In the second block of uncertainties, the wind speed was estimated using the ERA5 reanalysis product and averaged over the planetary boundary layer. This assumed that the plume was well mixed in the boundary layer, which is mostly true further away from the power plant. Especially near the power plant, the plume is located only around the height of the stacks. Therefore, the 1-sigma standard deviation of the wind speed across the boundary layer was used to estimate the wind speed uncertainty. The resulting wind speed uncertainty was ± 0.8 m s^{-1}, which converted to a flux uncertainty of ± 1.6 Mt CO_2 yr^{-1} (16 %) due to the wind speed. The wind direction perpendicular to each flight track was estimated from Google Earth by visual inspection of the plume direction relative to the orientation of the tracks. The uncertainty of this procedure was estimated to ± 10 °, resulting in a flux uncertainty of ± 0.22 Mt CO_2 yr^{-1} (2 %).

Finally, the uncertainty due to atmospheric variability was estimated from the 1 σ standard

deviation of the fluxes calculated for each cross-section divided by the number of cross-sections. The resulting flux uncertainty was ± 0.46 Mt CO_2 yr^{-1} (4 %).

All uncertainty contributions were added in quadrature for the final flux uncertainty, which then was ± 1.8 Mt CO_2 yr^{-1} (17 %). All uncertainties are also summarized in Table 6.8.

Table 6.8.: Uncertainty estimation of the flux inversion for the WFM-DOAS retrieval results of the MAMAP2D-Light Jänschwalde power plant flight.

Uncertainty contribution	flux uncertainty
Background normalization	± 0.22 Mt CO_2 yr^{-1} (2 %)
Background total column	± 0.48 Mt CO_2 yr^{-1} (5 %)
Retrieval result noise	± 0.14 Mt CO_2 yr^{-1} (1 %)
Wind speed	± 1.6 Mt CO_2 yr^{-1} (16 %)
Wind direction	± 0.22 Mt CO_2 yr^{-1} (2 %)
Atmospheric variability	± 0.46 Mt CO_2 yr^{-1} (4 %)
Total uncertainty	± 1.8 Mt CO_2 yr^{-1} (17 %)

The power plant emissions for the overflight were not available. However, from comparison with weekly activity data an independent emission estimate could be performed. For the year 2020, the yearly CO_2 emissions of the power plant Jänschwalde were 13.4 Mt CO_2 yr^{-1} according to the official report for greenhouse gas emissions of Brandenburg (LfU Brandenburg, 2021), while the average activity for the power plant was 66.5 % [2]. For week 24 of 2021, where the flight took place on 17.06.2021, the weekly activity data was 57.4 %. With the rule of proportion, this gives an estimate for the emission during week 24 of 11.6 Mt CO_2 yr^{-1}. Therefore, the emission estimate of 10.3 ± 1.8 Mt CO_2 yr^{-1} estimated from MAMAP2D-Light data is slightly lower than the emission during this week. However, it is still well within the uncertainty range.

6.2.3. Performance summary of the MAMAP2D-Light instrument

The MAMAP2D-Light instrument was successfully built and initially characterized during the work on this thesis. The spectral resolution of 1.08 nm and the very linear wavelength distribution across the detector show a good instrument adjustment. With this spectral resolution, the absorption features of CO_2 and CH_4 are quite pronounced (Fig. 6.18), which translates to a retrieval background noise of the retrieved $CO_2(CH_4)$ proxy results of 0.7 %. Further binning of the data reduced the background noise to 0.22 %. Although the instrument is not temperature stabilized, the temperature drifts during the flight affected the dark currents by only 8 BU during the remote sensing part of the measurement flight, indicating that temperature drifts will not cause significant biases.

[2] The activity data of power plants in Germany for the whole year as well as weekly was obtained from `https://energy-charts.info/charts/percentage_full_load/chart.htm?l=de&c=DE&chartColumnSorting=default&source=fossil_brown_coal_lignite_unit&year=2020&interval=year&legendItems=00001111000000000000000000000000`, last access 30.04.2022

The instrument performance validation concerning the estimation of emissions targeting the power plant Jänschwalde was successful. The estimated emission from MAMAP2D-Light remote sensing data was $10.3 \pm 1.8\,\mathrm{Mt\ CO_2\,yr^{-1}}$ compared to the average emission for the according calendar week of $11.6\,\mathrm{Mt\ CO_2\ yr^{-1}}$. The plume was furthermore visible over $\sim 10\,\mathrm{km}$ from the source.

6.3. Investigation of the FOCAL AIR retrieval algorithm

The WFM-DOAS method in the prior sections relies on the proxy method for estimating local enhancements. Therefore, the proxy gas is assumed to be constant over the area and during the flight. However, this assumption is not valid in regions where additionally the proxy gas is emitted, or during flights covering large areas.

To address these issues, the FOCAL retrieval was adapted to airborne geometry (FOCAL AIR see Sect. 5.2.2). The retrieval itself supports arbitrary definitions of fit windows. The WFM-DOAS method had been applied to MAMAP data in two separate fit windows in the SWIR channel (see, e.g., Gerilowski et al., 2011; Krings et al., 2011; Krautwurst et al., 2021). Therefore, this fit window definition was also the basis for the FOCAL AIR retrieval and is named "2-window retrieval" in the following. Additionally, one large fit window covering nearly the whole SWIR channel of MAMAP was tested (in the following "1-window retrieval") for comparison. To assess the improvement in the retrieval results by including the parametrized scattering in the forward model, both fit windows were used in the FOCAL AIR retrieval with scattering included ("scattering") and excluded ("absorption-only"). This resulted in four different retrieval configurations (absorption-only 2-window, scattering 2-window, absorption-only 1-window, scattering 1-window), which are examined in the following sections.

First, the retrieval was tested against synthetic measurements in Sect. 6.3.1. Afterward, the adaption of the retrieval to real measurements by modifying the noise model and implementing a parametrization for the zero level offset for all retrieval configurations is described in Sect. 6.3.2. The retrieval results are compared between the different retrieval configurations and the WFM-DOAS retrieval results in Sect. 6.3.3. For the retrieved CO_2 columns, the emissions are estimated in Sect. 6.3.4, and the results of this chapter are summarized and assessed with regards to the third research question in Sect. 6.3.5.

6.3.1. FOCAL AIR retrieval on synthetic measurements

The forward model of the FOCAL AIR retrieval described in Sect. 5.2.2 is different from the satellite FOCAL retrieval forward model and contains two different light paths, depending on the position of the modeled scattering layer relative to the aircraft. Furthermore, two different fit window configurations were tested for the data recorded with the SWIR detector from MAMAP. The first variant used the fit windows as in the WFM-DOAS method (Krings et al., 2011; Gerilowski et al., 2011; Krautwurst et al., 2017, 2021). The second one used one wide fit window covering both the CO_2 and CH_4 absorption bands and the wavelength range in between, in which only water vapor absorbs minimally.

For the FOCAL AIR retrieval on MAMAP data, a slightly different approach to assessing the retrieval was taken than for the WFM-DOAS retrieval applied to AVIRIS-NG data (Sect. 6.1.2). The approach is more in line with the sensitivity study performed by Reuter et al. (2017b). As FOCAL AIR is an iterative optimal estimation-based retrieval with the forward model calculated for each measurement considering the measurement geometry, significant deviations of geometrical parameters not fitted in the retrieval are not expected.

However, as the goal of FOCAL AIR is to capture at least partly effects caused by scattering, different non-scattering and scattering scenarios with different total column enhancements for CO_2 and CH_4 were examined. The at-sensor radiances ("synthetic measurements") for the different scenarios were calculated with the SCIATRAN radiative transfer model.

In Table 6.9 the different simulation experiments with their differences are shown. The parameters and state vector elements in the **base scenario** are the same in the SCIATRAN calculation as the a priori in the FOCAL AIR retrieval. Additionally, in SCIATRAN, the aerosol scattering was deactivated, and rayleigh scattering was scaled so that it did not affect the simulated intensities. All other scenarios are deviations from this base scenario in SCIATRAN, while the a priori in FOCAL AIR was kept at the base scenario. The scenarios **co2_2perc**, **ch4_2perc** and **co2_ch4_2perc** are different non-scattering scenarios, in which the lowest layers of the profiles of CO_2, CH_4 or both were scaled by 2 %. The scenario **ray** is the base scenario expanded by pure rayleigh scattering with rayleigh optical thickness at 760 nm of 0.026. The three scenarios **aer_bg**, **aer_cont** and **aer_lowurb** are three different aerosol scenarios based on WMO aerosol definitions. All three scenarios comprise three aerosol layers, where the top layer is a background aerosol composition, while the lower two layers are either background, continental, or urban aerosol layers. The resulting aerosol optical thicknesses are 0.0197, 0.159 and 0.152 at 760 nm and 0.0026, 0.057 and 0.050 at 1650 nm. The properties of the aerosols are described in the Tables A.1, A.2 and A.3 in the appendix. The final scenarios are continental and urban aerosol scenarios combined with enhanced gas concentrations.

Table 6.9.: Overview of the simulation experiments carried out with the FOCAL AIR algorithm. Enhancements are total column enhancements originating from an increase in the lowest layers, simulating a near-surface plume.

Name	**CO_2**	**CH_4**	**Rayleigh**	**Aerosol**
base	+0 %	+0 %	No	No
co2_2perc	+2 %	+0 %	No	No
ch4_2perc	+0 %	+2 %	No	No
co2_ch4_2perc	+2 %	+2 %	No	No
ray	+0 %	+0 %	Yes	No
aer_bg	+0 %	+0 %	Yes	background
aer_cont	+0 %	+0 %	Yes	continental
aer_lowurb	+0 %	+0 %	Yes	urban (low)
aer_cont_co2_2perc	+2 %	+0 %	Yes	continental
aer_cont_ch4_2perc	+0 %	+2 %	Yes	continental
aer_cont_co2_ch4_2perc	+2 %	+2 %	Yes	continental
aer_lowurb_co2_2perc	+2 %	+0 %	Yes	urban (low)
aer_lowurb_ch4_2perc	+0 %	+2 %	Yes	urban (low)
aer_lowurb_co2_ch4_2perc	+2 %	+2 %	Yes	urban (low)

The resulting deviation of the retrieval result from the true CO_2 and CH_4 concentrations as

prescribed in the SCIATRAN simulations is given in Table 6.10 for the retrieval in one large fit window in the SWIR and in Table 6.11 for separated fit windows for CO_2 and CH_4 absorption features. First, the two fit window modes were compared, and then the differences between absorption-only and scattering retrieval results were covered.

Table 6.10.: Deviation of the retrieved CO_2 and CH_4 concentrations from the truth as input to the SCIATRAN simulations with one fit window covering the whole SWIR window. The abbreviations are described in Sect. 6.3.1

	absorption-only		**scattering**	
	Δ CO_2	Δ CH_4	Δ CO_2	Δ CH_4
Name	ppm (%)	ppb (%)	ppm (%)	ppb (%)
base	+0.03 (+0.008)	+0.09 (+0.005)	+0.03 (+0.008)	+0.09 (+0.005)
co2_2perc	+0.02 (+0.004)	+0.09 (+0.005)	+0.02 (+0.004)	+0.09 (+0.005)
ch4_2perc	+0.03 (+0.008)	−0.03 (−0.002)	+0.03 (+0.008)	−0.03 (−0.002)
co2_ch4_2perc	+0.02 (+0.004)	−0.03 (−0.002)	+0.02 (+0.005)	−0.03 (−0.001)
ray	+0.17 (+0.041)	+0.57 (+0.031)	+0.08 (+0.021)	+0.24 (+0.013)
aer_bg	+0.35 (+0.087)	+1.24 (+0.068)	+0.22 (+0.054)	+0.71 (+0.039)
aer_cont	+1.09 (+0.27)	+4.2 (+0.23)	+0.88 (+0.21)	+3.2 (+0.17)
aer_lowurb	+0.56 (+0.14)	+2.1 (+0.12)	+0.42 (+0.10)	+1.5 (+0.080)
aer_cont_co2_2perc	+1.12 (+0.27)	+4.2 (+0.23)	+0.57 (+0.14)	+3.3 (+0.18)
aer_cont_ch4_2perc	+1.09 (+0.27)	+4.2 (+0.23)	+0.89 (+0.22)	−0.41 (−0.022)
aer_cont_co2_ch4_2perc	+1.12 (+0.27)	+4.2 (+0.23)	+0.58 (+0.14)	−0.34 (−0.018)
aer_lowurb_co2_2perc	+0.56 (+0.14)	+2.1 (+0.12)	+0.21 (+0.052)	+1.7 (+0.095)
aer_lowurb_ch4_2perc	+0.56 (+0.14)	+2.1 (+0.11)	+0.47 (+0.12)	−1.00 (−0.053)
aer_lowurb_co2_ch4_2perc	+0.56 (+0.14)	+2.1 (+0.11)	+0.23 (+0.054)	−0.94 (−0.050)

In the base case, where the first guess and a priori in FOCAL AIR are the same as in the SCIATRAN simulations, and no scattering was simulated, the retrieval using two separate fit windows produced an order of magnitude larger errors than one large fit window. The cause is a slight interference of the polynomial and zero level offset fit with the absorption structure in these smaller fit windows. Although this discrepancy was reduced in the scenarios including scattering, for nearly all cases, the errors were larger in the 2-window retrievals compared to the 1-window retrievals. Only in the case of continental aerosols, the 2-window retrieval including scattering performed slightly better than the retrieval in one large fit window.

Comparing the absorption-only retrieval results with the scattering retrieval, in the case of no scattering being present in the simulated measurements (the first block in Table 6.10), the retrieval including and excluding scattering performed the same and introduced only minor errors. These were all well below ± 0.1 ppm. These biases may also be caused by the numerical precision (i.e., single versus double precision in SCIATRAN versus FOCAL AIR) or minimal differences in the layering of the atmosphere between SCIATRAN and FOCAL.

Table 6.11.: Same as Table 6.10, but with separate fitting windows for the absorption features of CO_2 and CH_4 in the SWIR.

	absorption-only		**scattering**	
	Δ CO_2	Δ CH_4	Δ CO_2	Δ CH_4
Name	ppm (%)	ppb (%)	ppm (%)	ppb (%)
base	+0.25 (+0.061)	+0.68 (+0.037)	+0.25 (+0.062)	+0.69 (+0.038)
co2_2perc	+0.16 (+0.038)	+0.42 (+0.023)	+0.16 (+0.038)	+0.43 (+0.023)
ch4_2perc	+0.20 (+0.049)	+0.27 (+0.014)	+0.20 (+0.049)	+0.28 (+0.015)
co2_ch4_2perc	+0.10 (+0.025)	−0.00 (−0.000)	+0.11 (+0.025)	+0.00 (+0.000)
ray	+0.37 (+0.090)	+1.2 (+0.065)	+0.26 (+0.063)	+0.75 (+0.041)
aer_bg	+0.53 (+0.13)	+1.9 (+0.10)	+0.37 (+0.091)	+1.2 (+0.067)
aer_cont	+1.2 (+0.29)	+4.9 (+0.27)	+0.76 (+0.18)	+3.0 (+0.16)
aer_lowurb	+0.71 (+0.17)	+2.8 (+0.15)	+0.48 (+0.12)	+1.8 (+0.099)
aer_cont_co2_2perc	+1.14 (+0.27)	+4.7 (+0.26)	+0.62 (+0.15)	+2.5 (+0.14)
aer_cont_ch4_2perc	+1.14 (+0.28)	+4.7 (+0.25)	+0.65 (+0.16)	+2.5 (+0.13)
aer_cont_co2_ch4_2perc	+1.08 (+0.26)	+4.4 (+0.23)	+0.51 (+0.12)	+1.9 (+0.10)
aer_lowurb_co2_2perc	+0.62 (+0.15)	+2.6 (+0.14)	+0.38 (+0.091)	+1.5 (+0.082)
aer_lowurb_ch4_2perc	+0.66 (+0.16)	+2.4 (+0.13)	+0.42 (+0.10)	+1.4 (+0.074)
aer_lowurb_co2_ch4_2perc	+0.57 (+0.14)	+2.2 (+0.12)	+0.31 (+0.076)	+1.07 (+0.058)

Including rayleigh scattering in the simulated measurements increased the bias by roughly one order of magnitude for the absorption-only retrieval from Δ CO_2 = 0.008 % and Δ CH_4 = 0.005 % to Δ CO_2 = 0.041 % and Δ CH_4 = 0.031 %. Including the scattering parameters in the retrieval, the bias was reduced again by approximately 50 % to Δ CO_2 = 0.021 % and Δ CH_4 = 0.013 %. Including aerosols in the scenarios, the errors in the retrieval got worse in the absorption-only retrieval, with biases up to 1.12 ppm($\sim$ 0.27 %) for CO_2 and 4.2 ppb($\sim$ 0.23 %) for CH_4 in the case of continental aerosols. In all cases, the scattering retrieval reduced the error compared to the absorption-only retrieval, however not as drastically as in the pure rayleigh scattering case. Surprisingly, the scattering retrieval performed better when the a priori was not exactly the truth. The effect was especially prominent in the case of continental aerosols, where the bias for CH_4 was $\sim$ 3.3 ppb without enhanced CH_4, and only $\sim$ −0.4 ppb when CH_4 was increased by 2 % above the a priori value.

In general, in the large fit window retrieval, the retrieval of the two gases CO_2 and CH_4 was mostly uncorrelated, with biases staying nearly the same (apart from rounding) in setups with the same concentrations for one gas and changes in concentrations in the other gas, e.g., the aer_cont, aer_cont_co2_2perc and aer_cont_ch4_2perc setups for both the absorption-only and the scattering retrievals.

6.3.2. Noise and zero-level offset model for FOCAL AIR on MAMAP measurements

The synthetic measurements indicated that the FOCAL AIR retrieval worked as intended, and including scattering could reduce single column biases. Therefore, the retrieval was applied to MAMAP data acquired over the power plant Jänschwalde on 23.05.2018 (see Sect. 5.1.2.2). This required the noise model to be adapted and the zero-level offset to be parametrized.

As described in Sect. 5.2.2, the noise model had to be adapted for mainly two reasons. On one hand the initial noise model (Eq. 5.135) for MAMAP measurements did not include the forward model error, which (according to, e.g., Rodgers (2000)) can be combined with the measurement noise (see also Reuter et al. (2017a)). Additionally, the complete instrument noise as a function of the detector filling has not yet been fully characterized. Therefore, the noise model was adapted according to Eq. (5.142) by running the retrieval with the measurement noise increased by quadratically adding 2 % of the continuum radiance to the MAMAP noise. From the retrieval results, the RSR and NSR were calculated, and the noise scaling parameters n_a and n_b were obtained by fitting Eq. (5.141) to the data (see figures 6.22 and 6.23) for both the absorption-only (figures (a)) and the scattering (figures (b)) FOCAL AIR retrieval. In the absorption-only case, the NIR fit window did not contain any information for the state vector elements and was therefore not considered in the retrieval.

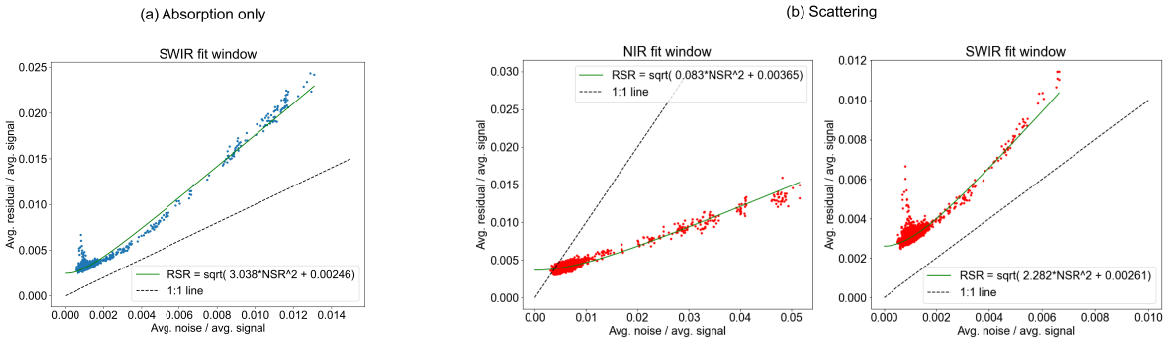

Figure 6.22.: Noise model fit for the 1-window retrieval configuration as described in Sect. 5.2.2. (a) shows the fit for the absorption-only retrieval and (b) for the scattering retrieval. Additionally, the ideal 1:1 line is added. The difference in data points in the SWIR channel between (a) and (b) is due to additional missing data in the scattering retrieval, see Fig. 6.3.3.

The noise model was adapted separately for each fit window, resulting in four sets of noise models. Additionally to the nomenclature for the four retrievals introduced in the intro-

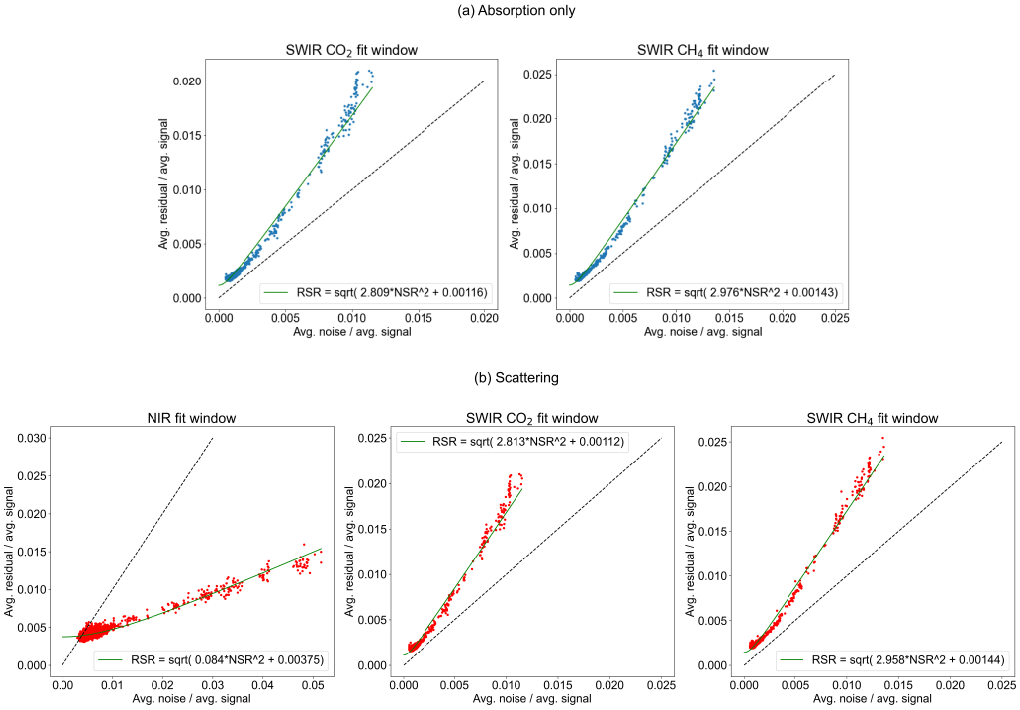

Figure 6.23.: Same as Fig. 6.22, but for the 2-window retrieval.

duction to this chapter, the different fit windows were named "NIR" for the NIR channel covering the O_2A absorption, "SWIR" for the SWIR channel in the 1-window retrieval, and "SWIR CO_2" and "SWIR CH_4" for the SWIR fit windows covering the absorption features of CO_2 and CH_4, respectively. The resulting noise models were as follows, with the SWIR noise models in the first and NIR noise models in the second column:

$$N'_{abs1,SWIR} = \sqrt{3.038 \cdot N^2 + 0.00246^2} \tag{6.158}$$

$$N'_{sca1,SWIR} = \sqrt{2.282 \cdot N^2 + 0.00261^2} \quad N'_{sca1,NIR} = \sqrt{0.083 \cdot N^2 + 0.00365^2} \tag{6.159}$$

$$\begin{aligned} N'_{abs2,SWIR\,CO_2} &= \sqrt{2.809 \cdot N^2 + 0.00116^2} \\ N'_{abs2,SWIR\,CH_4} &= \sqrt{2.976 \cdot N^2 + 0.00143^2} \end{aligned} \tag{6.160}$$

$$\begin{aligned} N'_{sca2,SWIR\,CO_2} &= \sqrt{2.813 \cdot N^2 + 0.00112^2} \quad N'_{sca2,NIR} = \sqrt{0.084 \cdot N^2 + 0.00375^2} \\ N'_{sca2,SWIR\,CH_4} &= \sqrt{2.958 \cdot N^2 + 0.00144^2} \end{aligned} \tag{6.161}$$

Furthermore, fitting the zero-level offset as a free fit parameter yielded noisy results. Therefore, also the zero-level offset was parametrized. First, the retrieval was run, fitting the zero-level offset for each measurement. Then, assuming that the zero-level offset, i.e., an additive offset to the radiance, is caused in some way by illumination, the fitted zero-level offset was plotted as a function of the continuum radiance I_{cont}. In the NIR, the continuum radiance was estimated from the 16 pixels on the edge of the fit window, and in the SWIR, the spectral data between the absorption features of CO_2 and CH_4 was used. Then, a low-order polynomial was fitted to the data trying to capture the dependency of the zero-level offset fit on the background intensity (see figures 6.24 and 6.25). In the final retrieval, the zero-level offset was not fitted but calculated based on the zero-level offset model. For the 1-window absorption-only ($ZLO_{abs,SWIR}$) and scattering ($ZLO_{sca,NIR}$ and $ZLO_{sca,SWIR}$) retrieval, the fitted model was

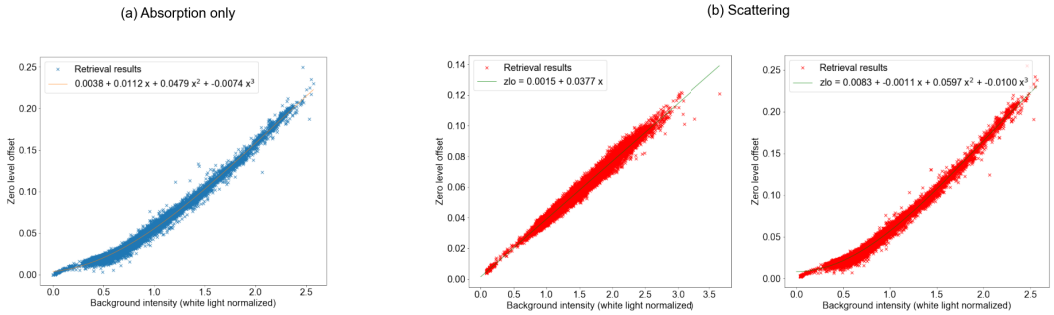

Figure 6.24.: Zero-level offset model fit for the 1-window retrieval configuration as described in Sect. 5.2.2. The fit for the absorption-only retrieval is shown in (a), and for the scattering retrieval including in (b).

$$ZLO_{abs,SWIR} = 0.0038 + 0.0112 \cdot I_{cont} + 0.0479 \cdot I_{cont}^2 - 0.0074 \cdot I_{cont}^3 \tag{6.162}$$

$$ZLO_{sca,NIR} = 0.0015 + 0.0377 \cdot I_{cont} \tag{6.163}$$

$$ZLO_{sca,SWIR} = 0.0083 - 0.0011 \cdot I_{cont} + 0.0597 \cdot I_{cont}^2 - 0.0100 \cdot I_{cont}^3, \tag{6.164}$$

and for the 2-window absorption-only ($ZLO_{abs,SWIRCO_2}$ and $ZLO_{abs,SWIRCH_4}$) and scattering ($ZLO_{sca,NIR}$, $ZLO_{sca,SWIRCO_2}$ and $ZLO_{sca,SWIRCH_4}$) retrieval, the fitted model

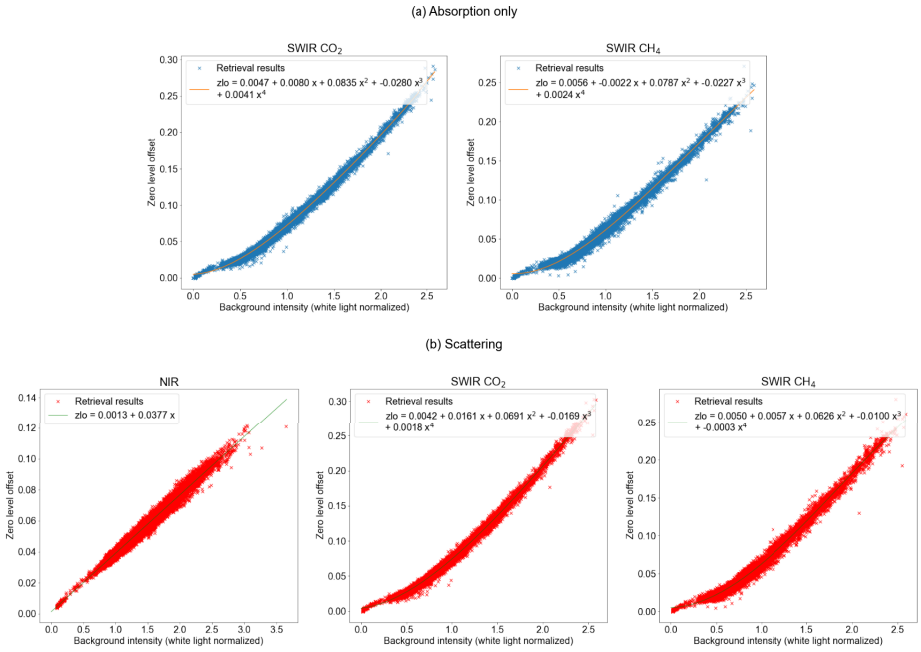

Figure 6.25.: Zero-level offset model fit for the 2-window retrieval configuration as described in Sect. 5.2.2. The fit for the absorption-only retrieval is shown in (a), and for the scattering retrieval including in (b).

was

$$ZLO_{abs,SWIRCO_2} = 0.0047 + 0.0080 \cdot I_{cont} + 0.0835 \cdot I_{cont}^2 - 0.0280 \cdot I_{cont}^3 + 0.0041 \cdot I_{cont}^4 \tag{6.165}$$

$$ZLO_{abs,SWIRCH_4} = 0.0056 - 0.0022 \cdot I_{cont} + 0.0787 \cdot I_{cont}^2 - 0.0227 \cdot I_{cont}^3 + 0.0024 \cdot I_{cont}^4 \tag{6.166}$$

$$ZLO_{sca,NIR} = 0.0013 + 0.0377 \cdot I_{cont} \tag{6.167}$$

$$ZLO_{sca,SWIRCO_2} = 0.0042 + 0.0161 \cdot I_{cont} + 0.0681 \cdot I_{cont}^2 - 0.0169 \cdot I_{cont}^3 + 0.0018 \cdot I_{cont}^4 \tag{6.168}$$

$$ZLO_{sca,SWIRCH_4} = 0.0050 + 0.0057 \cdot I_{cont} + 0.0626 \cdot I_{cont}^2 - 0.0100 \cdot I_{cont}^3 - 0.0003 \cdot I_{cont}^4 \tag{6.169}$$

6.3.3. Comparison of FOCAL AIR xCO_2, $xCO_2(CH_4)$ and WFM-DOAS retrieval results

With the adjusted noise model and zero-level offset parametrization in place, the retrieval was run on the remote sensing part of the Jänschwalde power plant flight in all four dif-

ferent retrieval configurations for comparison. The retrieval results contain, among others, the total column volume mixing ratios for CH_4 and CO_2 (xCO_2 and xCH_4, respectively), from which additionally the proxy was calculated according to Eq. (5.147). These results were then compared to WFM-DOAS retrieval results (see Sect. 5.1.2.2) retrieved by Sven Krautwurst similar to Krautwurst et al. (2021). The analyses in this section used single measurements without binning the retrieval results.

For the comparison, the 13830 single measurement retrieval results were quality filtered in the following way. First, all retrieval results with missing data (e.g., too low radiance in the preprocessing or for the scattering retrieval missing NIR data) were flagged. Of the remaining data points, all non-converging measurements were filtered out. Finally, all retrieval results with an RMS value (calculated in the same way as for WFM-DOAS results, see Eq. 5.95) lower than 0.7 were flagged as bad results. The number of data points filtered out by these three filters for the four retrieval configurations is shown in Table 6.12.

Table 6.12.: Overview of the data filtered out by the quality filters "missing data", "convergence" and "RMS".

Retrieval	missing data	convergence	RMS
absorption-only 2-window	16 (0.1 %)	0 (0.0 %)	134 (1.0 %)
scattering 2-window	1017 (7.4 %)	2 (0.0 %)	125 (0.9 %)
absorption-only 1-window	16 (0.1 %)	0 (0.0 %)	148 (1.1 %)
scattering 1-window	1017 (7.4 %)	0 (0.0 %)	139 (1.0 %)

The difference in missing data for the absorption-only and the scattering retrieval is due to the need to match the data from the NIR and SWIR channels to simultaneous measurements for the scattering retrieval. However, sometimes frames got lost on the NIR camera, so additionally to low radiance data in the SWIR, all data points not containing NIR data were skipped in the scattering retrieval. Much fewer data were rejected in the absorption-only retrieval, as only the SWIR data was needed there

For qualitative comparison of the different retrieval configurations and the plume visibility and noise in the xCO_2 and $xCO_2(CH_4)$ proxy retrieval results, the retrieved xCO_2 and $xCO_2(CH_4)$ were plotted next to each other for each retrieval in figures 6.26 - 6.29, with the raw xCO_2 in (a) and the proxy $xCO_2(CH_4)$ in (b) in all figures.

In all retrieval results, the plume is visible in the first cross-tracks at least. However, the plume is more pronounced in the 1-window than in the 2-window retrieval results for both absorption-only and scattering retrievals. On the other hand, also the negative values seemed to be more pronounced in the 1-window retrieval results. Additionally, especially for the 1-window retrieval result, the proxy retrieval results were more variable outside the plume than the raw xCO_2 results.

As the xCO_2 results were reasonably smooth, this might indicate a problem with the xCH_4 retrieval results. Therefore, the xCO_2 and xCH_4 retrieval results were investigated separately. The xCO_2 and xCH_4 normalized to the median of the flight were plotted for the first

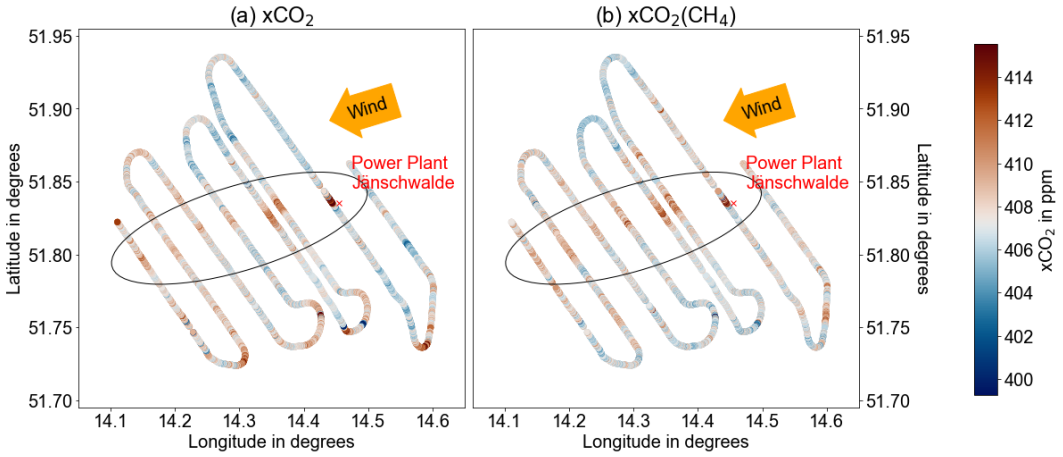

Figure 6.26.: Comparison of FOCAL AIR absorption-only 2-window xCO_2 (a) and proxy ($xCO_2(CH_4)$) (b) retrieval results. xCO_2 enhancements above the global median are red, while lower than average values are blue. Originating from the power plant, the exhaust plume is visible, pointing to the left.

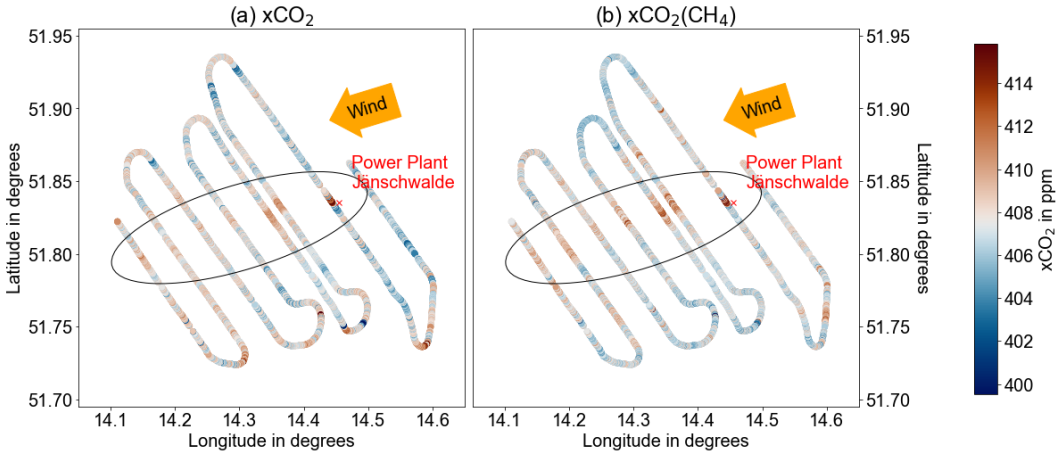

Figure 6.27.: Same as Fig. 6.26, but for the scattering 2-window retrieval. The plume is much feinter, especially in the cross-tracks further downwind.

cross-section in the figures 6.30 - 6.33. The gap directly beside the plume contained data acquired over a water body. Due to the low radiance backscattered from the water surface, the retrieval did not retrieve meaningful concentrations.

For all four retrieval configurations, xCH_4 showed higher variability than xCO_2. Furthermore, the variability was much more pronounced in the 1-window retrieval, where xCH_4 showed large values, e.g., around measurement number 2300 or 2210 (Fig. 6.32). The larger

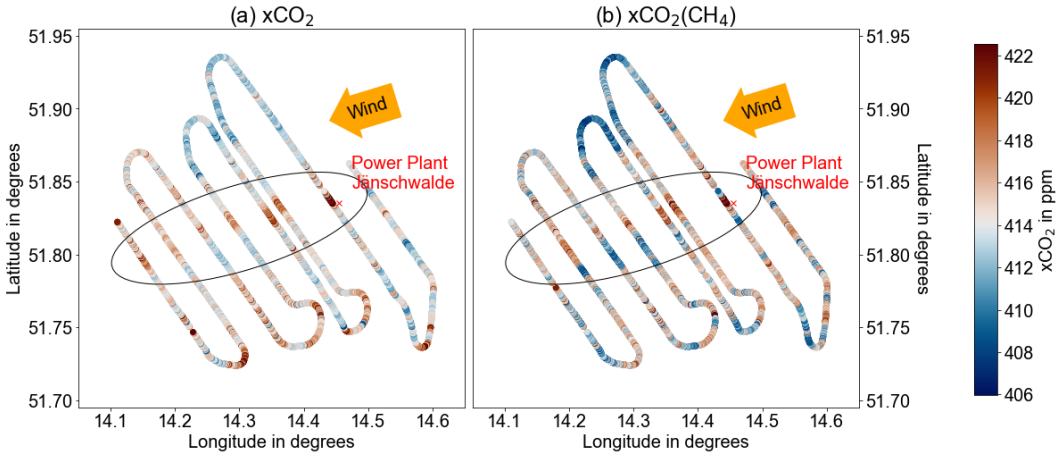

Figure 6.28.: Same as Fig. 6.26, but for the absorption-only 1-window retrieval.

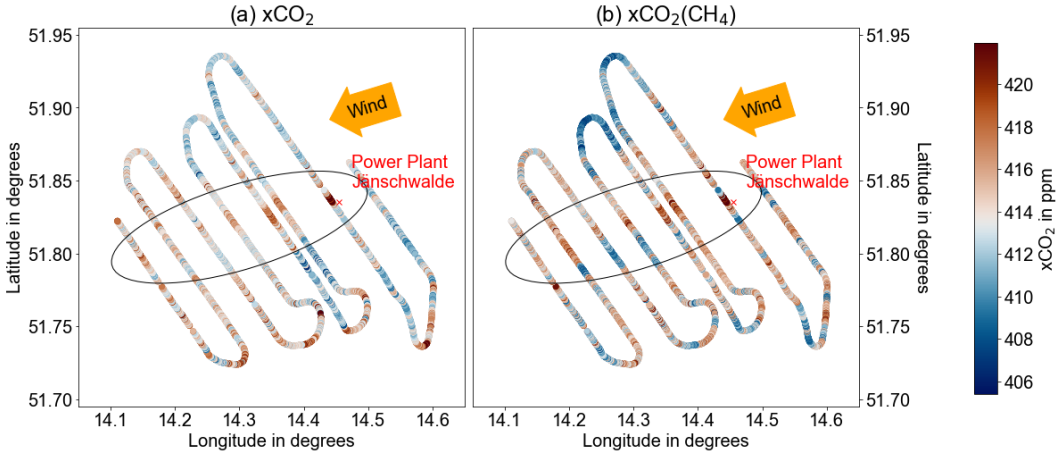

Figure 6.29.: Same as Fig. 6.26, but for the scattering 1-window retrieval.

variability in the 1-window retrieval compared to the 2-window retrieval might have originated from the large fit window, where the polynomial was not catching the actual surface reflectance sufficiently around the Q-branch, containing most of the absorption information of CH_4. This is also visible in Fig. 6.34 for the 1-window absorption-only retrieval, where the background white light corrected intensity was plotted beneath the xCH_4. When the background intensity was low, xCH_4 was slightly higher, and vice versa. This is discussed at the end of this section.

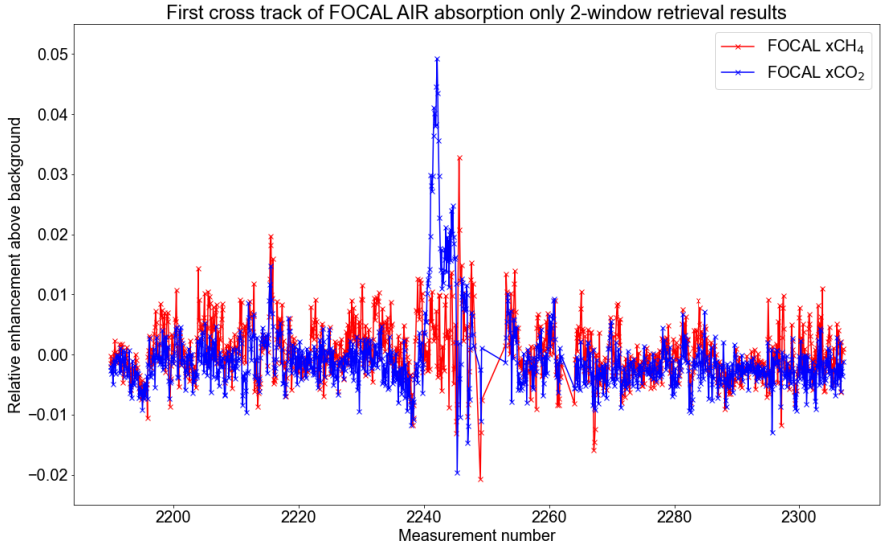

Figure 6.30.: Comparison of FOCAL-AIR absorption-only 2-window xCO_2 and xCH_4 enhancements above local background for the first downwind track of the Jänschwalde power plant plume.

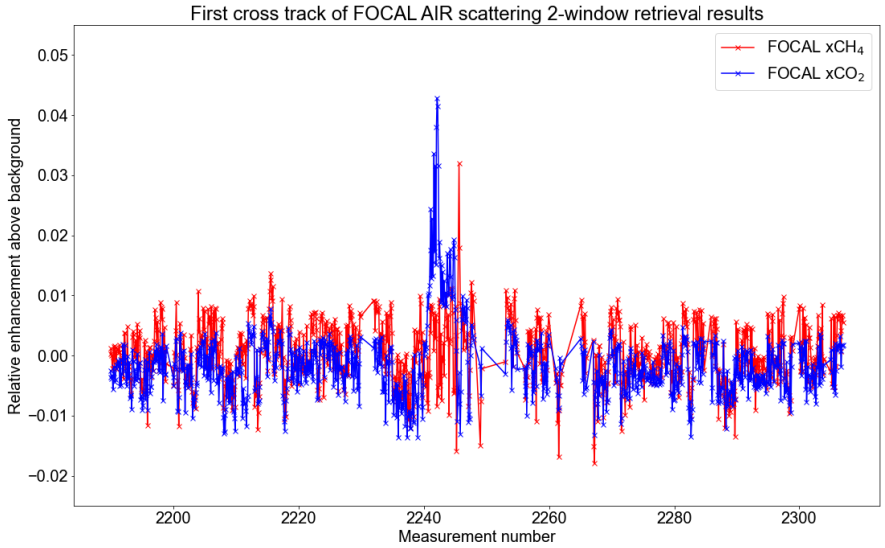

Figure 6.31.: Same as Fig. 6.30, but for the scattering 2-window retrieval results.

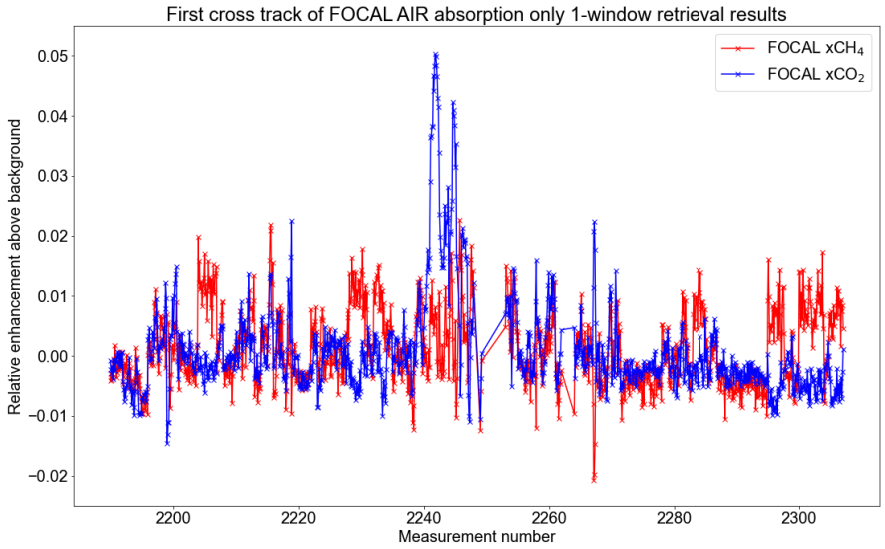

Figure 6.32.: Same as Fig. 6.30, but for the absorption-only 1-window retrieval results.

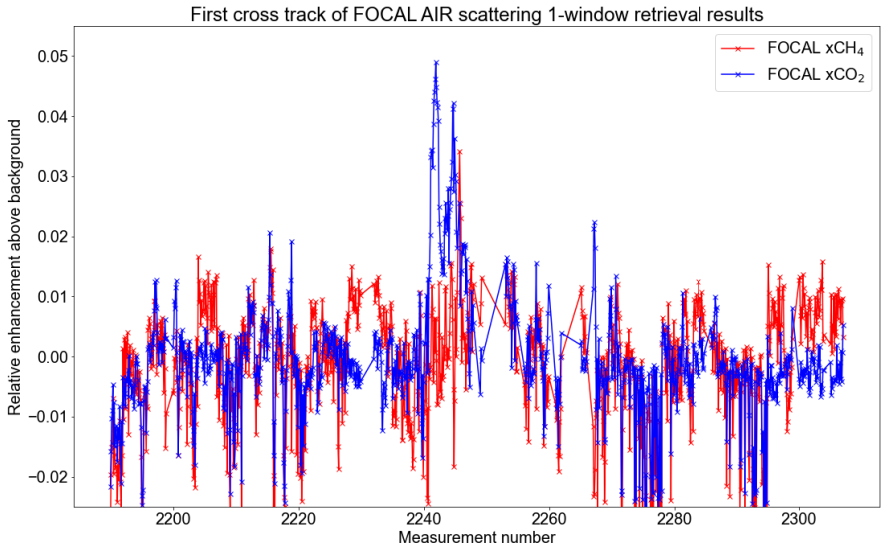

Figure 6.33.: Same as Fig. 6.30, but for the scattering 1-window retrieval results.

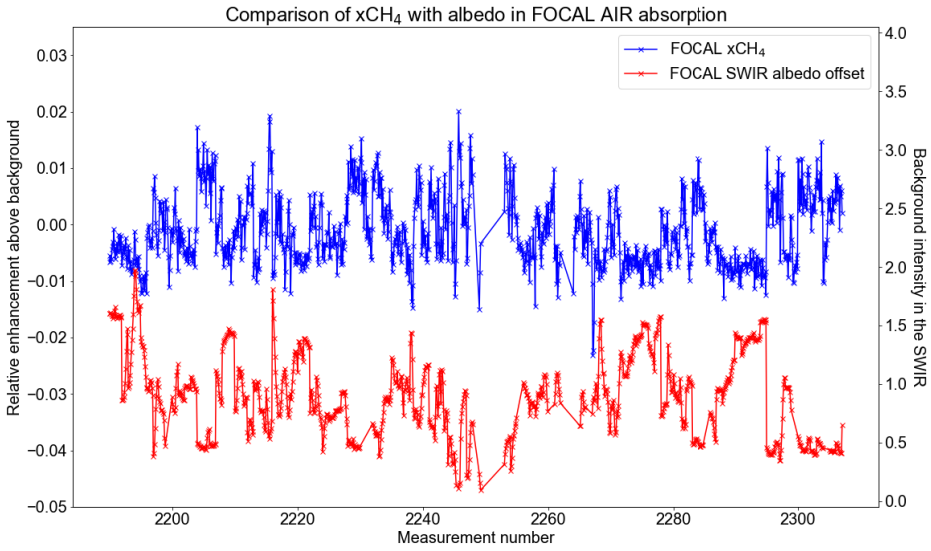

Figure 6.34.: Continuum radiance and xCH_4 for the absorption-only 1-window retrieval over measurement number. The xCH_4 seems anticorrelated to the background radiation.

Only in the 1-window scattering retrieval (Fig. 6.33) additional large "dips" in the retrieved concentrations of xCO_2 and xCH_4 were visible. Those occurred in the xCO_2 and xCH_4, leading to the proxy not being affected by this problem as much. Investigating this issue deeper, the extremely low values seemed to be correlated to very low fitted Angström coefficients (see Fig. 6.35). Likely, this was a retrieval artifact. Therefore, an additional filter was implemented for the FOCAL AIR scattering retrievals, flagging data with $\mathring{A} < 2.0$ as bad. This filter removed additional 974 (7.0 %) data points.

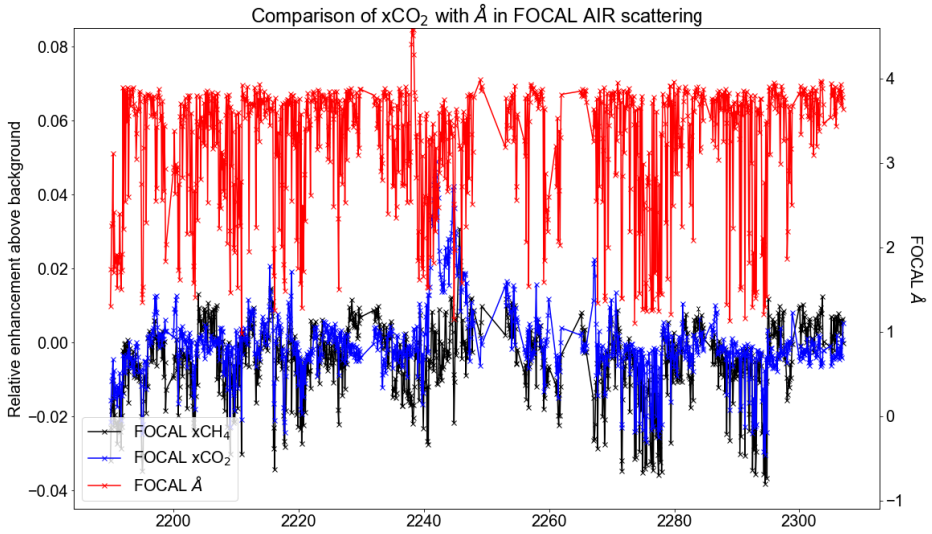

Figure 6.35.: Comparison of FOCAL-AIR scattering xCO_2 and Angstöm coefficient $\mathring{A}$ retrieval results for the first downwind track of the Jänschwalde power plant plume.

Furthermore, the retrieved column enhancements were compared to WFM-DOAS retrieval results for all retrieval configurations, zooming in on the first cross-track in figures 6.36 - 6.39. In all four retrieval configurations, the plume in the first track was similar to the WFM-DOAS retrieval results, although the extreme values were slightly higher in the FOCAL retrieval results. An extreme case is visible in Fig. 6.36 for the xCO_2 of the 2-window absorption-only retrieval. In the background beside the plume, the 1-window retrieval results were more variable than the 2-window retrieval results for absorption-only and scattering. However, with the Angström filter, the extremely low values in the scattering 1-window retrieval results were removed successfully. In general, the structure of the FOCAL AIR retrieved concentrations in the background was similar to the WFM-DOAS retrieval results.

To expand this for the whole flight track, scatter plots of the xCO_2 and $xCO_2(CH_4)$ retrieval results and the WFM-DOAS retrieval results were produced. These are plotted in the figures 6.40 - 6.43.

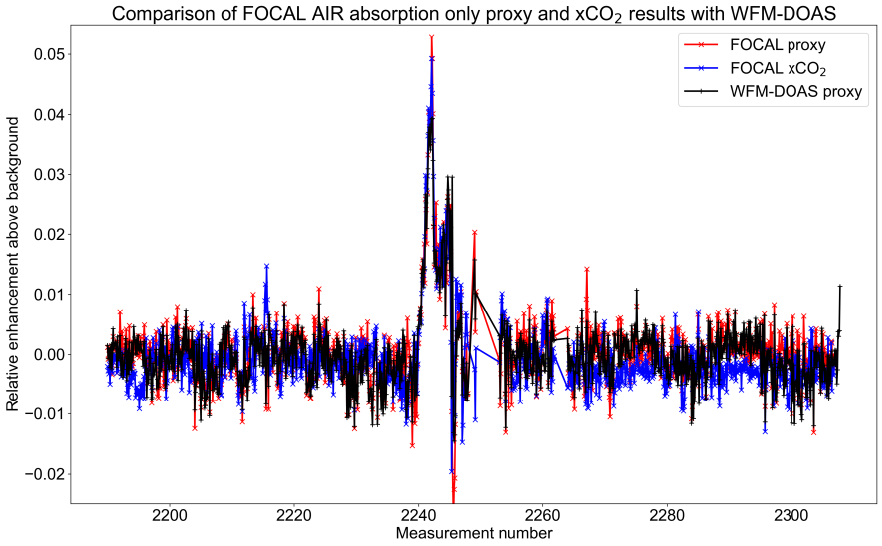

Figure 6.36.: Comparison of FOCAL-AIR absorption-only 2-window CO_2 enhancements above background for the first downwind track of the Jänschwalde power plant plume with WFM-DOAS retrieval results.

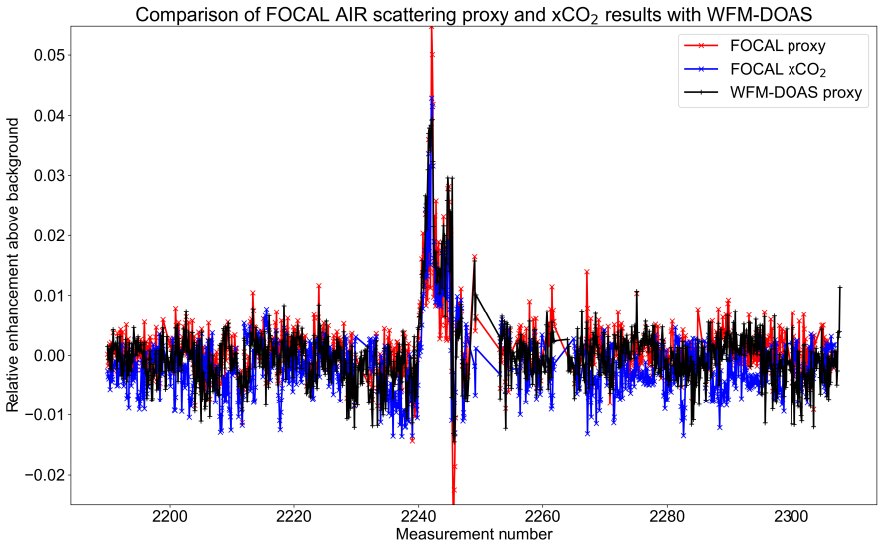

Figure 6.37.: Same as Fig. 6.36, but for the scattering 2-window retrieval.

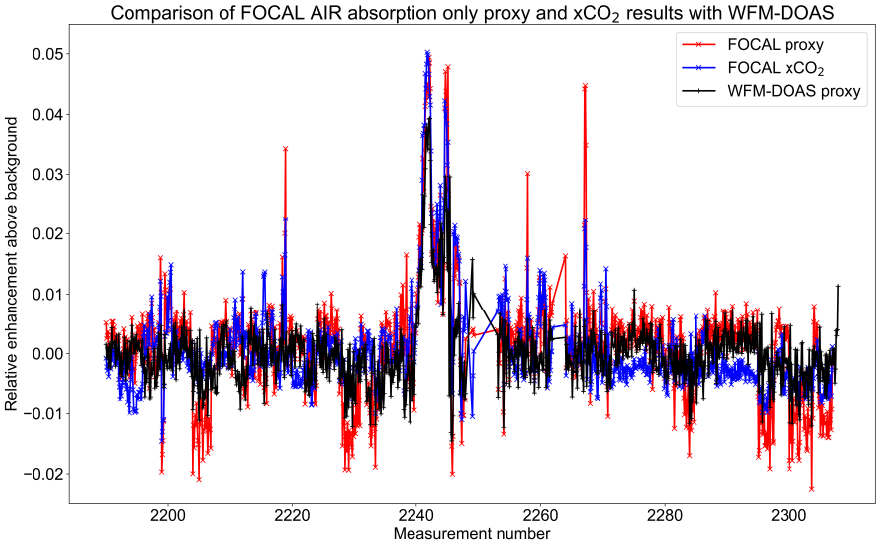

Figure 6.38.: Same as Fig. 6.36, but for the absorption-only 1-window retrieval.

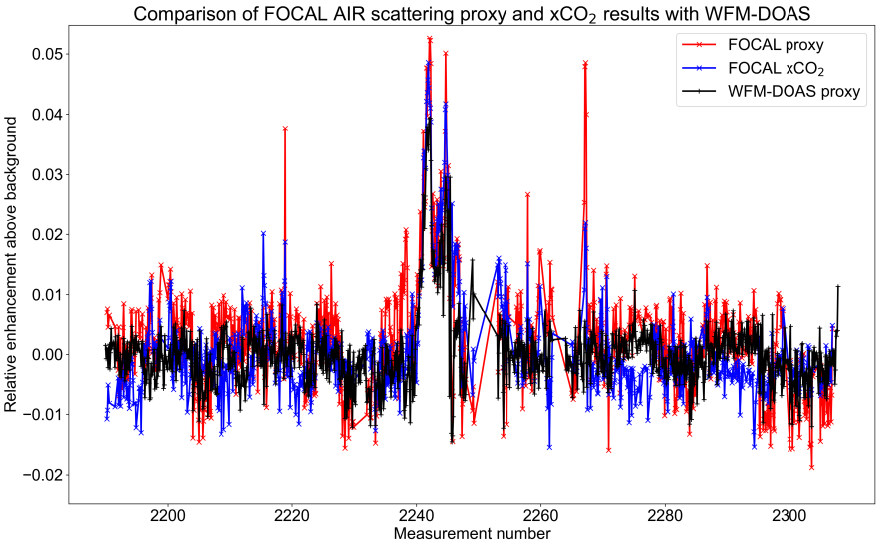

Figure 6.39.: Same as Fig. 6.36, but for the scattering 1-window retrieval.

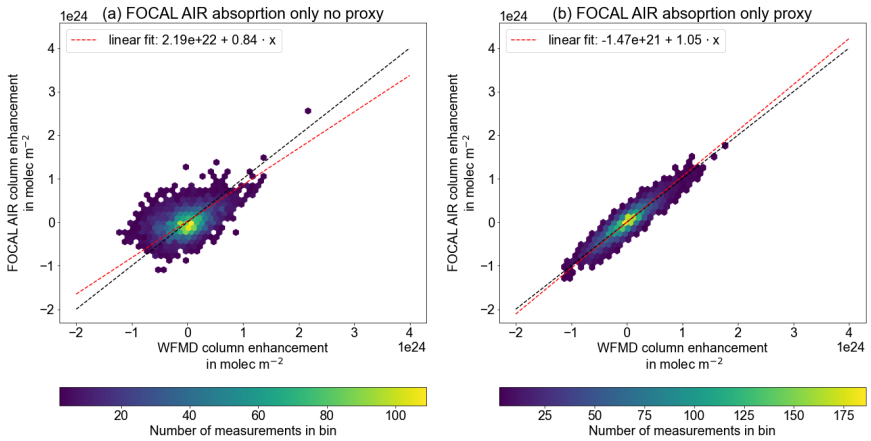

Figure 6.40.: Scatter plot of FOCAL-AIR absorption-only 2-window retrieval results of the Jänschwalde power plant plume over WFM-DOAS retrieval results. In (a), the FOCAL AIR xCO_2 enhancement over the background, and in (b), the FOCAL AIR $xCO_2(CH_4)$ enhancements over background are depicted. The black dashed line is the 1:1 line, and the red dashed line is the linear fit to the scatter plot.

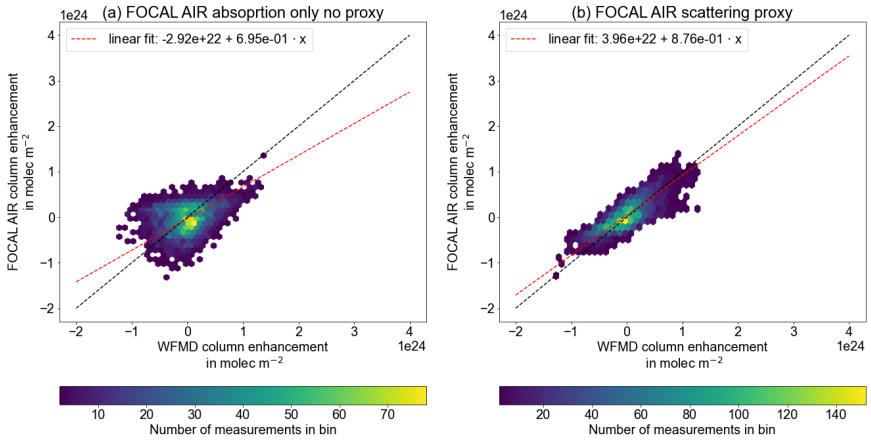

Figure 6.41.: Same as Fig. 6.40, but for the scattering 2-window retrieval.

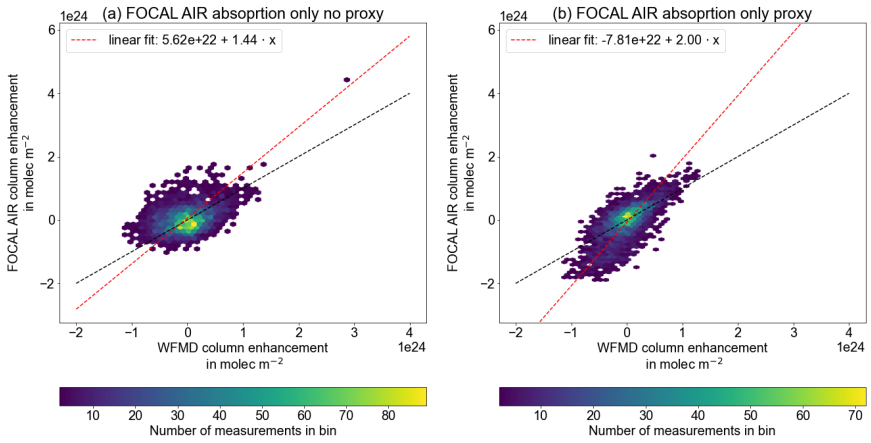

Figure 6.42.: Same as Fig. 6.40, but for the absorption-only 1-window retrieval.

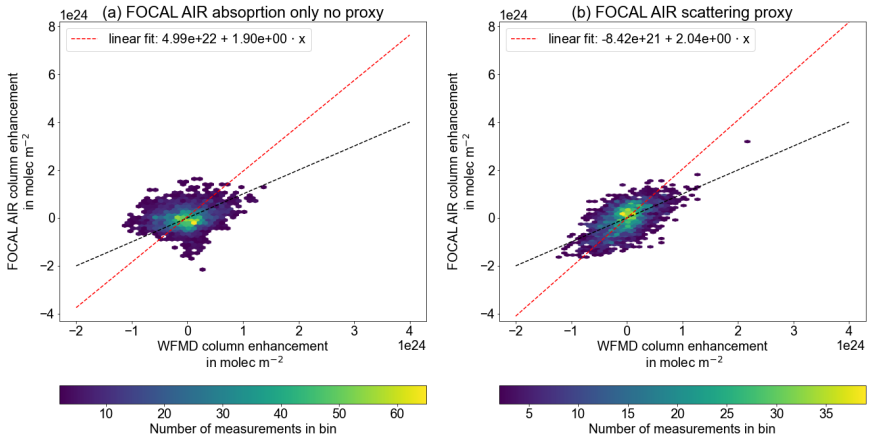

Figure 6.43.: Same as Fig. 6.40, but for the scattering 1-window retrieval.

The correlation of the retrieval results was better in the $CO_{2,col}(CH_{4,col})$ proxy results for the 2-window retrievals, while for the 1-window retrieval, the xCO_2 results correlated better with WFM-DOAS proxy retrieval results. The correlation was better in the 2-window retrievals compared to the 1-window retrievals. However, the linear fits are defined mainly by the values in the middle, which are around the background concentration. Already small variations in the distributions at the center can cause a large deviation of the fit from a 1:1 line fit. As was indicated in the cross-section figures, the plume was captured quite well in all retrieval results, at least in the first track.

Concerning the mean fit quality, measured as the mean of the root mean square difference between the fitted and measured spectra calculated with Eq. (5.95), all FOCAL AIR retrieval configurations performed better by a factor of 2-3 than the WFM-DOAS retrieval, see Table 6.13. Therefore, the fitted spectra were much closer to the measured spectra in the FOCAL AIR retrieval. The slightly larger RMS in the 1-window retrievals was dominated by the increased number of measurement points in one large fit window compared to the two smaller fit windows in the 2-window retrievals.

Table 6.13.: Mean fit RMS between measured and fitted spectra for the four different FOCAL AIR retrieval configurations and WFM-DOAS. For the 1-window retrieval, only one RMS value exists for the whole large fit window.

	RMS	
Retrieval	SWIR CO_2	SWIR CH_4
WFM-DOAS	0.64 %	0.48 %
FOCAL AIR absorption-only 2-window	0.19 %	0.23 %
FOCAL AIR scattering 2-window	0.19 %	0.23 %
	RMS SWIR	
FOCAL AIR absorption-only 1-window	0.32 %	
FOCAL AIR scattering 1-window	0.32 %	

Table 6.14.: Scatter of the retrieval results in the background regions undisturbed by the plume for xCO_2, $xCO_2(CH_4)$ and $CH_{4,col}$.

Retrieval	xCO_2	$CH_{4,col}$	$xCO_2(CH_4)$
absorption-only 2-window	± 0.20 %	± 0.31 %	± 0.23 %
scattering 2-window	± 0.22 %	± 0.31 %	± 0.20 %
absorption-only 1-window	± 0.33 %	± 0.46 %	± 0.52 %
scattering 1-window	± 0.37 %	± 0.51 %	± 0.50 %
WFM-DOAS	*not valid*	*not valid*	± 0.22 %

Finally, the retrieval scatter in the background, i.e., outside of the plume regions, was compared between the FOCAL AIR xCO_2 and $xCO_2(CH_4)$ and WFM-DOAS retrieval results. The background retrieval scatter was measured as the 1σ standard deviation in the background, i.e., not disturbed by the plume. Unlike the previous comparisons, the retrieval

scatter was calculated on the binned bursts, considering only bursts where more than five single measurements were valid (i.e., more than 50 % of the burst). The overview is given in Table 6.14. In general, the retrieval results were less noisy in the background for the 2-window retrievals than for the 1-window retrievals.

6.3.4. Emission estimation of the Jänschwalde power plant plume from FOCAL AIR retrieval results

In a final step to assess the FOCAL AIR retrieval, the emission of the power plant Jänschwalde was estimated from WFM-DOAS and the four FOCAL AIR retrieval configurations using the cross-sectional flux method (Sect. 5.3). As already described in Sect. 5.1.2.2, the wind speed was estimated from ECMWF ERA5 hourly horizontal wind data over the whole measurement area between 14.1 and 14.6 ° East and 51.72 and 51.94 ° North averaged over the whole time of overflight to $6.2 \pm 1.0\,\mathrm{m\,s^{-1}}$. The binned bursts were used for the emission estimate, where only bursts were considered with more than 50 % valid measurements per 10-measurement burst.

First, the WFM-DOAS retrieval results of the Jänschwalde power plant provided by Sven Krautwurst (see Sect. 5.1.2.2) were inverted with the cross-sectional flux method (see Sect. 5.3). For that, the plume region and background region at each side of the plume were extracted from each cross-track. The borders of each cross-section were selected so that the background region comprised at least a few data points but no data in turns or too far away from the plume. The cross-sections extracted and normalized to the local background are shown in Sect. A.5 in the appendix. The last two cross-tracks mainly contained noise, and the definition of a plume region was debatable. Therefore, these last two cross-sections were excluded from the flux comparison analysis, leaving five cross-sections for the emission estimate. The flux calculated from the first five cross-tracks of the plume for the WFM-DOAS retrieval results was $19.4 \pm 4.7\,\mathrm{Mt\ CO_2\ yr^{-1}}$. The relative uncertainty of the emission estimation was ± 24 %, and the detailed uncertainties are given in Sect. A.5 in the appendix.

The emission estimates were compared to reported emissions of the power plant Jänschwalde for the year 2018, too, analogously to Sect. 6.2. The German pollutant register (PRTR Data, 2022) listed the yearly emissions of the power plant Jänschwalde with $22.8\,\mathrm{Mt\ CO_2\,yr^{-1}}$. During the year, the average activity data [3] was 80.4 %. For the week of the overflight (week 21) the activity was 78.6 %, which translated to an emission of $22.3\,\mathrm{Mt\ CO_2\,yr^{-1}}$.

The cross-sectional flux was calculated for the xCO_2 and the $xCO_2(CH_4)$ proxy FOCAL AIR retrieval results for all four retrieval configurations, and the uncertainties were estimated as described in Sect. 5.3. The cross-sections and plume borders were the same as for the WFM-DOAS retrieval results. The resulting cross-sections for the enhancement over the local background ($CO_{2,col,enh}$ and $CO_{2,col,enh}(CH_{4,col})$) for the four retrieval configurations

[3] The activity data of power plants in Germany for the whole year as well as weekly was obtained from `https://energy-charts.info/charts/percentage_full_load/chart.htm?l=de&c=DE&chartColumnSorting=default&source=fossil_brown_coal_lignite_unit&year=2018&interval=year&legendItems=00001111110000000000000000000000000`, last access 30.04.2022

are shown in the appendix in Sect. A.6. For all four retrieval configurations, the last two cross-tracks mostly showed noise, as was the case for the WFM-DOAS retrieval results. Therefore, and for better comparison with WFM-DOAS retrieval results, only the first five cross-tracks were considered for the emission estimate.

The emission and uncertainty estimations for the different retrieval configurations for xCO_2 and $xCO_2(CH_4)$ retrieval results are summarized in Table 6.15. The emissions compared to the emission estimation based on activity data were underestimated by all FOCAL AIR 2-window retrieval configurations apart from the absorption-only 2-window $xCO_2(CH_4)$ retrieval results. The 2-window absorption-only retrieval design was closest to the WFM-DOAS retrieval configuration, i.e., no fitting of scattering parameters and splitting the SWIR into two fit windows. For the 1-window retrievals, the emission estimates were generally closer to the truth. However, the emissions were overestimated for the absorption-only $xCO_2(CH_4)$ retrieval. This might be due to the problems observable in the xCH_4 (see Fig. 6.32), which also translated to the $xCO_2(CH_4)$ retrieval results (see Fig. 6.42). The only retrieval giving consistent results between the xCO_2 and $xCO_2(CH_4)$ proxy was the scattering 1-window retrieval.

Compared to the flux estimation from activity data, the absorption-only 2-window $xCO_2(CH_4)$ and 1-window xCO_2 emission estimates as well as the scattering 1-window xCO_2 and $xCO_2(CH_4)$ emission estimates are slightly lower than the weekly average emission, although the reported emission was well within the uncertainty ranges of these emission estimates.

Table 6.15.: Emission estimation for the FOCAL AIR absorption-only and scattering 2-window and 1-window retrieval results for the xCO_2 and $xCO_2(CH_4)$ proxy retrieval results. The reported emission for the week during which the overflight took place was, on average, 22.3 Mt $CO_2\,yr^{-1}$. For the emission and uncertainty estimation calculation, see the main text.

Retrieval configuration	**Emission estimate from xCO_2**	**Emission estimate from $xCO_2(CH_4)$**
Absorption 2-window	15.7 ± 4.0 Mt $CO_2\,yr^{-1}$	19.8 ± 4.7 Mt $CO_2\,yr^{-1}$
Scattering 2-window	11.6 ± 3.7 Mt $CO_2\,yr^{-1}$	15.5 ± 4.1 Mt $CO_2\,yr^{-1}$
Absorption 1-window	20.4 ± 5.8 Mt $CO_2\,yr^{-1}$	27.8 ± 7.1 Mt $CO_2\,yr^{-1}$
Scattering 1-window	18.6 ± 6.8 Mt $CO_2\,yr^{-1}$	18.5 ± 5.6 Mt $CO_2\,yr^{-1}$
WFM-DOAS	*not valid*	19.4 ± 4.7 Mt $CO_2\,yr^{-1}$

The uncertainty estimation of the emission estimation was calculated as before for the AVIRIS-NG (Sect. 6.1.6) and MAMAP2D-Light (Sect. 6.2.2) data, and followed the procedure described in Sect. 5.3. The uncertainties were grouped into uncertainties due to the calculation of the column enhancement above background, uncertainties related to the wind, and the uncertainty due to atmospheric variability.

In the first block, the uncertainty due to the normalization was again calculated from the error curves of the background linear fit in the plume area. The second contribution comes from the uncertainty of the retrieved background concentration. In contrast to the

WFM-DOAS retrieval results in the sections before, FOCAL AIR retrieves absolute column concentrations. Therefore, a measure for the background concentration precision was the mean a posteriori uncertainty of the xCO_2 retrieval in the background (see for calculation of the enhancement over background also Eq. (5.148)). The uncertainty introduced by the retrieval was estimated as the standard deviation of the retrieval results in the background regions besides the plume after normalization.

In the second group, the major contribution to the uncertainty was the wind speed uncertainty and was estimated to 1.0 m s^{-1} as the standard deviation of all ECMWF ERA5 wind speed values used in the calculation of the mean wind speed. The wind direction uncertainty originated from both the precision with which the main plume direction was estimated, and a possible bending of the plume, and was estimated to $\pm 10\,°$.

Finally, the atmospheric variability was estimated as the standard deviation over the fluxes estimated from the individual cross-sections divided by $\sqrt{n-1}$, with $n = 5$ the number of cross-tracks. All uncertainties were added in quadrature to estimate the final flux uncertainties. The uncertainty values for the different retrieval configurations are given in the Tables 6.16 - 6.19.

Table 6.16.: Uncertainty estimation of the flux inversion for FOCAL AIR absorption-only 2-window xCO_2 and $xCO_2(CH_4)$ retrieval results. The percentages in parenthesis are the magnitude of the uncertainty relative to the estimated emission.

Uncertainty contribution	xCO_2	$xCO_2(CH_4)$
Background normalization	± 1.1 Mt CO_2 yr^{-1} (7 %)	± 1.2 Mt CO_2 yr^{-1} (6 %)
Background total column	± 0.3 Mt CO_2 yr^{-1} (2 %)	± 0.4 Mt CO_2 yr^{-1} (2 %)
Retrieval result noise	± 0.1 Mt CO_2 yr^{-1} (1 %)	± 0.1 Mt CO_2 yr^{-1} (1 %)
Wind speed	± 2.5 Mt CO_2 yr^{-1} (16 %)	± 3.2 Mt CO_2 yr^{-1} (16 %)
Wind direction	± 1.8 Mt CO_2 yr^{-1} (11 %)	± 2.3 Mt CO_2 yr^{-1} (12 %)
Atmospheric variability	± 2.1 Mt CO_2 yr^{-1} (13 %)	± 2.2 Mt CO_2 yr^{-1} (11 %)
Total uncertainty	± 4.0 Mt CO_2 yr^{-1} (25 %)	± 4.7 Mt CO_2 yr^{-1} (24 %)

Table 6.17.: Same as Table 6.16, but for the FOCAL AIR scattering 2-window retrieval.

Uncertainty contribution	xCO_2	$xCO_2(CH_4)$
Background normalization	± 1.5 Mt CO_2 yr^{-1} (13 %)	± 1.1 Mt CO_2 yr^{-1} (7 %)
Background total column	± 0.4 Mt CO_2 yr^{-1} (3 %)	± 0.5 Mt CO_2 yr^{-1} (3 %)
Retrieval result noise	± 0.1 Mt CO_2 yr^{-1} (1 %)	± 0.1 Mt CO_2 yr^{-1} (1 %)
Wind speed	± 1.9 Mt CO_2 yr^{-1} (16 %)	± 2.4 Mt CO_2 yr^{-1} (15 %)
Wind direction	± 1.3 Mt CO_2 yr^{-1} (11 %)	± 1.8 Mt CO_2 yr^{-1} (12 %)
Atmospheric variability	± 2.4 Mt CO_2 yr^{-1} (21 %)	± 2.4 Mt CO_2 yr^{-1} (15 %)
Total uncertainty	± 3.7 Mt CO_2 yr^{-1} (32 %)	± 4.1 Mt CO_2 yr^{-1} (26 %)

The uncertainties of the flux ranged from 24 to 37 % for the different FOCAL AIR retrieval configurations and 24 % for the WFM-DOAS retrieval results, which were in the upper

Table 6.18.: Same as Table 6.16, but for the FOCAL AIR absorption only 1-window retrieval.

Uncertainty contribution	xCO_2	$xCO_2(CH_4)$
Background normalization	± 2.0 Mt CO_2 yr^{-1} (10 %)	± 2.6 Mt CO_2 yr^{-1} (9 %)
Background total column	± 0.3 Mt CO_2 yr^{-1} (1 %)	± 0.5 Mt CO_2 yr^{-1} (2 %)
Retrieval result noise	± 0.1 Mt CO_2 yr^{-1} (1 %)	± 0.2 Mt CO_2 yr^{-1} (1 %)
Wind speed	± 3.3 Mt CO_2 yr^{-1} (16 %)	± 4.5 Mt CO_2 yr^{-1} (16 %)
Wind direction	± 2.4 Mt CO_2 yr^{-1} (12 %)	± 3.2 Mt CO_2 yr^{-1} (12 %)
Atmospheric variability	± 3.5 Mt CO_2 yr^{-1} (17 %)	± 3.7 Mt CO_2 yr^{-1} (13 %)
Total uncertainty	± 5.8 Mt CO_2 yr^{-1} (28 %)	± 7.1 Mt CO_2 yr^{-1} (26 %)

Table 6.19.: Same as Table 6.16, but for the FOCAL AIR scattering 1-window retrieval.

Uncertainty contribution	xCO_2	$xCO_2(CH_4)$
Background normalization	± 2.5 Mt CO_2 yr^{-1} (13 %)	± 2.6 Mt CO_2 yr^{-1}(14 %)
Background total column	± 0.7 Mt CO_2 yr^{-1} (4 %)	± 0.7 Mt CO_2 yr^{-1} (4 %)
Retrieval result noise	± 0.2 Mt CO_2 yr^{-1} (1 %)	± 0.2 Mt CO_2 yr^{-1} (1 %)
Wind speed	± 3.0 Mt CO_2 yr^{-1} (16 %)	± 3.0 Mt CO_2 yr^{-1} (16 %)
Wind direction	± 2.1 Mt CO_2 yr^{-1} (11 %)	± 2.1 Mt CO_2 yr^{-1} (11 %)
Atmospheric variability	± 5.1 Mt CO_2 yr^{-1} (27 %)	± 3.3 Mt CO_2 yr^{-1} (18 %)
Total uncertainty	± 6.8 Mt CO_2 yr^{-1} (37 %)	± 5.6 Mt CO_2 yr^{-1} (30 %)

range of uncertainty estimates for emission estimations from MAMAP data (Krautwurst et al., 2017; Krings et al., 2018; Krautwurst et al., 2021). The wind speed estimation and atmospheric variability introduced the largest uncertainties. Especially for the FOCAL AIR scattering 1-window xCO_2 retrieval-based flux estimation, the atmospheric variability was the largest contributor to uncertainty. For the other retrievals, wind speed and atmospheric variability contributed similarly. The uncertainty due to the wind direction was also relatively high, mainly because the main wind direction was far from orthogonal to the flight tracks ($\sim 55 - 60\,°$). This led to comparably small uncertainties in the wind direction introducing large uncertainties to the resulting flux. In general, the uncertainties were higher in the scattering retrieval configurations than in the according absorption-only retrieval configurations, and also for the xCO_2 compared to the $xCO_2(CH_4)$.

6.3.5. Conclusion on the improvement of total column retrievals by including scattering in the retrieval

In this chapter, the FOCAL AIR retrieval method was tested with synthetic and actual MAMAP measurements. For the synthetic measurements, different scenarios without and with a scattering atmosphere were calculated. Then, the atmospheric concentrations for xCO_2 and xCH_4 were retrieved with the FOCAL AIR retrieval in four different configurations (Sect. 6.3.1). These configurations comprised two fit window definitions in the

SWIR spectral range and two forward models including and excluding the treatment of scattering. The fit windows of the 2-window retrieval configuration were the same as of the WFM-DOAS retrieval applied to MAMAP data (e.g. Krautwurst et al., 2017, 2021). For the 1-window retrieval configuration, one large fit window covering the absorption bands of CO_2 and CH_4 in the SWIR was selected.

For synthetic measurements without scattering in the atmosphere, both absorption-only and scattering retrieval resulted in similar errors, indicating that including scattering in the forward model did not introduce any error by itself. However, separating the fit in the SWIR into two fit windows introduced errors up to 10 times larger for these non-scattering cases, albeit still low. Including scattering in the atmosphere, the errors in the retrieved xCO_2 and xCH_4 increased. There, the errors of the scattering retrieval were lower than in the absorption-only retrieval, although the errors were still larger than in a non-scattering atmosphere (Tables 6.10 and 6.11).

For the retrieval of actual MAMAP measurements, the measurement noise model was adapted to include the forward model error. Additionally, a model for a constant additive offset for each retrieval configuration and fit window was calculated, as retrieving this value introduced additional retrieval result scatter. For the NIR, this additive offset was linearly dependent on the background intensity, while it followed a fourth order polynomial in the SWIR fit windows (Sect. 6.3.2).

The retrieval of xCO_2 and $xCO_2(CH_4)$ as well as xCH_4 on real measurement data in both 2-window retrieval configurations showed lower retrieval result noise, i.e., variability of the retrieved xCO_2 and $xCO_2(CH_4)$ in the background, compared to the 1-window retrieval configuration. Especially the xCH_4 retrieval results of the absorption-only 1-window retrieval showed some residual structures likely linked to surface brightness (Fig. 6.34). The surface reflectance was modeled as a polynomial over the wavelength range, and the fit window might have been too large, or some surfaces might have a surface reflectance with a curvature not being captured completely by the applied third order polynomial.

The significantly lower retrieval noise of the 2-window retrieval results in both absorption-only and scattering retrieval configurations seemed to favor the 2-window retrieval. However, the emission estimate for these retrievals was too low compared to the emission estimate based on activity data and also based on WFM-DOAS retrieval results, except for the absorption-only 2-window $xCO_2(CH_4)$ retrieval results (Table 6.15). As the goal of the FOCAL AIR retrieval was to remove the need to apply the proxy, the 2-window retrieval did not perform satisfactorily.

The emissions estimated from the 1-window scattering retrieval matched the emission estimate using WFM-DOAS retrieval results better, while simultaneously, the emissions estimated from xCO_2 and $xCO_2(CH_4)$ retrieval results were very similar. Nevertheless, the uncertainty was higher (37 and 30 %) compared to the uncertainty of the emission estimated from WFM-DOAS retrieval results (24 %) using the same cross-track and plume definitions. Therefore, on small scales with only CO_2 or CH_4 sources, i.e., where the application of the proxy is possible, applying the FOCAL AIR scattering retrieval does not improve the retrieval results. However, the FOCAL AIR scattering 1-window retrieval using xCO_2 directly without application of the proxy performed reasonably well. Therefore, in areas with mixed

emissions or larger areas, the FOCAL AIR scattering 1-window retrieval could improve the quantification of emissions.

7. Discussion

In chapter 6, the three research questions have been studied separately by applying the respective methods to the relevant data sets and discussing the results. However, data sets from three different instruments were investigated with different retrieval methods, and, in all cases, emissions were estimated. This offered the opportunity to compare the different instruments, methods, and the influence of their combinations on the emission estimate using the cross-sectional flux method.

Therefore, in this chapter, the different instruments AVIRIS-NG, MAMAP, and MAMAP2D-Light with their advantages and disadvantages are compared in Sect. 7.1. Afterward, the different retrievals and their advantages and disadvantages obtained from this study are compared in Sect. 7.2. Finally, in the Sect. 7.3, the differences in estimating emissions from the different data sets is given, with a particular focus on comparing MAMAP 1D data on the one hand and 2D imaging data from AVIRIS-NG and MAMAP2D-Light on the other.

7.1. Comparison of instruments

All three instruments, MAMAP, MAMAP2D-Light, and AVIRIS-NG, are airborne passive remote sensing instruments. However, there are quite some differences regarding their design and capability to retrieve greenhouse gas emissions. In Table 7.1, the main characteristics for all three instruments are again shown[1]. The instruments are compared by their performance in the retrieval of greenhouse gases, their basic design, and practical use.

The main instrument characteristics for comparing the three instruments are the spectral properties in the SWIR spectral range used for retrieving CH_4 and CO_2 column enhancements. These comprise the spectral resolution, the wavelength range, and the SNR. Here, the MAMAP instrument shows the highest spectral resolution with 0.64 nm (Sect. A.4), while MAMAP2D-Light has a spectral resolution of 1.08 nm (Sect. 6.2.1). The AVIRIS-NG system has the lowest spectra resolution with $\sim 5 - 6$ nm, which resulted in the absorption features of CH_4 and CO_2 not being very pronounced around 1650 nm. However, the AVIRIS-NG instrument covers the broadest wavelength range ($380 - 2450$ nm), covering also the absorption bands of CH_4 around 2300 nm and CO_2 around 2000 nm. These absorption bands were better suited for retrieving column enhancements (Sect. 6.1.1) from AVIRIS-NG data. MAMAP2D-Light and MAMAP cover similar wavelength ranges in the

[1] based on table 5.1, repeated and supplemented with additional information for simplicity and ease of comparison between the instruments.

Table 7.1.: Summary of main characteristics of the three instruments MAMAP2D-Light, MAMAP, and AVIRIS-NG. This table is a duplicate of Table 5.1 for the discussion.

Parameter	**MAMAP2D-Light**	**MAMAP**	**AVIRIS-NG**
Spectral range	1559.54 – 1690.05 nm	1587.56 – 1686.90 nm*	380 – 2450 nm
		755.588 – 772.160 nm*	
Spectral sampling	0.34 nm	0.097 nm	5 nm
		0.065 nm	
Spectral resolution	1.08 nm	0.64 nm*	5 – 6 nm
(FWHM)		0.42 nm*	
# of spectral points	384 pixels	1024 pixels (SWIR)	425 pixels
		256 pixels (NIR)	
# of FOV	28	1	600
Across-track	22 m	45 m	1.5 m
spatial resolution			
Along-track	6 m	50 m	1.5 m
spatial resolution			
Data resolution	16-bit (65536 BU)	16-bit (65536 BU)	14-bit (16384 BU)
SNR	$\sim$ 760	$\sim$ 1300 (for SWIR)	$<$ 800 (at 2200 nm)
(illumination)	(at 33000 BU)	(at 33000 BU)	(conditions unclear)
Total weight	43.8 kg	$\sim$ 250 kg	$\sim$ 465 kg
and design	one structure	two Falcon racks	Instrument, racks,
	incl. electronics		and electronic boxes
Dimensions	Length: 875 cm	Length: 650 cm**	Diameter: 57 cm***
	Width: 450 cm	Width: 550 cm**	Height: 83 cm***
	Height: 30 cm	Height: 955 cm**	
Retrieval precision	$<$ 0.7 %	0.2 – 0.3 %	2.3 % (bright surface)
(unbinned)			

*according to recalibration fit described in Sect. A.4

**one Falcon rack

***Only the spectrometer and cylindrical vacuum housing without racks and electronic boxes.

SWIR (1559.54 – 1690.05 nm and 1587.56 – 1686.90 nm, respectively). The SNR is similar for AVIRIS-NG (up to 800) and MAMAP2D-Light ($\sim$ 760). However, the conditions for estimating the AVIRIS-NG SNR are not entirely documented, and for MAMAP2D-Light, this SNR is achieved by binning five detector rows illuminated homogeneously via a glass fiber. The SNR of $\sim$ 1300 of MAMAP for conditions similar to the estimation of SNR from MAMAP2D-Light is significantly higher than for AVIRIS-NG and MAMAP2D-Light.

These spectral characteristics have a direct impact on the fit quality and precision of the retrieved column enhancements for CH_4 and CO_2. For comparison, the results for the WFM-DOAS retrieval after applying the proxy are used for the three instruments. The mean fit

RMS, i.e., the difference between the fitted and measured spectra, for the MAMAP2D-Light Jänschwalde powerplant flight was $RMS = 0.54\,\%$ (see Sect. 6.2.2). Similarly, the RMS for the MAMAP Jänschwalde power plant flight retrieved with WFM-DOAS was $RMS = 0.65\,\%$. Contrary, the average RMS of the AVIRIS-NG data set was $RMS = 1.3\,\%$ after filtering (Sect. 6.1.3) and therefore significantly larger than for the MAMAP and MAMAP2D-Light instruments.

Furthermore, the background retrieval scatter for AVIRIS-NG data over a relatively bright, homogeneous surface was $\pm\,2.3\,\%$ (Table 6.1). The MAMAP and MAMAP2D-Light WFM-DOAS retrieval results showed similar lower background retrieval scatter of $\pm\,0.22\,\%$ and $\pm\,0.28\,\%$, where the MAMAP2D-Light data were binned to the MAMAP ground scene size. The background retrieval scatter for MAMAP2D-Light data without binning was still $\pm\,0.70\,\%$.

Additionally, the retrieval results for AVIRIS-NG data show a much larger surface property dependency than MAMAP and MAMAP2D-Light data (see, e.g., Fig. 6.6). Especially over surfaces with reflection properties similar to absorption features of CH_4, significant biases exist in AVIRIS-NG retrieval results even after applying the proxy, and the respective surfaces are visible in the retrieval results (see Sect. 6.1.4). Especially for MAMAP2D-Light, no strong residual dependency of the retrieval results from the surface type is visible (see Fig. 6.21).

Regarding the ground scene size, AVIRIS-NG observes small ground scenes ($\sim 1.5 \times 1.5\,\mathrm{m}^2$ at a flight altitude of 1500 m), by imaging the ground scenes onto the detector without spatial scrambling. MAMAP2D-Light and MAMAP instead use a fiber bundle, which, for MAMAP2D-Light, scrambles the light originating from $22 \times 6\,\mathrm{m}^2$ (across $\times$ along the flight track) ground scenes and project these onto the detector. For MAMAP, this results in ground scene sizes of $45 \times 90\,\mathrm{m}$. The along-track ground scene size also depends on the aircraft speed and integration time and is taken here for the most used aircraft. Using a glass fiber bundle in MAMAP2D-Light allows to average over at least five detector rows to improve the SNR (see above for SNR impact), and additionally guarantees homogeneous illumination of the entrance slit in spectral direction (see, e.g., Hummel et al., 2022). Inhomogeneous illumination of the slit, e.g., by different surface types in one observed ground scene, skew the ISRF, possibly introducing biases. The glass fiber scrambles the light; therefore, the slit is illuminated homogeneously even over heterogeneous scenes.

The imaging capability is the primary design difference between MAMAP2D-Light and AVIRIS-NG on one side and MAMAP on the other. While the MAMAP instrument observes one ground scene below the instrument simultaneously, MAMAP2D-Light observes 28 and AVIRIS-NG 600 ground scenes across the flight track simultaneously. Imaging allows for scanning larger areas and detecting small plumes (see, e.g., Sect. 6.1.4, Cusworth et al., 2021a), which might be overlooked with the sparesly sampled MAMAP data. Additionally, as also will be discussed in Sect. 7.3, imaging data allow using significantly more cross-sections in the cross-sectional flux method. For MAMAP2D-Light, the number of cross-sections could theoretically be enhanced to 36 ground scenes by rotating the detector at the cost of a reduced spectral range of slightly below 100 nm. As has been demonstrated by the MAMAP instrument, a wavelength range of 100 nm should be sufficient for the accurate retrieval of CH_4 and CO_2 from measurements with spectral resolution $\sim 1\,\mathrm{nm}$. Rotating

the detector will be tested in the future. However, a significant redesign of the detector mount is required and, therefore, not yet realized.

A design difference between MAMAP and AVIRIS-NG on one side and the MAMAP2D-Light instrument on the other side is the coverage of the O_2A absorption band, although for different reasons. In the case of AVIRIS-NG, this is part of the broad wavelength range covered by the one spectral channel of the instrument. The broad wavelength range was implemented to characterize surface types, while for MAMAP an additional channel covering the O_2A band with a spectral resolution of 0.42 mn is part of the complete instrument to correct for light path changes due to, e.g., scattering in the atmosphere, given an according retrieval making use of the channel (e.g. Reuter et al., 2017b), which is discussed in the next section 7.2. However, for AVIRIS-NG, the O_2A was not exploited as scattering is assumed to influence CH_4 and CO_2 similarly, and cancels out mostly with the $CH_4(CO_2)$ proxy (Sect. 6.1.2). Additionally, Ayasse et al. (2018) found in their study that errors due to the neglection of aerosols in the retrieval were small compared to errors introduced by the surface type. Finally, the goal of CH_4 retrievals on AVIRIS-NG data is the detection and quantification of emission point sources, which do not require the background total column to be determined precisely, as long as the column enhancement above the background is determined correctly. MAMAP2D-Light was designed without the O_2A spectral channel as the experience with MAMAP showed that the detection and quantification of point sources are possible using CO_2 or CH_4 as a proxy for the other gas.

Excluding the second spectral channel made the MAMAP2D-Light instrument significantly smaller and lighter compared to the other two instruments, enabling the instrument to be flown on much smaller aircraft than MAMAP (which requires at least an aircraft of the size of a Cessna 207) and AVIRIS-NG (requiring even larger aircraft). In combination with not being temperature stabilized or evacuated, this allows the MAMAP2D-Light instrument to be easily and quickly deployed for measurement campaigns.

MAMAP was, to the author's best knowledge, the first passive remote sensing airborne instrument dedicated to measuring CH_4 and CO_2 and paved the way for developing the MAMAP2D-Light and MAMAP2D instruments, the latter still being constructed. The MAMAP2D instrument will comprise a SWIR channel and a NIR channel covering the O_2A absorption bands with ~ 0.5 nm and ~ 0.2 nm spectral resolution. It will observe 36 ground scenes simultaneously with a spatial resolution slightly higher than MAMAP2D-Light. Currently, the MethaneAir instrument (Staebell et al., 2021) is the only other airborne imaging remote sensing instrument specifically designed to use SWIR measurements for the detection and quantification of CH_4 (and due to the design also CO_2) emissions. Initial calibration and test flight data for MethaneAir show a fit RMS of 0.45 % for the CH_4 fit window, which is similar to the fit RMS of MAMAP2D-Light and MAMAP.

In summary, the three instruments investigated in this thesis have different advantages and disadvantages. The high spatial resolution and good SNR of the AVIRIS-NG instrument allow for the detection of small point sources, and the wide swath allows to cover large areas in reasonable times. However, due to the lower spectral resolution and therefore smaller ground scene precision and dependency of the retrieval results on surface properties, detection of plumes over heterogeneous terrain or from areal sources is challenging. The higher spectral resolution of the MAMAP and MAMAP2D-Light instruments show significantly

less dependency of the retrieval results on the surface type, therefore being better suited for areal sources (e.g., quantifying emissions from a landfill, Krautwurst et al., 2017), and plumes will be observable over longer distances. However, the larger ground scene sizes of the MAMAP2D-Light instrument compared to AVIRIS-NG might make detecting very small point sources difficult. Following the classification of Jacob et al. (2022, in discussion), AVIRIS-NG clearly falls into the category of a point source imager. The MAMAP2D-Light instrument was designed as a point source imager, too. However, the spectral resolution in principle also allows the quantification of spatially limited areal emissions such as, e.g., from landfills. Nevertheless, the missing O_2A band renders retrieval of absolute columns more difficult. This will be enhanced significantly by the MAMAP2D instrument currently being built at IUP Bremen (see also Sect. 8).

7.2. Comparison of retrieval methods

Additionally to the instruments, different retrievals applied to different data sets were examined. The comparison of WFM-DOAS, MF, and IMAP-DOAS applied to AVIRIS-NG data was already quantitatively discussed in Sect. 6.1.5, where the author calculated the WFM-DOAS retrieval results, and Andrew Thorpe provided the MF and IMAP-DOAS retrieval results. While the WFM-DOAS and MF retrievals are very fast non-iterative retrievals using precalculated background spectra and weighting functions adapted to the atmospheric state during the overflight in the case of WFM-DOAS and a general precalculated absorption spectrum of CH_4 in the case of the MF retrieval (Thompson et al., 2015), the IMAP-DOAS retrieval is an iterative absorption-only retrieval incorporating forward model calculations in each iteration step for each ground scene (Thorpe et al., 2014). It is comparable with the FOCAL AIR absorption-only retrieval, with a different layering of the atmosphere and utilizing a Gauss-Newton solver (see, e.g., Thorpe et al., 2017) instead of a Levenberg-Marquardt-Fletcher solver, which might influence convergence speed (Rodgers, 2000). The main characteristics of each retrieval are summed up in table 7.2.

Table 7.2.: Overview over the main characteristics of the WFM-DOAS, FOCAL AIR, MF and IMAP-DOAS retrievals.

	WFM-DOAS	FOCAL AIR	MF	IMAP-DOAS
Iterative retrieval	no	yes	no	yes
Forward model	precalculated SCIATRAN spectrum	parametrized scattering	precalculated CH_4 target spectrum	absorption-only atmosphere
Absorption only?	yes	no	yes	yes
Spectral bands analyzed	$1590 - 1680\,\mathrm{nm}$ $2040 - 2380\,\mathrm{nm}$	$760 - 772\,\mathrm{nm}$ $1590 - 1680\,\mathrm{nm}$	$2100 - 2450\,\mathrm{nm}$	$2275 - 2360\,\mathrm{nm}$
Computation time	low - medium	high	low	high

In the following, WFM-DOAS and FOCAL AIR are compared in more detail. Therefore, sensitivity studies using simulated measurements and the retrieval of actual measurements are considered.

Regarding the simulated measurements, the FOCAL AIR retrieval without application of the proxy produced less noise for scenarios including aerosols in both the absorption-only and scattering retrieval (see Sect. 6.3.1) compared to WFM-DOAS (Krings et al., 2011). For FOCAL AIR, the biases for different aerosol scenarios varied between 0.09 % and 0.29 % for xCO_2, and 0.07 % and 0.27 % for xCH_4 in the absorption-only retrieval configurations. In the scattering 1-window retrieval, the biases in different aerosol scenarios were reduced to between 0.05 % and 0.22 % for xCO_2, and 0.04 % and 0.18 % for xCH_4. For the WFM-DOAS retrieval, including scattering in the simulated measurements produced biases of ± 0.33 %

(PSF CH_4) and $\pm 0.38\,\%$ (PSF CO_2) for an OPAC urban up to $\pm 1.07\,\%$ (PSF CH_4) and $\pm 1.26\,\%$ (PSF CO_2) for an OPAC desert scenario (Krings et al., 2011). After applying the $CO_2(CH_4)$ to the WFM-DOAS retrieval results, the bias was reduced to $0.05\,\% - 0.18\,\%$, depending on the scenario. Therefore, for scenarios where the proxy method is valid, similar biases due to aerosols are expected for the WFM-DOAS proxy and FOCAL AIR single gas results.

The simulated measurements were performed excluding measurement noise, i.e., showing an ideal measurement and only the influence of the retrieval to biases. Actual world measurements here provide an additional comparison. While the exact aerosol scenario is unknown in actual measurements, comparing WFM-DOAS and FOCAL AIR retrieval results for a case where the proxy method is valid should result in similar retrieval results (see Sect. 6.3.3).

In actual measurements, retrieving xCO_2 with FOCAL AIR scattering in the 1-window retrieval produced higher background retrieval noise ($\pm 0.37\,\%$ vs $\pm 0.22\,\%$, Table 6.14), but delivered very similar retrieval results (Sect. 6.3.3) and emission estimates ($18.6 \pm 6.8\,\mathrm{Mt\ CO_2\,yr^{-1}}$ vs $19.4 \pm 4.7\,\mathrm{Mt\ CO_2\,yr^{-1}}$, Table. 6.15) as the WFM-DOAS retrieval results. In contrast, for the 2-window scattering retrieval, the background retrieval scatter for xCO_2 was as low as for WFM-DOAS with $\pm 0.22\,\%$, but the emission estimation was significantly lower with $15.7 \pm 4.0\,\mathrm{Mt\ CO_2\,yr^{-1}}$.

Regarding pure correlation with WFM-DOAS results, the 2-window absorption-only retrieval after application of the $CO_2(CH_4)$ proxy performed best overall, with background retrieval scatter of $\pm 0.23\%$ (Table 6.14) and best correlation with WFM-DOAS proxy retrieval results (Sect. 6.3.3), while the emission estimation yielded $19.8 \pm 4.7\,\mathrm{Mt\ CO_2\,yr^{-1}}$ (Table. 6.15), and was therefore very similar to the WFM-DOAS proxy retrieval results.

In Fig. 7.1, the three FOCAL AIR retrieval configurations matching emissions best (1-window scattering xCO_2 and $xCO_2(CH_4)$, and absorption-only 2-window $xCO_2(CH_4)$) are displayed next to the WFM-DOAS $CO_2(CH_4)$ proxy results, showing the general agreement between the retrieval configurations (Sect. 6.3.3). The scattering 1-window retrieval $xCO_2(CH_4)$ shows larger variability due to the xCH_4 fit in the 1-window retrieval still exhibiting some surface brightness dependence.

In the scattering 1-window xCO_2 retrieval results, the plume is less visible due to the higher background retrieval noise (see above). Nevertheless, the matching inversion indicates the possibility of applying the FOCAL AIR scattering 1-window retrieval to examine larger areas or more complicated scenes, where sources of CH_4 and CO_2 are mixed or gradients over longer distances are of interest. For the FOCAL AIR $CO_2(CH_4)$ proxy results, the limitations of the proxy method still apply, so the much longer retrieval time of FOCAL AIR absorption-only 2-window while still having to apply the proxy method gives no advantage.

Nevertheless, several improvements to the FOCAL AIR retrieval are possible. First, as the retrieval "connects" the spectra of the O_2A band and the SWIR, the missing absolute radiometric calibration of MAMAP might introduce pseudo-noise if the white light source intensity is not constant over the complete spectral range, which is likely. Additionally,

while the improved spectral calibration for MAMAP improved the retrieval results, a more precise calibration including several high resolution measurements of the ISRF of MAMAP across both spectral channels could improve the retrieval further.

The computation time between different retrievals varied significantly, with longer computation times for iterative optimal estimation-based than for non-iterative retrievals. As an example, the processing of the overflight over the Jänschwalde power plant obtained with MAMAP2D-Light ($\sim$ 1.1 million data points) took approximately 14 hours, while the FOCAL AIR absorption-only 1-window retrieval of the remote sensing part of the Jänschwalde power plant flight recorded with MAMAP ($\sim$ 14000 data points) needed approximately 19 hours and the FOCAL AIR scattering 2-window retrieval took over two days. The most time-consuming step in the FOCAL AIR retrieval was the convolution of the high spectral resolution forward model with the ISRF calculated in each iteration for each ground scene. In WFM-DOAS, on the other hand, the high-resolution pre-calculated intensities and weighting functions are convolved with the ISRF only once, which is the main factor in retrieval time differences between FOCAL AIR and WFM-DOAS. As each data point is retrieved separately, parallelizing calculations could significantly speed up the retrieval as long as enough CPU cores are available. The time difference between FOCAL AIR absorption-only 1-window and FOCAL AIR scattering 2-window was mostly due to the different sizes of the state vectors, which again resulted in more convolutions needing to be calculated in the 2-window retrieval. For the MF and IMAP-DOAS retrieval methods, unfortunately, no comparable computation times were available. However, the IMAP-DOAS retrieval is not applied to whole AVIRIS-NG data sets due to the long computational times (Thorpe et al., 2014, 2017), while the MF is also applied to large AVIRIS-NG data sets (Frankenberg et al., 2016; Duren et al., 2019; Cusworth et al., 2021a), indicating a much faster retrieval.

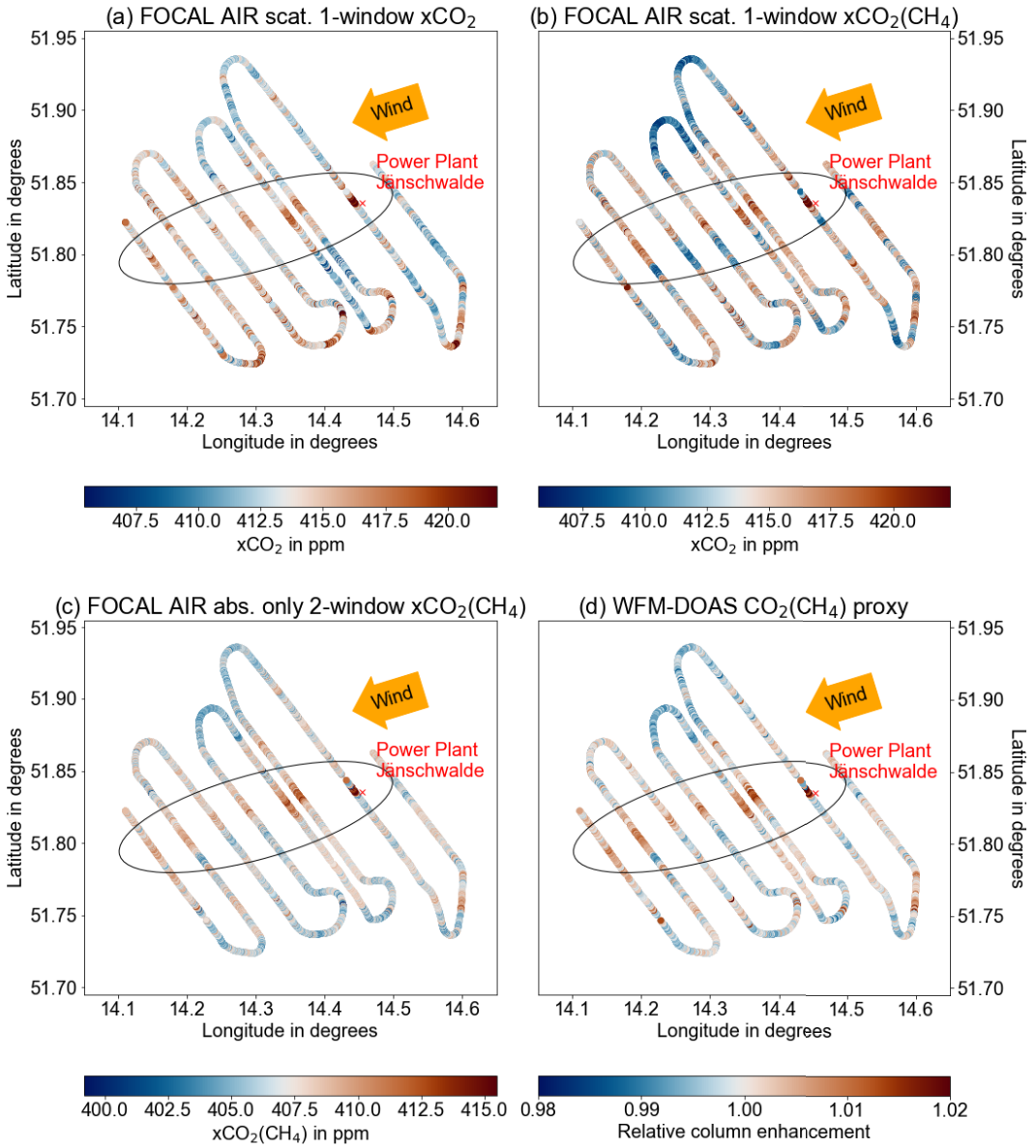

Figure 7.1.: Comparison of FOCAL AIR (a) scattering 1-window xCO_2, (b) scattering 1-window $xCO_2(CH_4)$ and (c) absorption-only 2-window retrieval results with (d) WFM-DOAS retrieval results.

7.3. Emission estimate from plume images

In this thesis, the emissions were estimated using the cross-sectional flux method (Sect. 5.3). Applying the cross-sectional flux method requires that enough measurements are taken besides the plume to determine the background and that the plume can be separated from the background. Additionally, averaging over multiple cross-sections was used to average over atmospheric variability caused by turbulence.

Calculating the cross-sectional flux from imaging data from AVIRIS-NG and MAMAP2D-Light provided several advantages over the emission estimate from 1D MAMAP data. As turbulence and wind direction changes break up the plume horizontally, averaging over a denser pattern of cross-sections gives a better emission estimate and reduces the uncertainty contribution due to the track-to-track variability of the flux estimate. In general, the more independent cross-sections through the plume are available, the lower the uncertainty due to atmospheric variability gets.

In the case of the MAMAP Jänschwalde power plant flight, only five cross-tracks through the plume showed definitive plume enhancements. Therefore, the atmospheric variability gave rise to large uncertainties. The track-to-track variability in the flux was large, and the number of cross-sections did not reduce this uncertainty drastically ($\pm 12\,\%$, see Sect. 6.3.4 and A.5). This effect has been studied by Wolff et al. (2021) for simulated measurements over the power plant Jänschwalde on 22 May 2018 with the CHARM-F instrument, which is also a non-imaging remote sensing instrument. For an overflight time of 10:00 - 12:00 h, local averaging over multiple cross-tracks reduced the error of the estimated emission compared to the true emission. However, depending on the exact realizations of the plume used for the emission estimate, the emissions were regularly underestimated by up to $-10\,\%$ (Wolff et al., 2021). As the flight strategy for CHARM-F and MAMAP are similar, the results of the simulation experiments are likely qualitatively comparable to the emission estimates calculated from MAMAP data in this thesis.

The MAMAP2D-Light measurements of the CO_2 plume of the Jänschwalde power plant on 17.06.2021 were performed at half the total emissions ($11.6\,\mathrm{Mt\ CO_2\ yr^{-1}}$, see Sect. 6.2.2) and only slightly lower wind speed than during the MAMAP measurements in 2018 ($22.3\,\mathrm{Mt\ CO_2\,yr^{-1}}$). Therefore, the plume was significantly smaller. Nevertheless, due to the imaging capabilities of MAMAP2D-Light, the flux was estimated from over 90 independent cross-sections after binning to $100 \times 100\,\mathrm{m^2}$ ground scenes (Sect. 6.2.2). In consequence, accumulations and dilutions in eddies were much better captured, which reduced the uncertainty contribution due to atmospheric variability drastically ($\pm 4\,\%$, Sect. 6.2.2). Additionally, the uncertainty due to the normalization to the background is reduced for larger numbers of cross tracks, as it is assumed that the error produced by the background fit is statistically distributed and not systematic over the whole flight.

For AVIRIS-NG data, even though the plumes detected in the ABoVE data set (P1 - P4) were much shorter, still 16 to 68 independent cross-sections could be defined for the different plumes due to the high spatial resolution (Sect. 6.1.6). For the coal mine ventilation shaft plume (P5) observable over 1 km, the uncertainty due to atmospheric variability was reduced

to $\pm 4\,\%$. For the shorter plumes, the uncertainty still remained in the order of $\pm 17\,\% - 32\,\%$ (Table 6.6).

A direct comparison between AVIRIS-NG and MAMAP2D-Light concerning the detection of CH_4 plumes is difficult. Primarily, for MAMAP2D-Light, an empirical detection limit has not yet been determined by controlled release experiments, which were initially planned but had to be postponed due to bad weather conditions during possible experiment times. For AVIRIS-NG, an empirical detection limit of $\sim 10\,\mathrm{kg\,h^{-1}}$ was estimated during controlled release experiments (Thorpe et al., 2016) under favorable conditions. These comprised a relatively low flight altitude and bright surfaces for consistent detection. Additionally, the plume length appeared to be $10 - 20\,\mathrm{m}$. Therefore, with a ground scene size of $3 - 5\,\mathrm{m}$ as in the data set investigated in this thesis, these plumes would be only 2 - 3 ground scenes long and therefore challenging to be detected. Nevertheless, plumes with $100\,\mathrm{kg\,h^{-1}}$ are well detectable with AVIRIS-NG even under less favorable conditions, as was shown in this thesis.

For MAMAP2D-Light, a very preliminary detection limit was estimated by overlaying a CH_4 plume over actual retrieval results. The plume was modeled as a gauss plume of $114\,\mathrm{kg\,h^{-1}}$ at $5\,\mathrm{m\ s^{-1}}$ wind speed. The relative column enhancements of the model were gridded to the MAMAP2D-Light spatial resolution and added to a non-orthorectified flight track over a compressor station in Northern Germany (Fig. 7.2). The image indicated a point source detection limit for MAMAP2D-Light below $100\,\mathrm{kg\,h^{-1}}$ for a flight altitude of $\sim 1.5\,\mathrm{km}$.

However, for the emission estimate from all data sets, wind speed uncertainty is one of the largest uncertainties. It was especially large for the plumes recorded by AVIRIS-NG. For these near-surface plumes, a well-mixed behavior in the boundary layer can not be assumed. Therefore, averaging over the wind in the boundary layer, where the ERA5 model is more reliable than at the surface, was not possible. Instead, surface weather stations several kilometers away from the sources were used. Therefore, wind uncertainties were one of the major uncertainty contributors. This can only be mitigated entirely by measurements of the wind in the boundary layer or on-site during or close to the overflight time.

An alternate approach to estimate emissions was taken by, e.g., Varon et al. (2018) and Jongaramrungruang et al. (2019) Based on large eddy simulations, they established a relationship between the angular distribution of the enhancement, the total mass enhancement in the plume, and the flux. Applying this relationship to observed enhancements then allowed estimating emissions without knowing the surface wind. Still, the uncertainties of the fluxes obtained by this method are large. Furthermore, it has to be seen if this method can also be applied to non-point source emissions or for larger plumes not captured by a single overpass and containing gaps. An example of such measurements would be the MAMAP2D-Light measurements over the power plant Jänschwalde (Fig. 6.21).

Overall, the cross-sectional flux method proved applicable to imaging and non-imaging plumes, given that the retrieval showed no significant dependency on surface features besides the plume. Surface features visible in the retrieval results beside the plume prohibited the application of the cross-sectional flux method for some plumes detected in AVIRIS-NG

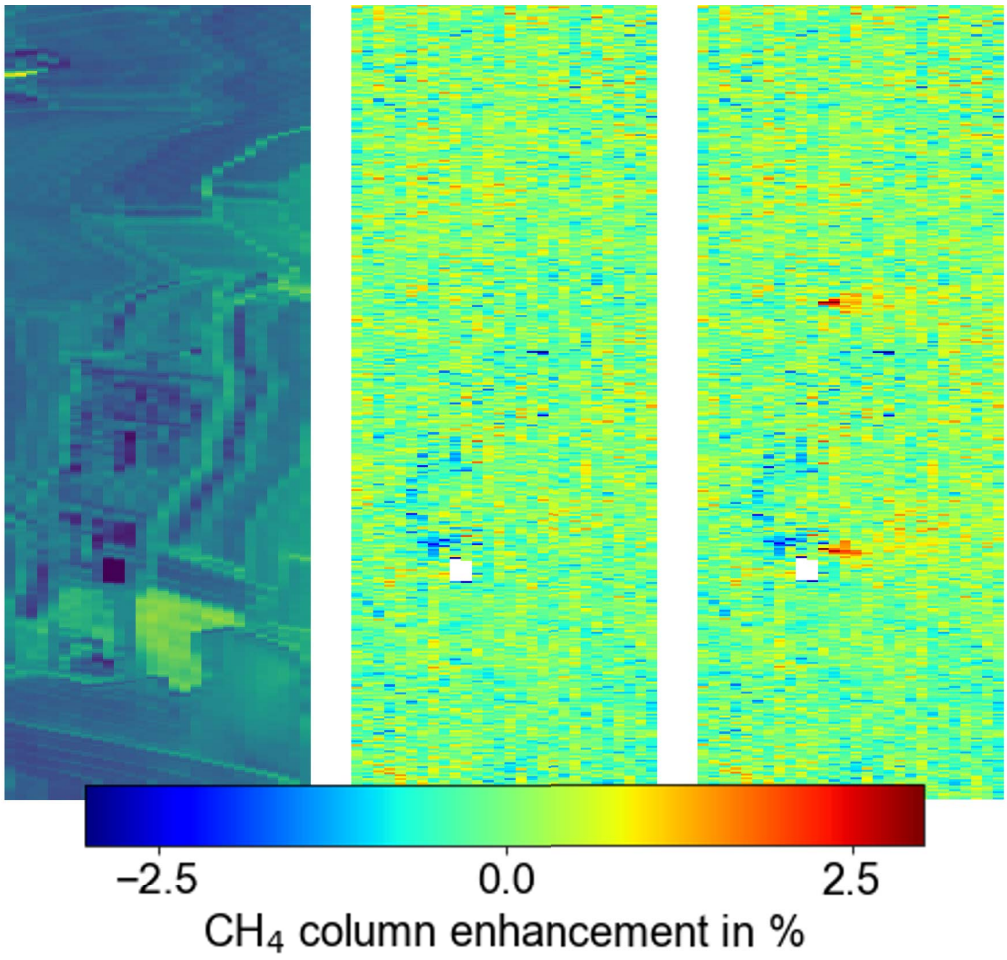

Figure 7.2.: Preliminary estimation of the detection limit for MAMAP2D-Light. A false-color image of a compressor station in northern Germany is shown on the left. The compressor station covers most of the scene shown. In the center, the WFM-DOAS $xCH_4(CO_2)$ retrieval results over this scene are shown. On the right, the CH_4 enhancements of two gaussian plumes simulated for $5\,\mathrm{m\ s^{-1}}$ and $114\,\mathrm{kg\,h^{-1}}$ CH_4 emissions are added onto the non-orthorectified data at two positions.

data (see Sect. 6.1.4). Also, the linear dependency on the wind speed requires precise wind speed estimations for the plume altitude. These wind speed estimates are not readily available in case of small (and therefore short) plumes at previously unknown locations. For the MAMAP2D-Light instrument, the cross-sectional flux method will remain a primary method of emission estimation even for smaller plumes due to the low dependency of retrieval results on surface properties. Nevertheless, the application of the IME method (Jongaramrungruang et al., 2019) to detected plumes might decrease uncertainties especially for smaller plumes which are captured during a single overflight (see, e.g., Varon et al., 2018, for an instrument with $\sim 1\,\%$ instrument precision).

8. Summary and outlook

The United Nations have pledged to reduce anthropogenic greenhouse gas emissions to keep global warming below 1.5 °. However, the global mean surface temperature has already reached 1.1 ° above preindustrial times for the average of the years 2011 – 2020 (S.K.Gulev et al., 2021). While for the global methane levels, a brief stabilization period could be observed at the end of the 20th and beginning of the 21st century, CO_2 levels have been rising continuously, and CH_4 level increases have accelerated since 2020. For a possibility of reaching the goal to limit temperature increases below 1.5 °, huge reductions in the emissions of CH_4 and CO_2 have to be implemented (IPCC 2018, 2018), and the reduction pledges monitored.

In this thesis, improvements of the detection and monitoring of CH_4 and CO_2 emissions were studied. Three major questions have been studied: First, the possibility and limitations of retrieving CH_4 enhancements from hyperspectral data with the WFM-DOAS retrieval algorithm; second, the development, characterization, and first validation measurement results obtained with MAMAP2D-Light, an imaging instrument specifically designed for the detection and quantification of CH_4 and CO_2 sources; third, the inclusion of fitting (aerosol) scattering properties in the FOCAL AIR retrieval scheme to enable the retrieval of total columns and column enhancements without the need for the proxy method. In the following, the results for these three research topics are summarized, and, finally, an outlook for future research is given.

Retrieval of greenhouse gas emissions and emission estimate from hyperspectral data with the WFM-DOAS retrieval method

The WFM-DOAS method was successfully adapted and applied to hyperspectral AVIRIS-NG data. It was the first application of the WFM-DOAS retrieval to lower spectral resolution data. Several plumes were detected (Sect. 6.1.4). For five of these plumes, the emissions could be estimated (Sect. 6.1.6) with the cross-sectional flux method. The emissions of a vent revealed emissions of $196 \pm 94\,\mathrm{kg\,h^{-1}}$ and $132 \pm 61\,\mathrm{kg\,h^{-1}}$ for two overflights on two consecutive days, while two other sources related to gas extraction emitted $157 \pm 98\,\mathrm{kg\,h^{-1}}$ and $204 \pm 108\,\mathrm{kg\,h^{-1}}$. Emissions of a coal mine ventilation shaft were estimated to be $1220 \pm 450\,\mathrm{kg\,h^{-1}}$. These source strengths are quite common, as indicated by the log-normal distribution of sources in the Four Corners region (Frankenberg et al., 2016). Major sources of uncertainty for the flux inversion proved to be the wind speed uncertainty and normalization to the background. The latter depended mostly on the surface type and surface type changes below the plume. For the shorter plumes, also atmospheric variability played an important but usually smaller role than the other two factors.

In simulation experiments (Sect. 6.1.2), it was assessed that applying the WFM-DOAS method to AVIRIS-NG data and applying the proxy method reduces biases due to the assumed background model calculated with SCIATRAN to well below 1 % on the scale of the observed plumes. Larger surface elevation deviations would lead to larger biases. However, below short plumes, the elevation would only change smoothly or by smaller amounts, e.g., over buildings, therefore not introducing significant biases. Large deviations of CH_4 from the linearisation point led to an underestimation of the true enhancement. However, such enhancements are only observed near the source for very strong emmitters. In these cases, the plume expands further so that the cross-sectional flux method for emission estimate could be applied to downwind tracks with less extreme enhancements where the bias becomes negligible. In addition, possibly co-emitted CO_2 leads to a bias in the proxy, potentially masking weak CH_4 emission plumes in the proxy results. Finally, different surface types lead to hugely varying biases, where many biases could be reduced to well below 1 % with the application of the proxy method. However, for surface types with reflection properties similar to the absorption spectrum of CH_4, biases up to 11 % (paving concrete) were estimated.

The comparison with IMAP-DOAS and MF retrieval results showed good agreement for the coal mine ventilation shaft plume and the oil or gas extraction plume P3 (Sect. 6.1.5). Larger discrepancies were observed between WFM-DOAS and MF results for the other three plumes for which emissions were estimated. A possible cause could be using a constant CH_4 absorption spectrum target for the MF, which was not adapted to the conditions during the overflight up to now. The retrieval scatter in the background over a homogeneous surface of the WFM-DOAS retrieval results was improved compared to the MF retrieval results for all plumes except the coal mine ventilation shaft plume. For this plume, all three retrievals produced similar background column scatter.

In conclusion, the WFM-DOAS method is well suited for retrieving CH_4 column enhancements from lower spectral resolution hyperspectral data. The more physically based retrieval reduced background retrieval scatter, increasing the precision in the retrieved CH_4 plumes. Further advancements could include using a look-up table for surface elevation to eliminate residual biases from elevation changes, although these have not been a factor for the detected plumes. Additionally, potentially fitting the surface type from parts of the spectra not affected by absorption and then using an appropriate spectrum from a spectral database in addition to the polynomial fit could further improve the retrieval. Furthermore, the WFM-DOAS retrieval being able to retrieve CH_4 enhancements over the local background from hyperspectral data now renders the application of the WFM-DOAS retrieval on hyperspectral satellites such as the EnMAP (Guanter et al., 2015) and PRISM (Mouroulis et al., 2014) satellite a possibility.

Improvement of quantification and observation of greenhouse gas emissions by MAMAP2D-Light

The Methane Airborne MAPper 2D breadboard (MAMAP2D-Light) was finalized, built, preliminarily characterized, and flown for a first measurement flight as a major part of this thesis. The author's main contributions beside the calculations and evaluations of

data presented in this thesis were the development of the control software, assisting in the assembly and adjustment of the instrument, conducting calibration measurements together with the MAMAP team of IUP Bremen, assisting in the flight planning and operating the instrument during the test and measurement flights.

The laboratory characterization showed an ISRF with FWHM of $\sim 1.08\,\mathrm{nm}$ and a spectral sampling of $\sim 0.34\,\mathrm{nm}$. Approximately 1.5 % of the detector pixels were classified as bad. The causes for a pixel to be flagged as bad were either too high dark noise, too low dark current ("dead pixels"), or too high or too low sensitivity to illumination.

As the instrument is not temperature stabilized, regular dark spectra with a closed shutter were recorded during the flight. These were compared to dark spectra acquired in the lab and showed only minor changes (below 10 BU) over the flight. Dark spectra recorded with an open shutter but closed lid on the front optics showed a dark current $\sim 380\,\mathrm{BU}$ lower than with the shutter closed. As spectra would see the dark current as with the open lid dark measurements, these laboratory dark measurements were used for the dark current correction. Additionally, 10 BU were subtracted from these dark spectra to account for the additional thermal dark current in-flight compared to the laboratory.

With the observations from the first measurement flight over the power plant Jänschwalde, an SNR of ~ 750 was calculated. It is slightly lower than the theoretical SNR of ~ 910. A possible cause for the lower SNR in actual measurements could be stray light contributions, which have not been investigated as part of this thesis. The background retrieval scatter was $\pm 0.7\,\%$ for the single measurement retrievals, and binning to $100 \times 100\,\mathrm{m}^2$ pixels reduced the retrieval noise to $\pm 0.28\,\%$, which is comparable to the retrieval noise of MAMAP measurements ($< 0.3\,\%$, Krautwurst et al., 2017, 2021). The flux inversion of the observed power plant plume of the power plant Jänschwalde gave a total emission of $10.3 \pm 1.8\,\mathrm{Mt\ CO_2\,yr^{-1}}$ ($\pm 17\,\%$), compared to $11.6\,\mathrm{Mt\ CO_2\,yr^{-1}}$ estimated from average weekly activity data for calendar week 24. The main uncertainty contribution by far was the wind speed uncertainty, followed by the uncertainty due to atmospheric variability. The uncertainty due to background normalization and retrieval noise were 2.1 % and 1.4 %. Therefore, validating the MAMAP2D-Light instrument with the power plant plume was successful.

With the successful validation and the instrument performing well, a unique, lightweight, precise measurement system for detecting and quantifying CH_4 and CO_2 emissions from point sources has been successfully deployed as part of this thesis. Furthermore, the design allows for flexible deployment of the instrument on multiple platforms. For example, the instrument will be flown on board the High Altitude Long range Operations (HALO) aircraft during the COMET 2.0 campaign targeting CH_4 emissions in Canada in the summer of 2022.

Improvement of greenhouse gas retrievals by including the treatment of scattering in FOCAL AIR

To enable the retrieval of CO_2 and CH_4 columns in more complex areas, e.g., over scales where the assumption of constant concentrations of the second gas are not valid, and there-

fore, the proxy approach can not be applied anymore, or in areas with changing and larger aerosol loads, the new FOCAL AIR retrieval, including the retrieval of scattering parameters, was developed for airborne geometry based on the FOCAL retrieval (Reuter et al., 2017b) and applied to simulated and real MAMAP measurements.

A combination of two fit windows and two state vector configurations was investigated, resulting in four retrieval configurations. The fit windows investigated comprised a large fit window covering the whole SWIR channel of the MAMAP instrument, i.e. both the main absorption features of CH_4 and CO_2, and separate fit windows covering the absorption bands of CO_2 and CH_4 separately, with a gap between the two fit windows. The two state vector configurations comprised an absorption-only retrieval scheme, which was used as the baseline to determine possible advances with the scattering retrieval, and the scattering retrieval configuration.

In simulated measurements, the separate fit window retrieval produced larger biases even for cases without scattering included in the simulated measurements and for both the scattering and absorption-only retrieval. Fitting the scattering parameters improved the retrieval results when aerosols and rayleigh scattering were included in the simulated measurements. However, this did not eliminate the bias completely, and, dependent on the scenario, biases of up to 0.22 % remained in the extreme cases (Sect. 6.3.1).

Applying the retrieval to MAMAP measurements acquired over the power plant Jänschwalde in Mai 2018, the 1-window retrieval results were more consistent with WFM-DOAS retrieval results. However, including scattering in the retrieval here increased the background retrieval scatter compared to the absorption-only retrieval and to WFM-DOAS retrieval results. The emission estimate from WFM-DOAS proxy retrieval results was $19.4 \pm 4.7\,\mathrm{Mt\,CO_2\,yr^{-1}}$, which was slightly lower than the estimated emissions from productivity data and yearly emissions. The latter gave an estimated emission of $22.3\,\mathrm{Mt\,CO_2\,yr^{-1}}$. The absorption-only 2-window proxy retrieval gave similar results, while the absorption-only 1-window proxy retrieval showed significantly higher emission estimates. These are caused most likely by less accurate CH_4 retrieval results in the large fit window, where higher retrieval scatter was observed. Including scattering in the retrieval, the 1-window retrieval for both the proxy and the pure xCO_2 retrieval yielded similar results, indicating that, in this case, both CO_2 and CH_4 could be retrieved well. Additionally, the estimated emissions of $18.6 \pm 6.8\,\mathrm{Mt\,CO_2\,yr^{-1}}$ for the CO_2 retrieval results matched the estimation using WFM-DOAS results and, although slightly lower, was consistent with the reported emissions in the uncertainty range estimated.

Therefore, the FOCAL AIR 1-window retrieval including scattering is a candidate for further investigations over more complex terrain and larger areas and could eliminate the use of the proxy. This is especially valuable for the validation of satellite measurements, where accurate xCO_2 and xCH_4 retrieval results are necessary. However, this comes at a substantial computational cost, with the retrieval taking more than 20 times as long as the WFM-DOAS retrieval for a similar data set.

Outlook

The detection and monitoring of greenhouse gas emission sources and validation of satellite systems will stay important in the future. In this regard, new instruments such as the MAMAP2D imaging instrument are vital. It incorporates higher spectral resolution and more across track ground scenes compared to MAMAP and MAMAP2D-Light. Furthermore, it contains a NIR spectrometer sampling the O_2A absorption features, enabling measuring gradients over larger distances. Finally, the temperature and pressure stabilization will reduce measurement noise, additionally enhancing the detection and quantification capabilities.

For both the MAMAP2D-Light and (when fully built) the MAMAP2D instrument, detection limits have to be examined. In this regard, controlled release experiments would be of great help, where defined low emissions are produced artificially (see, e.g., Thorpe et al., 2016). However, these are not easily realized, as they require significant amounts of CH_4 to be released into the atmosphere, without endangering the surroundings.

To fully exploit the future data of MAMAP2D, additional research regarding the FOCAL AIR retrieval is needed. Therefore, the FOCAL AIR retrieval will be applied to data sets over more complex regions, e.g., the landfill located in a mountainous region observed during the COMEX campaign in 2014 in California (Krautwurst et al., 2017), or additional data recorded during the COMET campaign over the Upper Silesian Coal Basin (e.g., the data set investigated by Krautwurst et al., 2021). Additionally, the performance must be parallelized to reduce the computation time. Finally, for the FOCAL AIR retrieval, radiometrically calibrated data are needed. While the retrieval worked with the white light corrected relative intensities, absolute radiometric calibration will likely improve the scattering retrieval.

The flux inversion from non-imaging and imaging data can significantly be improved with better knowledge about the wind speed and wind direction inside the plume or by eliminating the need for the knowledge of the wind speed from the inversion. Better knowledge of the wind speed could be gained by in situ wind observations during the overflight. However, this is only feasible for plumes for which the location is known prior to the flight. Also, it may be possible to improve wind speed knowledge by flying a wind lidar on the same aircraft as the remote sensing instrument (Thorpe et al., 2021), given that the aircraft is large enough. Removing the dependency of wind information at the plume location may be achieved with imaging data by taking the plume shape into account (Varon et al., 2018; Jongaramrungruang et al., 2019). The applicability to lower spatial resolution MAMAP2D and MAMAP2D-Light data and especially non-continuous plumes sampled in multiple overflights as the Jänschwalde power plant plume (Fig. 6.21) has to be explored in simulations.

Finally, with the methods investigated in this thesis and the instruments MAMAP2D-Light and MAMAP2D, emission estimates based on satellite data can be validated for selected target regions. Especially in cases where official reports and satellite-based emission estimates differ largely (Tu et al., 2022, e.g., the landfills around Madrid), these independent validations would improve confidence in satellite-based emission estimates.

A. Appendix

A.1. Comparison of ERA5 50m height averaged data with surface weather stations

For the AVIRIS-NG data, the plumes were mainly located near the ground and relatively short. To estimate if using ERA5 wind speed data for near-surface winds would lead to errors in the flux estimation, the average wind speed over the lowest 50 m of ERA5 data were compared to hourly mean wind speed data obtained from weather stations near the plumes P1 - P5. Wind speed data obtained at the Firebag weather station (Wood Buffalo Environmental Association, 2020) $\sim$ 20 km east of the plume were used for P1 and P2. For P3 and P4, hourly mean wind speed data from the weather stations "Sundre A" and "Patricia AGCM"[1], located 5 km and 17 km away from the source, were used. Finally, for P5, the mean hourly wind speed data from the Four Corners Regional Airport weather station from the MesoWest network (Horel et al., 01 Feb. 2002) $\sim$ 15 km east of the source was taken. The comparison with ERA5 data averaged over the boundary layer at the weather station locations is shown in Fig. A.1 for all those stations and the time of overflight.

The ERA5 data significantly deviated from the wind speeds measured by the weather stations, with a mean deviation of $\pm\,2.5\,\mathrm{m\,s^{-1}}$ and a maximum deviation of $\pm\,3.5\,\mathrm{m\,s^{-1}}$. Therefore, in the flux inversions, the wind speed data measured nearly "on-site" by the weather stations was used for a more realistic flux inversion.

[1]Data provided by Alberta Agriculture and Forestry, Alberta Climate Information Service (ACIS) `https://acis.alberta.ca` (retrieved in Dec. 2020)

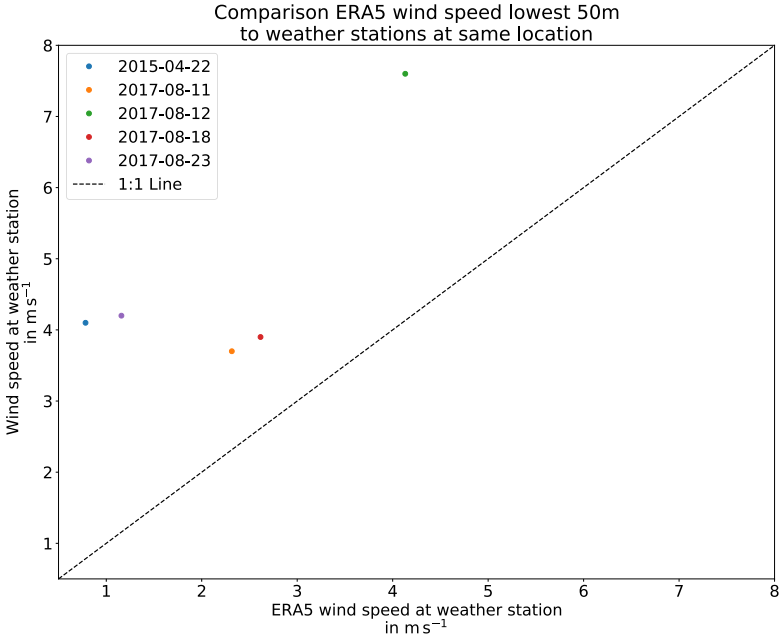

Figure A.1.: Comparison between wind speed averaged over the lowest 50 m above ground for ERA5 data and collocated wind station data. ERA5 data significantly underestimated the wind speed present at a given time.

A.2. Cross-sections through the plume for flux inversion of MAMAP2D-Light data

In this section, the background-normalized cross-sections for all binned viewing directions for each cross-track are shown. The plume borders are depicted in dashed green lines, while the colors represent the different viewing directions. The area outside the green dashed lines was used for calculating the linear background fit for background normalization of the data (see Sect. 5.3). The large data gaps, especially in the first flight tracks, are due to low radiances over water surfaces near the power plant, which resulted in bad fit results in the WFM-DOAS retrieval.

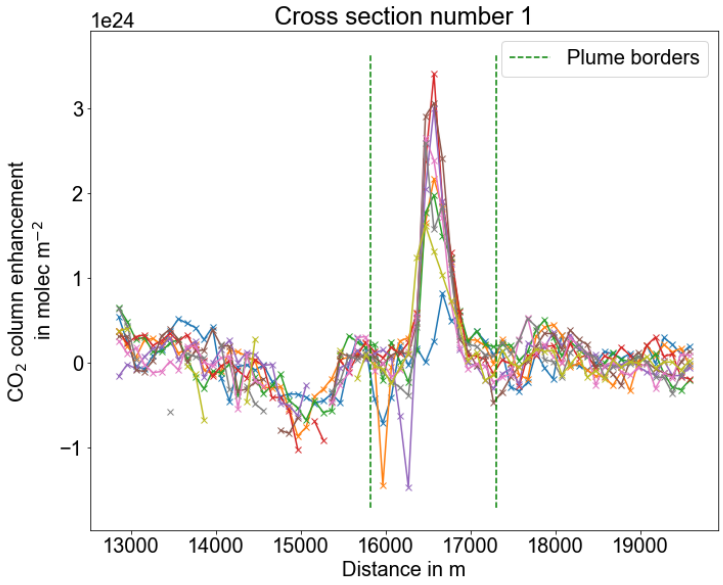

Figure A.2.: Cross tracks through the plume for MAMAP2D-Light data for the first flight track. The dashed green lines denote the plume borders, and the different colors denote the different binned viewing directions. The area outside the plume borders is used for the linear background fit, while the flux is estimated as integral over the enhancements inside the plume.

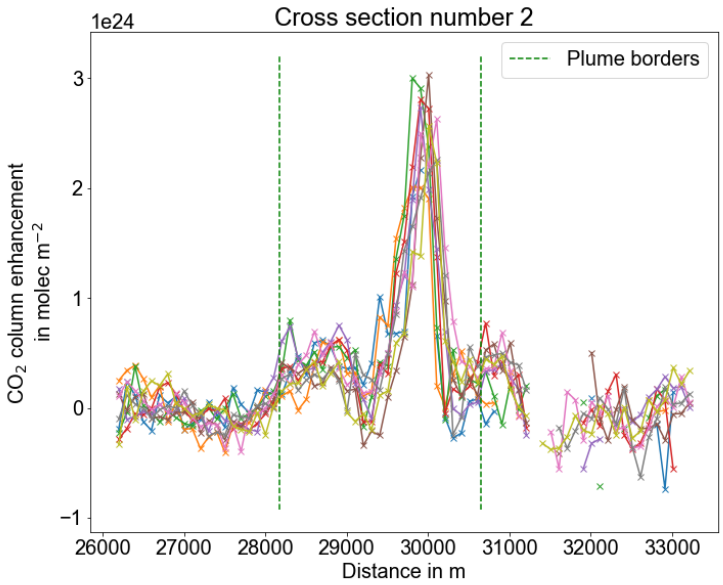

Figure A.3.: Same as Fig. A.2, but for the second flight track.

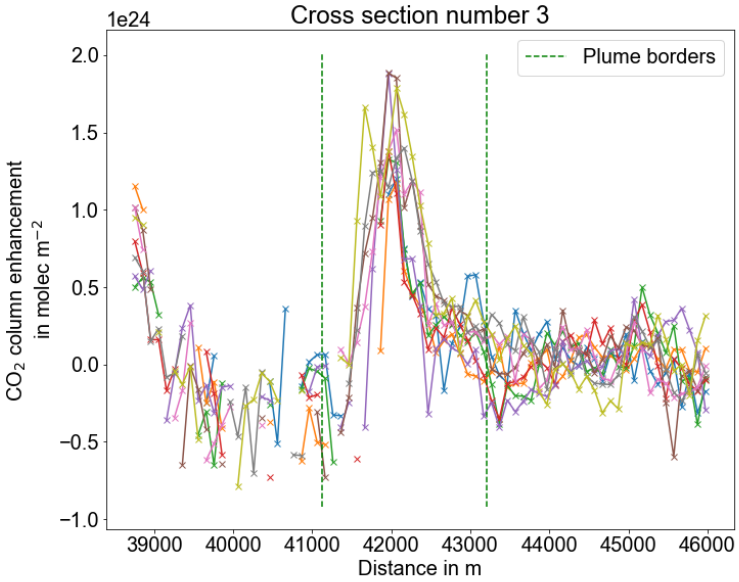

Figure A.4.: Same as Fig. A.2, but for the third flight track.

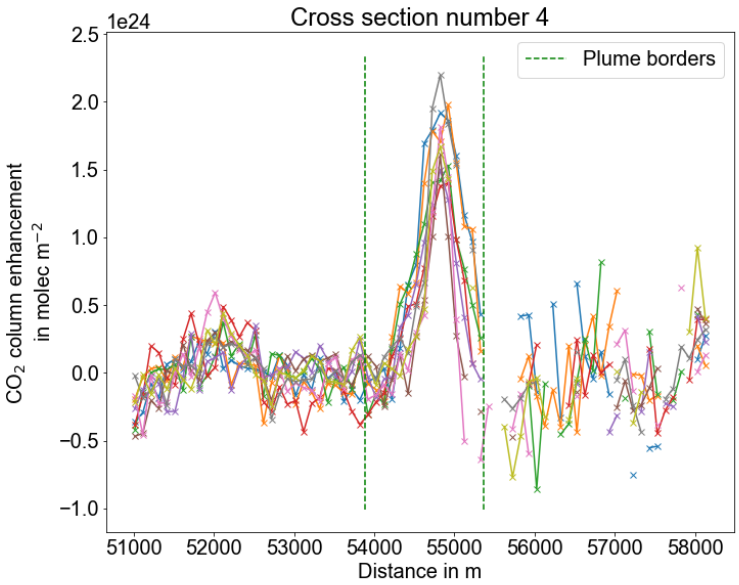

Figure A.5.: Same as Fig. A.2, but for the fourth flight track.

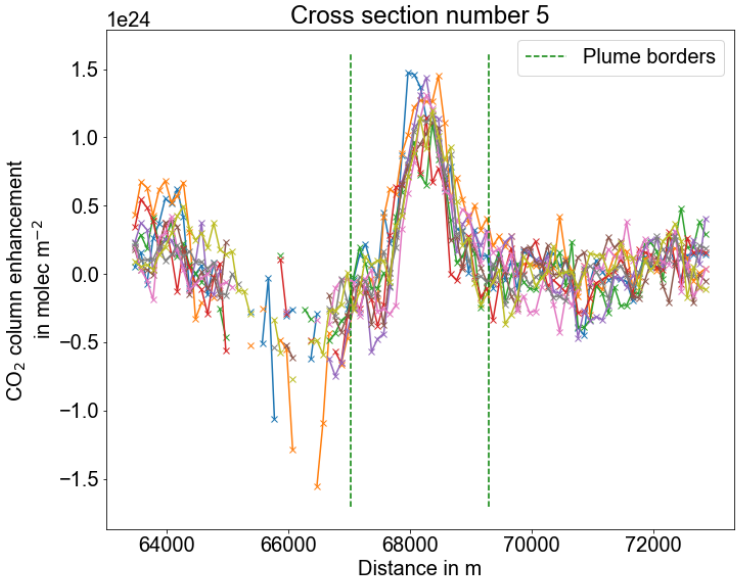

Figure A.6.: Same as Fig. A.2, but for the fifth flight track.

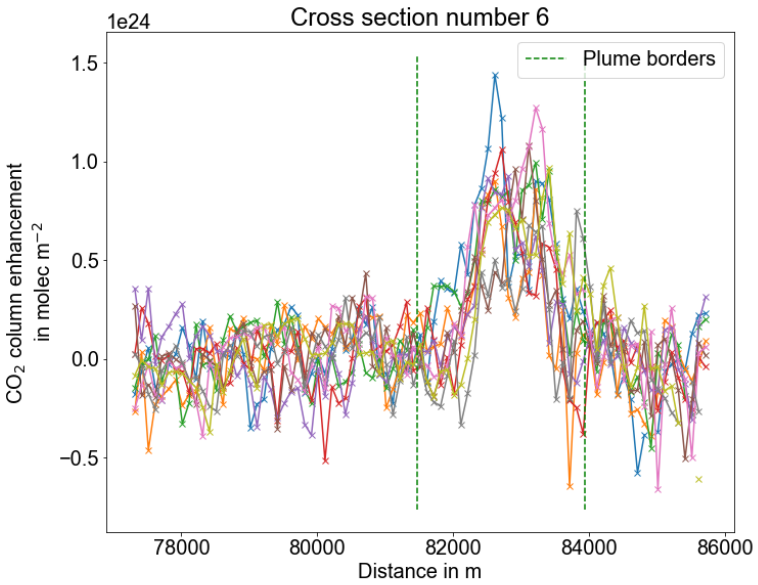

Figure A.7.: Same as Fig. A.2, but for the sixth flight track.

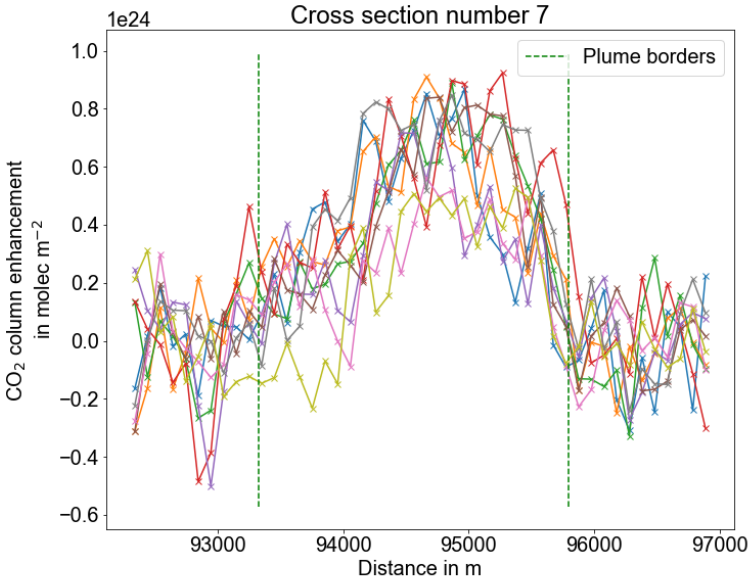

Figure A.8.: Same as Fig. A.2, but for the seventh flight track.

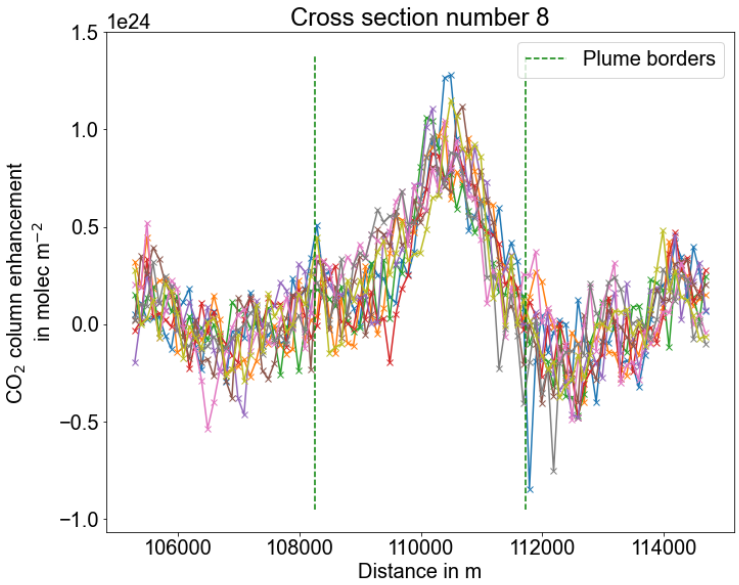

Figure A.9.: Same as Fig. A.2, but for the eighth flight track.

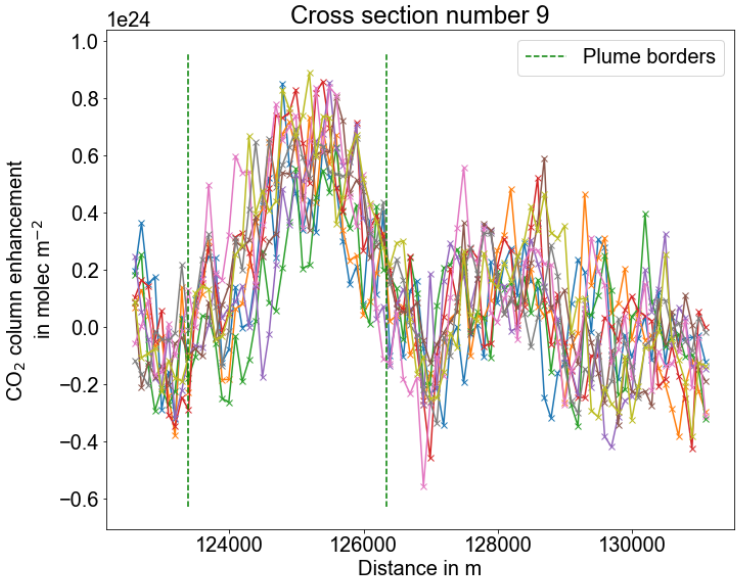

Figure A.10.: Same as Fig. A.2, but for the nineth flight track.

A.3. Aerosol scenarios for FOCAL AIR simulated measurements

The simulated measurements for the test of the FOCAL AIR retrieval described in Sect. 6.3.1 use the following three aerosol scenarios. These all comprise three layers of aerosols, spanning from the ground to 2 km, from 2 to 10 km and from 10 to 29 km. The aerosol types represent a background scenario (Table A.1), a continental scenario (Table A.2) and an urban aerosol scenario (Table A.3).

Table A.1.: Background aerosol scenario for the FOCAL AIR simulation experiments

parameter	**NIR**	**SWIR**
Aerosol layer 1		
Top altitude	29 km	29 km
Aerosol type	background	background
Phase function	Mie	Mie
Single scattering albedo	1.000 (694 nm)	0.998 (1536 nm)
Asymetry Factor	0.694 (694 nm)	0.447 (1536 nm)
Single scattering albedo	1.000 (860 nm)	0.989 (1800 nm)
Asymetry Factor	0.650 (860 nm)	0.372 (1800 nm)
Aerosol layer 2		
Top altitude	10 km	10 km
Aerosol type	background	background
Phase function	Mie	Mie
Single scattering albedo	1.000 (694 nm)	0.998 (1536 nm)
Asymetry Factor	0.694 (694 nm)	0.447 (1536 nm)
Single scattering albedo	1.000 (860 nm)	0.989 (1800 nm)
Asymetry Factor	0.650 (860 nm)	0.372 (1800 nm)
Aerosol layer 3		
Top altitude	2 km	2 km
Aerosol type	background	background
Phase function	Mie	Mie
Single scattering albedo	1.000 (694 nm)	0.998 (1536 nm)
Asymetry Factor	0.694 (694 nm)	0.447 (1536 nm)
Single scattering albedo	1.000 (860 nm)	0.989 (1800 nm)
Asymetry Factor	0.650 (860 nm)	0.372 (1800 nm)
Aerosol optical thickness	0.0197 (760 nm)	0.0026 (1650 nm)

Table A.2.: Continental aerosol scenario for the FOCAL AIR simulation experiments

parameter	**NIR**	**SWIR**
Aerosol layer 1		
Top altitude	29 km	29 km
Aerosol type	background	background
Phase function	Mie	Mie
Single scattering albedo	1.000 (694 nm)	0.998 (1536 nm)
Asymetry Factor	0.694 (694 nm)	0.447 (1536 nm)
Single scattering albedo	1.000 (860 nm)	0.989 (1800 nm)
Asymetry Factor	0.650 (860 nm)	0.372 (1800 nm)
Aerosol layer 2		
Top altitude	10 km	10 km
Aerosol type	continental	continental
Phase function	Mie	Mie
Single scattering albedo	0.884 (694 nm)	0.758 (1536 nm)
Asymetry Factor	0.630 (694 nm)	0.638 (1536 nm)
Single scattering albedo	0.847 (860 nm)	0.762 (1800 nm)
Asymetry Factor	0.630 (860 nm)	0.672 (1800 nm)
Aerosol layer 3		
Top altitude	2 km	2 km
Aerosol type	continental	continental
Phase function	Mie	Mie
Single scattering albedo	0.884 (694 nm)	0.758 (1536 nm)
Asymetry Factor	0.630 (694 nm)	0.638 (1536 nm)
Single scattering albedo	0.847 (860 nm)	0.762 (1800 nm)
Asymetry Factor	0.630 (860 nm)	0.672 (1800 nm)
Aerosol optical thickness	0.159 (760 nm)	0.057 (1650 nm)

Table A.3.: Urban aerosol scenario for the FOCAL AIR simulation experiments

parameter	**NIR**	**SWIR**
Aerosol layer 1		
Top altitude	29 km	29 km
Aerosol type	background	background
Phase function	Mie	Mie
Single scattering albedo	1.000 (694 nm)	0.998 (1536 nm)
Asymetry Factor	0.694 (694 nm)	0.447 (1536 nm)
Single scattering albedo	1.000 (860 nm)	0.989 (1800 nm)
Asymetry Factor	0.650 (860 nm)	0.372 (1800 nm)
Aerosol layer 2		
Top altitude	10 km	10 km
Aerosol type	urban	urban
Phase function	Mie	Mie
Single scattering albedo	0.636 (694 nm)	0.461 (1536 nm)
Asymetry Factor	0.586 (694 nm)	0.566 (1536 nm)
Single scattering albedo	0.593 (860 nm)	0.409 (1800 nm)
Asymetry Factor	0.584 (860 nm)	0.574 (1800 nm)
Aerosol layer 3		
Top altitude	2 km	2 km
Aerosol type	urban	urban
Phase function	Mie	Mie
Single scattering albedo	0.636 (694 nm)	0.461 (1536 nm)
Asymetry Factor	0.586 (694 nm)	0.556 (1536 nm)
Single scattering albedo	0.593 (860 nm)	0.409 (1800 nm)
Asymetry Factor	0.584 (860 nm)	0.574 (1800 nm)
Aerosol optical thickness	0.152 (760 nm)	0.050 (1650 nm)

A.4. Updated spectral calibration of the MAMAP instrument

A.4.1. Calibration setup and data description

Until now, for the MAMAP instrument, a line shape function derived from illuminating the instrument by spectral line lamps was used (Gerilowski et al., 2011). However, the grating of the MAMAP spectrometer had to be turned for a reasonably strong emission line of the lamp to hit the detector. This resulted in a double gaussian line shape function for the SWIR characterized by the coupled FWHM between the two gaussian terms, and a gaussian line shape function for the NIR. The FWHM of the (double) gaussian function was then adjusted in spectral measurements together with a wavelength shift and squeeze to minimize the residuals between the measured spectra and the fitted forward model in the WFM-DOAS method until an optimal set of the FWHM, the shift, and the squeeze was achieved.

With the acquisition of two tunable external cavity diode LASER covering the wavelength ranges $755 - 780\,\text{nm}$ (NIR) and $1590 - 1780\,\text{nm}$ (SWIR), an update of the line shape function and the wavelength grid calibration was possible. To illuminate the entrance fiber of MAMAP homogeneously, the calibration setup described in Sect. 5.1.3.2 and shown in Fig. 5.5 was used. Depending on the channel under investigation, the NIR or SWIR LASER was coupled into the integration sphere.

For the calibration of the MAMAP SWIR channel, 19 laser measurements at 5 nm intervals covering the wavelength range from 1593.85 to 1683.46 nm were acquired with an integration time of 30 ms. At each wavelength, 100 dark and 100 illuminated spectra were recorded to reduce the measurement noise by averaging.

For the calibration of the MAMAP NIR channel, 16 laser measurements at 1 nm intervals covering the wavelength range from 756.46 to 771.38 nm were recorded with an integration time of 1 second. Due to the longer integration time, 50 dark and 50 illuminated spectra were recorded at each wavelength.

A.4.2. Calibration caluclation and results

The new wavelength grid for the NIR and SWIR channel was fitted in the following way: First, for each set of measurements at a single wavelength, the mean illuminated and dark spectrum was calculated, and the dark spectrum was subtracted from the illuminated spectrum. Then, the spectrum was normalized to the peak value of the spectrum, and the wavelength of the LASER was attributed to the pixel with the highest intensity. Finally, a second-order polynomial was fitted to the data. The new nanometer wavelength grids $wl_{\text{NIR}}(x)$ and $wl_{\text{SWIR}}(x)$ for the MAMAP channels dependent on the pixel number x were

$$wl_{\text{NIR}}(x) = 755.5881 + 0.0653104 \cdot x - 2.252478 \cdot 10^{-6} \cdot x^2 \tag{A.170}$$

$$wl_{\text{SWIR}}(x) = 1587.560 + 0.1012153 \cdot x - 4.104408 \cdot 10^{-6} \cdot x^2. \tag{A.171}$$

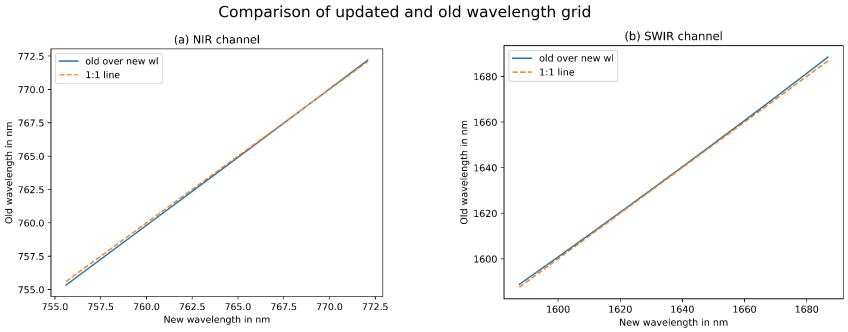

Figure A.11.: New and old wavelength grid for the NIR (a) and SWIR (b) channel of the MAMAP instrument. The chip's central spatial region was used for the NIR channel.

In Fig. A.11, the updated wavelength grid is displayed over the old wavelength grid. Especially at the edges of the detector, the wavelength grids differ, while in the middle, the wavelength grids are nearly identical. This is primarily due to the old wavelength grid being strictly linear.

The update of the instrument line shape function for the MAMAP instrument resulted from the requirement of FOCAL AIR for an instrument line shape function for each spectral pixel for the best fit. Additionally, it was known from previous measurements that there are differences in the average response function on the chip in the region where the absorption bands of CO_2 are recorded compared to the region where the CH_4 absorption bands are located on the detector. Measuring the ISRF at multiple pixels across the detector with high sampling would require an automated setup for the acquisition of the spectra and wavelengths of the LASER. This was out of the scope of this thesis. However, MAMAP has an oversampling of ~ 9, meaning the spectral sampling is $\sim$ nine times higher than the spectral resolution. This led to the wavelength-dependent ISRF calibration procedure described below.

For this approach, the measurements used for calibrating the wavelength grid of the instrument were used again. The average of each set of measurements at one wavelength is the detector response to light from this wavelength. In a first approximation, it was assumed that the center wavelength of the detector pixel with the highest response is the LASER wavelength. As a result of the measurements in both channels, a double gaussian ISRF

$$f_{dg}(x) = k \cdot \exp\left(-\left(2 \cdot \sqrt{\ln 2}\frac{x}{fwhm}\right)^2\right) + (1-k) \cdot \exp\left(-\left(2 \cdot \sqrt{\ln 2}\frac{x + fwhm \cdot sh}{fwhm \cdot sc}\right)^2\right) \tag{A.172}$$

with the four free fit parameters $fwhm$ (full width at half maximum of the main gaussian function), k (weighting term between the two gaussian functions), sh (shift of the maximum of the second gaussian function relative to the first in terms of the $fwhm$), and sc (scaling of the $fwhm$ of the second gaussian function) was fitted to each averaged measurement. This resulted in 19 fits of the ISRF across the detector. The results for the fit parameters for the NIR and SWIR are shown in Fig. A.13 and Fig. A.12 respectively. Most likely due to the difference between the true central pixel wavelength and LASER wavelength, as well as some instabilities of the LASER signal in the MAMAP instrument due to the entrance fiber, there are some oscillations in the parameters, although this is physically unrealistic. Therefore, a linear fit was calculated for all parameters, giving updated slit function definitions for each spectral pixel of both channels.

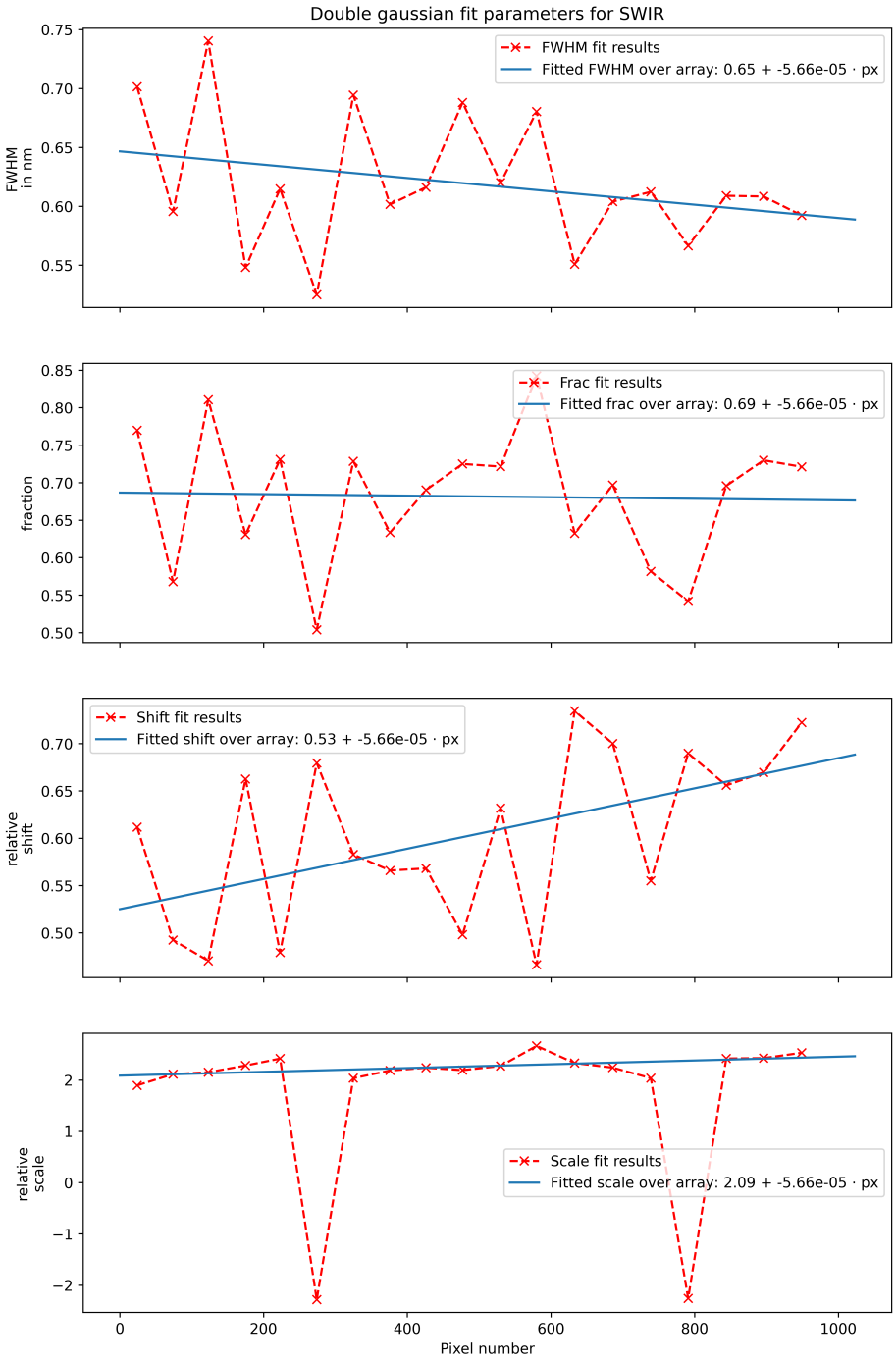

Figure A.12.: Fit results for the double gaussian parameters for each wavelength measurement in the SWIR channel. The strong (and periodic) variability in the parameters is most likely due to the position of the LASER peak wavelength relative to the true pixel center.

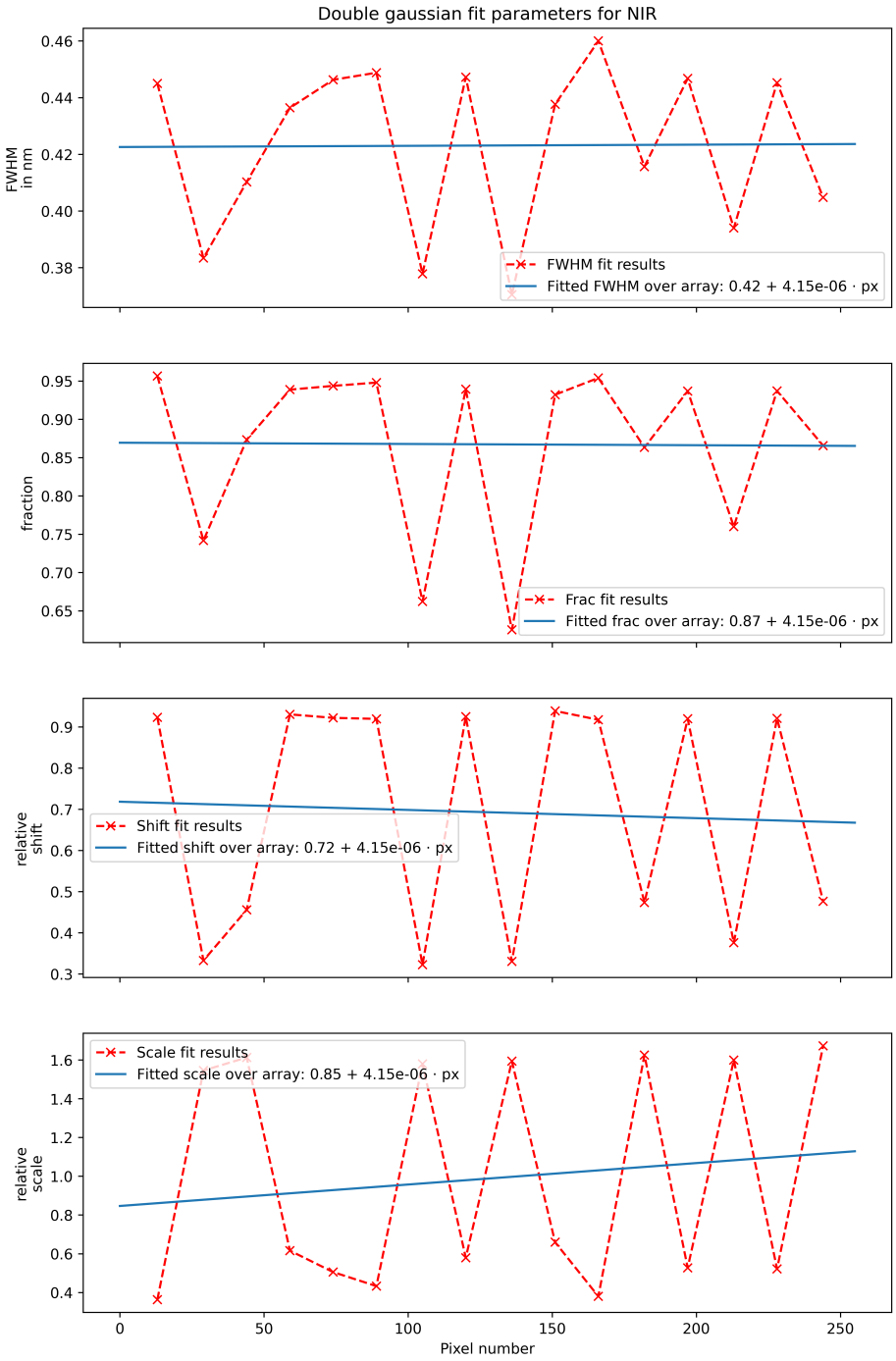

Figure A.13.: Fit results for the double gaussian parameters for each wavelength measurement. The strong (and periodic) variability in the parameters is most likely due to the position of the LASER peak wavelength relative to the true pixel center.

A.5. Flux inversion and uncertainty analysis of the WFM-DOAS retrieval results for the Jänschwalde power plant from MAMAP data

The cross-tracks for the cross-sectional flux method were extracted as described in Sect. 6.3.4. The resulting cross-tracks after normalization to the local background are shown in the figures A.14 to A.20.

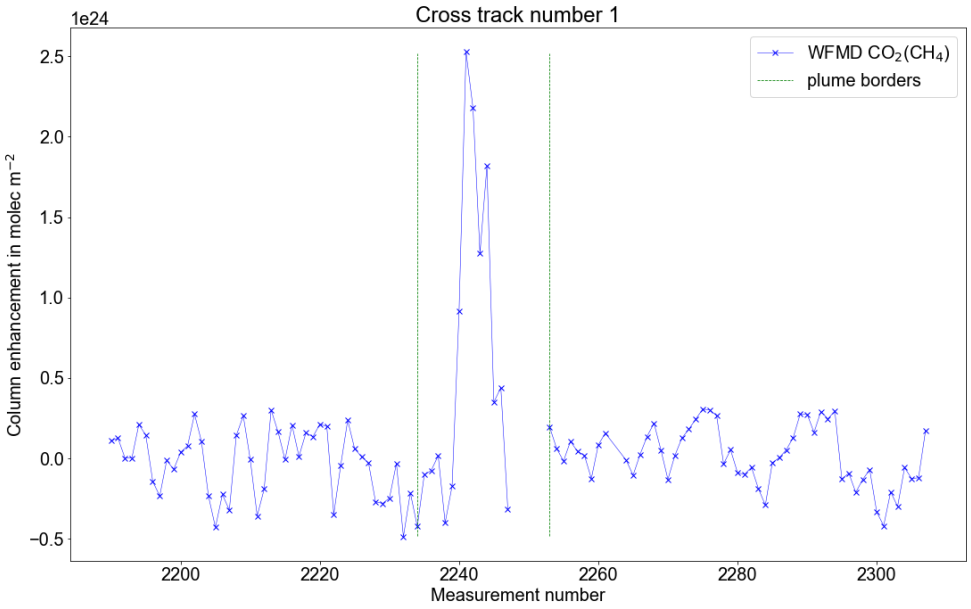

Figure A.14.: Background normalized and binned retrieval results of the first cross-track downwind of the source for the WFM-DOAS retrieval.

The flux uncertainty was calculated from the contributions described in Sect. 5.3 as follows (see also Table A.4), divided into the three blocks "enhancement above background", "wind-related" and "atmospheric variability":

In the first block, the background normalization contributes a flux uncertainty of ± 1.1 Mt CO_2 yr^{-1}, calculated from the residuum of the background fit and the resulting column uncertainty in the plume. The background total column for WFM-DOAS is not fitted and therefore assumed to be known to $\pm 5\,\%$ from the used models. This leads to a flux uncertainty of ± 1.0 Mt CO_2 yr^{-1}. The retrieval noise estimated from the $1\,\sigma$ standard deviation of the background retrieval results besides the plume introduces a flux uncertainty of ± 0.1 Mt CO_2 yr^{-1}.

The wind speed uncertainty introduces the largest flux uncertainty for the WFM-DOAS proxy retrieval results with ± 3.1 Mt CO_2 yr^{-1}, while the wind direction uncertainty causes

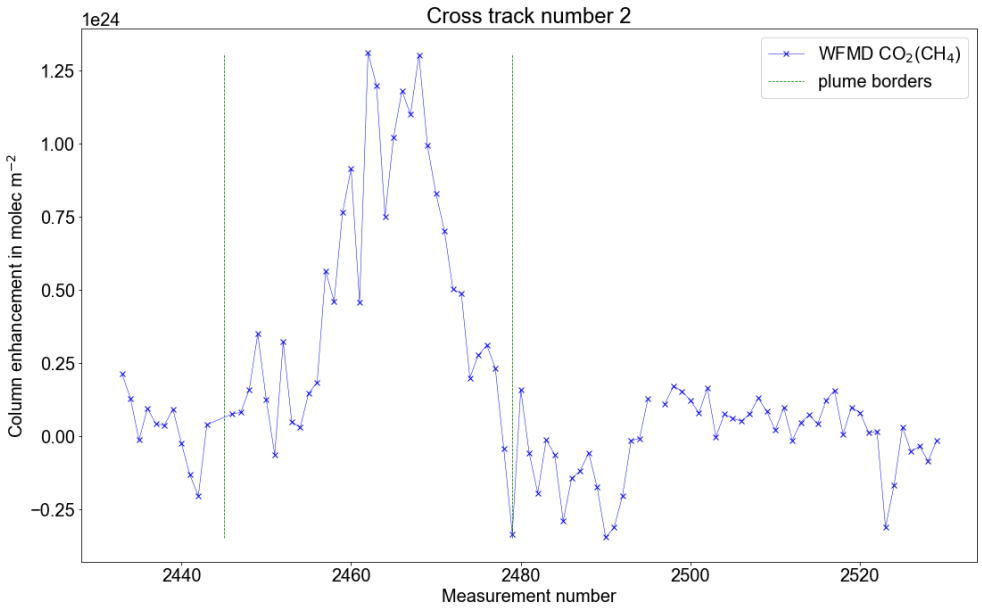

Figure A.15.: Same as Fig. A.14, but for the second cross-track downwind of the source.

a flux uncertainty of $\pm\,2.2\,\mathrm{Mt\ CO_2\ yr^{-1}}$.

The atmospheric variability, calculated as the $1\,\sigma$ standard deviation over the individual flux estimates per cross-track introduces a flux uncertainty of $\pm\,2.4\,\mathrm{Mt\ CO_2\ yr^{-1}}$.

Summing all uncertainty contributions quadratically, the resulting total flux uncertainty is $\pm\,4.7\,\mathrm{Mt\ CO_2\ yr^{-1}}$.

Table A.4.: Uncertainty estimation of the flux inversion for WFM-DOAS retrieval results after application of the proxy.

Uncertainty contribution	**proxy**
Background normalization	$\pm\,1.1\,\mathrm{Mt\ CO_2\ yr^{-1}}$ (6 %)
Background total column	$\pm\,1.0\,\mathrm{Mt\ CO_2\ yr^{-1}}$ (5 %)
Retrieval result noise	$\pm\,0.1\,\mathrm{Mt\ CO_2\ yr^{-1}}$ (1 %)
Wind speed	$\pm\,3.1\,\mathrm{Mt\ CO_2\ yr^{-1}}$ (16 %)
Wind direction	$\pm\,2.2\,\mathrm{Mt\ CO_2\ yr^{-1}}$ (11 %)
Atmospheric variability	$\pm\,2.4\,\mathrm{Mt\ CO_2\ yr^{-1}}$ (12 %)
Total uncertainty	$\pm\,4.7\,\mathrm{Mt\ CO_2\ yr^{-1}}$ (24 %)

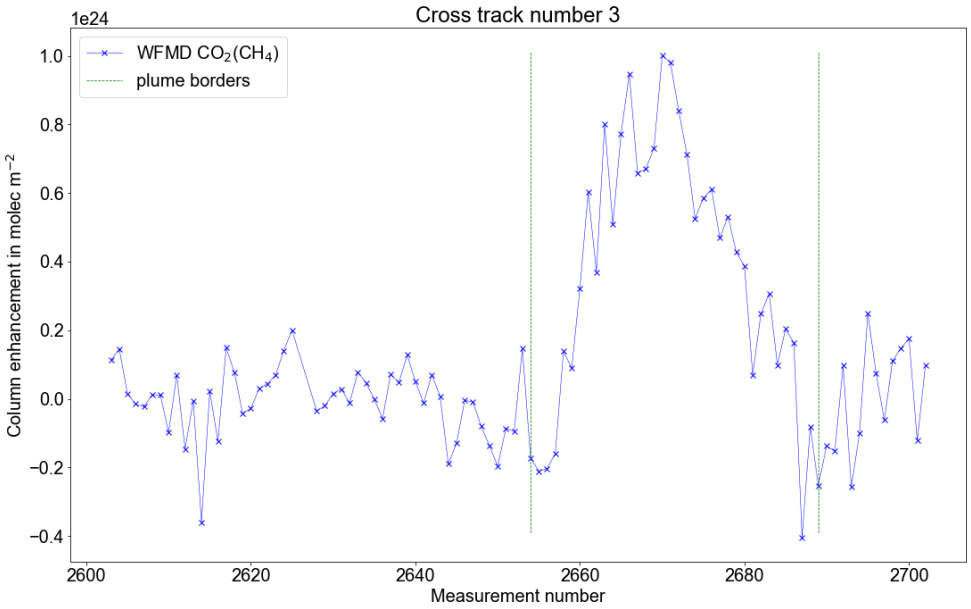

Figure A.16.: Same as Fig. A.14, but for the third cross-track downwind of the source.

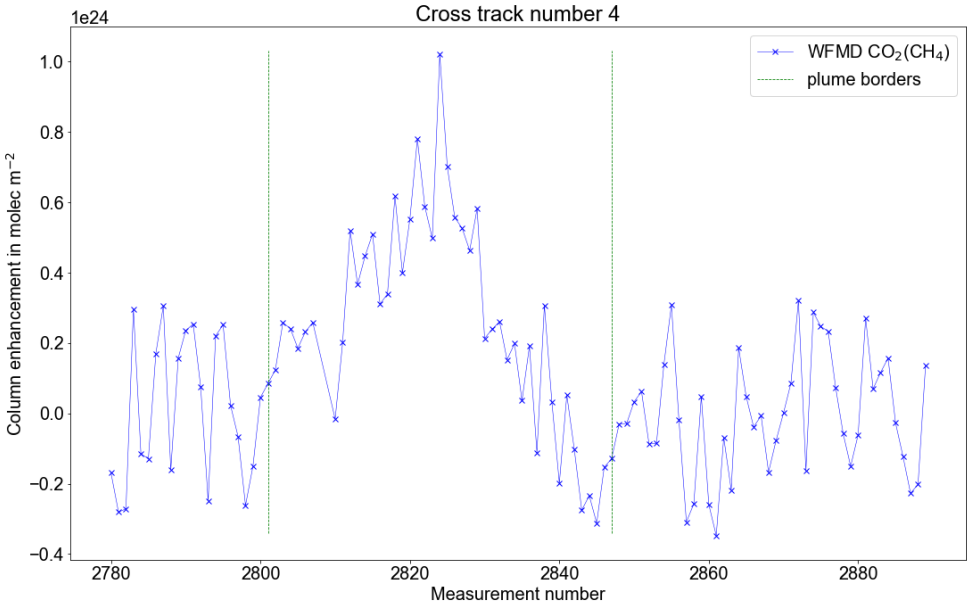

Figure A.17.: Same as Fig. A.14, but for the fourth cross-track downwind of the source.

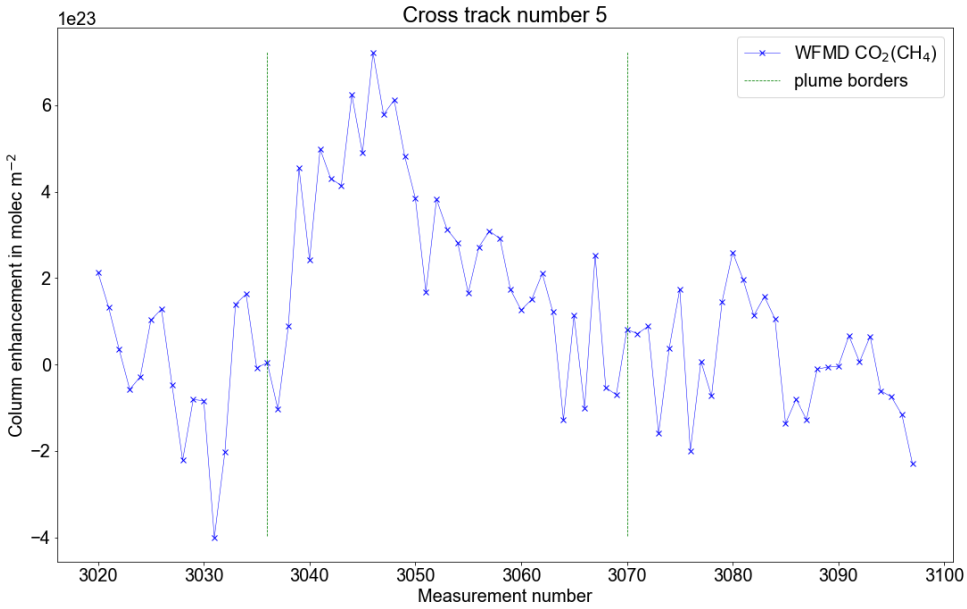

Figure A.18.: Same as Fig. A.14, but for the fifth cross-track downwind of the source.

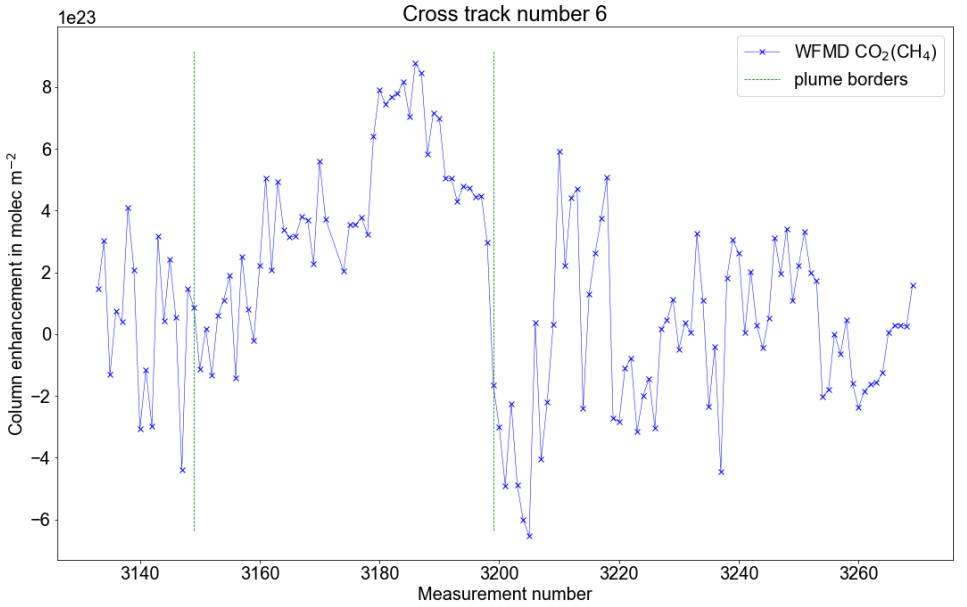

Figure A.19.: Same as Fig. A.14, but for the sixth cross-track downwind of the source.

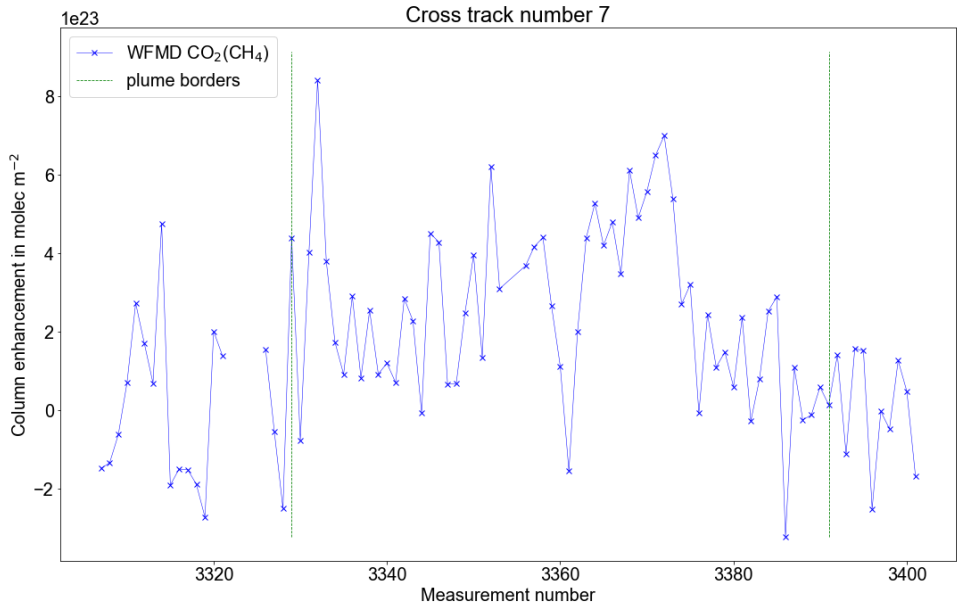

Figure A.20.: Same as Fig. A.14, but for the seventh cross-track downwind of the source.

A.6. FOCAL AIR cross-tracks for cross-sectional flux method

In this section of the appendix, the different cross-tracks of the plume for the four different FOCAL AIR retrieval settings (absorption-only and scattering with one or two fit windows in the SWIR) are shown in addition to the first cross-track shown for each retrieval in the main text. This follows the same order as the main retrieval result section (Sect. 6.3.4).

A.6.1. Cross-tracks for flux inversion of FOCAL AIR absorption-only 2-window retrieval results

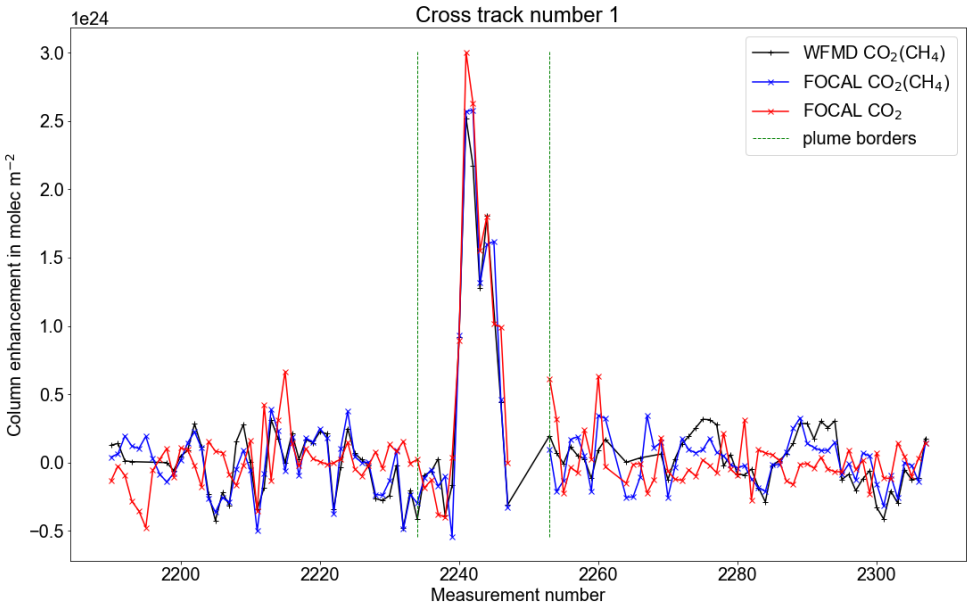

Figure A.21.: Background normalized and binned retrieval results of the first cross-track downwind of the source for the absorption-only 2-window FOCAL AIR retrieval. For comparison, also the WFM-DOAS retrieval results are shown in black.

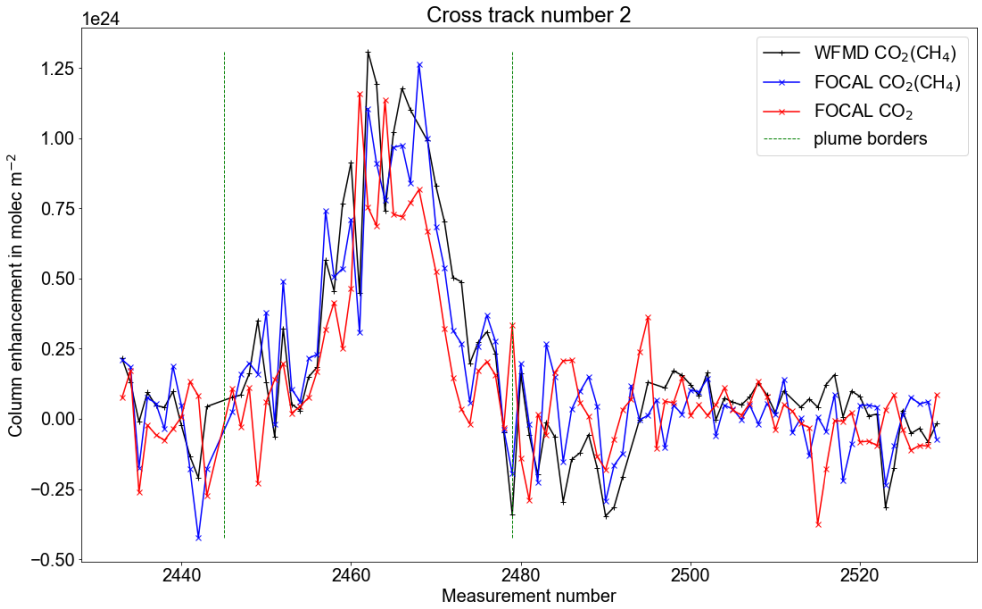

Figure A.22.: Same as Fig. A.21, but for the second cross-track downwind of the source.

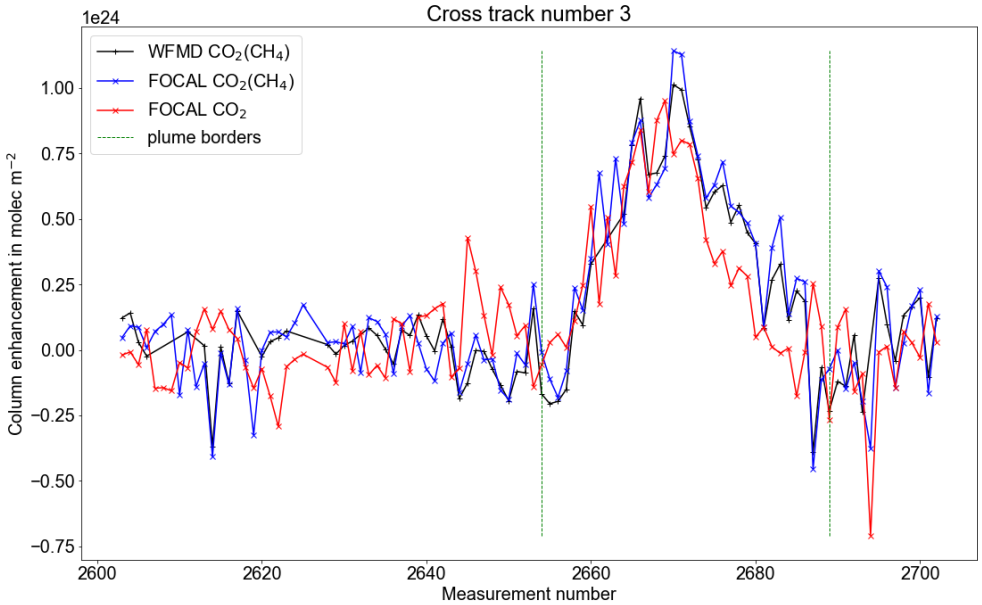

Figure A.23.: Same as Fig. A.21, but for the third cross-track downwind of the source.

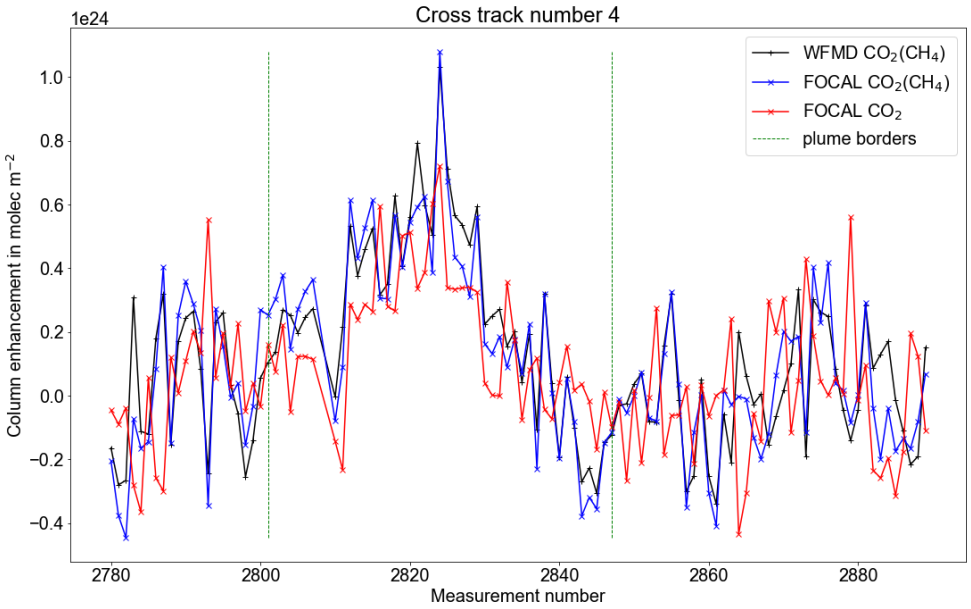

Figure A.24.: Same as Fig. A.21, but for the fourth cross-track downwind of the source.

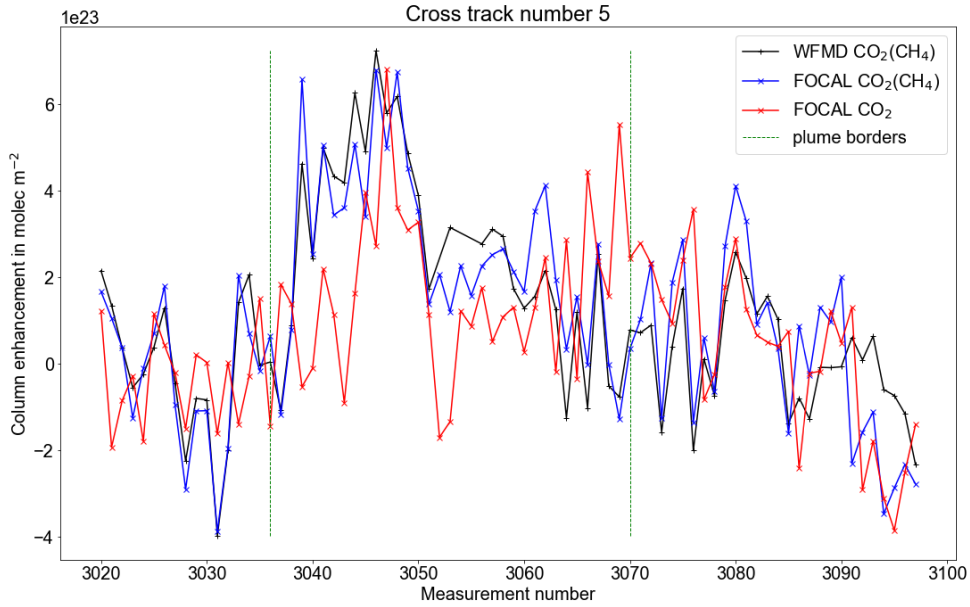

Figure A.25.: Same as Fig. A.21, but for the fifth cross-track downwind of the source.

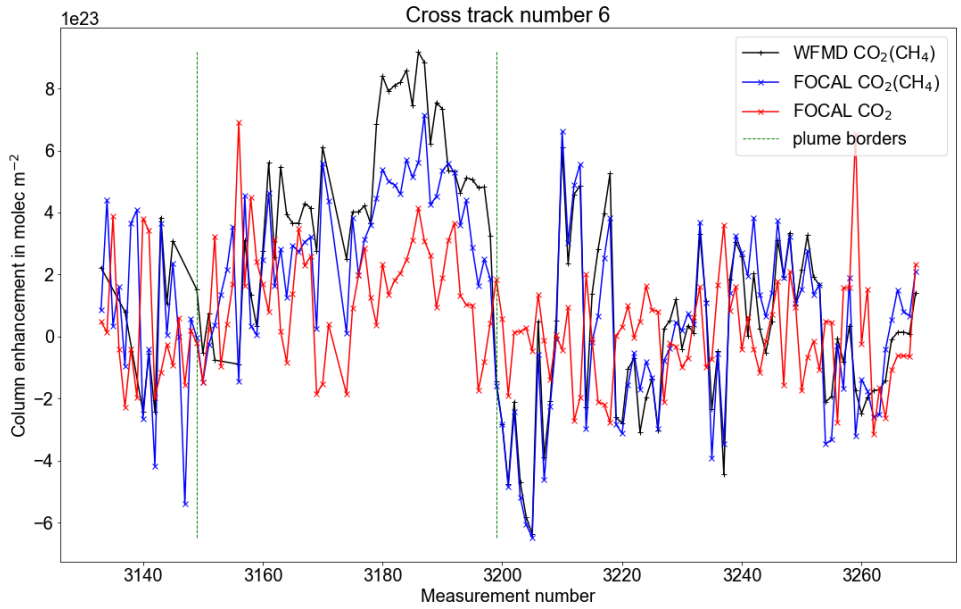

Figure A.26.: Same as Fig. A.21, but for the sixth cross-track downwind of the source.

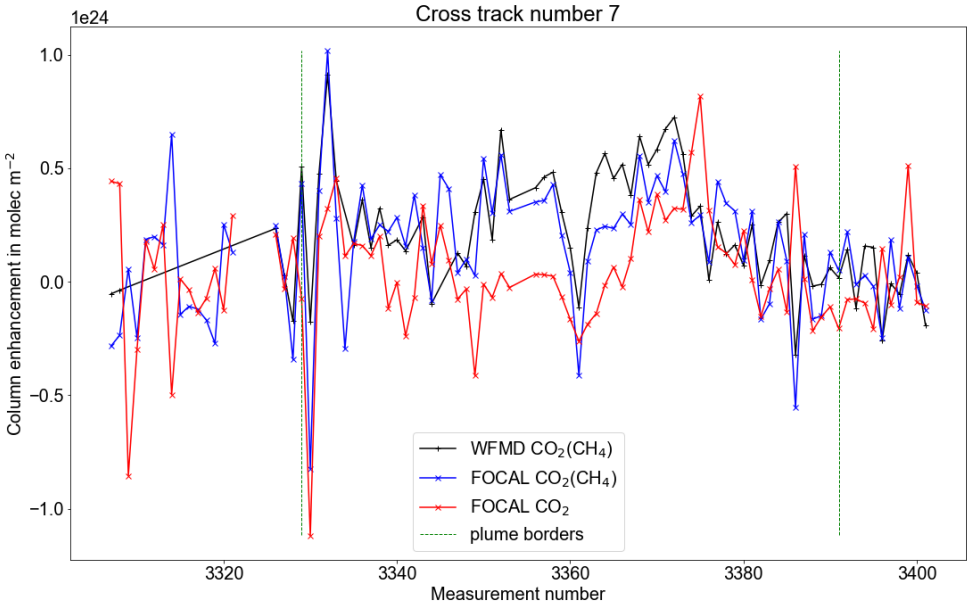

Figure A.27.: Same as Fig. A.21, but for the seventh cross-track downwind of the source.

A.6.2. Cross-tracks for flux inversion of FOCAL AIR scattering 2-window retrieval results

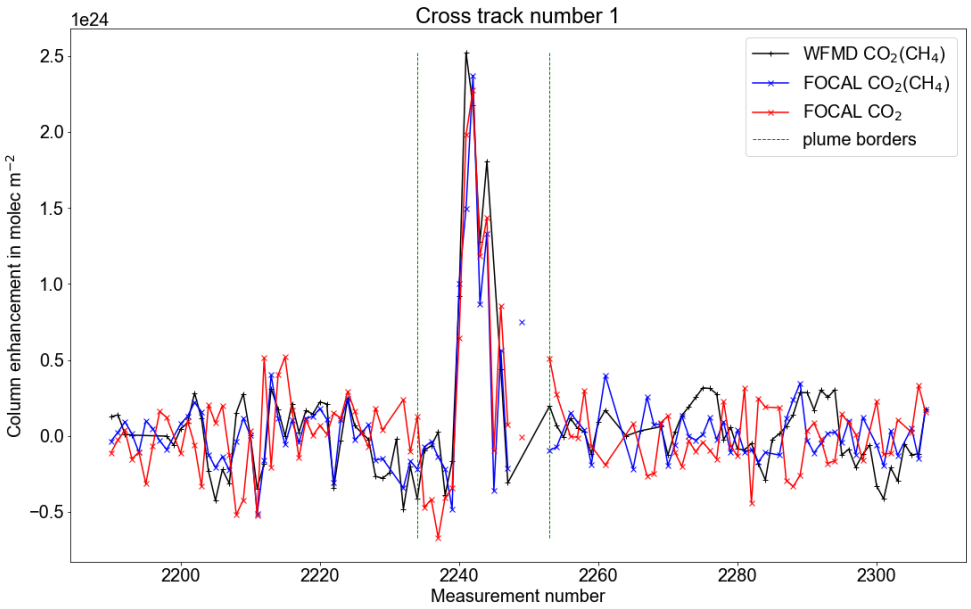

Figure A.28.: Background normalized and binned retrieval results of the first cross-track downwind of the source for the scattering 2-window FOCAL AIR retrieval. For comparison, also the WFM-DOAS retrieval results are shown in black.

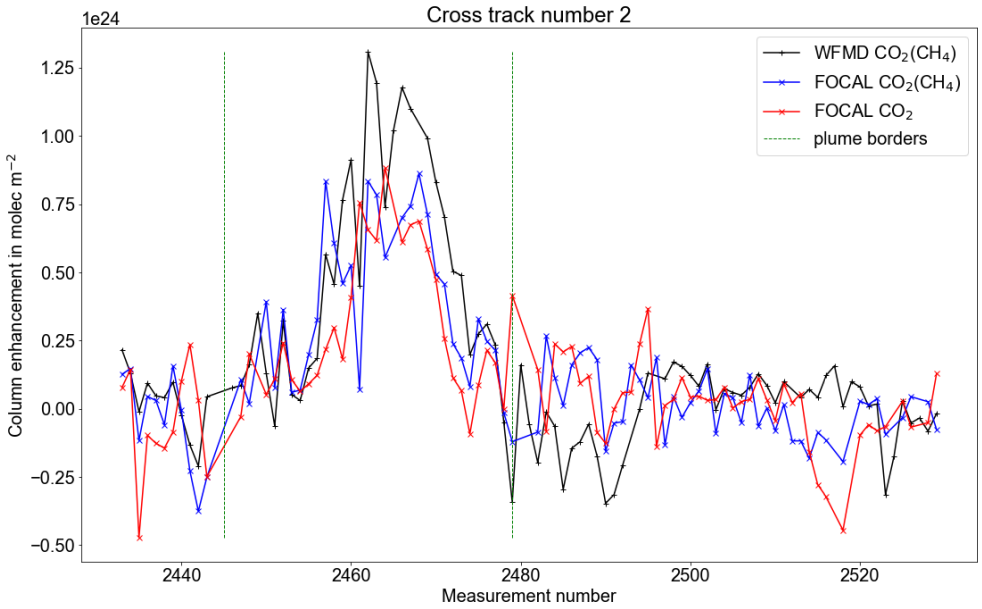

Figure A.29.: Same as Fig. A.28, but for the second cross-track downwind of the source.

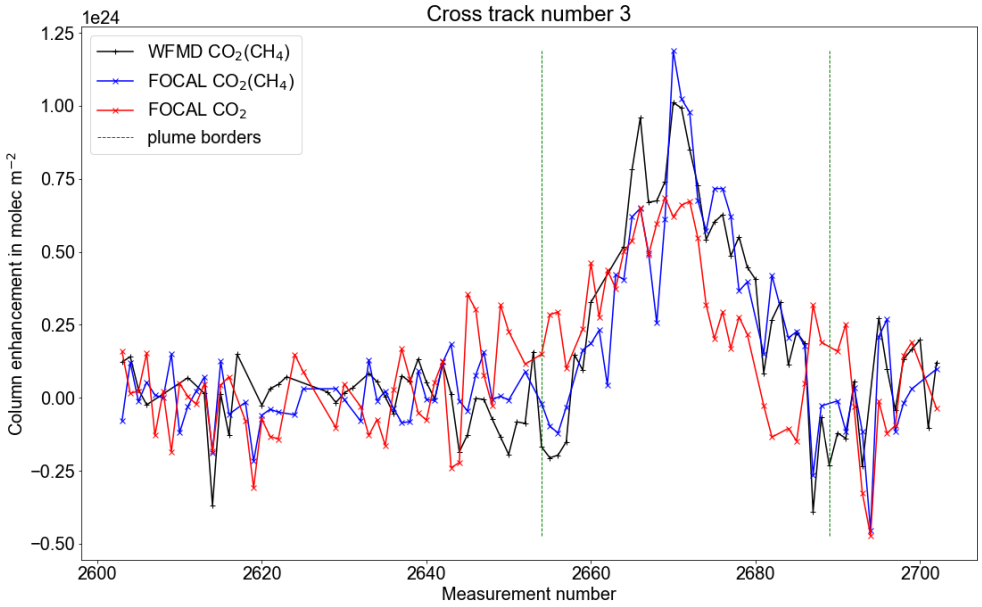

Figure A.30.: Same as Fig. A.28, but for the third cross-track downwind of the source.

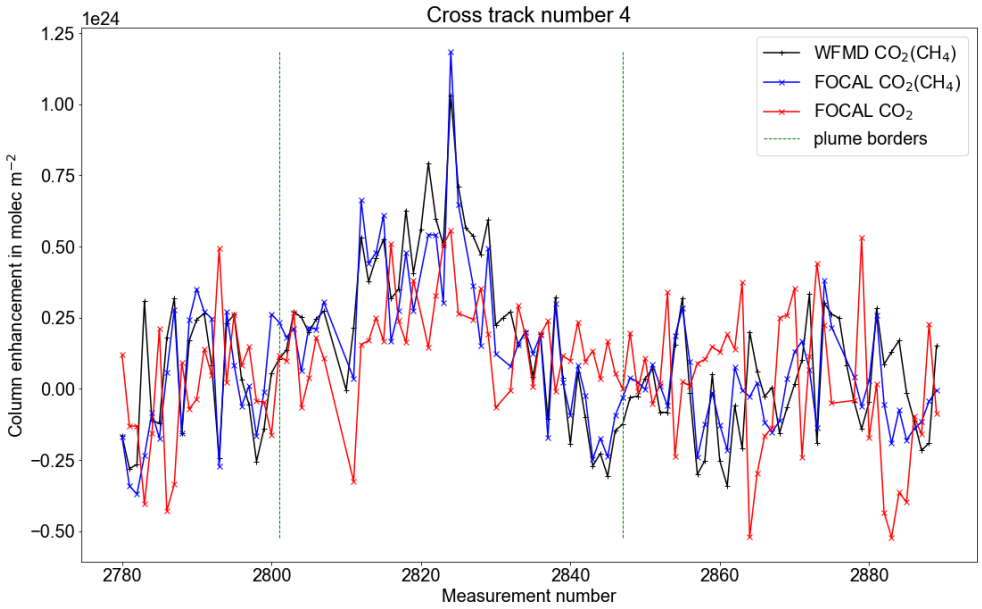

Figure A.31.: Same as Fig. A.28, but for the fourth cross-track downwind of the source.

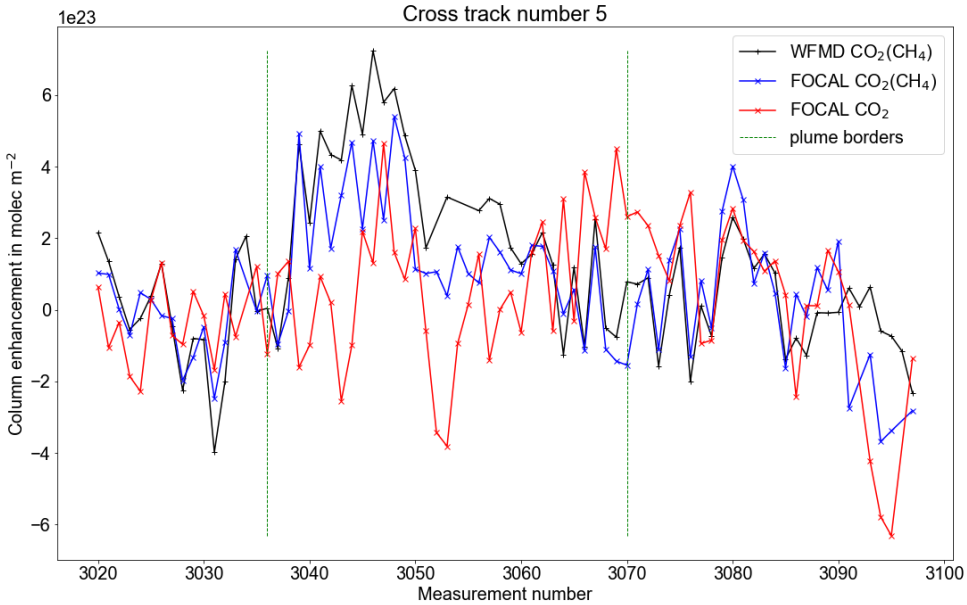

Figure A.32.: Same as Fig. A.28, but for the fifth cross-track downwind of the source.

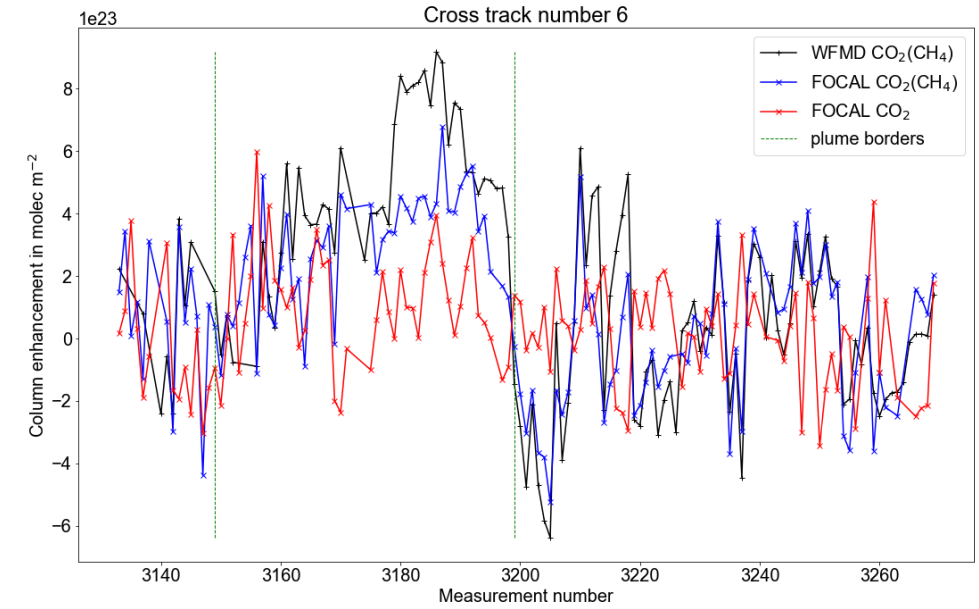

Figure A.33.: Same as Fig. A.28, but for the sixth cross-track downwind of the source.

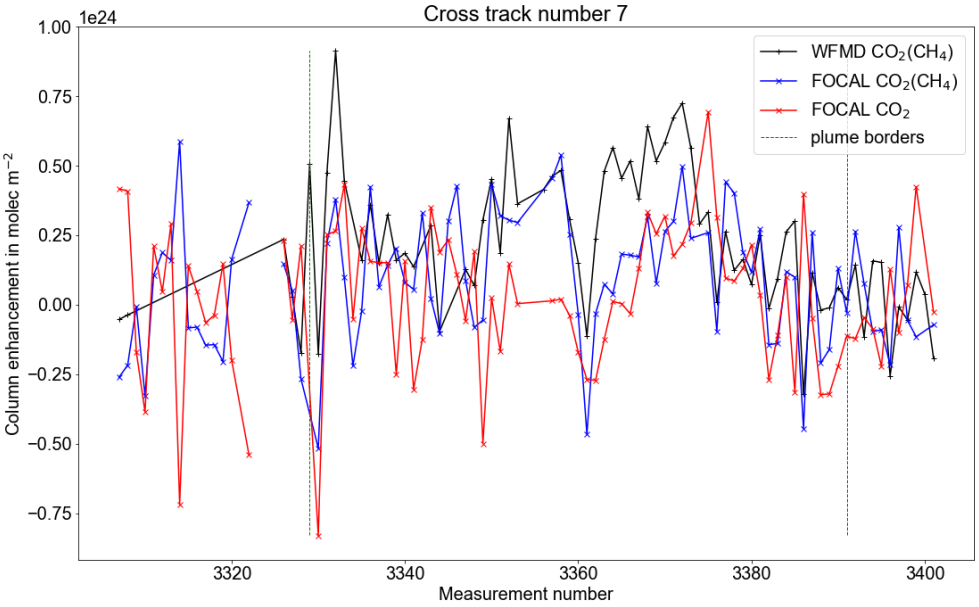

Figure A.34.: Same as Fig. A.28, but for the seventh cross-track downwind of the source.

A.6.3. Cross-tracks for flux inversion of FOCAL AIR absorption-only 1-window retrieval results

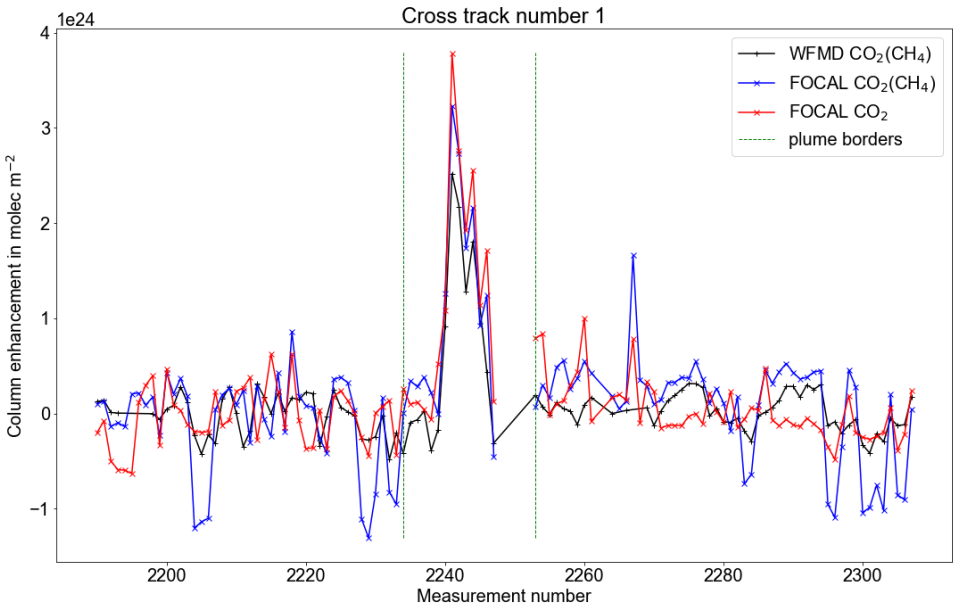

Figure A.35.: Background normalized and binned retrieval results of the first cross-track downwind of the source for the absorption-only 1-window FOCAL AIR retrieval. For comparison, also the WFM-DOAS retrieval results are shown in black.

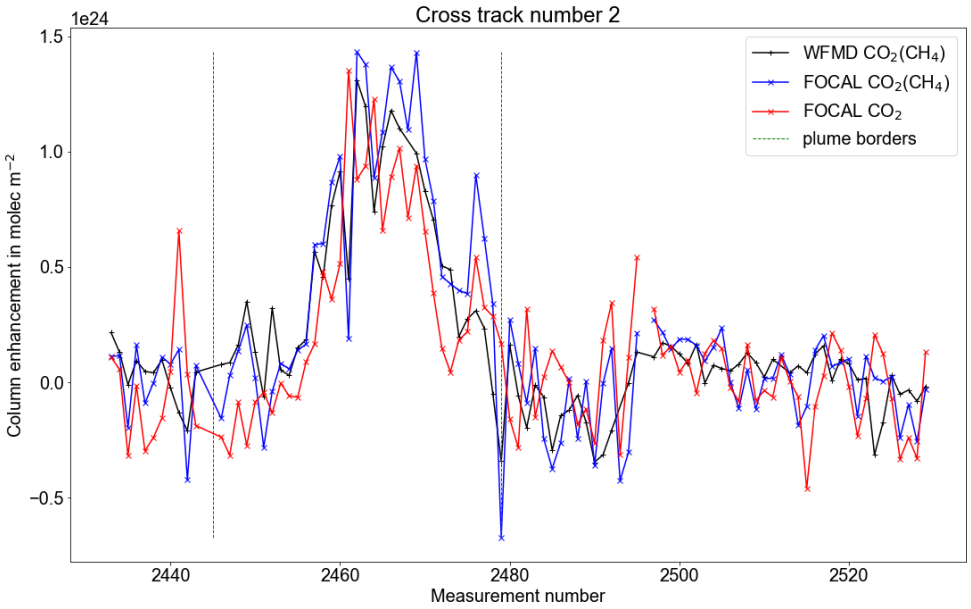

Figure A.36.: Same as Fig. A.35, but for the second cross-track downwind of the source.

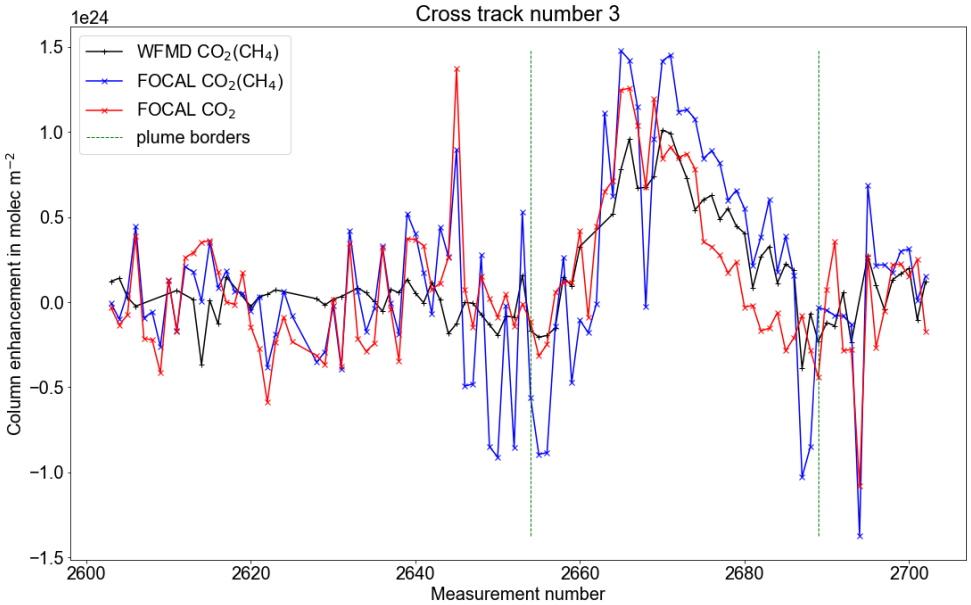

Figure A.37.: Same as Fig. A.35, but for the third cross-track downwind of the source.

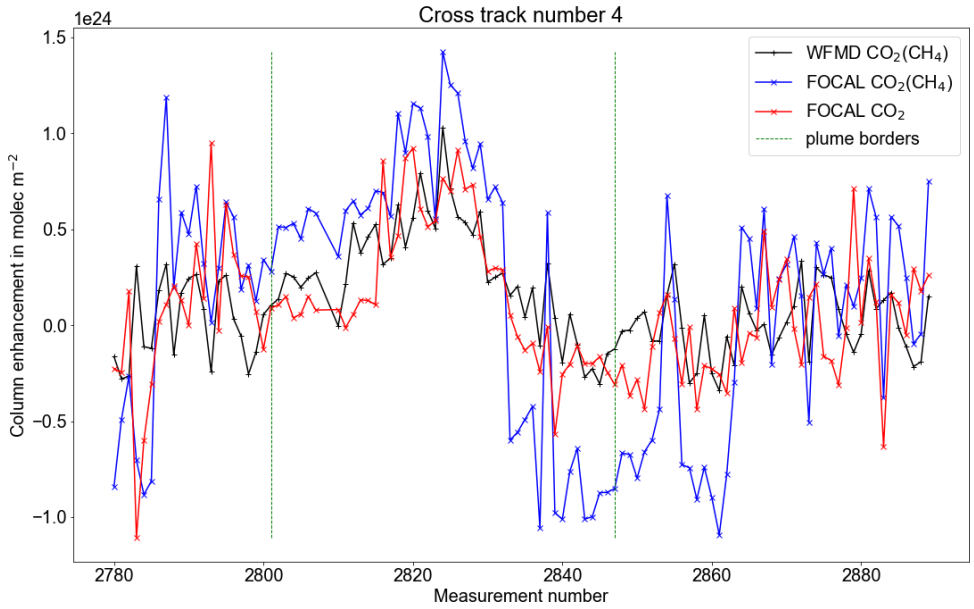

Figure A.38.: Same as Fig. A.35, but for the fourth cross-track downwind of the source.

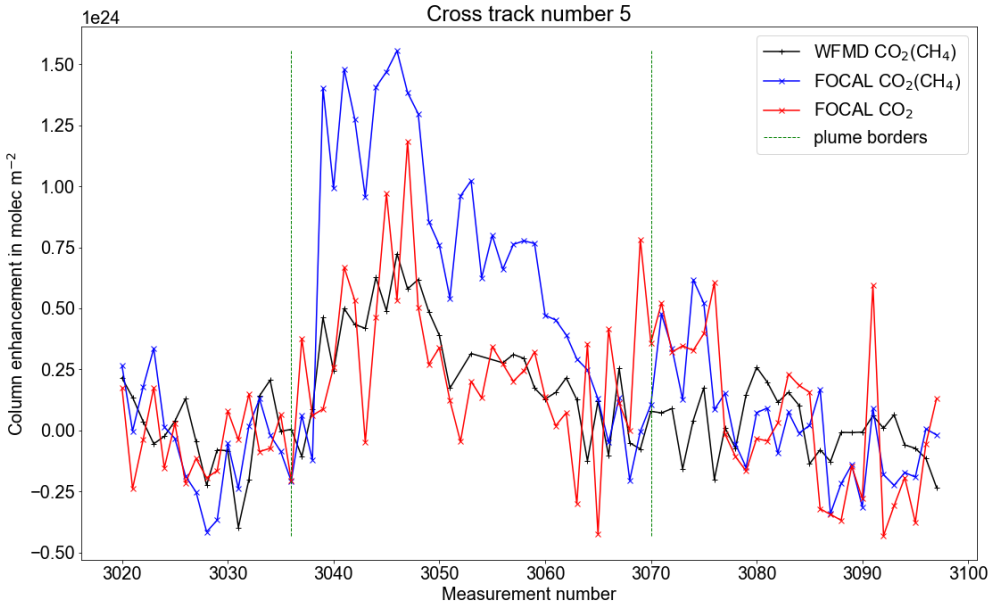

Figure A.39.: Same as Fig. A.35, but for the fifth cross-track downwind of the source.

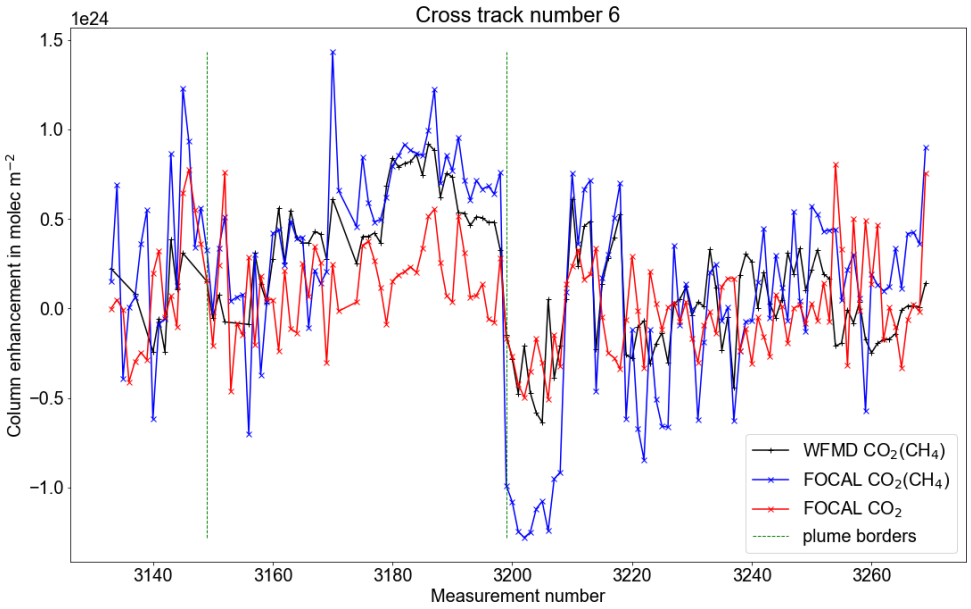

Figure A.40.: Same as Fig. A.35, but for the sixth cross-track downwind of the source.

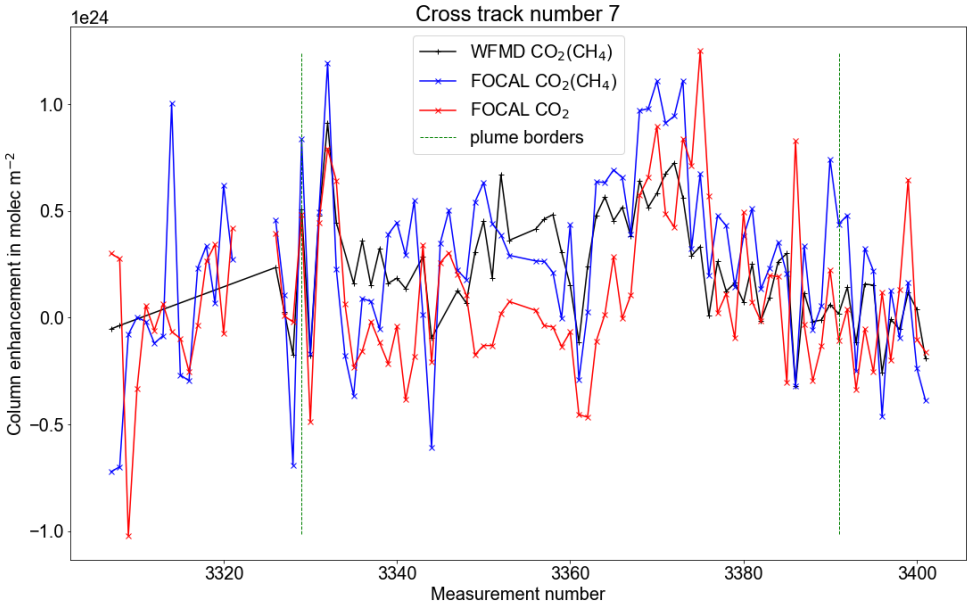

Figure A.41.: Same as Fig. A.35, but for the seventh cross-track downwind of the source.

A.6.4. Cross-tracks for flux inversion of FOCAL AIR scattering 1-window retrieval results

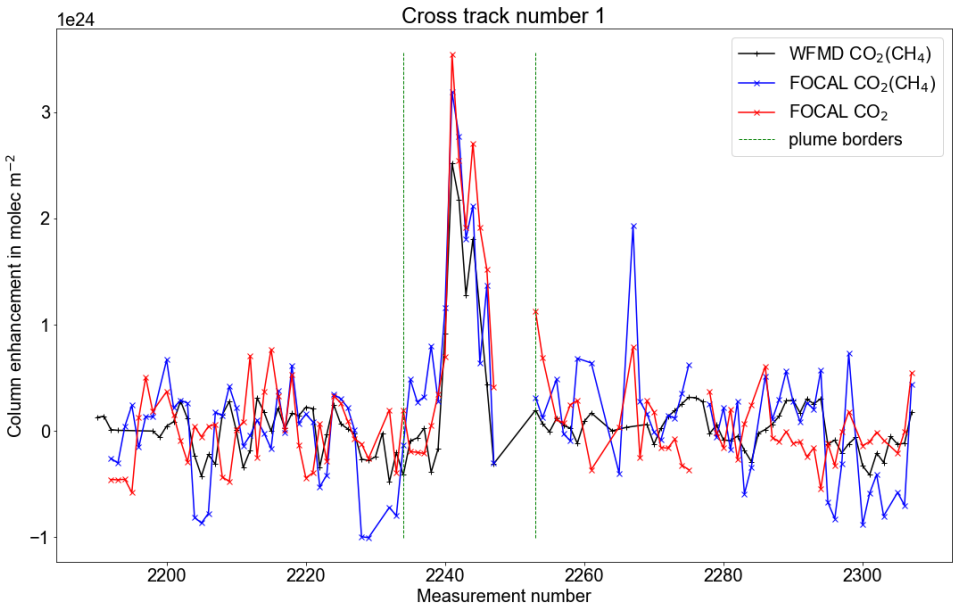

Figure A.42.: Background normalized and binned retrieval results of the first cross-track downwind of the source for the scattering 1-window FOCAL AIR retrieval. For comparison, also the WFM-DOAS retrieval results are shown in black.

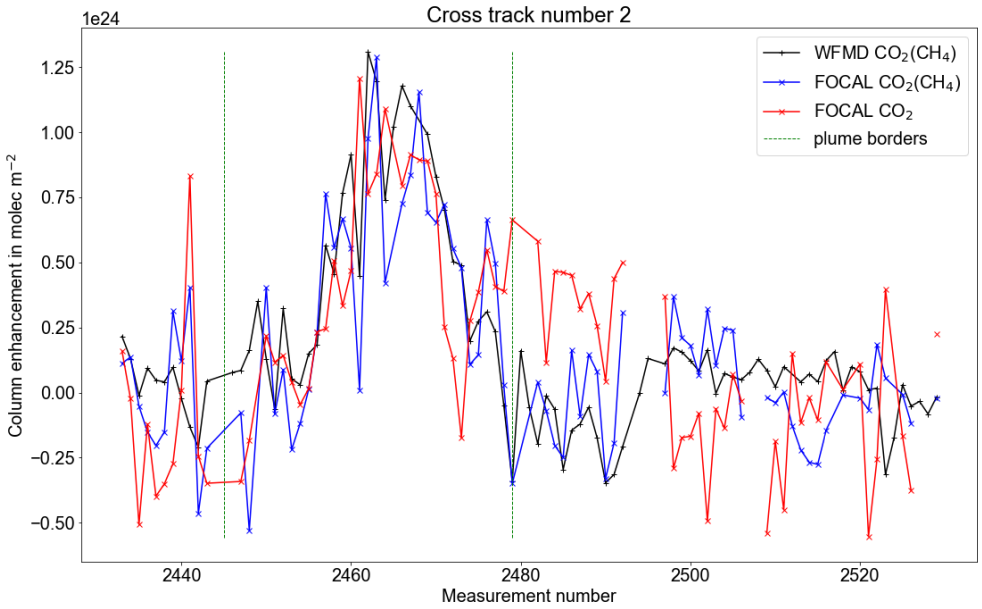

Figure A.43.: Same as Fig. A.42, but for the second cross-track downwind of the source.

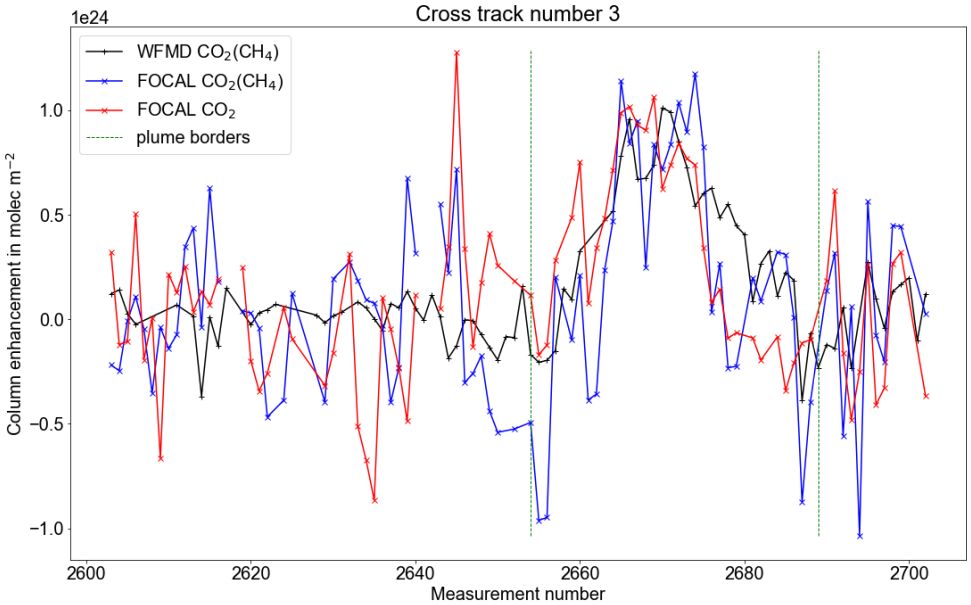

Figure A.44.: Same as Fig. A.42, but for the third cross-track downwind of the source.

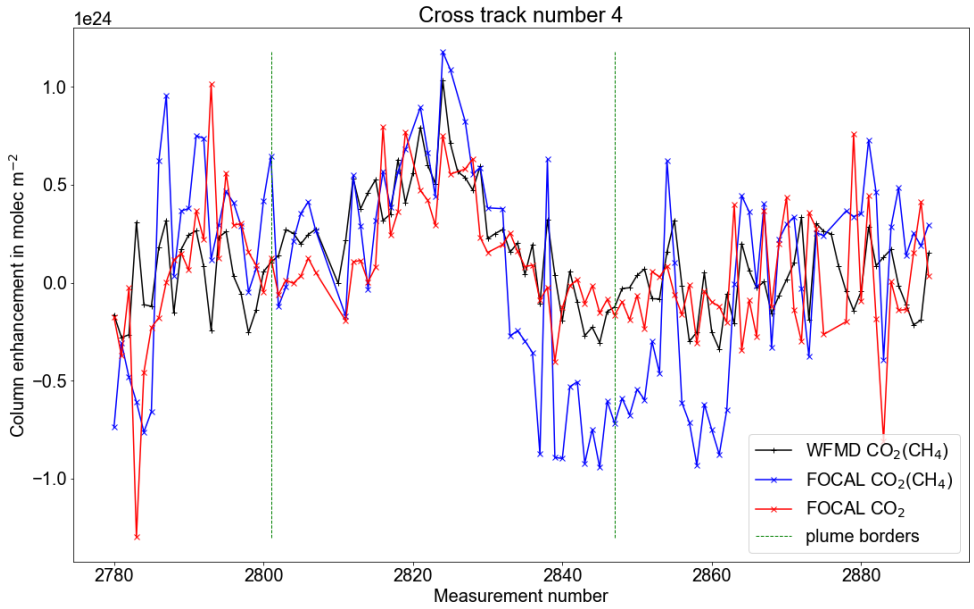

Figure A.45.: Same as Fig. A.42, but for the fourth cross-track downwind of the source.

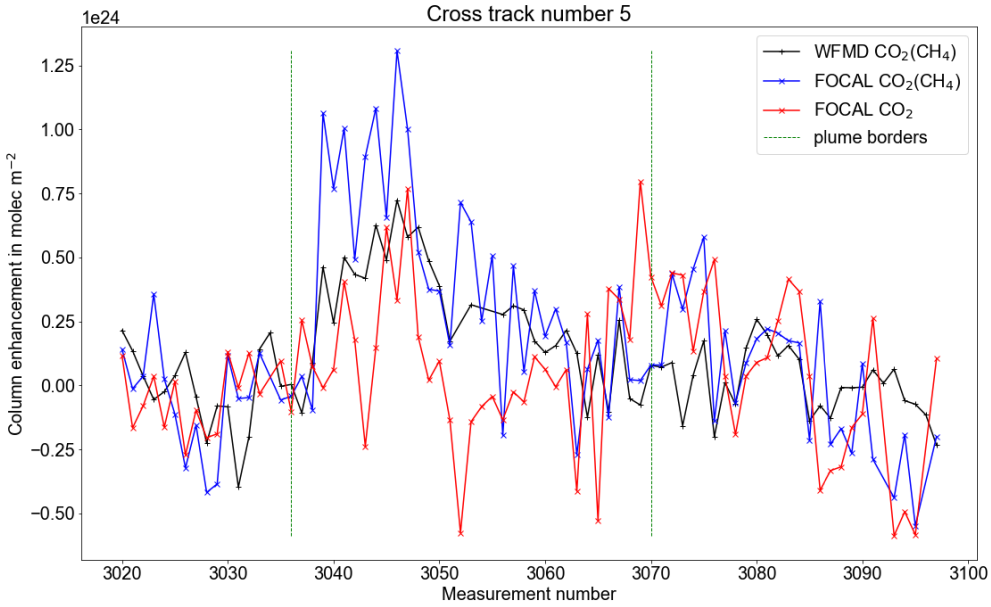

Figure A.46.: Same as Fig. A.42, but for the fifth cross-track downwind of the source.

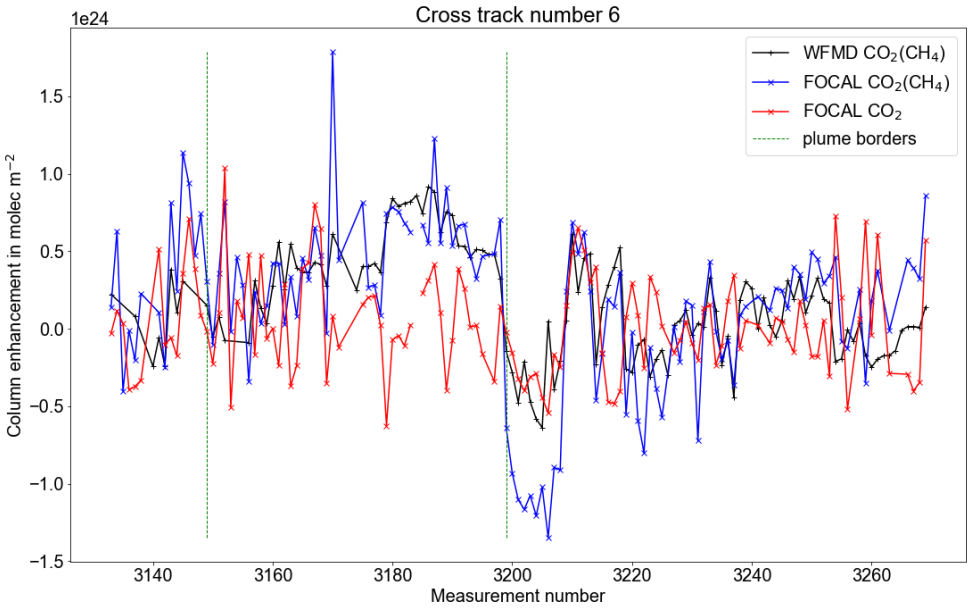

Figure A.47.: Same as Fig. A.42, but for the sixth cross-track downwind of the source.

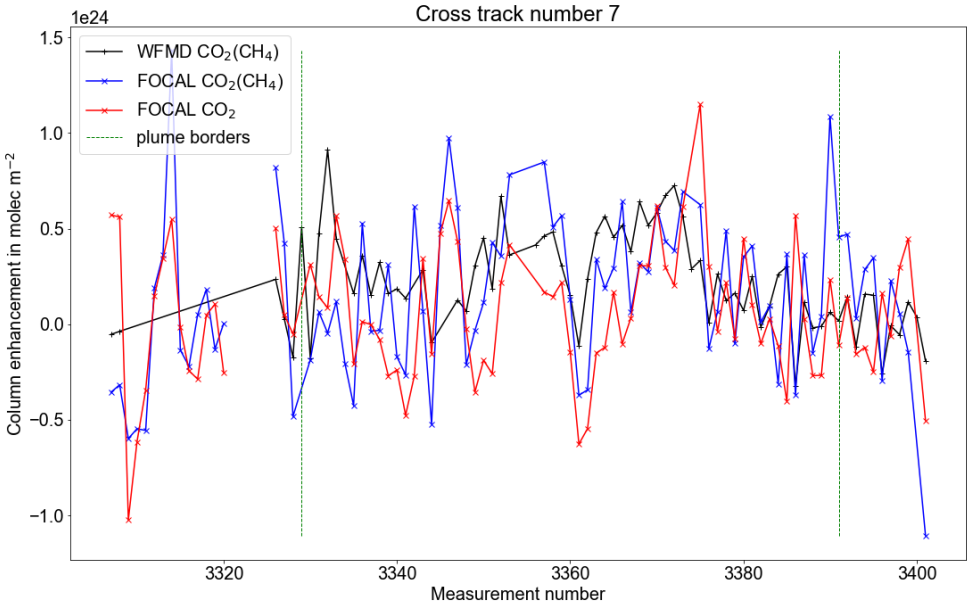

Figure A.48.: Same as Fig. A.42, but for the seventh cross-track downwind of the source.

List of Figures

2.1. Sources of atmospheric methane . . . 7
2.2. Globally averaged marine surface concentrations of CH_4 . . . 9
2.3. Global carbon budget 2020 . . . 13
2.4. Globally averaged marine surface concentrations of CO_2 . . . 14

3.1. Vertical temperature and pressure profile of the Earth . . . 18
3.2. Schematic of the radiative transfer in an air parcel . . . 19
3.3. Morse potential for two electronic states with according vibrational states . . . 28
3.4. Schematics of the vibrational-rotational transitions . . . 30
3.5. Molecular structure of methane and its four different vibrational modes . . . 32
3.6. Transmission in the atmosphere due to the presence of a CH_4 enhancement of 10 % . . . 33
3.7. Structure and vibrational modes of the CO_2 molecule . . . 34
3.8. Transmission in the atmosphere due to the presence of a CO_2 enhancement of 5 % . . . 35
3.9. Absorption characteristics of the O_2A band for a 5 % change in O_2 concentration 36
3.10. Radiation budget of the atmosphere . . . 37

5.1. Example spectrum of the MAMAP instrument . . . 53
5.2. Schematics of the MAMAP2D-Light instrument . . . 56
5.3. Image of the upper part of the MAMAP2D-Light instrument without protective cover . . . 57
5.4. MAMAP2D-Light in the Dimona wing pod . . . 59
5.5. MAMAP2D-Light spectral calibration setup . . . 61
5.6. FOCAL-AIR scattering forward model schematics . . . 66
5.7. Jacobians of the state vector elements for the FOCAL-AIR scattering 1-window retrieval . . . 80
5.8. Jacobians of the state vector elements for the FOCAL-AIR scattering 2-window retrieval . . . 81

6.1. Simulated AVIRIS-NG spectra and weighting functions around 1600 and 2300 nm . . . 88
6.2. Surface reflectance spectra for different surface types around 2300 nm . . . 92
6.3. AVIRIS-NG sensitivity study results apart from surface reflectance spectra . . . 93
6.4. AVIRIS-NG low radiance scene example . . . 96
6.5. Radiance and RMS filtering for AVIRIS-NG . . . 97
6.6. Methane plume originating from a flare at Fort McMurray, detected with AVIRIS-NG . . . 98

6.7. Methane plumes detected with AVIRIS-NG west of the Rocky Mountains in Alberta . . . 100
6.8. Methane plumes detected with AVIRIS-NG from oil and gas infrastructure . 101
6.9. Methane plumes detected with AVIRIS-NG west over two gas vents 102
6.10. Methane plumes from a coal mine ventilation shaft detected with AVIRIS-NG 102
6.11. Methane plumes detected with AVIRIS-NG over an open cast coal main . . . 103
6.12. Comparison of WFM-DOAS, MF, and IMAP-DOAS retrieval results for the coal mine ventilation shaft plume . . . 105
6.13. Comparison of WFM-DOAS and MF retrieval results for four additional plumes 106
6.14. Defective pixel mask of the MAMAP2D-Light detector . . . 110
6.15. Wavelength calibration results for the MAMAP2D-Light instrument . . . 111
6.16. Instrument spectral response function of the MAMAP2D-Light instrument . 112
6.17. Mean dark currents measured during the measurement flight over the power plant Jänschwalde in June 2021 . . . 114
6.18. Example spectrum of MAMAP2D-Light . . . 115
6.19. RMS filtering of MAMAP2D-Light data . . . 117
6.20. MAMAP2D-Light data set after correction for signal dependency of the retrieval results . . . 118
6.21. Image of the power plant plume of Jänschwalde retrieved from MAMAP2D-Light data . . . 118
6.22. Noise model fit for the FOCAL AIR 1-window retrieval configuration . . . 126
6.23. Noise model fit for the FOCAL AIR 2-window retrieval configuration . . . 127
6.24. Zero-level offset model fit for the FOCAL AIR 1-window retrieval configuration 128
6.25. Zero-level offset model fit for the FOCAL AIR 2-window retrieval configuration 129
6.26. Comparison of FOCAL AIR absorption-only 2-window xCO_2 and proxy ($xCO_2(CH_4)$) retrieval results . . . 131
6.27. Comparison of FOCAL AIR scatterin 2-window xCO_2 and proxy ($xCO_2(CH_4)$) retrieval results . . . 131
6.28. Comparison of FOCAL AIR absorption-only 1-window xCO_2 and proxy ($xCO_2(CH_4)$) retrieval results . . . 132
6.29. Comparison of FOCAL AIR scattering 1-window xCO_2 and proxy ($xCO_2(CH_4)$) retrieval results . . . 132
6.30. Comparison of FOCAL-AIR absorption-only 2-window xCO_2 and xCH_4 enhancements . . . 133
6.31. Comparison of FOCAL-AIR scattering 2-window xCO_2 and xCH_4 enhancements . . . 133
6.32. Comparison of FOCAL-AIR absorption-only 1-window xCO_2 and xCH_4 enhancements . . . 134
6.33. Comparison of FOCAL-AIR scattering 1-window xCO_2 and xCH_4 enhancements . . . 134
6.34. Continuum radiance and xCH_4 for the absorption-only 1-window retrieval . . 135
6.35. Comparison of FOCAL-AIR scattering xCO_2 and Angstöm coefficient $\mathring{A}$ retrieval results . . . 136
6.36. Comparison of FOCAL-AIR absorption-only 2-window CO_2 and WFM-DOAS enhancements . . . 137

6.37. Comparison of FOCAL-AIR scattering 2-window CO_2 and WFM-DOAS enhancements . . . 137
6.38. Comparison of FOCAL-AIR absorption-only 1-window CO_2 and WFM-DOAS enhancements . . . 138
6.39. Comparison of FOCAL-AIR scattering 1-window CO_2 and WFM-DOAS enhancements . . . 138
6.40. Scatter plot of FOCAL-AIR absorption-only 2-window and WFM-DOAS retrieval results . . . 139
6.41. Scatter plot of FOCAL-AIR scattering 2-window and WFM-DOAS retrieval results . . . 139
6.42. Scatter plot of FOCAL-AIR absorption-only 1-window and WFM-DOAS retrieval results . . . 140
6.43. Scatter plot of FOCAL-AIR scattering 1-window and WFM-DOAS retrieval results . . . 140

7.1. Comparison of the FOCAL AIR retrieval results of the best performing retrieval configurations and WFM-DOAS retrieval results . . . 156
7.2. Preliminary estimation of the detection limit for MAMAP2D-Light . . . 159

A.1. Comparison of ERA5 and ground station wind speed . . . 166
A.2. Cross tracks through the Jänschwalde power plant plume for MAMAP2D-Light data for the first flight track . . . 167
A.3. Cross tracks through the Jänschwalde power plant plume for MAMAP2D-Light data for the second flight track . . . 168
A.4. Cross tracks through the Jänschwalde power plant plume for MAMAP2D-Light data for the third flight track . . . 168
A.5. Cross tracks through the Jänschwalde power plant plume for MAMAP2D-Light data for the fourth flight track . . . 169
A.6. Cross tracks through the Jänschwalde power plant plume for MAMAP2D-Light data for the fifth flight track . . . 169
A.7. Cross tracks through the Jänschwalde power plant plume for MAMAP2D-Light data for the sixth flight track . . . 170
A.8. Cross tracks through the Jänschwalde power plant plume for MAMAP2D-Light data for the seventh flight track . . . 170
A.9. Cross tracks through the Jänschwalde power plant plume for MAMAP2D-Light data for the eighth flight track . . . 171
A.10. Cross tracks through the Jänschwalde power plant plume for MAMAP2D-Light data for the nineth flight track . . . 171
A.11. New and old wavelength grid for the MAMAP instrument . . . 176
A.12. ISRF fit results for the SWIR channel of the MAMAP instrument . . . 178
A.13. Fit results for the double gaussian parameters for each wavelength measurement. The strong (and periodic) variability in the parameters is most likely due to the position of the LASER peak wavelength relative to the true pixel center. . . . 179
A.14. CO_2 column enhancement in the first cross-track of the Jänschwalde power plant plume retrieved with the WFM-DOAS retrieval . . . 180

A.15. CO_2 column enhancement in the second cross-track of the Jänschwalde power plant plume retrieved with the WFM-DOAS retrieval 181
A.16. CO_2 column enhancement in the third cross-track of the Jänschwalde power plant plume retrieved with the WFM-DOAS retrieval 182
A.17. CO_2 column enhancement in the fourth cross-track of the Jänschwalde power plant plume retrieved with the WFM-DOAS retrieval 182
A.18. CO_2 column enhancement in the fifth cross-track of the Jänschwalde power plant plume retrieved with the WFM-DOAS retrieval 183
A.19. CO_2 column enhancement in the sixth cross-track of the Jänschwalde power plant plume retrieved with the WFM-DOAS retrieval 183
A.20. CO_2 column enhancement in the seventh cross-track of the Jänschwalde power plant plume retrieved with the WFM-DOAS retrieval 184
A.21. CO_2 column enhancement in the first cross-track of the Jänschwalde power plant plume retrieved with the FOCAL AIR absorption only 2-window retrieval 185
A.22. CO_2 column enhancement in the second cross-track of the Jänschwalde power plant plume retrieved with the FOCAL AIR absorption only 2-window retrieval 186
A.23. CO_2 column enhancement in the third cross-track of the Jänschwalde power plant plume retrieved with the FOCAL AIR absorption only 2-window retrieval 186
A.24. CO_2 column enhancement in the fourth cross-track of the Jänschwalde power plant plume retrieved with the FOCAL AIR absorption only 2-window retrieval 187
A.25. CO_2 column enhancement in the fifth cross-track of the Jänschwalde power plant plume retrieved with the FOCAL AIR absorption only 2-window retrieval 187
A.26. CO_2 column enhancement in the sixth cross-track of the Jänschwalde power plant plume retrieved with the FOCAL AIR absorption only 2-window retrieval 188
A.27. CO_2 column enhancement in the seventh cross-track of the Jänschwalde power plant plume retrieved with the FOCAL AIR absorption only 2-window retrieval 188
A.28. CO_2 column enhancement in the first cross-track of the Jänschwalde power plant plume retrieved with the FOCAL AIR scattering 2-window retrieval . . 189
A.29. CO_2 column enhancement in the second cross-track of the Jänschwalde power plant plume retrieved with the FOCAL AIR scattering 2-window retrieval . . 190
A.30. CO_2 column enhancement in the third cross-track of the Jänschwalde power plant plume retrieved with the FOCAL AIR scattering 2-window retrieval . . 190
A.31. CO_2 column enhancement in the fourth cross-track of the Jänschwalde power plant plume retrieved with the FOCAL AIR scattering 2-window retrieval . . 191
A.32. CO_2 column enhancement in the fifth cross-track of the Jänschwalde power plant plume retrieved with the FOCAL AIR scattering 2-window retrieval . . 191
A.33. CO_2 column enhancement in the sixth cross-track of the Jänschwalde power plant plume retrieved with the FOCAL AIR scattering 2-window retrieval . . 192
A.34. CO_2 column enhancement in the seventh cross-track of the Jänschwalde power plant plume retrieved with the FOCAL AIR scattering 2-window retrieval 192
A.35. CO_2 column enhancement in the first cross-track of the Jänschwalde power plant plume retrieved with the FOCAL AIR absorption-only 1-window retrieval 193
A.36. CO_2 column enhancement in the second cross-track of the Jänschwalde power plant plume retrieved with the FOCAL AIR absorption-only 1-window retrieval 194

A.37. CO_2 column enhancement in the third cross-track of the Jänschwalde power plant plume retrieved with the FOCAL AIR absorption-only 1-window retrieval 194
A.38. CO_2 column enhancement in the fourth cross-track of the Jänschwalde power plant plume retrieved with the FOCAL AIR absorption-only 1-window retrieval 195
A.39. CO_2 column enhancement in the fifth cross-track of the Jänschwalde power plant plume retrieved with the FOCAL AIR absorption-only 1-window retrieval 195
A.40. CO_2 column enhancement in the sixth cross-track of the Jänschwalde power plant plume retrieved with the FOCAL AIR absorption-only 1-window retrieval 196
A.41. CO_2 column enhancement in the seventh cross-track of the Jänschwalde power plant plume retrieved with the FOCAL AIR absorption-only 1-window retrieval 196
A.42. CO_2 column enhancement in the first cross-track of the Jänschwalde power plant plume retrieved with the FOCAL AIR scattering 1-window retrieval . . 197
A.43. CO_2 column enhancement in the second cross-track of the Jänschwalde power plant plume retrieved with the FOCAL AIR scattering 1-window retrieval . . 198
A.44. CO_2 column enhancement in the third cross-track of the Jänschwalde power plant plume retrieved with the FOCAL AIR scattering 1-window retrieval . . 198
A.45. CO_2 column enhancement in the fourth cross-track of the Jänschwalde power plant plume retrieved with the FOCAL AIR scattering 1-window retrieval . . 199
A.46. CO_2 column enhancement in the fifth cross-track of the Jänschwalde power plant plume retrieved with the FOCAL AIR scattering 1-window retrieval . . 199
A.47. CO_2 column enhancement in the sixth cross-track of the Jänschwalde power plant plume retrieved with the FOCAL AIR scattering 1-window retrieval . . 200
A.48. CO_2 column enhancement in the seventh cross-track of the Jänschwalde power plant plume retrieved with the FOCAL AIR scattering 1-window retrieval 200

List of Tables

5.1. Main instrument characteristics of MAMAP, MAMAP2D-Light, and AVIRIS-NG . . . 49
5.2. Wind speed for the plumes P1 - P5 for AVIRIS-NG data . . . 51
5.3. FOCAL AIR state vector for the 1-window retrieval . . . 77
5.4. FOCAL AIR state vector for the 2-window retrieval . . . 78

6.1. Comparison of the two possible fit windows for AVIRIS-NG using the retrieval scatter . . . 89
6.2. AVIRIS-NG sensitivity study parameters . . . 90
6.3. Uncertainty estimate resulting from the sensitivity study for AVIRIS-NG . . . 94
6.4. Uncertainty due to different surface types in the sensitivity study for AVIRIS-NG . . . 95
6.5. Comparison of the retrieval scatter for WFM-DOAS, MF and IMAP-DOAS applied to AVIRIS-NG data . . . 104
6.6. Emission and uncertainty estimation calculated with the cross-sectional flux method for the plumes P1 - P5 . . . 108
6.7. Main characteristics of the MAMAP2D-Light instrument . . . 109
6.8. Uncertainty estimation of the flux inversion for the WFM-DOAS retrieval results of the MAMAP2D-Light Jänschwalde power plant flight . . . 120
6.9. Simulation experiment definitions for FOCAL AIR . . . 123
6.10. Simulation experiment results for the FOCAL AIR 1-window retrieval . . . 124
6.11. Simulation experiment results for the FOCAL AIR 2-window retrieval . . . 125
6.12. Quality filtering of the FOCAL AIR retrieval results . . . 130
6.13. Mean fit RMS between measured and fitted spectra for the four different FOCAL AIR retrieval configurations and WFM-DOAS . . . 141
6.14. Background retrieval result scatter for FOCAL AIR and WFM-DOAS retrieval results . . . 141
6.15. Emission estimate from FOCAL AIR and WFM-DOAS retrieval results . . . 143
6.16. Uncertainty estimation of the flux inversion for FOCAL AIR absorption-only 2-window retrieval results . . . 144
6.17. Uncertainty estimation of the flux inversion for FOCAL AIR scattering 2-window retrieval results . . . 144
6.18. Uncertainty estimation of the flux inversion for FOCAL AIR absorption-only 1-window retrieval results . . . 145
6.19. Uncertainty estimation of the flux inversion for FOCAL AIR scattering 1-window retrieval results . . . 145

7.1. Summary of main characteristics of the three instruments MAMAP2D-Light, MAMAP, and AVIRIS-NG 149
7.2. Overview over the main characteristics of the WFM-DOAS, FOCAL AIR, MF and IMAP-DOAS retrievals 153

A.1. Background aerosol scenario for the FOCAL AIR simulation experiments . . 172
A.2. Continental aerosol scenario for the FOCAL AIR simulation experiments . . 173
A.3. Urban aerosol scenario for the FOCAL AIR simulation experiments 174
A.4. Uncertainty estimation of the flux inversion for WFM-DOAS retrieval results after application of the proxy 181

List of Abbreviations

- (i)FOV: (instantaneous) field of view
- ADC: Analog-to-digital converter
- AIRS: Atmospheric Infrared Sounder
- AVIRIS-NG: Airborne Visible-InfraRed Imaging Spectrometer - Next Generation
- BRDF: Bidirectional reflectance-distribution function
- BU: binary units
- CFC: chlorofluorocarbons
- CHARM-F: CO_2 and CH_4 Remote Monitoring - Flugzeug
- COMET: CO_2 and METhane mission
- CotS: Commercial off-the-shelf
- DIO: digital input/output
- ECMWF: European Centre for Medium-Range Weather Forecasts
- ERF: effective radiative forcing
- EU: European Union
- FOCAL: Fast atmOspheric traCe gAs retrievaL
- FPA: focal plane array
- FTIR: Fourier-transform infrared spectrometers
- FWHM: full width at half maximum
- GCP: Global carbon project
- GHG: GreenHouse Gas(es)
- GHGSat: GreenHouse Gas Satellite
- GMST: Global mean surface temperature
- GOSAT: Greenhouse gas Observing Satellite
- HCFC: ydrofluorocarbons
- HyTES: Hyperspectral Thermal Emission Spectrometer

- IASI: Infrared Atmospheric Sounding Instrument
- ICOS: Integrated Carbon Observation System
- IMAP-DOAS: Iterative Maximum A-Posteriori Differential Optical Absorption Spectroscopy
- IMU: inertial measurement unit
- IRF: instantaneous radiative forcing
- ISRF: instrument spectral response function
- IUP: Institut für Umweltphysik (Institute for environmental physics)
- IZA: instrument zenith angle
- LASER: Light amplification by stimulated emission of radiation
- MAMAP: Methane Airborne MAPper
- MCT: mercury cadmium telluride
- MF: matched filter
- NDACC: Network for the Detection of Atmospheric Composition Change
- NIR: near infrared
- NOAA ESRL/GMD: National Oceanic and Atmospheric Administration Earth System Lab, Global Monitoring Division
- NOAA: National Oceanic and Atmospheric Administration
- NSR: noise-to-signal ratio
- OCO: Orbiting Carbon Observatory
- OPAC: optical property of aerosols and clouds
- PRISMA: PRecursore IperSpettrale della Missione Applicativa
- PSF: profile scaling factor
- QE: quantum efficiency
- RMS: root mean square error
- RSR: residuum-to-signal ratio
- SCIAMACHY: Scanning Imaging Absorption Spectrometer for Atmospheric CHartographY
- SEBASS: Spatially Enhanced Broadband Array Spectrograph System
- SECM: Simple Empirical CO_2 model
- SLIM: Simple cLImatological Mode
- SNR: signal-to-noise ratio

- SRTM: Shuttle Radar Topospheric Mission
- SWIR: short wave infrared
- SZA: solar zenith angle
- TCCON: Total Carbon Column Observing Network
- TES: Tropospheric Emission Spectrometer
- TIR: thermal infrared
- TROPOMI: TROPOspheric Monitoring Instrument
- UAV: Unmanned aerial vehicle
- UNFCCC: United Nations Framework Convention on Climate Change
- USA: United States of America
- UV: ultra-violett
- WFM-DOAS: Weighting Function Modified Differential Optical Absorption Spectroscopy
- ZLO: zero-level offset
- ppb: parts per billion
- ppm: parts per million

Acknowledgements

First of all, I would like to thank my Ph.D. supervisor Prof. Dr. John P. Burrows, for offering the possibility to research these interesting questions in his department, providing financial support for my work, and giving very helpful advice, especially during the last phases of my Ph.D. I would like to thank Heinrich Bovensmann for helping me put my work in a broader context and pushing me back on track to finishing the thesis. Additionally, I'd like to thank him, Konstantin Gerilowski, and Sven Krautwurst for their constructive and critical comments that have improved this work. I am especially thankful for Konstantin Gerilowski, who helped me in understanding the difficulties in designing and building an airborne remote sensing instrument. I thank Andreas Fix for being part of my Ph.D. committee in the last years. I thank Mihalis Vrekoussis, who agreed to be the second reviewer of my thesis.

A special thank you goes to the whole MAMAP team, namely Sven Krautwurst, Konstantin Gerilowski, Heinrich Bovensmann, and Oke Huhs, for the great working spirit and friendly and welcoming working environment. It really is a pleasure to work with all of you! Furthermore, I'd like to thank the whole greenhouse gas group for the valuable and helpful discussions. A special thank you goes to Max Reuter, Michael Hilker, and Stefan Noel for their help with the FOCAL retrieval. You always had time to answer my questions and helped me improve the FOCAL AIR retrieval a lot! I'd also like to use these lines to remember Andreas Hilboll, who passed away way too early. Thank you for your support especially with switching to Python, and for the nice conversations.

The work on AVIRIS-NG data was done in cooperation with the AVIRIS-NG team in California. My special thank goes to Christian Frankenberg, Andrew Thorpe and David Thompson, who provided interesting AVIRIS-NG data sets, and helped me get started with AVIRIS-NG data. The MAMAP2D-Light instrument was developed and built in cooperation with the Institute for Integrated Product Development (BIK) of the University of Bremen. I'd like to thank Jan Franke for the pleasant cooperation during the design and drawing stages of the development.

During this thesis, several measurement campaigns were performed. I am very thankful for Thomas Ruhtz (FU Berlin), Carsten Lindemann (FU Berlin), Jerry Gordon (FU Berlin), Andreas Fix (DLR Oberpfaffenhofen), as well as the whole MAMAP team for the successful COMET campaigns. Furthermore, I'd like to thank the team of the Dimona motor glider from the Jadehochschule Wilhelmshaven, namely Martin Kumm, Pascal Janßen, and Jens Wellhausen for their support in mounting the MAMAP2D-Light instrument in the underwing pod of the Dimona motor glider and performing the test and measurement flights. This work has been financed partly by the University and the State of Bremen, partly through the BMBF project AIRSPACE (grant 01LK1701B).

I also want to thank our secretaries, namely Geraldine Schmiechen (who hopefully enjoys her retirement), Stephanie Drath, and Isabelle Fokke, for helping with the administrative side of the research. Furthermore, I'd like to thank Heiko Schellhorn, Heiko Schröter, and Pablo Echevarria for IT support.

This work would not have been possible without my friends. A special thank you to Chrissy and Patrick, for all the time we spent together and for motivating me in more challenging times. Also a big thank you to Philipp Heyken for proofreading large parts of the work in a short time frame.

I like to thank especially my wife Paddi for the continuous support, for being always there for me, and for motivating me.

Der letzte Dank gilt meinen Eltern, die mich unterstützen und immer für mich da sind.

Bibliography

Allan, W., Struthers, H., and Lowe, D. C. Methane carbon isotope effects caused by atomic chlorine in the marine boundary layer: Global model results compared with Southern Hemisphere measurements. *Journal of Geophysical Research*, 112, no. D4. doi:10.1029/2006jd007369, 2007.

Amat, G. and Pimbert, M. On Fermi resonance in carbon dioxide. *Journal of Molecular Spectroscopy*, 16, no. 2:pp. 278–290. doi:10.1016/0022-2852(65)90123-2, 1965.

Amediek, A., Ehret, G., Fix, A., Wirth, M., Büdenbender, C., Quatrevalet, M., Kiemle, C., and Gerbig, C. CHARM-F—a new airborne integrated-path differential-absorption lidar for carbon dioxide and methane observations: measurement performance and quantification of strong point source emissions. *Applied Optics*, 56, no. 18:p. 5182. doi:10.1364/ao.56.005182, 2017.

Anagnostou, E., John, E. H., Babila, T. L., Sexton, P. F., Ridgwell, A., Lunt, D. J., Pearson, P. N., Chalk, T. B., Pancost, R. D., and Foster, G. L. Proxy evidence for state-dependence of climate sensitivity in the Eocene greenhouse. *Nature Communications*, 11, no. 1. doi:10.1038/s41467-020-17887-x, 2020.

Andersen, T., Scheeren, B., Peters, W., and Chen, H. A UAV-based active AirCore system for measurements of greenhouse gases. *Atmospheric Measurement Techniques*, 11, no. 5:pp. 2683–2699. doi:10.5194/amt-11-2683-2018, 2018.

Andrews, A. E., Kofler, J. D., Trudeau, M. E., Williams, J. C., Neff, D. H., Masarie, K. A., Chao, D. Y., Kitzis, D. R., Novelli, P. C., Zhao, C. L., Dlugokencky, E. J., Lang, P. M., Crotwell, M. J., Fischer, M. L., Parker, M. J., Lee, J. T., Baumann, D. D., Desai, A. R., Stanier, C. O., Wekker, S. F. J. D., Wolfe, D. E., Munger, J. W., and Tans, P. P. CO2, CO, and CH4 measurements from tall towers in the NOAA Earth System Research Laboratory's Global Greenhouse Gas Reference Network: instrumentation, uncertainty analysis, and recommendations for future high-accuracy greenhouse gas monitoring efforts. *Atmospheric Measurement Techniques*, 7, no. 2:pp. 647–687. doi:10.5194/amt-7-647-2014, 2014.

Archer, D. *The Global Carbon Cycle*. Princeton University Press. doi:10.1515/9781400837076, 2011.

Archer, D., Eby, M., Brovkin, V., Ridgwell, A., Cao, L., Mikolajewicz, U., Caldeira, K., Matsumoto, K., Munhoven, G., Montenegro, A., and Tokos, K. Atmospheric Lifetime of Fossil Fuel Carbon Dioxide. *Annual Review of Earth and Planetary Sciences*, 37, no. 1:pp. 117–134. doi:10.1146/annurev.earth.031208.100206, 2009.

Aumann, H. H. Atmospheric Infrared Sounder on the Earth Observing System. *Optical Engineering*, 33, no. 3:p. 776. doi:10.1117/12.159325, 1994.

Ayasse, A. K., Thorpe, A. K., Roberts, D. A., Funk, C. C., Dennison, P. E., Frankenberg, C., Steffke, A., and Aubrey, A. D. Evaluating the effects of surface properties on methane retrievals using a synthetic airborne visible/infrared imaging spectrometer next generation (AVIRIS-NG) image. *Remote Sensing of Environment*, 215:pp. 386–397. doi:10.1016/j.rse.2018.06.018, 2018.

Babcock, H. D. and Herzberg, L. Fine Structure of the Red System of Atmospheric Oxygen Bands. *The Astrophysical Journal*, 108:p. 167. doi:10.1086/145062, 1948.

Bakkaloglu, S., Lowry, D., Fisher, R. E., France, J. L., Brunner, D., Chen, H., and Nisbet, E. G. Quantification of methane emissions from UK biogas plants. *Waste Management*, 124:pp. 82–93. doi:10.1016/j.wasman.2021.01.011, 2021.

Baldridge, A., Hook, S., Grove, C., and Rivera, G. The ASTER spectral library version 2.0. *Remote Sensing of Environment*, 113, no. 4:pp. 711–715. doi:10.1016/j.rse.2008.11.007, 2009.

Beer, R., Glavich, T. A., and Rider, D. M. Tropospheric emission spectrometer for the Earth Observing System's Aura satellite. *Applied Optics*, 40, no. 15:p. 2356. doi:10.1364/ao.40.002356, 2001.

Blake, D. R., Mayer, E. W., Tyler, S. C., Makide, Y., Montague, D. C., and Rowland, F. S. Global increase in atmospheric methane concentrations between 1978 and 1980. *Geophysical Research Letters*, 9, no. 4:pp. 477–480. doi:10.1029/gl009i004p00477, 1982.

Blumstein, D., Chalon, G., Carlier, T., Buil, C., Hebert, P., Maciaszek, T., Ponce, G., Phulpin, T., Tournier, B., Simeoni, D., Astruc, P., Clauss, A., Kayal, G., and Jegou, R. IASI instrument: technical overview and measured performances. In Strojnik, M., editor, *Infrared Spaceborne Remote Sensing XII*. SPIE. doi:10.1117/12.560907, 2004.

Borchardt, J., Gerilowski, K., Krautwurst, S., Bovensmann, H., Thorpe, A. K., Thompson, D. R., Frankenberg, C., Miller, C. E., Duren, R. M., and Burrows, J. P. Detection and quantification of CH4 plumes using the WFM-DOAS retrieval on AVIRIS-NG hyperspectral data. *Atmospheric Measurement Techniques*, 14, no. 2:pp. 1267–1291. doi:10.5194/amt-14-1267-2021, 2021.

Boucher, O., Randall, D., Artaxo, P., Bretherton, C., Feingold, G., Forster, P., Kerminen, V.-M., Kondo, Y., Liao, H., Lohmann, U., Rasch, P., Satheesh, S., S.Sherwood, Stevens, B., and Zhang, X. Clouds and Aerosols. In on Climate Change, I. P., editor, *Climate Change 2013 - The Physical Science Basis. Contribution of Working Group Ito the Fifth Assessment Report of the Intergovernmental Panel on Climate Change*, pp. 571–658. Cambridge University Press. doi:10.1017/cbo9781107415324.016, 2013.

Boudon, V., Rey, M., and Loëte, M. The vibrational levels of methane obtained from analyses of high-resolution spectra. *Journal of Quantitative Spectroscopy and Radiative Transfer*, 98, no. 3:pp. 394–404. doi:10.1016/j.jqsrt.2005.06.003, 2006.

Bovensmann, H., Burrows, J. P., Buchwitz, M., Frerick, J., Noël, S., Rozanov, V. V., Chance, K. V., and Goede, A. P. H. SCIAMACHY: Mission Objectives and Measurement Modes. *Journal of the Atmospheric Sciences*, 56, no. 2:pp. 127–150. doi: 10.1175/1520-0469(1999)056⟨0127:smoamm⟩2.0.co;2, 1999.

Buchwitz, M., de Beek, R., Noël, S., Burrows, J. P., Bovensmann, H., Bremer, H., Bergamaschi, P., Körner, S., and Heimann, M. Carbon monoxide, methane and carbon dioxide columns retrieved from SCIAMACHY by WFM-DOAS: year 2003 initial data set. *Atmospheric Chemistry and Physics*, 5, no. 12:pp. 3313–3329. doi:10.5194/acp-5-3313-2005, 2005.

Buchwitz, M., Rozanov, V. V., and Burrows, J. P. A near-infrared optimized DOAS method for the fast global retrieval of atmospheric CH4, CO, CO2, H2O, and N2O total column amounts from SCIAMACHY Envisat-1 nadir radiances. *Journal of Geophysical Research: Atmospheres*, 105, no. D12:pp. 15231–15245. ISSN 2156-2202. doi:10.1029/2000jd900191, 2000.

Buchwitz, M., Schneising, O., Reuter, M., Heymann, J., Krautwurst, S., Bovensmann, H., Burrows, J. P., Boesch, H., Parker, R. J., Somkuti, P., Detmers, R. G., Hasekamp, O. P., Aben, I., Butz, A., Frankenberg, C., and Turner, A. J. Satellite-derived methane hotspot emission estimates using a fast data-driven method. *Atmospheric Chemistry and Physics*, 17, no. 9:pp. 5751–5774. doi:10.5194/acp-17-5751-2017, 2017.

Bue, B. D., Thompson, D. R., Eastwood, M., Green, R. O., Gao, B.-C., Keymeulen, D., Sarture, C. M., Mazer, A. S., and Luong, H. H. Real-Time Atmospheric Correction of AVIRIS-NG Imagery. *IEEE Transactions on Geoscience and Remote Sensing*, 53, no. 12:pp. 6419–6428. doi:10.1109/tgrs.2015.2439215, 2015.

Burrows, J., Hölzle, E., Goede, A., Visser, H., and Fricke, W. SCIAMACHY—scanning imaging absorption spectrometer for atmospheric chartography. *Acta Astronautica*, 35, no. 7:pp. 445–451. doi:10.1016/0094-5765(94)00278-T, 1995.

Butz, A., Guerlet, S., Hasekamp, O., Schepers, D., Galli, A., Aben, I., Frankenberg, C., Hartmann, J.-M., Tran, H., Kuze, A., Keppel-Aleks, G., Toon, G., Wunch, D., Wennberg, P., Deutscher, N., Griffith, D., Macatangay, R., Messerschmidt, J., Notholt, J., and Warneke, T. Toward accurate CO2 and CH4 observations from GOSAT. *Geophysical Research Letters*, 38, no. 14:pp. n/a–n/a. doi:10.1029/2011gl047888, 2011.

Canadell, J., Dickinson, R., Hibbard, K., Raupach, M., and Young, O. Global Carbon Project, the Science Framework and Implementation: ESSP Report No. 1, 2003.

Canadell, J., Monteiro, P., Costa, M., da Cunha, L. C., Cox, P., Eliseev, A., Henson, S., Ishii, M., Jaccard, S., Koven, C., Lohila, A., Patra, P., Piao, S., Rogelj, J., Syampungani, S., Zaehle, S., and Zickfeld, K. Global Carbon and other Biogeochemical Cycles and Feedbacks. In Masson-Delmotte, V., Zhai, P., Pirani, A., Connors, S., Péan, C., Berger, S., Caud, N., Chen, Y., Goldfarb, L., Gomis, M., Huang, M., Leitzell, K., Lonnoy, E., Matthews, J., Maycock, T., Waterfield, T., Yelekçi, O., Yu, R., and Zhou, B., editors, *Climate Change 2021: The Physical Science Basis. Contribution ofWorking Group I to*

the Sixth Assessment Report of the Intergovernmental Panel on Climate Change, pp. 673–816. Cambridge University Press, Cambridge, United Kingdom and New York, NY, USA. doi:10.1017/9781009157896.013, 2021.

Canfield, D. THE EARLY HISTORY OF ATMOSPHERIC OXYGEN: Homage to Robert M. Garrels. *Annual Review of Earth and Planetary Sciences*, 33, no. 1:pp. 1–36. doi:10.1146/annurev.earth.33.092203.122711, 2005.

Caulton, D. R., Li, Q., Bou-Zeid, E., Fitts, J. P., Golston, L. M., Pan, D., Lu, J., Lane, H. M., Buchholz, B., Guo, X., McSpiritt, J., Wendt, L., and Zondlo, M. A. Quantifying uncertainties from mobile-laboratory-derived emissions of well pads using inverse Gaussian methods. *Atmospheric Chemistry and Physics*, 18, no. 20:pp. 15145–15168. doi:10.5194/acp-18-15145-2018, 2018.

Caulton, D. R., Shepson, P. B., Santoro, R. L., Sparks, J. P., Howarth, R. W., Ingraffea, A. R., Cambaliza, M. O. L., Sweeney, C., Karion, A., Davis, K. J., Stirm, B. H., Montzka, S. A., and Miller, B. R. Toward a better understanding and quantification of methane emissions from shale gas development. *Proceedings of the National Academy of Sciences*, 111, no. 17:pp. 6237–6242. doi:10.1073/pnas.1316546111, 2014.

Chapman, J. W., Thompson, D. R., Helmlinger, M. C., Bue, B. D., Green, R. O., Eastwood, M. L., Geier, S., Olson-Duvall, W., and Lundeen, S. R. Spectral and Radiometric Calibration of the Next Generation Airborne Visible Infrared Spectrometer (AVIRIS-NG). *Remote Sensing*, 11, no. 18:p. 2129. doi:10.3390/rs11182129, 2019.

Chen, D., Rojas, M., Samset, B. H., Cobb, K., Niang, A. D., Edwards, P., Emori, S., Faria, S. H., Hawkins, E., Hope, P., Huybrechts, P., Meinshausen, M., Mustafa, S. K., Plattner, G. K., and Tréguier, A. M. Framing, Context, and Methods. In Masson-Delmotte, V., Zhai, P., Pirani, A., Connors, S., Péan, C., Berger, S., Caud, N., Chen, Y., Goldfarb, L., Gomis, M., Huang, M., Leitzell, K., Lonnoy, E., Matthews, J., Maycock, T., Waterfield, T., Yelekçi, O., Yu, R., and Zhou, B., editors, *Climate Change 2021: The Physical Science Basis. Contribution ofWorking Group I to the Sixth Assessment Report of the Intergovernmental Panel on Climate Change*, pp. 147–286. Cambridge University Press, Cambridge, United Kingdom and New York, NY, USA. doi:10.1017/9781009157896.013, 2021.

Chen, Y., Sun-Mack, S., Arduini, R. F., Trepte, Q., and Minnis, P. Clear -Sky and Surface Narrowband Albedo Datasets Derived from MODIS Data. doi:10.1117/12.511180, 2006.

Copernicus Climate Change Service (C3S) (2017). ERA5: Fifth generation of ECMWF atmospheric reanalyses of the global climate. Copernicus Climate Change Service Climate Data Store (CDS). URL `https://cds.climate.copernicus.eu/cdsapp#!/home`, 2017.

Crisp, D., Pollock, H. R., Rosenberg, R., Chapsky, L., Lee, R. A. M., Oyafuso, F. A., Frankenberg, C., O'Dell, C. W., Bruegge, C. J., Doran, G. B., Eldering, A., Fisher, B. M., Fu, D., Gunson, M. R., Mandrake, L., Osterman, G. B., Schwandner, F. M., Sun, K., Taylor, T. E., Wennberg, P. O., and Wunch, D. The on-orbit performance of the Orbiting Carbon Observatory-2 (OCO-2) instrument and its radiometrically calibrated products.

Atmospheric Measurement Techniques, 10, no. 1:pp. 59–81. doi:10.5194/amt-10-59-2017, 2017.

Cusworth, D. H., Duren, R. M., Thorpe, A. K., Olson-Duvall, W., Heckler, J., Chapman, J. W., Eastwood, M. L., Helmlinger, M. C., Green, R. O., Asner, G. P., Dennison, P. E., and Miller, C. E. Intermittency of Large Methane Emitters in the Permian Basin. *Environmental Science & Technology Letters*, 8, no. 7:pp. 567–573. doi:10.1021/acs.estlett.1c00173, 2021a.

Cusworth, D. H., Duren, R. M., Thorpe, A. K., Pandey, S., Maasakkers, J. D., Aben, I., Jervis, D., Varon, D. J., Jacob, D. J., Randles, C. A., Gautam, R., Omara, M., Schade, G. W., Dennison, P. E., Frankenberg, C., Gordon, D., Lopinto, E., and Miller, C. E. Multisatellite Imaging of a Gas Well Blowout Enables Quantification of Total Methane Emissions. *Geophysical Research Letters*, 48, no. 2. doi:10.1029/2020gl090864, 2021b.

Cusworth, D. H., Duren, R. M., Thorpe, A. K., Tseng, E., Thompson, D., Guha, A., Newman, S., Foster, K. T., and Miller, C. E. Using remote sensing to detect, validate, and quantify methane emissions from California solid waste operations. *Environmental Research Letters*, 15, no. 5:p. 054012. doi:10.1088/1748-9326/ab7b99, 2020.

Cusworth, D. H., Jacob, D. J., Varon, D. J., Miller, C. C., Liu, X., Chance, K., Thorpe, A. K., Duren, R. M., Miller, C. E., Thompson, D. R., Frankenberg, C., Guanter, L., and Randles, C. A. Potential of next-generation imaging spectrometers to detect and quantify methane point sources from space. *Atmospheric Measurement Techniques*, 12, no. 10:pp. 5655–5668. doi:10.5194/amt-12-5655-2019, 2019.

Dalrymple, G. B. The age of the Earth in the twentieth century: a problem (mostly) solved. *Geological Society, London, Special Publications*, 190, no. 1:pp. 205–221. doi:10.1144/gsl.sp.2001.190.01.14, 2001.

Dennison, P. E., Thorpe, A. K., Pardyjak, E. R., Roberts, D. A., Qi, Y., Green, R. O., Bradley, E. S., and Funk, C. C. High spatial resolution mapping of elevated atmospheric carbon dioxide using airborne imaging spectroscopy: Radiative transfer modeling and power plant plume detection. *Remote Sensing of Environment*, 139:pp. 116–129. doi:10.1016/j.rse.2013.08.001, 2013.

Dlugokencky, E. *Globaly Averaged marine surface annual mean growth rate*. URL `www.esrl.noaa.gov/gmd/ccgg/trends_ch4/`, 2018.

Dlugokencky, E. and Tans, P. *Trends in Atmospheric Carbon Dioxide and Methane*. National Oceanic and Atmospheric Administration (NOAA) Global Monitoring Laboratory (GML), Boulder, CO, USA. URL `www.esrl.noaa.gov/gmd/ccgg/trends/gl_data.html`, 2020 [last access 28.03.2022].

Dlugokencky, E. J. Atmospheric methane levels off: Temporary pause or a new steady-state? *Geophysical Research Letters*, 30, no. 19. doi:10.1029/2003gl018126, 2003.

Duren, R. M., Thorpe, A. K., Foster, K. T., Rafiq, T., Hopkins, F. M., Yadav, V., Bue, B. D., Thompson, D. R., Conley, S., Colombi, N. K., Frankenberg, C., McCubbin, I. B.,

Eastwood, M. L., Falk, M., Herner, J. D., Croes, B. E., Green, R. O., and Miller, C. E. California's methane super-emitters. *Nature*, 575, no. 7781:pp. 180–184. doi:10.1038/s41586-019-1720-3, 2019.

Farr, T. G., Rosen, P. A., Caro, E., Crippen, R., Duren, R., Hensley, S., Kobrick, M., Paller, M., Rodriguez, E., Roth, L., Seal, D., Shaffer, S., Shimada, J., Umland, J., Werner, M., Oskin, M., Burbank, D., and Alsdorf, D. The Shuttle Radar Topography Mission. *Reviews of Geophysics*, 45, no. 2. ISSN 1944-9208. doi:10.1029/2005RG000183, 2007.

Fiehn, A., Kostinek, J., Eckl, M., Klausner, T., Gałkowski, M., Chen, J., Gerbig, C., Röckmann, T., Maazallahi, H., Schmidt, M., Korbeń, P., Nęcki, J., Jagoda, P., Wildmann, N., Mallaun, C., Bun, R., Nickl, A.-L., Jöckel, P., Fix, A., and Roiger, A. Estimating CH4, CO2 and CO emissions from coal mining and industrial activities in the Upper Silesian Coal Basin using an aircraft-based mass balance approach. *Atmospheric Chemistry and Physics*, 20, no. 21:pp. 12675–12695. doi:10.5194/acp-20-12675-2020, 2020.

von Fischer, J. C., Cooley, D., Chamberlain, S., Gaylord, A., Griebenow, C. J., Hamburg, S. P., Salo, J., Schumacher, R., Theobald, D., and Ham, J. Rapid, Vehicle-Based Identification of Location and Magnitude of Urban Natural Gas Pipeline Leaks. *Environmental Science & Technology*, 51, no. 7:pp. 4091–4099. doi:10.1021/acs.est.6b06095, 2017.

Fletcher, R. A modified Marquardt subroutine for non-linear least squares. *Tech. Rep. AERE-R 6799*. URL `https://ntrl.ntis.gov/NTRL/dashboard/searchResults/titleDetail/AERER6799.xhtml(lastaccess:09.03.2022`, 1971.

Foote, M. D., Dennison, P. E., Thorpe, A. K., Thompson, D. R., Jongaramrungruang, S., Frankenberg, C., and Joshi, S. C. Fast and Accurate Retrieval of Methane Concentration From Imaging Spectrometer Data Using Sparsity Prior. *IEEE Transactions on Geoscience and Remote Sensing*, 58, no. 9:pp. 6480–6492. doi:10.1109/tgrs.2020.2976888, 2020.

Fourier, J.-B. J. Mémoire sur les Températures du Globe Terrestre et des Espaces Planétaires. *Mémoires d l'Académie Royale des Sciences del'Institute de France*, VII:pp. 570–604, 1827.

Frankenberg, C., Meirink, J. F., Bergamaschi, P., Goede, A. P. H., Heimann, M., Körner, S., Platt, U., van Weele, M., and Wagner, T. Satellite chartography of atmospheric methane from SCIAMACHY on board ENVISAT: Analysis of the years 2003 and 2004. *Journal of Geophysical Research*, Volume 111, no. D7. doi:10.1029/2005jd006235, 2006.

Frankenberg, C., Platt, U., and Wagner, T. Iterative maximum a posteriori (IMAP)-DOAS for retrieval of strongly absorbing trace gases: Model studies for CH_4 and CO_2 retrieval from near infrared spectra of SCIAMACHY onboard ENVISAT. *Atmospheric Chemistry and Physics*, 5, no. 1:pp. 9–22. doi:10.5194/acp-5-9-2005. URL `http://www.atmos-chem-phys.net/5/9/2005`, 2005.

Frankenberg, C., Pollock, R., Lee, R. A. M., Rosenberg, R., Blavier, J.-F., Crisp, D., O'Dell, C. W., Osterman, G. B., Roehl, C., Wennberg, P. O., and Wunch, D. The Orbiting Carbon Observatory (OCO-2): spectrometer performance evaluation using pre-launch direct sun measurements. *Atmospheric Measurement Techniques*, 8, no. 1:pp. 301–313. doi:10.5194/amt-8-301-2015, 2015.

Frankenberg, C., Thorpe, A. K., Thompson, D. R., Hulley, G., Kort, E. A., Vance, N., Borchardt, J., Krings, T., Gerilowski, K., Sweeney, C., Conley, S., Bue, B. D., Aubrey, A. D., Hook, S., and Green, R. O. Airborne methane remote measurements reveal heavy-tail flux distribution in Four Corners region. *Proceedings of the National Academy of Sciences*, 113, no. 35:pp. 9734–9739. doi:10.1073/pnas.1605617113. `http://www.pnas.org/content/early/2016/08/10/1605617113.full.pdf`, URL `http://www.pnas.org/content/early/2016/08/10/1605617113.abstract`, 2016.

Franz, D., Acosta, M., Altimir, N., Arriga, N., Arrouays, D., Aubinet, M., Aurela, M., Ayres, E., López-Ballesteros, A., Barbaste, M., Berveiller, D., Biraud, S., Boukir, H., Brown, T., Brümmer, C., Buchmann, N., Burba, G., Carrara, A., Cescatti, A., Ceschia, E., Clement, R., Cremonese, E., Crill, P., Darenova, E., Dengel, S., D'Odorico, P., Filippa, G., Fleck, S., Fratini, G., Fuß, R., Gielen, B., Gogo, S., Grace, J., Graf, A., Grelle, A., Gross, P., Grünwald, T., Haapanala, S., Hehn, M., Heinesch, B., Heiskanen, J., Herbst, M., Herschlein, C., Hörtnagl, L., Hufkens, K., Ibrom, A., Jolivet, C., Joly, L., Jones, M., Kiese, R., Klemedtsson, L., Kljun, N., Klumpp, K., Kolari, P., Kolle, O., Kowalski, A., Kutsch, W., Laurila, T., de Ligne, A., Linder, S., Lindroth, A., Lohila, A., Longdoz, B., Mammarella, I., Manise, T., Jiménez, S. M., Matteucci, G., Mauder, M., Meier, P., Merbold, L., Mereu, S., Metzger, S., Migliavacca, M., Mölder, M., Montagnani, L., Moureaux, C., Nelson, D., Nemitz, E., Nicolini, G., Nilsson, M. B., de Beeck, M. O., Osborne, B., Löfvenius, M. O., Pavelka, M., Peichl, M., Peltola, O., Pihlatie, M., Pitacco, A., Pokorný, R., Pumpanen, J., Ratié, C., Rebmann, C., Roland, M., Sabbatini, S., Saby, N. P., Saunders, M., Schmid, H. P., Schrumpf, M., Sedlák, P., Ortiz, P. S., Siebicke, L., Šigut, L., Silvennoinen, H., Simioni, G., Skiba, U., Sonnentag, O., Soudani, K., Soulé, P., Steinbrecher, R., Tallec, T., Thimonier, A., Tuittila, E.-S., Tuovinen, J.-P., Vestin, P., Vincent, G., Vincke, C., Vitale, D., Waldner, P., Weslien, P., Wingate, L., Wohlfahrt, G., Zahniser, M., and Vesala, T. Towards long-term standardised carbon and greenhouse gas observations for monitoring Europe's terrestrial ecosystems: a review. *International Agrophysics*, 32, no. 4:pp. 439–455. doi:10.1515/intag-2017-0039, 2018.

Friedlingstein, P., O'Sullivan, M., Jones, M. W., Andrew, R. M., Hauck, J., Olsen, A., Peters, G. P., Peters, W., Pongratz, J., Sitch, S., Quéré, C. L., Canadell, J. G., Ciais, P., Jackson, R. B., Alin, S., Aragão, L. E. O. C., Arneth, A., Arora, V., Bates, N. R., Becker, M., Benoit-Cattin, A., Bittig, H. C., Bopp, L., Bultan, S., Chandra, N., Chevallier, F., Chini, L. P., Evans, W., Florentie, L., Forster, P. M., Gasser, T., Gehlen, M., Gilfillan, D., Gkritzalis, T., Gregor, L., Gruber, N., Harris, I., Hartung, K., Haverd, V., Houghton, R. A., Ilyina, T., Jain, A. K., Joetzjer, E., Kadono, K., Kato, E., Kitidis, V., Korsbakken, J. I., Landschützer, P., Lefèvre, N., Lenton, A., Lienert, S., Liu, Z., Lombardozzi, D., Marland, G., Metzl, N., Munro, D. R., Nabel, J. E. M. S., Nakaoka, S.-I., Niwa, Y., O'Brien, K., Ono, T., Palmer, P. I., Pierrot, D., Poulter, B., Resplandy, L., Robertson, E., Rödenbeck, C., Schwinger, J., Séférian, R., Skjelvan, I., Smith, A. J. P., Sutton, A. J., Tanhua, T., Tans, P. P., Tian, H., Tilbrook, B., van der Werf, G., Vuichard, N., Walker, A. P., Wanninkhof, R., Watson, A. J., Willis, D., Wiltshire, A. J., Yuan, W., Yue, X., and Zaehle, S. Global Carbon Budget 2020. *Earth System Science Data*, 12, no. 4:pp. 3269–3340. doi:10.5194/essd-12-3269-2020, 2020.

Gałkowski, M., Jordan, A., Rothe, M., Marshall, J., Koch, F.-T., Chen, J., Agusti-Panareda,

A., Fix, A., and Gerbig, C. In situ observations of greenhouse gases over Europe during the CoMet 1.0 campaign aboard the HALO aircraft. *Atmospheric Measurement Techniques*, 14, no. 2:pp. 1525–1544. doi:10.5194/amt-14-1525-2021, 2021.

Gerilowski, K., Krings, T., Hartmann, J., Buchwitz, M., Sachs, T., Erzinger, J., Burrows, J. P., and Bovensmann, H. Atmospheric remote sensing constraints on direct sea-air methane flux from the 22/4b North Sea massive blowout bubble plume. *Marine and Petroleum Geology*, 68:pp. 824–835. doi:10.1016/j.marpetgeo.2015.07.011, 2015.

Gerilowski, K., Tretner, A., Krings, T., Buchwitz, M., Bertagnolio, P. P., Belemezov, F., Erzinger, J., Burrows, J. P., and Bovensmann, H. MAMAP – a new spectrometer system for column-averaged methane and carbon dioxide observations from aircraft: instrument description and performance analysis. *Atmospheric Measurement Techniques*, 4, no. 2:pp. 215–243. doi:10.5194/amt-4-215-2011. URL `http://www.atmos-meas-tech.net/4/215/2011`, 2011.

Gordon, I., Rothman, L., Hill, C., Kochanov, R., Tan, Y., Bernath, P., Birk, M., Boudon, V., Campargue, A., Chance, K., Drouin, B., Flaud, J.-M., Gamache, R., Hodges, J., Jacquemart, D., Perevalov, V., Perrin, A., Shine, K., Smith, M.-A., Tennyson, J., Toon, G., Tran, H., Tyuterev, V., Barbe, A., Császár, A., Devi, V., Furtenbacher, T., Harrison, J., Hartmann, J.-M., Jolly, A., Johnson, T., Karman, T., Kleiner, I., Kyuberis, A., Loos, J., Lyulin, O., Massie, S., Mikhailenko, S., Moazzen-Ahmadi, N., Müller, H., Naumenko, O., Nikitin, A., Polyansky, O., Rey, M., Rotger, M., Sharpe, S., Sung, K., Starikova, E., Tashkun, S., Auwera, J. V., Wagner, G., Wilzewski, J., Wcisło, P., Yu, S., and Zak, E. The HITRAN2016 molecular spectroscopic database. *Journal of Quantitative Spectroscopy and Radiative Transfer*, 203:pp. 3–69. doi:10.1016/j.jqsrt.2017.06.038, 2017.

Govil, H., Tripathi, M. K., Diwan, P., and and, S. G. IDENTIFICATION OF IRON OXIDES MINERALS IN WESTERN JAHAJPUR REGION, INDIA USING AVIRIS-NG HYPERSPECTRAL REMOTE SENSING. *The International Archives of the Photogrammetry, Remote Sensing and Spatial Information Sciences*, XLII-5:pp. 233–237. doi:10.5194/isprs-archives-xlii-5-233-2018, 2018.

Green, R. O., Eastwood, M. L., Sarture, C. M., Chrien, T. G., Aronsson, M., Chippendale, B. J., Faust, J. A., Pavri, B. E., Chovit, C. J., Solis, M., Olah, M. R., and Williams, O. Imaging Spectroscopy and the Airborne Visible/Infrared Imaging Spectrometer (AVIRIS). *Remote Sensing of Environment*, 65, no. 3:pp. 227–248. doi:10.1016/s0034-4257(98)00064-9, 1998.

Guanter, L., Kaufmann, H., Segl, K., Foerster, S., Rogass, C., Chabrillat, S., Kuester, T., Hollstein, A., Rossner, G., Chlebek, C., Straif, C., Fischer, S., Schrader, S., Storch, T., Heiden, U., Mueller, A., Bachmann, M., Mühle, H., Müller, R., Habermeyer, M., Ohndorf, A., Hill, J., Buddenbaum, H., Hostert, P., van der Linden, S., Leitão, P., Rabe, A., Doerffer, R., Krasemann, H., Xi, H., Mauser, W., Hank, T., Locherer, M., Rast, M., Staenz, K., and Sang, B. The EnMAP Spaceborne Imaging Spectroscopy Mission for Earth Observation. *Remote Sensing*, 7, no. 7:pp. 8830–8857. doi:10.3390/rs70708830, 2015.

Haken, H. and Wolf, H. C. *Molekülphysik und Quantenchemie: Einführung in die experimentellen und theoretischen Grundlagen*. Springer-Verlag, 5th edition edition, 2006.

Hakkarainen, J., Ialongo, I., and Tamminen, J. Direct space-based observations of anthropogenic CO2 emission areas from OCO-2. *Geophysical Research Letters*, 43, no. 21. doi:10.1002/2016gl070885, 2016.

Hamlin, L., Green, R. O., Mouroulis, P., Eastwood, M., Wilson, D., Dudik, M., and Paine, C. Imaging spectrometer science measurements for Terrestrial Ecology: AVIRIS and new developments. In *2011 Aerospace Conference*. IEEE. doi:10.1109/aero.2011.5747395, 2011.

Hausmann, P., Sussmann, R., and Smale, D. Contribution of oil and natural gas production to renewed increase in atmospheric methane (2007–2014): top–down estimate from ethane and methane column observations. *Atmospheric Chemistry and Physics*, 16, no. 5:pp. 3227–3244. doi:10.5194/acp-16-3227-2016, 2016.

Hess, M., Koepke, P., and Schult, I. Optical Properties of Aerosols and Clouds: The Software Package OPAC. *Bulletin of the American Meteorological Society*, 79, no. 5:pp. 831–844. doi:10.1175/1520-0477(1998)079⟨0831:opoaac⟩2.0.co;2, 1998.

Hilico, J.-C., Robert, O., Loëte, M., Toumi, S., Pine, A., and Brown, L. Analysis of the Interacting Octad System of 12CH4. *Journal of Molecular Spectroscopy*, 208, no. 1:pp. 1–13. doi:10.1006/jmsp.2001.8364, 2001.

Hook, S. J., Johnson, W. R., and Abrams, M. J. NASA's Hyperspectral Thermal Emission Spectrometer (HyTES). In *Thermal Infrared Remote Sensing*, pp. 93–115. Springer Netherlands. doi:10.1007/978-94-007-6639-6_5, 2013.

Horel, J., Splitt, M., Dunn, L., Pechmann, J., White, B., Ciliberti, C., Lazarus, S., Slemmer, J., Zaff, D., and Burks, J. MESOWEST: COOPERATIVE MESONETS IN THE WESTERN UNITED STATES. *Bulletin of the American Meteorological Society*, 83, no. 2:pp. 211 – 226. doi:10.1175/1520-0477(2002)083⟨0211:MCMITW⟩2.3.CO;2. URL `https://journals.ametsoc.org/view/journals/bams/83/2/1520-0477_2002_083_0211_mcmitw_2_3_co_2.xml`, 01 Feb. 2002.

Houweling, S., Hartmann, W., Aben, I., Schrijver, H., Skidmore, J., Roelofs, G.-J., and Breon, F.-M. Evidence of systematic errors in SCIAMACHY-observed CO2 due to aerosols. *Atmospheric Chemistry and Physics*, 5, no. 11:pp. 3003–3013. doi:10.5194/acp-5-3003-2005, 2005.

Hu, H., Hasekamp, O., Butz, A., Galli, A., Landgraf, J., de Brugh, J. A., Borsdorff, T., Scheepmaker, R., and Aben, I. The operational methane retrieval algorithm for TROPOMI. *Atmospheric Measurement Techniques*, 9, no. 11:pp. 5423–5440. doi:10.5194/amt-9-5423-2016, 2016.

Hu, H., Landgraf, J., Detmers, R., Borsdorff, T., de Brugh, J. A., Aben, I., Butz, A., and Hasekamp, O. Toward Global Mapping of Methane With TROPOMI: First Results and Intersatellite Comparison to GOSAT. *Geophysical Research Letters*, 45, no. 8:pp. 3682–3689. doi:10.1002/2018gl077259, 2018.

Huang, Y., Natraj, V., Zeng, Z.-C., Kopparla, P., and Yung, Y. L. Quantifying the impact of aerosol scattering on the retrieval of methane from airborne remote sensing measurements. *Atmospheric Measurement Techniques*, 13, no. 12:pp. 6755–6769. doi: 10.5194/amt-13-6755-2020, 2020.

Hulley, G. C., Duren, R. M., Hopkins, F. M., Hook, S. J., Vance, N., Guillevic, P., Johnson, W. R., Eng, B. T., Mihaly, J. M., Jovanovic, V. M., Chazanoff, S. L., Staniszewski, Z. K., Kuai, L., Worden, J., Frankenberg, C., Rivera, G., Aubrey, A. D., Miller, C. E., Malakar, N. K., Tomás, J. M. S., and Holmes, K. T. High spatial resolution imaging of methane and other trace gases with the airborne Hyperspectral Thermal Emission Spectrometer (HyTES). *Atmospheric Measurement Techniques*, 9, no. 5:pp. 2393–2408. doi:10.5194/amt-9-2393-2016, 2016.

Hummel, T., Coatantiec, C., Gnata, X., Lamour, T., Rivière, R., Meister, C., Stute, A., Krauser, J., Weise, D., and Wenig, M. A fibre-based 2D-slit homogenizer concept for high-precision space-based spectrometer missions. *CEAS Space Journal*. doi:10.1007/s12567-021-00419-8, 2022.

ICOS ERIC. *ICOS Handbook 2022*. ICOS ERIC, 3rd revised edition edition, 2022.

Inglis, G. N., Bragg, F., Burls, N. J., Cramwinckel, M. J., Evans, D., Foster, G. L., Huber, M., Lunt, D. J., Siler, N., Steinig, S., Tierney, J. E., Wilkinson, R., Anagnostou, E., de Boer, A. M., Jones, T. D., Edgar, K. M., Hollis, C. J., Hutchinson, D. K., and Pancost, R. D. Global mean surface temperature and climate sensitivity of the early Eocene Climatic Optimum (EECO), Paleocene–Eocene Thermal Maximum (PETM), and latest Paleocene. *Climate of the Past*, 16, no. 5:pp. 1953–1968. doi:10.5194/cp-16-1953-2020, 2020.

IPCC 2018. *Global Warming of 1.5°C. An IPCC Special Report on the impacts of global warming of 1.5°C above pre-industrial levels and related global greenhouse gas emission pathways, in the context of strengthening the global response to the threat of climate change, sustainable development, and efforts to eradicate poverty*. Masson-Delmotte, V., P. Zhai, H.-O. Pörtner, D. Roberts, J. Skea, P.R. Shukla, A. Pirani, W. Moufouma-Okia, C. Péan, R. Pidcock, S. Connors, J.B.R. Matthews, Y. Chen, X. Zhou, M.I. Gomis, E. Lonnoy, T. Maycock, M. Tignor, and T. Waterfield, 2018.

Jacob, D. J., Varon, D. J., Cusworth, D. H., Dennison, P. E., Frankenberg, C., Gautam, R., Guanter, L., Kelley, J., McKeever, J., Ott, L. E., Poulter, B., Qu, Z., Thorpe, A. K., Worden, J. R., and Duren, R. M. Quantifying methane emissions from the global scale down to point sources using satellite observations of atmospheric methane. *Atmospheric Chemistry and Physics Discussions*. doi:10.5194/acp-2022-246, 2022.

JCGM. JCGM 100: 2008, Evaluation of measurement data—guide to the expression of uncertainty in measurement (ISO GUM 1995 with minor corrections), 2008.

Jervis, D., McKeever, J., Durak, B. O. A., Sloan, J. J., Gains, D., Varon, D. J., Ramier, A., Strupler, M., and Tarrant, E. The GHGSat-D imaging spectrometer. *Atmospheric Measurement Techniques*, 14, no. 3:pp. 2127–2140. doi:10.5194/amt-14-2127-2021, 2021.

John H. Seinfeld, S. N. P. *Atmospheric Chemistry and Physics*. John Wiley & Sons. URL `https://www.ebook.de/de/product/26072145/john_h_seinfeld_spyros_n_pandis_atmospheric_chemistry_and_physics.html`, 2016.

Jones, T. S., Franklin, J. E., Chen, J., Dietrich, F., Hajny, K. D., Paetzold, J. C., Wenzel, A., Gately, C., Gottlieb, E., Parker, H., Dubey, M., Hase, F., Shepson, P. B., Mielke, L. H., and Wofsy, S. C. Assessing urban methane emissions using column-observing portable Fourier transform infrared (FTIR) spectrometers and a novel Bayesian inversion framework. *Atmospheric Chemistry and Physics*, 21, no. 17:pp. 13131–13147. doi:10.5194/acp-21-13131-2021, 2021.

Jongaramrungruang, S., Frankenberg, C., Matheou, G., Thorpe, A. K., Thompson, D. R., Kuai, L., and Duren, R. M. Towards accurate methane point-source quantification from high-resolution 2-D plume imagery. *Atmospheric Measurement Techniques*, 12, no. 12:pp. 6667–6681. doi:10.5194/amt-12-6667-2019, 2019.

Jongaramrungruang, S., Matheou, G., Thorpe, A. K., Zeng, Z.-C., and Frankenberg, C. Remote sensing of methane plumes: instrument tradeoff analysis for detecting and quantifying local sources at global scale. *Atmospheric Measurement Techniques*, 14, no. 12:pp. 7999–8017. doi:10.5194/amt-14-7999-2021, 2021.

Joos, F., Roth, R., Fuglestvedt, J. S., Peters, G. P., Enting, I. G., von Bloh, W., Brovkin, V., Burke, E. J., Eby, M., Edwards, N. R., Friedrich, T., Frölicher, T. L., Halloran, P. R., Holden, P. B., Jones, C., Kleinen, T., Mackenzie, F. T., Matsumoto, K., Meinshausen, M., Plattner, G.-K., Reisinger, A., Segschneider, J., Shaffer, G., Steinacher, M., Strassmann, K., Tanaka, K., Timmermann, A., and Weaver, A. J. Carbon dioxide and climate impulse response functions for the computation of greenhouse gas metrics: a multi-model analysis. *Atmospheric Chemistry and Physics*, 13, no. 5:pp. 2793–2825. doi:10.5194/acp-13-2793-2013, 2013.

Karion, A., Callahan, W., Stock, M., Prinzivalli, S., Verhulst, K. R., Kim, J., Salameh, P. K., Lopez-Coto, I., and Whetstone, J. Greenhouse gas observations from the Northeast Corridor tower network. *Earth System Science Data*, 12, no. 1:pp. 699–717. doi:10.5194/essd-12-699-2020, 2020.

Karman, T., Koenis, M. A. J., Banerjee, A., Parker, D. H., Gordon, I. E., van der Avoird, A., van der Zande, W. J., and Groenenboom, G. C. O2-O2 and O2-N2 collision-induced absorption mechanisms unravelled. *Nature Chemistry*, 10, no. 5:pp. 549–554. doi:10.1038/s41557-018-0015-x, 2018.

Keeling, C. D. The Concentration and Isotopic Abundances of Carbon Dioxide in the Atmosphere. *Tellus*, 12, no. 2:pp. 200–203. doi:10.3402/tellusa.v12i2.9366, 1960.

Keeling, R. F., Graven, H. D., Welp, L. R., Resplandy, L., Bi, J., Piper, S. C., Sun, Y., Bollenbacher, A., and Meijer, H. A. J. Atmospheric evidence for a global secular increase in carbon isotopic discrimination of land photosynthesis. *Proceedings of the National Academy of Sciences*, 114, no. 39:pp. 10361–10366. doi:10.1073/pnas.1619240114, 2017.

Knox, S. H., Jackson, R. B., Poulter, B., McNicol, G., Fluet-Chouinard, E., Zhang, Z., Hugelius, G., Bousquet, P., Canadell, J. G., Saunois, M., Papale, D., Chu, H., Keenan, T. F., Baldocchi, D., Torn, M. S., Mammarella, I., Trotta, C., Aurela, M., Bohrer, G., Campbell, D. I., Cescatti, A., Chamberlain, S., Chen, J., Chen, W., Dengel, S., Desai, A. R., Euskirchen, E., Friborg, T., Gasbarra, D., Goded, I., Goeckede, M., Heimann, M., Helbig, M., Hirano, T., Hollinger, D. Y., Iwata, H., Kang, M., Klatt, J., Krauss, K. W., Kutzbach, L., Lohila, A., Mitra, B., Morin, T. H., Nilsson, M. B., Niu, S., Noormets, A., Oechel, W. C., Peichl, M., Peltola, O., Reba, M. L., Richardson, A. D., Runkle, B. R. K., Ryu, Y., Sachs, T., Schäfer, K. V. R., Schmid, H. P., Shurpali, N., Sonnentag, O., Tang, A. C. I., Ueyama, M., Vargas, R., Vesala, T., Ward, E. J., Windham-Myers, L., Wohlfahrt, G., and Zona, D. FLUXNET-CH4 Synthesis Activity: Objectives, Observations, and Future Directions. *Bulletin of the American Meteorological Society*, 100, no. 12:pp. 2607 – 2632. doi:10.1175/BAMS-D-18-0268.1. URL `https://journals.ametsoc.org/view/journals/bams/100/12/bams-d-18-0268.1.xml`, 2019.

Kokaly, R. F., Clark, R. N., Swayze, G. A., Livo, K. E., Hoefen, T. M., Pearson, N. C., Wise, R. A., Benzel, W. M., Lowers, H. A., Driscoll, R. L., and Klein, A. J. USGS Spectral Library Version 7. doi:10.3133/ds1035, 2017.

Kopp, G., Lawrence, G., and Rottman, G. The Total Irradiance Monitor TIM: Science Results. *Solar Physics*, 230, no. 1-2:pp. 129–139. doi:10.1007/s11207-005-7433-9, 2005.

Kort, E. A., Frankenberg, C., Costigan, K. R., Lindenmaier, R., Dubey, M. K., and Wunch, D. Four corners: The largest US methane anomaly viewed from space. *Geophysical Research Letters*, 41, no. 19:pp. 6898–6903. doi:10.1002/2014gl061503, 2014.

Kostinek, J., Roiger, A., Eckl, M., Fiehn, A., Luther, A., Wildmann, N., Klausner, T., Fix, A., Knote, C., Stohl, A., and Butz, A. Estimating Upper Silesian coal mine methane emissions from airborne in situ observations and dispersion modeling. *Atmospheric Chemistry and Physics*, 21, no. 11:pp. 8791–8807. doi:10.5194/acp-21-8791-2021, 2021.

Krautwurst, S., Gerilowski, K., Borchardt, J., Wildmann, N., Gałkowski, M., Swolkień, J., Marshall, J., Fiehn, A., Roiger, A., Ruhtz, T., Gerbig, C., Necki, J., Burrows, J. P., Fix, A., and Bovensmann, H. Quantification of CH4 coal mining emissions in Upper Silesia by passive airborne remote sensing observations with the Methane Airborne MAPper (MAMAP) instrument during the CO2 and Methane (CoMet) campaign. *Atmospheric Chemistry and Physics*, 21, no. 23:pp. 17345–17371. doi:10.5194/acp-21-17345-2021, 2021.

Krautwurst, S., Gerilowski, K., Jonsson, H. H., Thompson, D. R., Kolyer, R. W., Iraci, L. T., Thorpe, A. K., Horstjann, M., Eastwood, M., Leifer, I., Vigil, S. A., Krings, T., Borchardt, J., Buchwitz, M., Fladeland, M. M., Burrows, J. P., and Bovensmann, H. Methane emissions from a Californian landfill, determined from airborne remote sensing and in situ measurements. *Atmospheric Measurement Techniques*, 10, no. 9:pp. 3429–3452. doi:10.5194/amt-10-3429-2017, 2017.

Krings, T. Greenhouse gas emission rate estimates from airborne remote sensing in the short-wave infrared. Ph.D. thesis, Bremen, Universität Bremen, 2013.

Krings, T., Gerilowski, K., Buchwitz, M., Hartmann, J., Sachs, T., Erzinger, J., Burrows, J. P., and Bovensmann, H. Quantification of methane emission rates from coal mine ventilation shafts using airborne remote sensing data. *Atmospheric Measurement Techniques*, 6, no. 1:pp. 151–166. doi:10.5194/amt-6-151-2013. URL `http://www.atmos-meas-tech.net/6/151/2013`, 2013.

Krings, T., Gerilowski, K., Buchwitz, M., Reuter, M., Tretner, A., Erzinger, J., Heinze, D., Pflüger, U., Burrows, J. P., and Bovensmann, H. MAMAP – a new spectrometer system for column-averaged methane and carbon dioxide observations from aircraft: retrieval algorithm and first inversions for point source emission rates. *Atmospheric Measurement Techniques*, 4, no. 9:pp. 1735–1758. doi:10.5194/amt-4-1735-2011. URL `http://www.atmos-meas-tech.net/4/1735/2011`, 2011.

Krings, T., Neininger, B., Gerilowski, K., Krautwurst, S., Buchwitz, M., Burrows, J. P., Lindemann, C., Ruhtz, T., Schüttemeyer, D., and Bovensmann, H. Airborne remote sensing and in situ measurements of atmospheric CO_2 to quantify point source emissions. *Atmospheric Measurement Techniques*, 11, no. 2:pp. 721–739. doi:10.5194/amt-11-721-2018, 2018.

Kuze, A., Kikuchi, N., Kataoka, F., Suto, H., Shiomi, K., and Kondo, Y. Detection of Methane Emission from a Local Source Using GOSAT Target Observations. *Remote Sensing*, 12, no. 2:p. 267. doi:10.3390/rs12020267, 2020.

Kuze, A., Suto, H., Shiomi, K., Kawakami, S., Tanaka, M., Ueda, Y., Deguchi, A., Yoshida, J., Yamamoto, Y., Kataoka, F., Taylor, T. E., and Buijs, H. L. Update on GOSAT TANSO-FTS performance, operations, and data products after more than 6 years in space. *Atmospheric Measurement Techniques*, 9, no. 6:pp. 2445–2461. doi:10.5194/amt-9-2445-2016, 2016.

de Lange, A. and Landgraf, J. Methane profiles from GOSAT thermal infrared spectra. *Atmospheric Measurement Techniques*, 11, no. 6:pp. 3815–3828. doi:10.5194/amt-11-3815-2018, 2018.

Leifer, I., Melton, C., Fischer, M. L., Fladeland, M., Frash, J., Gore, W., Iraci, L. T., Marrero, J. E., Ryoo, J.-M., Tanaka, T., and Yates, E. L. Atmospheric characterization through fused mobile airborne and surface in situ surveys: methane emissions quantification from a producing oil field. *Atmospheric Measurement Techniques*, 11, no. 3:pp. 1689–1705. doi:10.5194/amt-11-1689-2018, 2018.

LfU Brandenburg. Abschätzung der Treibhausgasemissionen im Land Brandenburg in 2020. URL `https://lfu.brandenburg.de/sixcms/media.php/9/Klimagase-Corona2020.pdf,lastaccess12.11.2021`, 2021.

Loulergue, L., Schilt, A., Spahni, R., Masson-Delmotte, V., Blunier, T., Lemieux, B., Barnola, J.-M., Raynaud, D., Stocker, T. F., and Chappellaz, J. Orbital and millennial-scale features of atmospheric CH4 over the past 800,000 years. *Nature*, 453, no. 7193:pp. 383–386. doi:10.1038/nature06950, 2008.

Luther, A., Kleinschek, R., Scheidweiler, L., Defratyka, S., Stanisavljevic, M., Forstmaier, A., Dandocsi, A., Wolff, S., Dubravica, D., Wildmann, N., Kostinek, J., Jöckel, P., Nickl, A.-L., Klausner, T., Hase, F., Frey, M., Chen, J., Dietrich, F., Necki, J., Swolkien, J., Fix, A., Roiger, A., and Butz, A. Quantifying CH4 emissions from hard coal mines using mobile sun-viewing Fourier transform spectrometry. *Atmospheric Measurement Techniques*, 12, no. 10:pp. 5217–5230. doi:10.5194/amt-12-5217-2019, 2019.

Luther, A., Kostinek, J., Kleinschek, R., Defratyka, S., Stanisavljevic, M., Forstmaier, A., Dandocsi, A., Scheidweiler, L., Dubravica, D., Wildmann, N., Hase, F., Frey, M. M., Chen, J., Dietrich, F., Necki, J., Swolkien, J., Knote, C., Vardag, S. N., Roiger, A., and Butz, A. Observational constraints on methane emissions from Polish coal mines using a ground-based remote sensing network. *Atmospheric Chemistry and Physics*, 22, no. 9:pp. 5859–5876. doi:10.5194/acp-22-5859-2022, 2022.

Lüthi, D., Floch, M. L., Bereiter, B., Blunier, T., Barnola, J.-M., Siegenthaler, U., Raynaud, D., Jouzel, J., Fischer, H., Kawamura, K., and Stocker, T. F. High-resolution carbon dioxide concentration record 650,000–800,000 years before present. *Nature*, 453, no. 7193:pp. 379–382. doi:10.1038/nature06949, 2008.

Maasakkers, J. D., Jacob, D. J., Sulprizio, M. P., Scarpelli, T. R., Nesser, H., Sheng, J.-X., Zhang, Y., Hersher, M., Bloom, A. A., Bowman, K. W., Worden, J. R., Janssens-Maenhout, G., and Parker, R. J. Global distribution of methane emissions, emission trends, and OH concentrations and trends inferred from an inversion of GOSAT satellite data for 2010–2015. *Atmospheric Chemistry and Physics*, 19, no. 11:pp. 7859–7881. doi:10.5194/acp-19-7859-2019, 2019.

Martinez, B., Miller, T. W., and Yalin, A. P. Cavity Ring-Down Methane Sensor for Small Unmanned Aerial Systems. *Sensors*, 20, no. 2:p. 454. doi:10.3390/s20020454, 2020.

Mazière, M. D., Thompson, A. M., Kurylo, M. J., Wild, J. D., Bernhard, G., Blumenstock, T., Braathen, G. O., Hannigan, J. W., Lambert, J.-C., Leblanc, T., McGee, T. J., Nedoluha, G., Petropavlovskikh, I., Seckmeyer, G., Simon, P. C., Steinbrecht, W., and Strahan, S. E. The Network for the Detection of Atmospheric Composition Change (NDACC): history, status and perspectives. *Atmospheric Chemistry and Physics*, 18, no. 7:pp. 4935–4964. doi:10.5194/acp-18-4935-2018, 2018.

Meerdink, S. K., Hook, S. J., Roberts, D. A., and Abbott, E. A. The ECOSTRESS spectral library version 1.0. *Remote Sensing of Environment*, 230:p. 111196. doi:10.1016/j.rse.2019.05.015, 2019.

Menoud, M., van der Veen, C., Necki, J., Bartyzel, J., Szénási, B., Stanisavljević, M., Pison, I., Bousquet, P., and Röckmann, T. Methane (CH4) sources in Krakow, Poland: insights from isotope analysis. *Atmospheric Chemistry and Physics*, 21, no. 17:pp. 13167–13185. doi:10.5194/acp-21-13167-2021, 2021.

Monteiro, V. C., Miles, N. L., Richardson, S. J., Barkley, Z., Haupt, B. J., Lyon, D., Hmiel, B., and Davis, K. J. Methane, carbon dioxide, hydrogen sulfide, and isotopic ratios of methane observations from the Permian Basin tower network. doi:10.5194/essd-2022-33, 2022.

Morse, P. M. Diatomic molecules according to the wave mechanics. II. Vibrational levels. *Physical review*, 34, no. 1:p. 57, 1929.

Mouroulis, P., Gorp, B. V., Green, R. O., Dierssen, H., Wilson, D. W., Eastwood, M., Boardman, J., Gao, B.-C., Cohen, D., Franklin, B., Loya, F., Lundeen, S., Mazer, A., McCubbin, I., Randall, D., Richardson, B., Rodriguez, J. I., Sarture, C., Urquiza, E., Vargas, R., White, V., and Yee, K. Portable Remote Imaging Spectrometer coastal ocean sensor: design, characteristics, and first flight results. *Applied Optics*, 53, no. 7:p. 1363. doi:10.1364/ao.53.001363, 2014.

Myhre, G., Shindell, D., Breon, F.-M., Collins, W., Fuglestvedt, J., Huang, J., Koch, D., Lamarque, J.-F., Lee, D., Mendoza, B., Nakajima, T., Robock, A., Stephens, G., Takemura, T., and Zhang, H. Anthropogenic and Natural Radiative Forcing. In on Climate Change, I. P., editor, *Climate Change 2013 - The Physical Science Basis: Contribution of Working Group I to the Fifth Assessment Report of the Intergovernmental Panel on Climate Change*, pp. 659–740. Cambridge University Press. doi: 10.1017/CBO9781107415324.018, 2013.

Nassar, R., Mastrogiacomo, J.-P., Bateman-Hemphill, W., McCracken, C., MacDonald, C. G., Hill, T., O'Dell, C. W., Kiel, M., and Crisp, D. Advances in quantifying power plant CO2 emissions with OCO-2. *Remote Sensing of Environment*, 264:p. 112579. doi: 10.1016/j.rse.2021.112579, 2021.

Neininger, B. G., Kelly, B. F. J., Hacker, J. M., LU, X., and Schwietzke, S. Coal seam gas industry methane emissions in the Surat Basin, Australia: comparing airborne measurements with inventories. *Philosophical Transactions of the Royal Society A: Mathematical, Physical and Engineering Sciences*, 379, no. 2210:p. 20200458. doi:10.1098/rsta.2020.0458, 2021.

Nickless, A., Scholes, R. J., Vermeulen, A., Beck, J., López-Ballesteros, A., Ardö, J., Karstens, U., Rigby, M., Kasurinen, V., Pantazatou, K., Jorch, V., and Kutsch, W. Greenhouse gas observation network design for Africa. *Tellus B: Chemical and Physical Meteorology*, 72, no. 1:pp. 1–30. doi:10.1080/16000889.2020.1824486, 2020.

Nicodemus, F. E., Richmond, J. C., Hsia, J. J., Ginsberg, I. W., and Limperis, T. Geometrical considerations and nomenclature for reflectance. *Final Report National Bureau of Standards*, 1977.

Niederer, J. M. G. The Infrared Spectrum of Methane. Ph.D. thesis, ETH Zürich. doi: 10.3929/ethz-a-007316862, 2012.

Nielsen, H. *Damping Parameter in Marquardt's Method*. Informatics and Mathematical Modelling, Technical University of Denmark, DTU, 1999.

Nisbet, E. G., Dlugokencky, E. J., Manning, M. R., Lowry, D., Fisher, R. E., France, J. L., Michel, S. E., Miller, J. B., White, J. W. C., Vaughn, B., Bousquet, P., Pyle, J. A., Warwick, N. J., Cain, M., Brownlow, R., Zazzeri, G., Lanoisellé, M., Manning, A. C., Gloor, E., Worthy, D. E. J., Brunke, E.-G., Labuschagne, C., Wolff, E. W., and Ganesan, A. L. Rising atmospheric methane: 2007-2014 growth and isotopic shift. *Global Biogeochemical Cycles*, 30, no. 9:pp. 1356–1370. doi:10.1002/2016gb005406, 2016.

Nisbet, E. G., Manning, M. R., Dlugokencky, E. J., Fisher, R. E., Lowry, D., Michel, S. E., Myhre, C. L., Platt, S. M., Allen, G., Bousquet, P., Brownlow, R., Cain, M., France, J. L., Hermansen, O., Hossaini, R., Jones, A. E., Levin, I., Manning, A. C., Myhre, G., Pyle, J. A., Vaughn, B. H., Warwick, N. J., and White, J. W. C. Very Strong Atmospheric Methane Growth in the 4 Years 2014–2017: Implications for the Paris Agreement. *Global Biogeochemical Cycles*, 33, no. 3:pp. 318–342. doi:10.1029/2018gb006009, 2019.

Noël, S., Reuter, M., Buchwitz, M., Borchardt, J., Hilker, M., Bovensmann, H., Burrows, J. P., Di Noia, A., Suto, H., Yoshida, Y., Buschmann, M., Deutscher, N. M., Feist, D. G., Griffith, D. W. T., Hase, F., Kivi, R., Morino, I., Notholt, J., Ohyama, H., Petri, C., Podolske, J. R., Pollard, D. F., Sha, M. K., Shiomi, K., Sussmann, R., Té, Y., Velazco, V. A., and Warneke, T. XCO_2 retrieval for GOSAT and GOSAT-2 based on the FOCAL algorithm. *Atmospheric Measurement Techniques*, 14, no. 5:pp. 3837–3869. doi:10.5194/amt-14-3837-2021. URL `https://amt.copernicus.org/articles/14/3837/2021/`, 2021.

Noël, S., Reuter, M., Buchwitz, M., Borchardt, J., Hilker, M., Schneising, O., Bovensmann, H., Burrows, J. P., Noia, A. D., Parker, R. J., Suto, H., Yoshida, Y., Buschmann, M., Deutscher, N. M., Feist, D. G., Griffith, D. W. T., Hase, F., Kivi, R., Liu, C., Morino, I., Notholt, J., Oh, Y.-S., Ohyama, H., Petri, C., Pollard, D. F., Rettinger, M., Roehl, C., Rousogenous, C., Sha, M. K., Shiomi, K., Strong, K., Sussmann, R., Té, Y., Velazco, V. A., Vrekoussis, M., and Warneke, T. Retrieval of greenhouse gases from GOSAT and GOSAT-2 using the FOCAL algorithm. *Atmospheric Measurement Techniques*, 15, no. 11:pp. 3401–3437. doi:10.5194/amt-15-3401-2022, 2022.

O'Dell, C. W., Connor, B., Bösch, H., O'Brien, D., Frankenberg, C., Castano, R., Christi, M., Eldering, D., Fisher, B., Gunson, M., McDuffie, J., Miller, C. E., Natraj, V., Oyafuso, F., Polonsky, I., Smyth, M., Taylor, T., Toon, G. C., Wennberg, P. O., and Wunch, D. The ACOS CO2 retrieval algorithm – Part 1: Description and validation against synthetic observations. *Atmospheric Measurement Techniques*, 5, no. 1:pp. 99–121. doi:10.5194/amt-5-99-2012, 2012.

O'Neill, C., Lenardic, A., and Condie, K. C. Earth's punctuated tectonic evolution: cause and effect. *Geological Society, London, Special Publications*, 389, no. 1:pp. 17–40. doi:10.1144/sp389.4, 2013.

Pandey, S., Gautam, R., Houweling, S., van der Gon, H. D., Sadavarte, P., Borsdorff, T., Hasekamp, O., Landgraf, J., Tol, P., van Kempen, T., Hoogeveen, R., van Hees, R., Hamburg, S. P., Maasakkers, J. D., and Aben, I. Satellite observations reveal extreme methane leakage from a natural gas well blowout. *Proceedings of the National Academy of Sciences*, p. 201908712. doi:10.1073/pnas.1908712116, 2019.

Paris Agreement. United Nations Framework Convention on Climate Change. *Paris, France*, 2015.

Park, J. and Kim, H. M. Design and evaluation of CO2 observation network to optimize surface CO2 fluxes in Asia using observation system simulation experiments. *Atmospheric Chemistry and Physics*, 20, no. 8:pp. 5175–5195. doi:10.5194/acp-20-5175-2020, 2020.

Plant, G., Kort, E. A., Murray, L. T., Maasakkers, J. D., and Aben, I. Evaluating urban methane emissions from space using TROPOMI methane and carbon monoxide observations. *Remote Sensing of Environment*, 268:p. 112756. doi:10.1016/j.rse.2021.112756, 2022.

Pouillet, C. S. M. Memoire sur le chaleur solaire. *Paris*, 1838.

PRTR Data. German Pollutant Release and Transfer Register. URL `https://thru.de/thrude/,lastaccess30.04.2022`, 2022.

Reinelt, T. and Liebetrau, J. Monitoring and Mitigation of Methane Emissions from Pressure Relief Valves of a Biogas Plant. *Chemical Engineering & Technology*, 43, no. 1:pp. 7–18. doi:10.1002/ceat.201900180, 2019.

Reuter, M., Bovensmann, H., Buchwitz, M., Borchardt, J., Krautwurst, S., Gerilowski, K., Lindauer, M., Kubistin, D., and Burrows, J. P. Development of a small unmanned aircraft system to derive CO2 emissions of anthropogenic point sources. *Atmospheric Measurement Techniques*, 14, no. 1:pp. 153–172. doi:10.5194/amt-14-153-2021, 2021.

Reuter, M., Buchwitz, M., Schneising, O., Hase, F., Heymann, J., Guerlet, S., Cogan, A. J., Bovensmann, H., and Burrows, J. P. A simple empirical model estimating atmospheric CO_2 background concentrations. *Atmospheric Measurement Techniques*, 5, no. 6:pp. 1349–1357. doi:10.5194/amt-5-1349-2012. URL `http://www.atmos-meas-tech.net/5/1349/2012`, 2012.

Reuter, M., Buchwitz, M., Schneising, O., Krautwurst, S., O'Dell, C. W., Richter, A., Bovensmann, H., and Burrows, J. P. Towards monitoring localized CO2 emissions from space: co-located regional CO2 and NO2 enhancements observed by the OCO-2 and S5P satellites. *Atmospheric Chemistry and Physics*, 19, no. 14:pp. 9371–9383. doi:10.5194/acp-19-9371-2019, 2019.

Reuter, M., Buchwitz, M., Schneising, O., Noël, S., Bovensmann, H., and Burrows, J. A Fast Atmospheric Trace Gas Retrieval for Hyperspectral Instruments Approximating Multiple Scattering—Part 2: Application to XCO2 Retrievals from OCO-2. *Remote Sensing*, 9, no. 11:p. 1102. doi:10.3390/rs9111102, 2017a.

Reuter, M., Buchwitz, M., Schneising, O., Noël, S., Bovensmann, H., Burrows, J. P., Boesch, H., Noia, A. D., Anand, J., Parker, R. J., Somkuti, P., Wu, L., Hasekamp, O. P., Aben, I., Kuze, A., Suto, H., Shiomi, K., Yoshida, Y., Morino, I., Crisp, D., O'Dell, C. W., Notholt, J., Petri, C., Warneke, T., Velazco, V. A., Deutscher, N. M., Griffith, D. W. T., Kivi, R., Pollard, D. F., Hase, F., Sussmann, R., Té, Y. V., Strong, K., Roche, S., Sha, M. K., Mazière, M. D., Feist, D. G., Iraci, L. T., Roehl, C. M., Retscher, C., and Schepers, D. Ensemble-based satellite-derived carbon dioxide and methane column-averaged dry-air mole fraction data sets (2003-2018) for carbon and climate applications. *Atmospheric Measurement Techniques*, 13, no. 2:pp. 789–819. doi:10.5194/amt-13-789-2020, 2020.

Reuter, M., Buchwitz, M., Schneising, O., Noël, S., Rozanov, V., Bovensmann, H., and Burrows, J. A Fast Atmospheric Trace Gas Retrieval for Hyperspectral Instruments Approximating Multiple Scattering—Part 1: Radiative Transfer and a Potential OCO-2 XCO2 Retrieval Setup. *Remote Sensing*, 9, no. 11:p. 1159. doi:10.3390/rs9111159, 2017b.

Revelle, R. and Suess, H. E. Carbon Dioxide Exchange Between Atmosphere and Ocean and the Question of an Increase of Atmospheric CO2 during the Past Decades. *Tellus*, 9, no. 1:pp. 18–27. doi:10.3402/tellusa.v9i1.9075, 1957.

Rice, A. L., Butenhoff, C. L., Teama, D. G., Röger, F. H., Khalil, M. A. K., and Rasmussen, R. A. Atmospheric methane isotopic record favors fossil sources flat in 1980s and 1990s with recent increase. *Proceedings of the National Academy of Sciences*, 113, no. 39:pp. 10791–10796. doi:10.1073/pnas.1522923113, 2016.

Riddick, S. N., Mauzerall, D. L., Celia, M., Harris, N. R. P., Allen, G., Pitt, J., Staunton-Sykes, J., Forster, G. L., Kang, M., Lowry, D., Nisbet, E. G., and Manning, A. J. Methane emissions from oil and gas platforms in the North Sea. *Atmospheric Chemistry and Physics*, 19, no. 15:pp. 9787–9796. doi:10.5194/acp-19-9787-2019, 2019.

Rigby, M., Montzka, S. A., Prinn, R. G., White, J. W. C., Young, D., O'Doherty, S., Lunt, M. F., Ganesan, A. L., Manning, A. J., Simmonds, P. G., Salameh, P. K., Harth, C. M., Mühle, J., Weiss, R. F., Fraser, P. J., Steele, L. P., Krummel, P. B., McCulloch, A., and Park, S. Role of atmospheric oxidation in recent methane growth. *Proceedings of the National Academy of Sciences*, 114, no. 21:pp. 5373–5377. doi:10.1073/pnas.1616426114, 2017.

Ritter, K. and Wilkerson, T. High-resolution spectroscopy of the oxygen A band. *Journal of Molecular Spectroscopy*, 121, no. 1:pp. 1–19. doi:10.1016/0022-2852(87)90167-6, 1987.

Rodgers, C. D. *Inverse methods for atmospheric sounding : theory and practice*. World Scientific, Singapore River Edge, N.J. ISBN 981022740x, 2000.

Roedel, W. and Wagner, T. *Physik unserer Umwelt: Die Atmosphäre*. Springer Berlin Heidelberg. doi:10.1007/978-3-662-54258-3, 2017.

Rozanov, V., Dinter, T., Rozanov, A., Wolanin, A., Bracher, A., and Burrows, J. Radiative transfer modeling through terrestrial atmosphere and ocean accounting for inelastic processes: Software package SCIATRAN. *Journal of Quantitative Spectroscopy and Radiative Transfer*, 194:pp. 65–85. doi:10.1016/j.jqsrt.2017.03.009, 2017.

Sadavarte, P., Pandey, S., Maasakkers, J. D., Lorente, A., Borsdorff, T., van der Gon, H. D., Houweling, S., and Aben, I. Methane Emissions from Superemitting Coal Mines in Australia Quantified Using TROPOMI Satellite Observations. *Environmental Science & Technology*, 55, no. 24:pp. 16573–16580. doi:10.1021/acs.est.1c03976, 2021.

Salby, M. *Physics of the atmosphere and climate*. Cambridge University Press, Cambridge New York. ISBN 9780521767187, 2012.

Saunois, M., Bousquet, P., Poulter, B., Peregon, A., Ciais, P., Canadell, J. G., Dlugokencky, E. J., Etiope, G., Bastviken, D., Houweling, S., Janssens-Maenhout, G., Tubiello, F. N., Castaldi, S., Jackson, R. B., Alexe, M., Arora, V. K., Beerling, D. J., Bergamaschi, P., Blake, D. R., Brailsford, G., Brovkin, V., Bruhwiler, L., Crevoisier, C., Crill, P., Covey, K., Curry, C., Frankenberg, C., Gedney, N., Höglund-Isaksson, L., Ishizawa, M., Ito, A., Joos, F., Kim, H.-S., Kleinen, T., Krummel, P., Lamarque, J.-F., Langenfelds, R., Locatelli,

R., Machida, T., Maksyutov, S., McDonald, K. C., Marshall, J., Melton, J. R., Morino, I., Naik, V., O'Doherty, S., Parmentier, F.-J. W., Patra, P. K., Peng, C., Peng, S., Peters, G. P., Pison, I., Prigent, C., Prinn, R., Ramonet, M., Riley, W. J., Saito, M., Santini, M., Schroeder, R., Simpson, I. J., Spahni, R., Steele, P., Takizawa, A., Thornton, B. F., Tian, H., Tohjima, Y., Viovy, N., Voulgarakis, A., van Weele, M., van der Werf, G. R., Weiss, R., Wiedinmyer, C., Wilton, D. J., Wiltshire, A., Worthy, D., Wunch, D., Xu, X., Yoshida, Y., Zhang, B., Zhang, Z., and Zhu, Q. The global methane budget 2000–2012. *Earth System Science Data*, 8, no. 2:pp. 697–751. doi:10.5194/essd-8-697-2016, 2016.

Saunois, M., Stavert, A. R., Poulter, B., Bousquet, P., Canadell, J. G., Jackson, R. B., Raymond, P. A., Dlugokencky, E. J., Houweling, S., Patra, P. K., Ciais, P., Arora, V. K., Bastviken, D., Bergamaschi, P., Blake, D. R., Brailsford, G., Bruhwiler, L., Carlson, K. M., Carrol, M., Castaldi, S., Chandra, N., Crevoisier, C., Crill, P. M., Covey, K., Curry, C. L., Etiope, G., Frankenberg, C., Gedney, N., Hegglin, M. I., Höglund-Isaksson, L., Hugelius, G., Ishizawa, M., Ito, A., Janssens-Maenhout, G., Jensen, K. M., Joos, F., Kleinen, T., Krummel, P. B., Langenfelds, R. L., Laruelle, G. G., Liu, L., Machida, T., Maksyutov, S., McDonald, K. C., McNorton, J., Miller, P. A., Melton, J. R., Morino, I., Müller, J., Murguia-Flores, F., Naik, V., Niwa, Y., Noce, S., O'Doherty, S., Parker, R. J., Peng, C., Peng, S., Peters, G. P., Prigent, C., Prinn, R., Ramonet, M., Regnier, P., Riley, W. J., Rosentreter, J. A., Segers, A., Simpson, I. J., Shi, H., Smith, S. J., Steele, L. P., Thornton, B. F., Tian, H., Tohjima, Y., Tubiello, F. N., Tsuruta, A., Viovy, N., Voulgarakis, A., Weber, T. S., van Weele, M., van der Werf, G. R., Weiss, R. F., Worthy, D., Wunch, D., Yin, Y., Yoshida, Y., Zhang, W., Zhang, Z., Zhao, Y., Zheng, B., Zhu, Q., Zhu, Q., and Zhuang, Q. The Global Methane Budget 2000–2017. *Earth System Science Data*, 12, no. 3:pp. 1561–1623. doi:10.5194/essd-12-1561-2020, 2020.

Scafutto, R. D. M., de Souza Filho, C. R., Riley, D. N., and de Oliveira, W. J. Evaluation of thermal infrared hyperspectral imagery for the detection of onshore methane plumes: Significance for hydrocarbon exploration and monitoring. *International Journal of Applied Earth Observation and Geoinformation*, 64:pp. 311–325. doi:10.1016/j.jag.2017.07.002, 2018.

Schaefer, H. On the Causes and Consequences of Recent Trends in Atmospheric Methane. *Current Climate Change Reports*. doi:10.1007/s40641-019-00140-z, 2019.

Schaefer, H., Fletcher, S. E. M., Veidt, C., Lassey, K. R., Brailsford, G. W., Bromley, T. M., Dlugokencky, E. J., Michel, S. E., Miller, J. B., Levin, I., Lowe, D. C., Martin, R. J., Vaughn, B. H., and White, J. W. C. A 21st-century shift from fossil-fuel to biogenic methane emissions indicated by 13CH4. *Science*, 352, no. 6281:pp. 80–84. doi:10.1126/science.aad2705, 2016.

Schaefer, L. and Fegley, B. Outgassing of ordinary chondritic material and some of its implications for the chemistry of asteroids, planets, and satellites. *Icarus*, 186, no. 2:pp. 462–483. doi:10.1016/j.icarus.2006.09.002, 2007.

Schaefer, L. and Fegley, B. Chemistry of atmospheres formed during accretion of the Earth and other terrestrial planets. *Icarus*, 208, no. 1:pp. 438–448. doi:10.1016/j.icarus.2010.01.026, 2010.

Schneising, O., Buchwitz, M., Burrows, J. P., Bovensmann, H., Bergamaschi, P., and Peters, W. Three years of greenhouse gas column-averaged dry air mole fractions retrieved from satellite – Part 2: Methane. *Atmospheric Chemistry and Physics*, 9, no. 2:pp. 443–465. doi:10.5194/acp-9-443-2009, 2009.

Schneising, O., Buchwitz, M., Burrows, J. P., Bovensmann, H., Reuter, M., Notholt, J., Macatangay, R., and Warneke, T. Three years of greenhouse gas column-averaged dry air mole fractions retrieved from satellite – Part 1: Carbon dioxide. *Atmospheric Chemistry and Physics*, 8, no. 14:pp. 3827–3853. doi:10.5194/acp-8-3827-2008, 2008.

Schneising, O., Buchwitz, M., Reuter, M., Bovensmann, H., Burrows, J. P., Borsdorff, T., Deutscher, N. M., Feist, D. G., Griffith, D. W. T., Hase, F., Hermans, C., Iraci, L. T., Kivi, R., Landgraf, J., Morino, I., Notholt, J., Petri, C., Pollard, D. F., Roche, S., Shiomi, K., Strong, K., Sussmann, R., Velazco, V. A., Warneke, T., and Wunch, D. A scientific algorithm to simultaneously retrieve carbon monoxide and methane from TROPOMI onboard Sentinel-5 Precursor. *Atmospheric Measurement Techniques*, 12, no. 12:pp. 6771–6802. doi:10.5194/amt-12-6771-2019, 2019.

Schneising, O., Burrows, J. P., Dickerson, R. R., Buchwitz, M., Reuter, M., and Bovensmann, H. Remote sensing of fugitive methane emissions from oil and gas production in North American tight geologic formations. *Earth's Future*, 2, no. 10:pp. 548–558. doi:10.1002/2014ef000265, 2014.

Schopf, J. W., Kudryavtsev, A. B., Czaja, A. D., and Tripathi, A. B. Evidence of Archean life: Stromatolites and microfossils. *Precambrian Research*, 158, no. 3-4:pp. 141–155. doi:10.1016/j.precamres.2007.04.009, 2007.

Schowengerdt, R. A. *Remote Sensing: Models and Methods for Image Processing*. Academic Press. ISBN 0-12-369407-8. URL `https://www.amazon.com/Remote-Sensing-Models-Methods-Processing/dp/0123694078?SubscriptionId=AKIAIOBINVZYXZQZ2U3A&tag=chimbori05-20&linkCode=xm2&camp=2025&creative=165953&creativeASIN=0123694078`, 2006.

Schwietzke, S., Sherwood, O. A., Bruhwiler, L. M. P., Miller, J. B., Etiope, G., Dlugokencky, E. J., Michel, S. E., Arling, V. A., Vaughn, B. H., White, J. W. C., and Tans, P. P. Upward revision of global fossil fuel methane emissions based on isotope database. *Nature*, 538, no. 7623:pp. 88–91. doi:10.1038/nature19797, 2016.

Sherwood, S. C., Bony, S., Boucher, O., Bretherton, C., Forster, P. M., Gregory, J. M., and Stevens, B. Adjustments in the Forcing-Feedback Framework for Understanding Climate Change. *Bulletin of the American Meteorological Society*, 96, no. 2:pp. 217–228. doi:10.1175/bams-d-13-00167.1, 2015.

Shindell, D. T., Faluvegi, G., Koch, D. M., Schmidt, G. A., Unger, N., and Bauer, S. E. Improved Attribution of Climate Forcing to Emissions. *Science*, 326, no. 5953:pp. 716–718. doi:10.1126/science.1174760, 2009.

S.K.Gulev, Thorne, P., Ahn, J., Dentener, F., Domingues, C., Gerland, S., Gong, D., Kaufman, D., H.C.Nnamchi, Quaas, J., Rivera, J., Sathyendranath, S., Smith, S., Trewin, B.,

von Schuckmann, K., and Vose, R. Changing State of the Climate System. In Masson-Delmotte, V., Zhai, P., Pirani, A., Connors, S., Péan, C., Berger, S., Caud, N., Chen, Y., Goldfarb, L., Gomis, M., Huang, M., Leitzell, K., Lonnoy, E., Matthews, J., Maycock, T., Waterfield, T., Yelekçi, O., Yu, R., and Zhou, B., editors, *Climate Change 2021: The Physical Science Basis. Contribution ofWorking Group I to the Sixth Assessment Report of the Intergovernmental Panel on Climate Change*, pp. 287–422. Cambridge University Press, Cambridge, United Kingdom and New York, NY, USA. doi: 10.1017/9781009157896.004, 2021.

Spahni, R., Chappellaz, J., Stocker, T. F., Loulergue, L., Hausammann, G., Kawamura, K., Flückiger, J., Schwander, J., Raynaud, D., Masson-Delmotte, V., and Jouzel, J. Atmospheric Methane and Nitrous Oxide of the Late Pleistocene from Antarctic Ice Cores. *Science*, 310, no. 5752:pp. 1317–1321. ISSN 0036-8075. doi:10.1126/science.1120132. `http://science.sciencemag.org/content/310/5752/1317.full.pdf`, URL `http://science.sciencemag.org/content/310/5752/1317`, 2005.

Staebell, C., Sun, K., Samra, J., Franklin, J., Miller, C. C., Liu, X., Conway, E., Chance, K., Milligan, S., and Wofsy, S. Spectral calibration of the MethaneAIR instrument. *Atmospheric Measurement Techniques*, 14, no. 5:pp. 3737–3753. doi:10.5194/amt-14-3737-2021, 2021.

Stavert, A. R., Saunois, M., Canadell, J. G., Poulter, B., Jackson, R. B., Regnier, P., Lauerwald, R., Raymond, P. A., Allen, G. H., Patra, P. K., Bergamaschi, P., Bousquet, P., Chandra, N., Ciais, P., Gustafson, A., Ishizawa, M., Ito, A., Kleinen, T., Maksyutov, S., McNorton, J., Melton, J. R., Müller, J., Niwa, Y., Peng, S., Riley, W. J., Segers, A., Tian, H., Tsuruta, A., Yin, Y., Zhang, Z., Zheng, B., and Zhuang, Q. Regional trends and drivers of the global methane budget. *Global Change Biology*, 28, no. 1:pp. 182–200. doi:10.1111/gcb.15901, 2021.

Steele, L. P., Fraser, P. J., Rasmussen, R. A., Khalil, M. A. K., Conway, T. J., Crawford, A. J., Gammon, R. H., Masarie, K. A., and Thoning, K. W. The Global Distribution of Methane in the Troposphere. In *Scientific Application of Baseline Observations of Atmospheric Composition (SABOAC)*, pp. 417–463. Springer Netherlands. doi:10.1007/978-94-009-3909-7_21, 1987.

Suto, H., Kataoka, F., Kikuchi, N., Knuteson, R. O., Butz, A., Haun, M., Buijs, H., Shiomi, K., Imai, H., and Kuze, A. Thermal and near-infrared sensor for carbon observation Fourier transform spectrometer-2 (TANSO-FTS-2) on the Greenhouse gases Observing SATellite-2 (GOSAT-2) during its first year in orbit. *Atmospheric Measurement Techniques*, 14, no. 3:pp. 2013–2039. doi:10.5194/amt-14-2013-2021, 2021.

Taylor, T. E., Eldering, A., Merrelli, A., Kiel, M., Somkuti, P., Cheng, C., Rosenberg, R., Fisher, B., Crisp, D., Basilio, R., Bennett, M., Cervantes, D., Chang, A., Dang, L., Frankenberg, C., Haemmerle, V. R., Keller, G. R., Kurosu, T., Laughner, J. L., Lee, R., Marchetti, Y., Nelson, R. R., O'Dell, C. W., Osterman, G., Pavlick, R., Roehl, C., Schneider, R., Spiers, G., To, C., Wells, C., Wennberg, P. O., Yelamanchili, A., and Yu, S. OCO-3 early mission operations and initial (vEarly) XCO2 and SIF retrievals. *Remote Sensing of Environment*, 251:p. 112032. doi:10.1016/j.rse.2020.112032, 2020.

le Texier, H., Solomon, S., and Garcia, R. R. The role of molecular hydrogen and methane oxidation in the water vapour budget of the stratosphere. *Quarterly Journal of the Royal Meteorological Society*, 114, no. 480:pp. 281–295. doi:10.1002/qj.49711448002, 1988.

Thomas Engel, P. R. *Physical Chemistry: Pearson New International Edition*. Pearson Education Limited. ISBN 1292022248. URL `https://www.ebook.de/de/product/30394532/thomas_engel_philip_reid_physical_chemistry_pearson_new_international_edition.html`, 2013.

Thompson, D. R., Leifer, I., Bovensmann, H., Eastwood, M., Fladeland, M., Frankenberg, C., Gerilowski, K., Green, R. O., Kratwurst, S., Krings, T., Luna, B., and Thorpe, A. K. Real-time remote detection and measurement for airborne imaging spectroscopy: a case study with methane. *Atmospheric Measurement Techniques*, 8, no. 10:pp. 4383–4397. doi:10.5194/amt-8-4383-2015. URL `http://www.atmos-meas-tech.net/8/4383/2015`, 2015.

Thorpe, A., Frankenberg, C., Aubrey, A., Roberts, D., Nottrott, A., Rahn, T., Sauer, J., Dubey, M., Costigan, K., Arata, C., Steffke, A., Hills, S., Haselwimmer, C., Charlesworth, D., Funk, C., Green, R., Lundeen, S., Boardman, J., Eastwood, M., Sarture, C., Nolte, S., Mccubbin, I., Thompson, D., and McFadden, J. Mapping methane concentrations from a controlled release experiment using the next generation airborne visible/infrared imaging spectrometer (AVIRIS-NG). *Remote Sensing of Environment*, 179:pp. 104–115. doi:10.1016/j.rse.2016.03.032, 2016.

Thorpe, A. K., Duren, R. M., Conley, S., Prasad, K. R., Bue, B. D., Yadav, V., Foster, K. T., Rafiq, T., Hopkins, F. M., Smith, M. L., Fischer, M. L., Thompson, D. R., Frankenberg, C., McCubbin, I. B., Eastwood, M. L., Green, R. O., and Miller, C. E. Methane emissions from underground gas storage in California. *Environmental Research Letters*, 15, no. 4:p. 045005. doi:10.1088/1748-9326/ab751d, 2020.

Thorpe, A. K., Frankenberg, C., and Roberts, D. A. Retrieval techniques for airborne imaging of methane concentrations using high spatial and moderate spectral resolution: application to AVIRIS. *Atmospheric Measurement Techniques*, 7, no. 2:pp. 491–506. doi:10.5194/amt-7-491-2014. URL `http://www.atmos-meas-tech.net/7/491/2014`, 2014.

Thorpe, A. K., Frankenberg, C., Thompson, D. R., Duren, R. M., Aubrey, A. D., Bue, B. D., Green, R. O., Gerilowski, K., Krings, T., Borchardt, J., Kort, E. A., Sweeney, C., Conley, S., Roberts, D. A., and Dennison, P. E. Airborne DOAS retrievals of methane, carbon dioxide, and water vapor concentrations at high spatial resolution: application to AVIRIS-NG. *Atmospheric Measurement Techniques*, 10, no. 10:pp. 3833–3850. doi:10.5194/amt-10-3833-2017, 2017.

Thorpe, A. K., O'Handley, C., Emmitt, G. D., DeCola, P. L., Hopkins, F. M., Yadav, V., Guha, A., Newman, S., Herner, J. D., Falk, M., and Duren, R. M. Improved methane emission estimates using AVIRIS-NG and an Airborne Doppler Wind Lidar. *Remote Sensing of Environment*, 266:p. 112681. doi:10.1016/j.rse.2021.112681, 2021.

Thorpe, A. K., Roberts, D. A., Bradley, E. S., Funk, C. C., Dennison, P. E., and Leifer, I. High resolution mapping of methane emissions from marine and terrestrial sources using

a Cluster-Tuned Matched Filter technique and imaging spectrometry. *Remote Sensing of Environment*, 134:pp. 305–318. doi:10.1016/j.rse.2013.03.018, 2013.

Tisza, L. Zur Deutung der Spektren mehratomiger Moleküle. *Zeitschrift für Physik*, 82, no. 1-2:pp. 48–72. doi:10.1007/bf01342114, 1933.

Toon, G. C. Solar Line List for the TCCON 2014 Data Release. doi:10.14291/TCCON.GGG2014.SOLAR.R0/1221658, 2015.

Toon, O. B., Maring, H., Dibb, J., Ferrare, R., Jacob, D. J., Jensen, E. J., Luo, Z. J., Mace, G. G., Pan, L. L., Pfister, L., Rosenlof, K. H., Redemann, J., Reid, J. S., Singh, H. B., Thompson, A. M., Yokelson, R., Minnis, P., Chen, G., Jucks, K. W., and Pszenny, A. Planning, implementation, and scientific goals of the Studies of Emissions and Atmospheric Composition, Clouds and Climate Coupling by Regional Surveys (SEAC4RS) field mission. *Journal of Geophysical Research: Atmospheres*, 121, no. 9:pp. 4967–5009. doi:10.1002/2015jd024297, 2016.

Toth, R., Brown, L., Miller, C., Devi, V. M., and Benner, D. Spectroscopic database of CO2 line parameters: 4300–7000cm-1. *Journal of Quantitative Spectroscopy and Radiative Transfer*, 109, no. 6:pp. 906–921. doi:10.1016/j.jqsrt.2007.12.004, 2008.

Tu, Q., Hase, F., Schneider, M., García, O., Blumenstock, T., Borsdorff, T., Frey, M., Khosrawi, F., Lorente, A., Alberti, C., Bustos, J. J., Butz, A., Carreño, V., Cuevas, E., Curcoll, R., Diekmann, C. J., Dubravica, D., Ertl, B., Estruch, C., León-Luis, S. F., Marrero, C., Morgui, J.-A., Ramos, R., Scharun, C., Schneider, C., Sepúlveda, E., Toledano, C., and Torres, C. Quantification of CH4 emissions from waste disposal sites near the city of Madrid using ground- and space-based observations of COCCON, TROPOMI and IASI. *Atmospheric Chemistry and Physics*, 22, no. 1:pp. 295–317. doi:10.5194/acp-22-295-2022, 2022.

Turner, A. J., Frankenberg, C., and Kort, E. A. Interpreting contemporary trends in atmospheric methane. *Proceedings of the National Academy of Sciences*, 116, no. 8:pp. 2805–2813. doi:10.1073/pnas.1814297116, 2019.

Turner, A. J., Frankenberg, C., Wennberg, P. O., and Jacob, D. J. Ambiguity in the causes for decadal trends in atmospheric methane and hydroxyl. *Proceedings of the National Academy of Sciences*, 114, no. 21:pp. 5367–5372. doi:10.1073/pnas.1616020114, 2017.

Turner, A. J., Jacob, D. J., Wecht, K. J., Maasakkers, J. D., Lundgren, E., Andrews, A. E., Biraud, S. C., Boesch, H., Bowman, K. W., Deutscher, N. M., Dubey, M. K., Griffith, D. W. T., Hase, F., Kuze, A., Notholt, J., Ohyama, H., Parker, R., Payne, V. H., Sussmann, R., Sweeney, C., Velazco, V. A., Warneke, T., Wennberg, P. O., and Wunch, D. Estimating global and North American methane emissions with high spatial resolution using GOSAT satellite data. *Atmospheric Chemistry and Physics*, 15, no. 12:pp. 7049–7069. doi:10.5194/acp-15-7049-2015, 2015.

Tuzson, B., Graf, M., Ravelid, J., Scheidegger, P., Kupferschmid, A., Looser, H., Morales, R. P., and Emmenegger, L. A compact QCL spectrometer for mobile, high-precision methane sensing aboard drones. *Atmospheric Measurement Techniques*, 13, no. 9:pp. 4715–4726. doi:10.5194/amt-13-4715-2020, 2020.

United States National Oceanic and Atmospheric Administration and United States Air Force. *US standard atmosphere, 1976*, volume 76. National Oceanic and Atmospheric Administration, Washington, D.C., 1976.

Vane, G., Green, R. O., Chrien, T. G., Enmark, H. T., Hansen, E. G., and Porter, W. M. The airborne visible/infrared imaging spectrometer (AVIRIS). *Remote Sensing of Environment*, 44, no. 2-3:pp. 127–143. doi:10.1016/0034-4257(93)90012-m, 1993.

Vankranendonk, M., Philippot, P., Lepot, K., Bodorkos, S., and Pirajno, F. Geological setting of Earth's oldest fossils in the ca. 3.5Ga Dresser Formation, Pilbara Craton, Western Australia. *Precambrian Research*, 167, no. 1-2:pp. 93–124. doi:10.1016/j.precamres.2008.07.003, 2008.

Varon, D. J., Jacob, D. J., McKeever, J., Jervis, D., Durak, B. O. A., Xia, Y., and Huang, Y. Quantifying methane point sources from fine-scale satellite observations of atmospheric methane plumes. *Atmospheric Measurement Techniques*, 11, no. 10:pp. 5673–5686. doi:10.5194/amt-11-5673-2018, 2018.

Varon, D. J., Jervis, D., McKeever, J., Spence, I., Gains, D., and Jacob, D. J. High-frequency monitoring of anomalous methane point sources with multispectral Sentinel-2 satellite observations. *Atmospheric Measurement Techniques*, 14, no. 4:pp. 2771–2785. doi:10.5194/amt-14-2771-2021, 2021.

Varon, D. J., McKeever, J., Jervis, D., Maasakkers, J. D., Pandey, S., Houweling, S., Aben, I., Scarpelli, T., and Jacob, D. J. Satellite Discovery of Anomalously Large Methane Point Sources From Oil/Gas Production. *Geophysical Research Letters*, 46, no. 22:pp. 13507–13516. doi:10.1029/2019gl083798, 2019.

Vaughan, R., Calvin, W. M., and Taranik, J. V. SEBASS hyperspectral thermal infrared data: surface emissivity measurement and mineral mapping. *Remote Sensing of Environment*, 85, no. 1:pp. 48–63. doi:10.1016/s0034-4257(02)00186-4, 2003.

Veefkind, J., Aben, I., McMullan, K., Förster, H., de Vries, J., Otter, G., Claas, J., Eskes, H., de Haan, J., Kleipool, Q., van Weele, M., Hasekamp, O., Hoogeveen, R., Landgraf, J., Snel, R., Tol, P., Ingmann, P., Voors, R., Kruizinga, B., Vink, R., Visser, H., and Levelt, P. TROPOMI on the ESA Sentinel-5 Precursor: A GMES mission for global observations of the atmospheric composition for climate, air quality and ozone layer applications. *Remote Sensing of Environment*, 120:pp. 70–83. doi:10.1016/j.rse.2011.09.027, 2012.

Veefkind, P., Levelt, P., Rozemeijer, N., Hoogeveen, R., Aben, I., de Vries, J., Otter, G., Dobber, M. R., and Kleipool, Q. From ozone monitoring instrument (OMI) to tropospheric monitoring instrument (TROPOMI). In Costeraste, J., Armandillo, E., and Karafolas, N., editors, *International Conference on Space Optics — ICSO 2008*. SPIE. doi:10.1117/12.2308268, 2017.

Vinković, K., Andersen, T., de Vries, M., Kers, B., van Heuven, S., Peters, W., Hensen, A., van den Bulk, P., and Chen, H. Evaluating the use of an Unmanned Aerial Vehicle (UAV)-based active AirCore system to quantify methane emissions from dairy cows. *Science of The Total Environment*, 831:p. 154898. doi:10.1016/j.scitotenv.2022.154898, 2022.

Wallace, J. and Hobbs, P. *Atmospheric Science: An Introductory Survey*. International Geophysics Series. Elsevier Academic Press. ISBN 9780127329512, 2006.

Warneck, P. *Chemistry of the natural atmosphere*. Academic Press, San Diego. ISBN 9780127356327, 2000.

White, W., Anderson, J., Blumenthal, D., Husar, R., Gillani, N., Husar, J., and Wilson, W. Formation and transport of secondary air pollutants: ozone and aerosols in the St. Louis urban plume. *Science*, 194, no. 4261:pp. 187–189. doi:10.1126/science.959846, 1976.

Wild, M., Folini, D., Hakuba, M. Z., Schär, C., Seneviratne, S. I., Kato, S., Rutan, D., Ammann, C., Wood, E. F., and König-Langlo, G. The energy balance over land and oceans: an assessment based on direct observations and CMIP5 climate models. *Climate Dynamics*, 44, no. 11-12:pp. 3393–3429. doi:10.1007/s00382-014-2430-z, 2014.

Wolff, S., Ehret, G., Kiemle, C., Amediek, A., Quatrevalet, M., Wirth, M., and Fix, A. Determination of the emission rates of CO2 point sources with airborne lidar. *Atmospheric Measurement Techniques*, 14, no. 4:pp. 2717–2736. doi:10.5194/amt-14-2717-2021, 2021.

Wood Buffalo Environmental Association. Ambient Air Monitoring Station Site Documentation - AMS 19 Firebag. Available under https://wbea.org/stations/firebag/, 2020.

Wu, L., Hasekamp, O., Hu, H., Landgraf, J., Butz, A., aan de Brugh, J., Aben, I., Pollard, D. F., Griffith, D. W. T., Feist, D. G., Koshelev, D., Hase, F., Toon, G. C., Ohyama, H., Morino, I., Notholt, J., Shiomi, K., Iraci, L., Schneider, M., de Mazière, M., Sussmann, R., Kivi, R., Warneke, T., Goo, T.-Y., and Té, Y. Carbon dioxide retrieval from OCO-2 satellite observations using the RemoTeC algorithm and validation with TCCON measurements. *Atmospheric Measurement Techniques*, 11, no. 5:pp. 3111–3130. doi:10.5194/amt-11-3111-2018, 2018.

Wunch, D., Toon, G. C., Blavier, J.-F. L., Washenfelder, R. A., Notholt, J., Connor, B. J., Griffith, D. W. T., Sherlock, V., and Wennberg, P. O. The Total Carbon Column Observing Network. *Philosophical Transactions of the Royal Society A: Mathematical, Physical and Engineering Sciences*, 369, no. 1943:pp. 2087–2112. doi:10.1098/rsta.2010.0240, 2011.

W. Paltridge, G. and R. Platt, C. M. *Radiative processes in meteorology and climatology*. Developments in atmospheric science ; 5. Elsevier, Amsterdam [u.a.]. ISBN 0444414444 and 9780444414441. XVII, 318 S : graph. Darst. URL `https://suche.suub.uni-bremen.de/peid=B03962270`, 1976.

Zahnle, K., Schaefer, L., and Fegley, B. Earth's Earliest Atmospheres. *Cold Spring Harbor Perspectives in Biology*, 2, no. 10:pp. a004895–a004895. doi:10.1101/cshperspect.a004895, 2010.

Modifications to the initial submission

Location	Original text	Modified text
Page iv	Is it possible to apply the weighting function modified differential absorption spectroscopy (WFM-DOAS) retrieval method to hyperspectral data to infer greenhouse gas emissions?	Is it possible to apply the weighting function modified differential optical absorption spectroscopy (WFM-DOAS) retrieval method to hyperspectral data to infer greenhouse gas emissions?
Page 3	These include measurements in the thermal infrared spectral region (e.g., the Spatially Enhanced Broadband Array Spectrograph System (SEBASS, Vaughan et al., 2003) or the Hyperspectral Thermal Emission Spectrometer (HyTES, Hook et al., 2013)) successfully detected CH_4 plumes when flying low.	These include measurements in the thermal infrared spectral region (e.g., the Spatially Enhanced Broadband Array Spectrograph System (SEBASS, Vaughan et al., 2003) or the Hyperspectral Thermal Emission Spectrometer (HyTES, Hook et al., 2013)), which successfully detected CH_4 plumes when flying low.
Page 3	Successful methane retrievals were done using either a cluster tuned match filter approach (Thompson et al., 2015), which uses a hypothesis test between the presence and absence of additional CH_4 to infer CH_4 increases.	Successful methane retrievals were mostly done using a cluster tuned match filter approach (Thompson et al., 2015), which uses a hypothesis test between the presence and absence of additional CH_4 to infer CH_4 increases.
Page 5	The results of the methods applied to the data sets are given in Chapter 6. First, the retrieval of column enhancements from AVIRIS-NG with the WFM-DOAS method is given in Sect. 6.1, comparisons with other retrievals and inversion of detected plumes with the cross-sectional flux method are also shown.	The results of the methods applied to the data sets are given in Chapter 6. First, the retrieval of column enhancements from AVIRIS-NG with the WFM-DOAS method is given in Sect. 6.1, where comparisons with other retrievals and inversion of detected plumes with the cross-sectional flux method are also shown.
Page 13	The yearly net carbon fluxes for the decade 20010 - 2019 estimated by the GCP are given in Fig. 2.3 in $\mathrm{Gt\,C\,yr^{-1}}$.	The yearly net carbon fluxes for the decade 2010 - 2019 estimated by the GCP are given in Fig. 2.3 in $\mathrm{Gt\,C\,yr^{-1}}$.

Location	Original text	Modified text
Page 15	$CO_2 + CO_2^{2-} + H_2O \rightleftharpoons {}_2HCO_3^-$	$CO_2 + CO_2^{2-} + H_2O \rightleftharpoons 2\,HCO_3^-$
Page 15	$Ca^{2+} + {}_2HCO_3^- \longrightarrow CaCO_3 + H_2CO_3$	$Ca^{2+} + 2\,HCO_3^- \longrightarrow CaCO_3 + H_2CO_3$
Page 15	The lifetime calculated in this manner is more in the order of several ten thousand years and might even be more than 100 000 thousand years (see e.g. Archer et al., 2009, and sources within).	The lifetime calculated in this manner is more in the order of several ten thousand years and might even be more than 100 000 years (see e.g. Archer et al., 2009, and sources within).
Page 18	(x-axis pressure label not visible)	Changed image so that pressure label for x-axis is visible
Page 46	, they have significant difficulties detecting sources at the surface when flying higher	, they had significant difficulties detecting sources at the surface when flying higher
Page 54	The solar spectrum I_0 for the forward model is a combination of a polynomial fitted to the Thullier-Kurucz solar spectrum for the solar background radiation and the Toon high-resolution solar spectrum (Toon et al., 2016) in the 2016 version, calculated by Max Reuter.	The solar spectrum I_0 for the forward model is a combination of a polynomial fitted to the Thullier-Kurucz solar spectrum for the solar background radiation and the Toon high-resolution solar spectrum (Toon, 2015) in the 2016 version, calculated by Max Reuter.
Page 132	For the 1-window absorption-only retrieval, the xCH_4 was plotted against the also visible in Fig. 6.34, where the background white light corrected intensity was plotted beneath the xCH_4.	This is also visible in Fig. 6.34 for the 1-window absorption-only retrieval, where the background white light corrected intensity was plotted beneath the xCH_4.